THE UNIVERSITY OF CHICAGO

TRANSITION METAL MEDIATED NON-DIRECTED C-H FUNCTIONALIZATION

A DISSERTATION SUBMITTED TO
THE FACULTY OF THE DIVISION OF THE PHYSICAL SCIENCES
IN CANDIDACY FOR THE DEGREE OF
DOCTOR OF PHILOSOPHY

DEPARTMENT OF CHEMISTRY

BY
JOSEPH J. GAIR

CHICAGO, ILLINOIS
AUGUST 2018

To my parents,

for encouraging curiosity

and exemplifying kindness.

Table of Contents

List of Figures

List of Tables

List of Equations

Abstract

The structure and reactivity of organometallic species relevant to non-directed C-H activation and C-H functionalization are studied to inform the design of discrete pre-catalysts suitable for incorporation into supramolecular scaffolds. First, a study of transmetallation of hydrocarbyl ligands between transition metals demonstrates potential for dual-metal catalysis, in which one species cleaves C-H bonds and transfers the metallated fragment to a second metal suited for functionalization of the metal-carbon bond. Ligand modification of a rhodium (PNP) pincer complex gives rise to 100-fold rate enhancements toward non-directed C-H activation and this stoichiometric reactivity is leveraged to develop a catalytic method for non-directed C-H functionalization. During investigation of C-H activation with (PNP)Rh complexes, a heterobimetallic transition state analogue was isolated and characterized. Bonding analysis of the analogue demonstrates that the unusual geometry is supported by the same types of bonding interactions as those found in the putative transition state. Isolation and characterization of palladacycles coordinated by mono-protected amino acids (MPAA) reveals an unexpected MPAA-bridged di-palladium structure. Steady state kinetic analysis of Pd-MPAA catalyzed C-H functionalization, in particular the kinetic method of continuous variation, reveals that MPAA-bridged di-palladium complexes are responsible for MPAA-dependent rate acceleration and enantioinduction.

Acknowledgements

I am thankful to my advisor, Jared Lewis, for giving me the freedom to explore new ideas while helping me to keep the bigger picture in focus. I feel incredibly fortunate to have been mentored by someone who clearly loves discussing new ideas with students.

My committee members, John Anderson and Richard Jordan, were of great help throughout my graduate education. Their thoughtful questions at organometallic super group meetings expanded my view of catalysis and their technical expertise led to significant advances in my own research.

It was a true delight to collaborate with and mentor Natalie Chan. Her dedication to detail and her persistence in pushing through challenging research has been an inspiration. When others would have given up, she came in early. In what proved to be a tumultuous final year in Chicago, Natalie's support and friendship kept me afloat. I cannot thank her enough.

I was incredibly fortunate to have mentored two talented undergraduate researchers, Michael Roy and Yehao Qiu. Their contributions to our projects were invaluable and the speed with which they learned was remarkable. Rocketing ahead in promising graduate careers of their own, soon they will be the ones teaching me.

If a picture is worth a thousand words, it is only because Alexander Filatov took ten-thousand pictures. Much of my graduate work began with furrowed brows at Alex's desk as it slowly dawned on us that we had found something unexpected and remarkable. Alex's patience with tricky crystals and his willingness to tinker and teach until we came to a satisfactory structure set the stage for much of my graduate research.

Our computational collaborators Brandon Haines and Jamal Musaev at Emory University as well as Rahul Khade and Yong Zhang at Stevens Institute of Technology helped us to peer beyond the limits of experimental observation to gain insight into the molecular details that enable catalytic outcomes. Working with talented experts in computational science forced me to appreciate the enormous complexity of outwardly simple systems. Their insights sharpened my thinking and improved my science.

My research would not have been possible without the patient assistance of several dedicated staff scientists; especially Sunyin Grass at the Advanced Photon Source, Antoni Jurkiewicz at University of Chicago NMR Facilities, and Jonathan Skone at the University of Chicago's Research Computing Center.

The hallmark of my graduate work was time spent in lab with wonderful lab mates. As a whole, the members of the Lewis group were inclusive, curious, thoughtful, and so much fun. They were not formal, so I will do away with transitional phrases and just list what I loved so much about each of them. Landon taught me how to make molecules. He taught me how to mentor and care for younger lab mates. He showed me how be a patient listener and observer, but I don't think that skill stuck. Ken made me wonder. His chemical daydreams made working in lab a creative playground. There was nothing we couldn't dream up and test. He was also an entertainer; I'm thankful for the many times he made me laugh. Yifan is a diligent helper, a thoughtful lab mate, and very often the source of unexpected, soft-spoken hilarity. If it was possible to be a loving parent of a household of rambunctious scientific instruments, that is what David would be. I could have a panic attack just thinking about the heaps of leaky tubing and hours of streaky peaks that David tends to, but somehow, he manages to fix instruments with what appears to be affection and good humor. I could not have done my research without his constant maintenance and frequent emergency assistance. I did not spend nearly enough time with Atreyi, Brian, Christian, Harrison, or Krysten, but I am thankful for them all the same. They continue to make the Lewis group a supportive, cheerful, and inclusive place. I am proud to be associated with them and I can't wait to see the great work that they will do at Indiana University.

Judith Kamm was a perfect roommate for three years. I am grateful for her friendship, support, and pretzel rolls. More recently, I am incredibly thankful to both Judith and Hunter Vibbert for inviting me to stay in their home while I finished my work in Chicago.

Tony and Marie Andorfer have welcomed me into their home and given me the sense that I have a second family a short car ride away. Mary Andorfer has been there for every part of my graduate education and made every moment better.

Most of all, I am grateful to my parents. By encouraging curiosity throughout my life, they have instilled in me a sense of wonder that makes coming to work a joy. By constantly putting the needs of others before their own, they remind me that I have an obligation to use the skills and knowledge obtained in my education to lessen the suffering of others. They have provided for me and supported me in every way imaginable and I cannot thank them enough.

Chapter 1: Introduction

The ability to construct molecules in a controlled manner has had an indelible impact on the quality and duration of human life. This technology is built on a useful approximation—the functional group. By conceiving molecules as a collection of convertible functional groups on an inert framework, chemists can distill the overwhelming complexity of the wave function of an organic molecule down to a few moving pieces. The reliable reactivity of functional groups is the conceptual basis for synthetic chemistry. This useful approximation, however, obscures the most abundant structural element in organic molecules, the C-H bond.

The ability to convert a given C-H bond into a C-C bond or a new functional group has the potential to revolutionize the logic of chemical synthesis.[1,2] Rather than depending exclusively on the sequential interconversion of compatible functional groups, C-H functionalization could enable direct conversion of a conventionally inert C-H bond into desired functionality. Such reactivity would improve the efficiency of chemical synthesis by eliminating the need for pre-functionalized substrates, protecting group strategies, and interconversions of functional groups that are not in the target structure.

Given the ubiquity of C-H bonds in organic molecules, reliable methods for predictable, selective C-H functionalization will transform the way chemists make molecules.[3] On the other edge of this sword lies the greatest challenge in developing methods for C-H functionalization: site selectivity. How can chemists develop catalysts that reliably and predictably convert one C-H bonds in a molecule that contains multiple, inequivalent, and relatively inert C-H bonds? Moreover, how can a such a catalyst be generalized to give predictable selectivity on number of substrates?

A common approach to this challenge is the use of substrate-based catalyst directing groups (Figure 1A-C).[4] The term directing group does not have a single agreed upon definition. In this thesis, I will use directing group to describe any functional group within a substrate that provides predictable site selectivity in C-H functionalization. Different catalysts may respond to the directing group to give different selectivities, but moving or removing this functional group will either alter selectivity or eliminate the desired reactivity all together. Defined in this way, "directing group" describes functional groups that bind a metal catalyst to hold the metal in proximity to one C-H bond (Figure 1A). It also includes functional groups that impart an electronic bias for reactivity at a given C-H bond (Figure 1B and C). Many clever and nuanced iterations of directed C-H functionalization have been developed. Some of these methods provide predictable selectivity and useful reactivity on a variety of related substrates and constitute an important addition to the toolkit of synthetic chemists.[5] The unifying feature of directed C-H functionalization, however, is a dependence on functional groups and, ultimately, substrate control. As such, directed methods, by their nature, cannot harness the full potential of C-H functionalization to bring about a paradigm shift in chemical synthesis by enabling reactivity independent of functional groups.

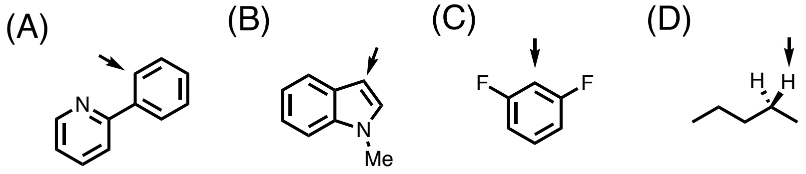

Figure 1 (A-C) Directed and (D) non-directed C-H functionalization.

An alternative approach to developing catalysts for C-H functionalization, frequently called non-directed, depends on generating of highly reactive intermediates capable of cleaving many C-H bonds in a given substrate (Figure 1D). [6-8] Selectivity is then achieved by developing ligands which enable differentiation by subtle steric and electronic differences between C-H bonds that do not depend on the presence of particular functional groups.[6] Even the most advanced methods for non-directed C-H functionalization offer no solution to controlling predictable site selectivity with slightly larger and more complicated substrates containing multiple C-H bonds with similar steric profiles.

Nature, on the other hand, has evolved catalysts that selectively functionalize C-H bonds on substrates large and small: some with exquisite substrate specificity and others with remarkable generality.[9] The molecular machinery that enables evolution in nature can be controlled by chemists to optimize catalysts for a wide variety of transformations.[10,11] Whereas conventional catalyst development requires ligand synthesis for each new hypothesis, directed evolution allows chemists to assess the reactivity and selectivity of libraries of hundred to tens of thousands of catalyst variants. By iterative incorporation of beneficial catalysts modifications, directed evolution provides a platform for catalyst optimization that is limited only by the initial reactivity and the number of rounds of mutagenesis and screening that can be completed during the duration of the evolution campaign.

A unifying objective of the Lewis group is to develop chemistry and molecular biology that enables the incorporation of synthetic organometallic co-factors capable of non-directed C-H functionalization into evolvable scaffolds. Within this program, my role has been to study the reactivity and mechanisms of organometallic complexes and catalysts relevant to non-directed C-H bond cleavage as part of combined effort to develop artificial metalloenzymes for catalyst controlled non-directed C-H functionalization.[12]

Chapter 2: Transmetallation Between Transition Metals

Introduction

Fundamental studies of stoichiometric, non-directed C-H activation predate much of the recent boom in transition metal catalyzed C-H functionalization, and this valuable research continues today.[3] Mechanistic studies of well-defined organometallic complexes reacting with hydrocarbons to give stable, spectroscopically observable adducts form the basis for much of our current understanding of the intimate details of transition metal mediated C-H bond cleavage. Many of these foundational studies demonstrated complexes with reactivity at room temperature toward a variety of hydrocarbons without assistance from substrate directing effects (electronic bias, chelation, etc.). Reactive intermediates that readily and indiscriminately cleave a wide variety of C-H bonds are ideal candidates for incorporation into evolvable scaffolds to control selectivity.

Despite the important contributions to basic science from studies of stoichiometric hydrocarbon C-H activation, none of this stoichiometric chemistry has translated to practical catalysts for C-H functionalization (with the notable exception of catalytic H/D exchange). One of the key challenges in leveraging stoichiometric chemistry to develop new catalysts is the stability of the resulting hydrocarbyl complexes. Complexes that are sufficiently stable to enable quantification of product formation in stoichiometric studies are often relatively inert by design and require harsh reagents to enable functionalization of the metallated hydrocarbyl fragment. We hypothesized that we could harness the remarkably mild non-directed C-H activation chemistry of complexes like those in (Figure 2A, M^1) and translate that reactivity into catalysis by transferring the activated hydrocarbyl fragment from a relatively inert organometallic adduct (M^1) to a second organometallic species (M^2) via transmetallation (Figure 2B).

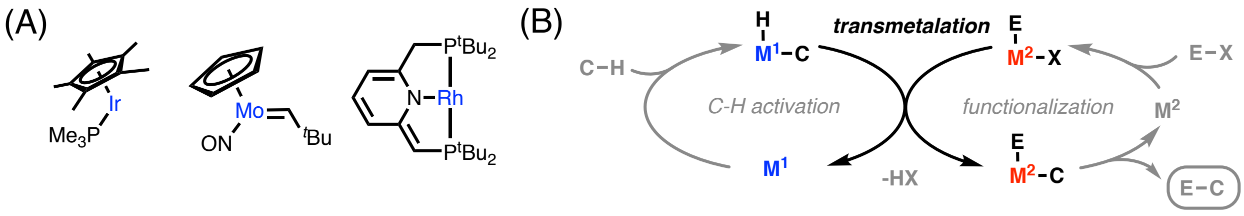

Figure 2. (A) Proposed cycle for dual catalytic, non-directed C-H functionalization (B) Reactive fragments reported to mediate room temperature, non-directed C-H bond cleavage.

The stoichiometric transfer of alkyl and aryl ligands between transition metals has been reported for a wide range of transition metals.[13-16] Some of the earliest and most extensively studied examples of this reactivity involve transfer of an alkyl or aryl ligand from a late transition metal complex to the soft Lewis acids gold (I) and mercury (II).[17-21] The connection between C-H activation and transmetallation was established early on when Bergman reported that $(\mathrm{Cp}^*)(\mathrm{PMe}_3)\mathrm{Ir}$ (hereafter [Ir]) complexes could activate neopentane and transfer the activated neopentyl fragment to $\mathrm{Hg(Cl)}_2$ (Figure 3A).[22] Notably, the other examples of reagents suitable for cleaving the [Ir]-neopentyl bond involved either fluorosulfonic acid or bromine and were thus the much harsher.[22] Most hydrocarbyl group transfer reactions involve substitution of an R type ligand for an X type ligand; however there are also instances in which R type ligands exchange without a labile X type ligand to drive the equilibrium (Figure 3B[23] and C[24]). Instances of aryl group transfer that are relevant to the work in this chapter and that are sufficiently exothermic to drive the reaction to complete conversion are shown in Figure 3 C-E.[25] Reviews by Osakada provide an excellent summary of additional examples of transmetallation between group 10 electrophiles with ligands other than cyclooctadiene (cod).[13,14]

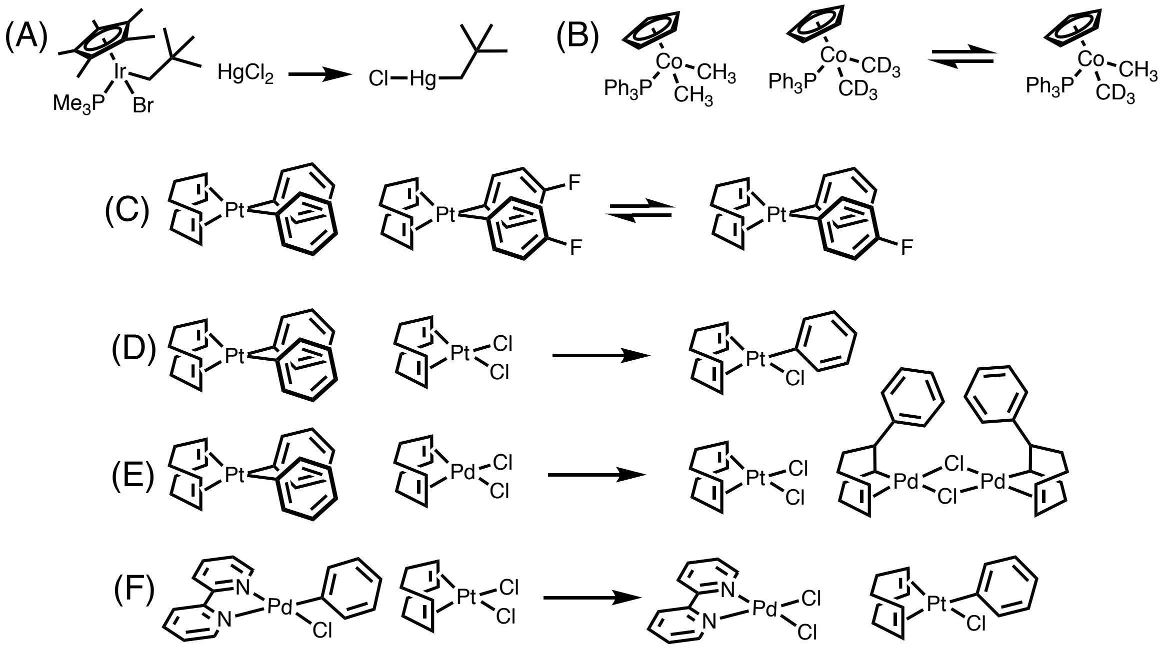

Figure 3. Relevant examples of hydrocarbyl group transfer between transition metals yielding stable, organometallic products.

The type of alkyl and aryl group transfer chemistry illustrated in Figure 3 has been invoked as a key step in a number of recent catalytic processes (Figure 4). The reactions in Figure 4A[26] and B[27] show catalytic transformations that were developed based on the hypothesis that two independent modes of organometallic reactivity could be coupled via transmetallation of an activated fragment from one organometallic intermediate to another. The chemistry in Figure 4C provides an instance of dual catalytic C-H functionalization built up from the observation of stoichiometric reactions and the reactivity of putative intermediates; namely C-H activation by a phosphino silver pivalate complex and transmetallation of the isolated silver aryl species to a putative Pd(II) intermediate.[28] The chemistry in Figure 4C is a highly encouraging precedent for the use of transmetallation between transition metals as a strategy in metal catalyzed C-H functionalization; however, because this chemistry depends on the presence of acidifying functional groups for reactivity and selectivity, it is not a good candidate for incorporation in evolvable scaffolds because evolving for altered selectivity depends on some observable reactivity on an alternate position to start with.

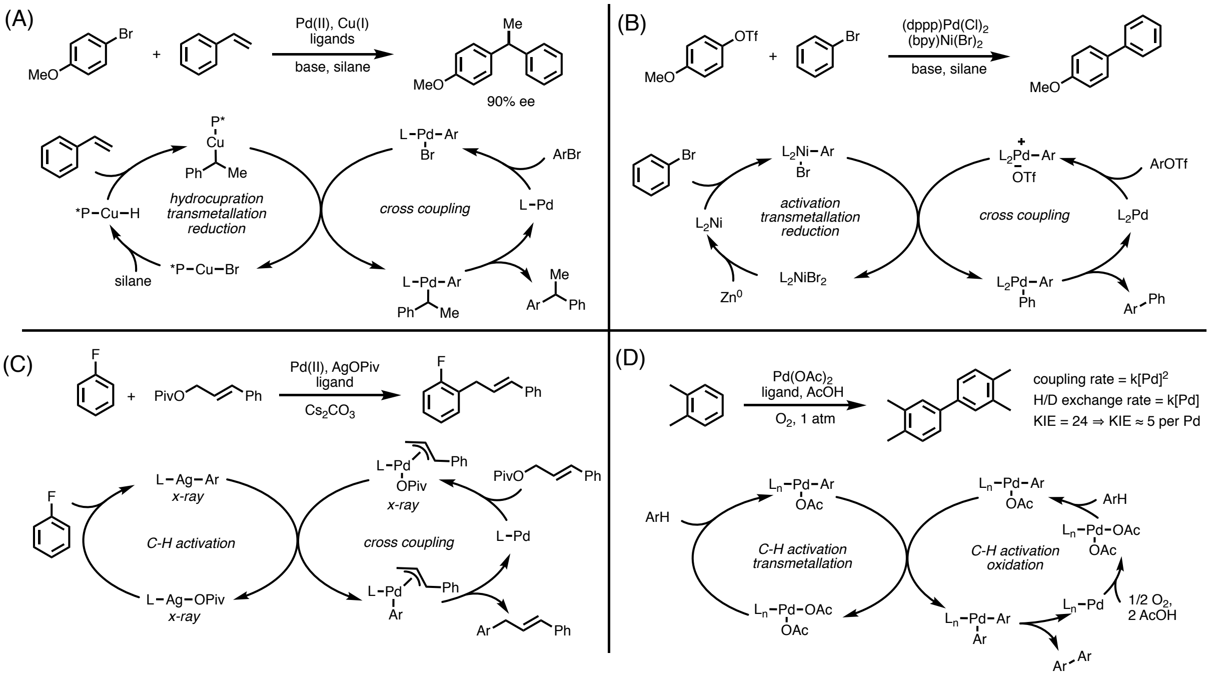

Figure 4 Recent examples of catalytic reactions that invoke transmetallation between transition metals.

In contrast to the approach taken in Figure 4C (isolation and testing reactivity of putative intermediates), the chemistry in Figure 4D provides a wonderful example of the application of steady state kinetics to reveal entirely new and unexpected catalytic pathways.[29] The resulting reaction is also dual catalytic C-H functionalization, but rather than operating through two separate catalytic cycles with different metals, the reaction proceeds through an unexpected, rate limiting transmetallation between two fragments that underwent independent C-H activations. This mechanism can be understood through three key observations. First, there is a second order rate dependence on palladium indicating that two palladium centers come together in the turnover limiting transition state. In contrast to second order dependence on palladium for the overall reaction, the rate of H/D exchange is first order in palladium indicating that C-H activation occurs at a palladium complex with the same nuclearity as the catalyst resting state. Taken together, these two observations nicely account for the abnormally high global kinetic isotope effect ($k_H/k_D = 24$), which is consistent with two palladium centers each with a KIE of ~5 coming together in a bimolecular transmetallation.

In light of the precedent for spectroscopically observable transmetallation between two organometallic complexes (Figure 3) and the encouraging reports of dual catalytic processes in the literature (Figure 4), we set out to develop a method that would harness the non-directed C-H activation reactivity of intermediates like those in Figure 2A for dual catalytic, non-directed C-H functionalization.

Previous Work

The mechanism of benzyl group transfer from [Ir](Bn)$_2$ to (cod)Pt(Me)(TFA) was studied in detail in the Lewis group. [30] The proposed mechanism in the presence of a large excess of [Ir](Bn)$_2$ consists of pre-equilibrium ionization of (cod)Pt(Me)(TFA), to generate the reactive electrophilic platinum cation (cod)Pt(Me)$^+$, followed by rate limiting benzyl group transfer (Figure 5). The proposed mechanism is supported by first order decays in (cod)Pt(Me)(TFA), saturation behavior under varying excesses of [Ir](Bn)$_2$, inhibition by exogenous trifluoroacetate, a positive correlation between pseudo-first order rate constants and solvent dielectric constant, and a similar correlation with platinum counter anion electrofugacity. [30]

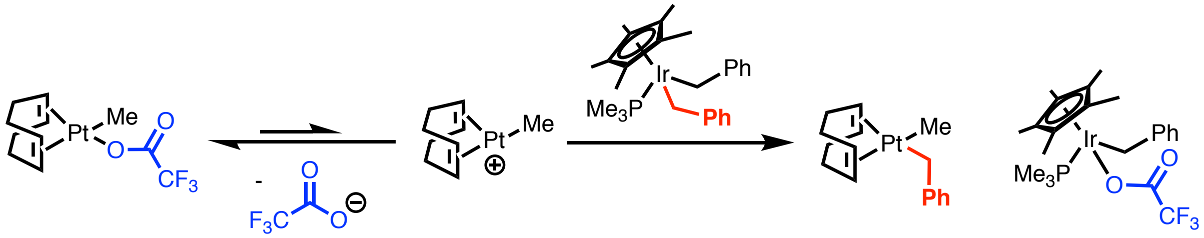

Figure 5. Proposed mechanism of benzyl group transfer from $[Ir](Bn)_2$ to (cod)Pt(Me)(TFA)

Based on these observations, Liwei Chen calculated a related methyl group transfer transition state (Figure 6). A preliminary analysis of the calculated transition state suggested that group transfer should proceed with retention of stereochemistry. Subsequent work by Yehao Qiu, however, clarified that the stereochemical course of the calculated transition state was, in fact, pre-determined by the atomic labeling of the three methyl hydrogens in the input reactant and product structures.

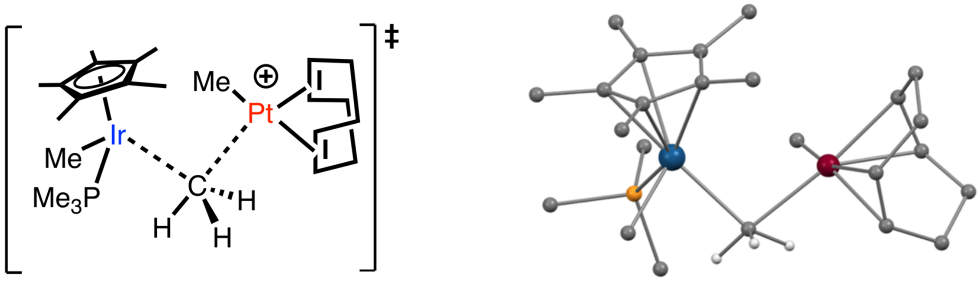

Figure 6. Calculated transition state for methyl group transfer.

With new insight into the mechanism of hydrocarbyl group transfer from $[Ir](R)_2$ to Pt(II) electrophiles, Dr. Landon Durak sought to leverage this understanding toward the target catalytic cycle (Figure 2).[31] Key to this endeavor was recognizing the importance of equilibrating cationic Pt(II) electrophiles to promote group transfer. This insight motivated screening the effect of halide abstracting salts (e.g. potassium polyfluoro-tetrakis-phenyl borates, $KBAr^F{}_4$), which led to the discovery of mild conditions suitable for palladium catalyzed cross coupling of aryl halides with $[Ir](CH_2Ar)_2$ nucleophiles (Figure

7). The observed cross coupling reactivity established the feasibility of transmetallation from organometallic fragments related to C-H activation (Figure 2, transmetallation) to a second transition metal (M^2) suitable for M-C functionalization under conditions relevant to M^2 catalysis (Figure 2, functionalization).[31]

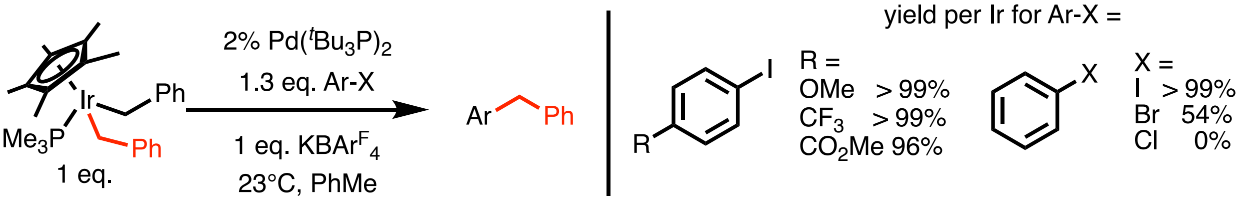

Figure 7. Palladium catalyzed cross coupling of aryl halides with $[Ir](Bn)_2$.

In a key breakthrough toward achieving dual catalytic, non-directed C-H functionalization (Figure 2), Dr. Durak developed conditions for iridium promoted, palladium catalyzed cross coupling of simple arenes with aryl halides (Figure 8). Once again, insight gleaned from initial mechanistic studies (the importance of cationic group 10 electrophiles) was essential in the development of this reactivity–the reaction is effectively shut down in the absence of ionizing additive $KBAr^4_F$. Importantly, this iridium promoted, palladium catalyzed non-directed C-H functionalization of simple arenes establishes conditions that are simultaneously suitable for Ir promoted C-H activation, Ir to Pd transmetallation, and Pd catalyzed cross coupling, nearly completing the target cycle outlined in Figure 2.

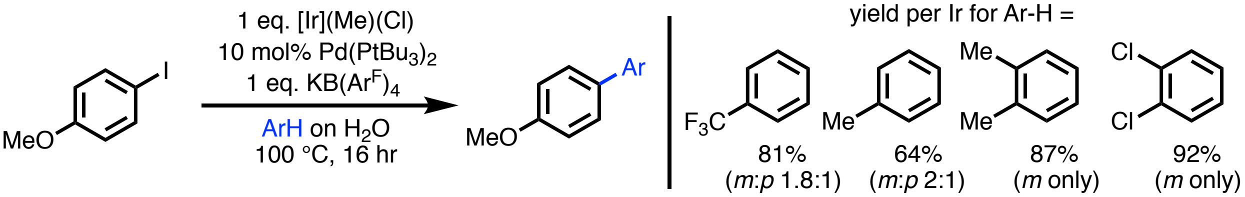

Figure 8 [Ir] promoted Pd(II) catalyzed non-directed C-H functionalization of simple arenes with aryl iodides.

At this point in the Lewis group's campaign toward dual catalytic C-H functionalization, the only remaining obstacle was to develop conditions amenable to turnover of the C-H activating [Ir] fragment (Figure 9, dashed arrow indicates obstacle to turnover). Under these conditions, the first C-H activation is driven by elimination of methane; however, the likely iridium dihalide product of sequential iridium promoted C-H activation and transmetallation ([Ir]$(X)_2$) does not undergo exothermic C-H bond cleavage to form a stable organometallic product. Although [Ir]$(X)_2$ cannot form stable C-H activation adducts, it is capable of mediating reversible C-H bond cleavage as evidenced by its utility as an efficient catalyst for H/D exchange of simple arenes with D_2O (Figure 9, dashed arrow). Given the known reactivity of [Ir]$(X)_2$ toward C-H bond cleavage, we hypothesized that perhaps a dual catalytic system could be achieved by accelerating the sluggish transmetallation, so that short lived organo-iridium intermediates (those trapped by D_2O in H/D exchange) could be trapped by transmetallation to Pd. In order accelerate transmetallation under catalytic conditions, we sought to develop a deeper understanding of the factors that control the rate and mechanism of transmetallation by probing the substituent effects, stereochemistry, and scope of transmetallation of hydrocarbyl fragments from complexes relevant to C-H activation.

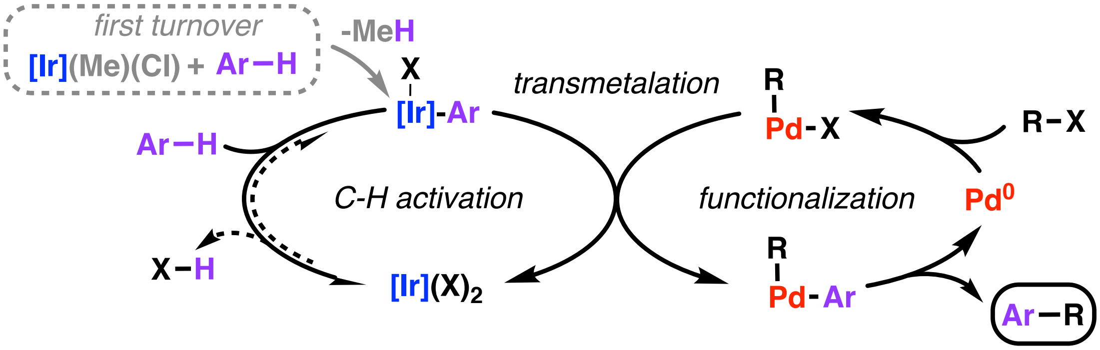

Figure 9 Putative reactivity and obstacle to iridium turnover in [Ir] promoted Pd(II) catalyzed non-directed C-H functionalization of simple arenes with aryl iodides.

Substituent Effects

The proposed mechanism of benzyl group transfer from $[Ir](Bn)_2$ to (cod)Pt(Me)(TFA) (Figure 5) suggests a buildup of positive charge on $[Ir](Bn)_2$ as it proceeds from a neutral reactant to a charged transition state in the bimolecular benzyl group transfer (Figure 10A). Substituent effects were determined by the ratio of transmetallation products at early time points under pseudo first order competition conditions to eliminate interference from competing chloride impurities using procedure was originally reported in studies of transmetallation of benzyl stannanes.[32] Under these conditions, transmetallation to Pt(II) is suppressed by electron withdrawing substituents and slightly accelerated by electron donating substituents, consistent with partial positive charge build up in the rate limiting transition structure (Figure 10B). These relatively small substituent effects were not promising with regard to our goal of enhancing transmetallation to enable iridium turnover (Figure 9). Notably, the same effects are more pronounced in the more relevant system, transmetallation to catalytic Pd(II) (Figure 10C).

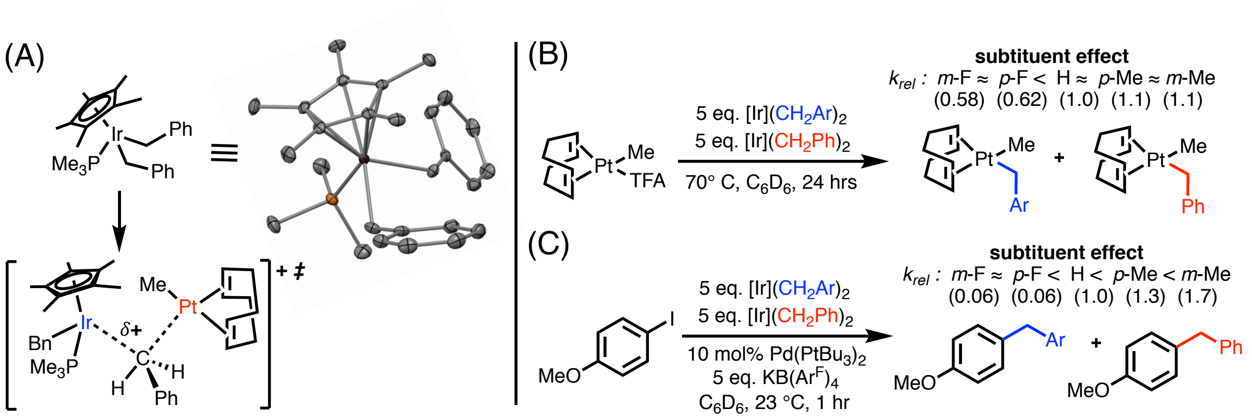

Figure 10. Substituent effects: (A) positive charge developing on transmetallation transition state and ORTEP of $[Ir](Bn)_2$ with 50% ellipsoids; (B) relative rates of transmetallation to stoichiometric Pt(II) consistent with partial positive charge build up in rate limiting transition state; (C) relative rates of transmetallation to catalytic Pd(II) consistent with partial positive charge build up in turnover limiting transition state.

Although there is a correlation between substituent parameter and rate of transmetallation of benzyl groups to group 10 electrophiles, the effect is decidedly non-linear using any of the standard substituent constants (σ, σ^+, σ^-, σ^{CEBE}). One possible cause for the observed non-linear behavior is the inequivalence of the substituted benzyl groups in the transmetallation transition state. Differential resonance and inductive contributions from the ancillary benzyl group (modifying electron density on iridium) and the benzyl group being transferred may contribute to non-linearity. Overall, our investigation of the electronic demands of benzyl group transfer from $[Ir](Bn)_2$ to group 10 electrophiles is consistent with our hypothesis that positive charge develops on the iridium nucleophile in the group transfer transition state. The rate enhancement provided by electron rich substituents, however, is not sufficiently large to trap fleeting organo-iridium intermediates generated under catalytic conditions (Figure 9).

Stereochemical Probe

Motivated by a desired to understand to the molecular details of hydrocarbyl group transfer between two transition metals we designed a stereochemical probe with the end goal of leveraging the resulting insights to accelerate transmetallation and thereby enable dual catalysis. We predicted that a stereochemical probe could shed light on the orbital symmetry requirements of hydrocarbyl group transfer between transition metals and validate the DFT model shown in Figure 6. An understanding of the orbitals participating in hydrocarbyl group transfer would allow for the rational design of catalyst and substrate modifications to accelerate transmetallation. We hypothesized that a calculated transition state built on rigorous kinetic analysis and validated by a Hammett study and stereochemical probe could serve as a reliable model for exploring a wide variety of catalyst modifications *in-silico* to guide our synthetic efforts.

Our original stereochemical hypothesis–retention of stereochemistry, based on the calculated transition state in Figure 6–and our proposed probe of this hypothesis are outlined in Figure 11. Diagnostic $^3J_{HH}$ coupling in stereospecifically labeled 1,2-di-deuterio-neohexyl ligands has made this fragment a useful stereochemical probe for a variety of organometallic chemistries.[21,33,34] The Bergman group previously reported stereospecific (S_N2) addition of deuterium labeled neohexyl ligands to [Ir].[35] Moreover, Dr. Durak reported unpublished evidence to suggests that [Ir](neohexyl)$_2$ was capable of transferring a neohexyl ligand to (cod)Pt(Me)(TFA), albeit in low yield. We hypothesized that tuning the ancillary ligand on [Ir](neohexyl)(R), the leaving group on the platinum electrophile, and the reaction conditions could enable the application of a deuterium labeled neohexyl probe to elucidate the stereochemical outcome of hydrocarbyl group transfer between transition metals.

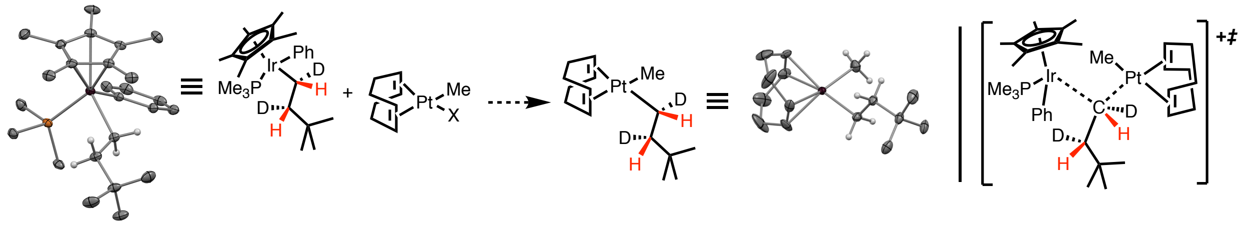

Figure 11 Stereochemical hypothesis (retention) and proposed probe of this hypothesis.

We chose the phenyl substituted complex [Ir](neohexyl)(Ph) as our target probe because previous results from Dr. Durak demonstrated perfect selectivity for alkyl transfer to (cod)Pt(Me)(TFA) in intramolecular competitions ([Ir](R^1)(R^2), R^1=alkyl R^2=aryl). The per-protio probe was synthesized in one step from the previously reported complex [Ir](neohexyl)(Cl). A preliminary screen of reaction conditions for neohexyl group transfer did not provide any of the desired (cod)Pt(Me)(neohexyl) complex (Figure 12 and Table 1). Monitoring the reaction by ^{1}H NMR, however, revealed consumption of (cod)Pt(Me)(X) with formation of byproducts neohexene and methane, consistent with intermediacy of the desired (cod)Pt(Me)(neohexyl) and subsequent beta-hydride elimination followed by methane reductive elimination.

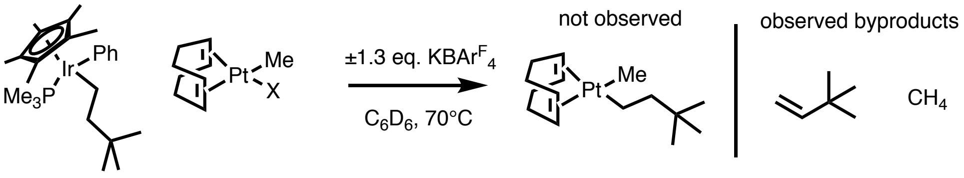

Figure 12 Preliminary reactivity of per-protio stereochemical probe.

Table 1 Preliminary reactivity of per-protio stereochemical probe.

X =	Cl	OTFA	Cl
temperature (°C)	70	70	23
$KBAr^F_4$ (±)	-	-	+
observation	no reaction	trace byproducts	major byproducts

The results in Figure 12 and Table 1 indicate that (cod)Pt(Me)(neohexyl) is unlikely to be sufficiently stable to allow for spectroscopic determination of the stereochemistry of transmetallation. We hypothesized, however, that stereospecific beta-elimination would conserve the stereochemistry of transmetallation and yield up to four isotopomers of neohexene (Figure 13). Of the four possible elimination products, only two have protons at the position vicinal to the *t*-butyl substituent: thus, analysis of the $^3J_{HH}$ coupling constant of the vicinal proton by $^1H\{^2H\}$ NMR should clearly indicate whether transmetallation occurs with retention, inversion, or follows both pathways.

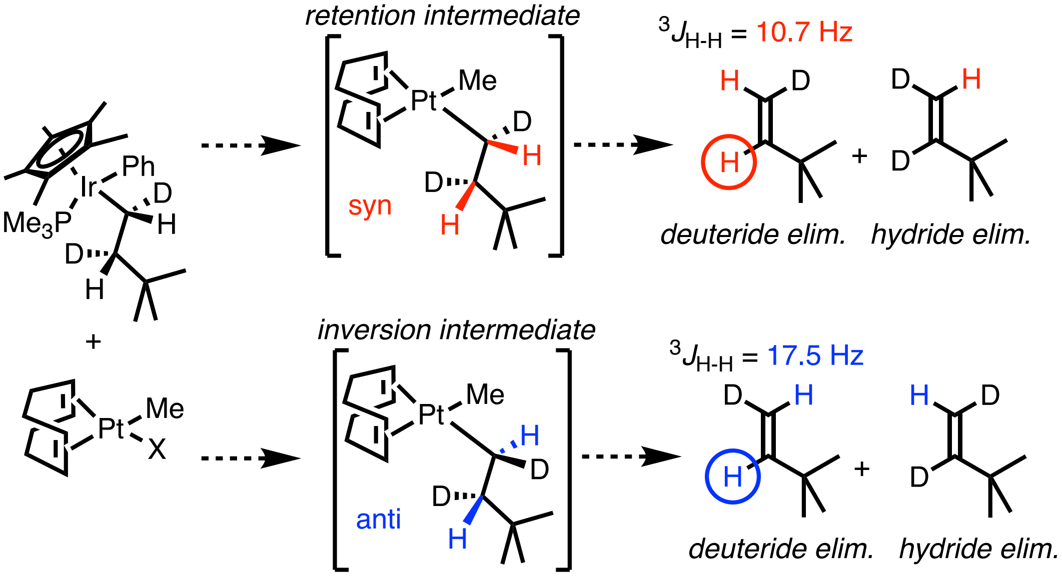

Figure 13 Modified approach to probe stereochemistry of transmetallation via subsequent stereospecific beta-hydride/deuteride elimination.

The results in Figure 12 and Table 1 indicate, once again, that transmetallation of hydrocarbyl fragments from [Ir](R)$_2$ to (cod)Pt(Me)(X) depends on formation of a cationic Pt intermediate either by equilibrium ionization or salt metathesis with a non-coordinating counter anion. Unfortunately, heterogeneous KBAr$^F{}_4$ reactions resulted in poor mass balance and reproducibility. To side step the use of heterogeneous metathesis salts, the more ionizing complexes (cod)Pt(Me)(OSO$_2$R) (R=Me and p-tolyl) were prepared. Michael Roy studied the reactivity of these complexes toward the per-protio stereochemical probe; the results, from his undergraduate thesis, are shown in Table 2 (the reaction is the same as in Figure 12).

Table 2 Stereochemical probe reaction optimization.

entry	1	2	3	4	5	6	7
X =	Cl	OTFA	Cl+KBAr$^F{}_4$	OTs	OMs	OMs	no Pt
temperature	70 °C	70 °C	23 °C	70 °C	70 °C	70 °C	70 °C
solvent	C_6D_6	C_6D_6	C_6D_6	C_6D_6	C_6D_6	$CDCl_3$	$CDCl_3$
time	days	days	1 hour	days	days	8 hr	days
yield	0%	trace	43%	58%	43%	90%	0%

With conditions for high yielding group transfer established by Mr. Roy using the per-protio stereochemical probe, Natalie Chan synthesized the stereo-selectively deuterated probe. ^{1}H NMR analysis of the volatile reaction products after vacuum transfer revealed a complicated mixture of isotopomers. Especially concerning was the observation of products with vicinal $^2J_{HH}$ coupling: these products could only be formed in the presence of some additional H/D scrambling mechanism. Notably, [Ir](R)$^+$ cations (the presumed product of transmetallation) are efficient catalysts for sp^2 H/D exchange (for an example with similar scrambling see[33]).

Whereas the stereochemical course of transmetallation to Pt(II) is obscured by beta-elimination and H/D scrambling, Ms. Chan observed rapid transmetallation to Hg(II) with retention of stereochemistry (Figure 14). Although this result does not directly inform our understanding of transmetallation to group 10 electrophiles, it offers indirect support to our understanding of hydrocarbyl group transfer to soft electrophiles via a 3c2e interaction in which the bonding electrons are transferred directly from $\sigma_{Ir\text{-}C}$ to form a new $\sigma_{M\text{-}C}$ bond (see Figure 6). Moreover, this result is consistent with other studies of the stereochemistry of metal-carbon bond cleavage by Hg(II) and other soft electrophiles.[19,34]

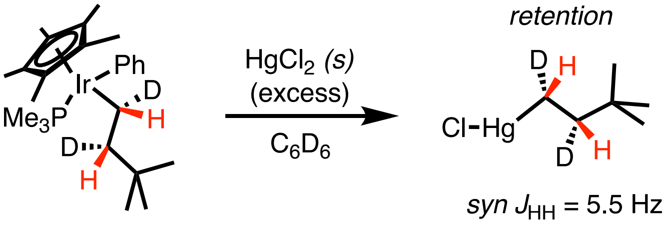

Figure 14 Transmetallation to $HgCl_2$ with retention of stereochemistry.

Scope of Hydrocarbyl Donors

While studying the reactivity [Ir] complexes with the goal of eventually enabling M^1 turnover by accelerating transmetallation (Figure 2 and Figure 9), we simultaneously explored the scope of transition metal complexes relevant to C-H activation and capable of transferring a hydrocarbyl ligands to (cod)Pt(Me)(X). Our study of hydrocarbyl donors was focused on the three classes of organometallic complexes, all of which are capable of cleaving aromatic and some aliphatic C-H bonds at ambient temperature without the assistance of directing groups or electronic bias (Figure 2). Notably, these three classes of organometallics generate reactive intermediates and cleave C-H bonds with widely varying mechanisms (Figure 15). The complex in Figure 15A cleaves C-H bonds by photo-induced reductive elimination of hydrogen to generate a 16-electron intermediate capable of oxidative addition into C-H bonds of saturated and unsaturated hydrocarbons.[22] The complex in Figure 15B, on the other hand, undergoes thermal-alpha elimination of neo-pentane to generate an alkylidene which reacts with hydrocarbons by C-H addition across the metal carbon double bond.[36] The third class of C-H activation complexes (Figure 15C) mediates C-H bond cleavage by initial ligand deprotonation, which gives rise to a coordinatively unsaturated, dearomatized complex with enhanced pi-basicity.[37-39] The dearomatized intermediate then undergoes redox neutral C-H activation via sequential oxidative addition and metal to ligand proton transfer.

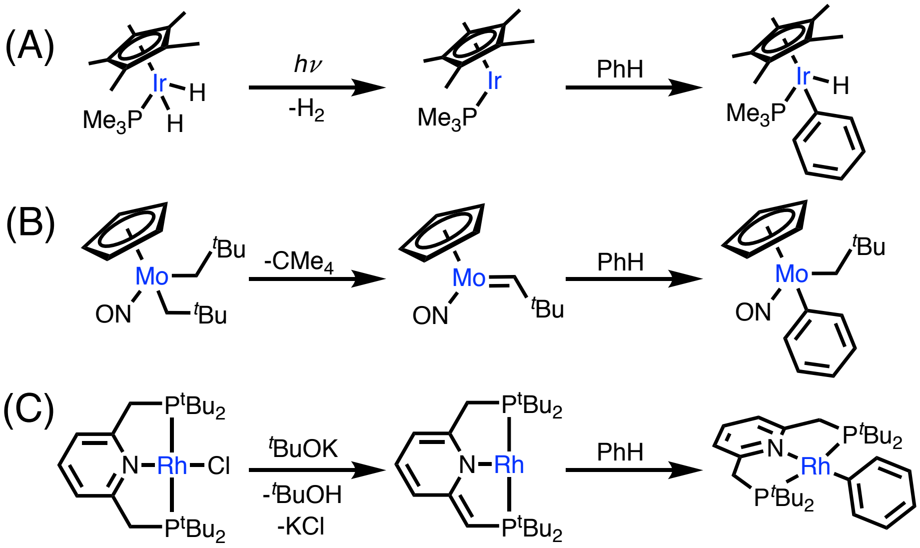

Figure 15 Three classes of organometallic complexes capable of room temperature, non-directed C-H activation of benzene.

Despite the wide diversity of structure and organometallic reactivity represented in Figure 15, all three classes were capable of transferring hydrocarbyl ligands to platinum electrophiles as illustrated in the general reaction in Figure 16A. Although yields were typically higher in transmetallations to (cod)Pt(Me)(TFA), transmetallation to (cod)Pt(Me)(Cl) gave good yields for all hydrocarbyl donors with heating to 70 °C. In addition to the wide variety of ligand platforms that support hydrocarbyl group transfer, it is notable that the reaction is viable with second and third row metals (Ir, Rh, W, Mo) and a variety of simple hydrocarbyl fragments (Me, Bn, Ph). It should be noted, however, that only one of these complexes is capable of stoichiometric aryl group transfer—^{i}Pr(PNP)Rh(Ph). The ability to transfer aryl ligands is important toward achieving dual catalysis (Figure 2) because, for all the complexes we studied, aromatic substrates have the lowest barriers to C-H activation and result in organometallic products that are less prone to undesired reactivity (elimination, rearrangement).

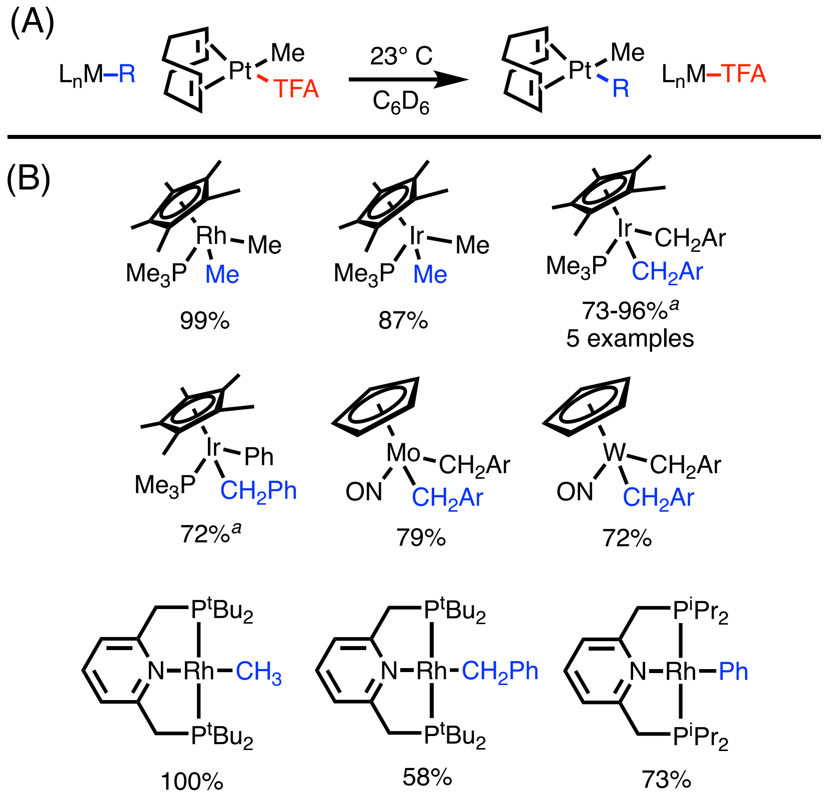

Figure 16 (A) General transmetallation reaction (B) yields of hydrocarbyl group transfer to (cod)Pt(Me)(TFA) with various organometallic donors [a] yields for reactions conducted at 70 °C.

Although the diverse hydrocarbyl donors in Figure 16 all participate in the same overall reaction, these reactions proceed with initial rates spanning nearly three orders of magnitude (the initial rates of the fastest reactions are rough approximations and represent a lower bound for initial rate because the reactions had already progressed beyond linearity in the time it took to thaw the sample and shim the spectrometer.) Qualitative comparison of rates of group transfer were conducted at room temperature to allow for fair comparison between complexes (notably, higher yields are achieved with higher reaction temperatures for the slowest reactions, even when room temperature reactions are monitored over a period of months). Figure 17 shows that [Ir] complexes used in our earlier endeavors toward dual catalysis are in fact the slowest benzyl group donors, followed closely by the similarly sluggish (Cp)(NO)Mo(Bn)$_2$. The tungsten congener (Cp)(NO)W(Bn)$_2$, on the other hand, reacted much more rapidly as did the pincer complex ^{t}Bu(PNP)Rh(Bn).

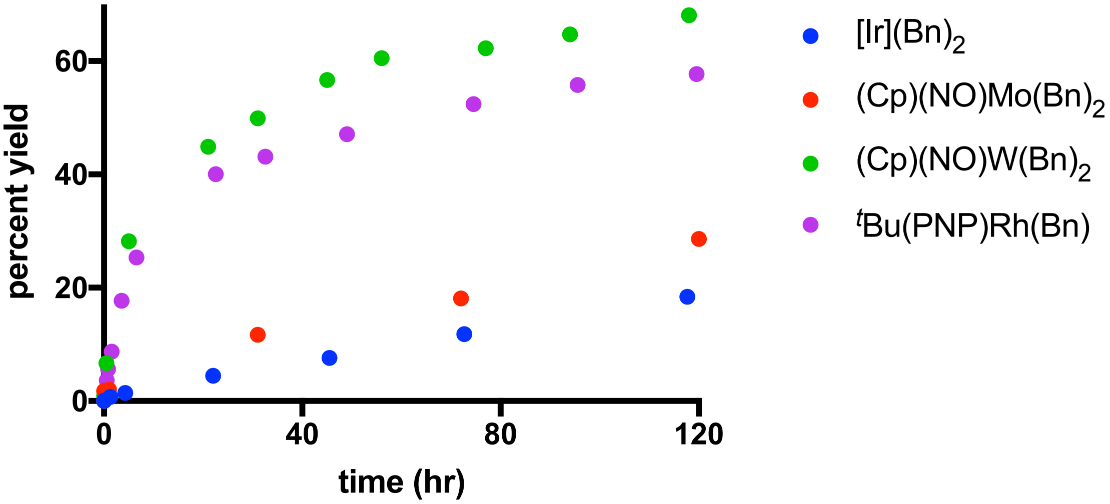

Figure 17 Comparison of reaction profiles of benzyl group transfer from various benzyl donors to (cod)Pt(Me)(TFA) at room temperature.

Methyl transfer was generally much faster than benzyl transfer as illustrated in Figure 18 by comparing the reaction profiles of [Ir](Bn)$_2$ and [Ir](Me)$_2$. In contrast to the group 6 metals (W faster than Mo, Figure 17), methyl transfer from was much faster from [Rh](Me)$_2$ than from [Ir](Me)$_2$. Remarkably, methyl group transfer from ^{t}Bu(PNP)Rh(Me) to (cod)Pt(Me)(TFA) was complete with quantitative yield within 5 minutes in thawing C_6D_6. To better assess the difference in rates of methyl transfer, the reactions were repeated with the less reactive electrophile (cod)Pt(Me)(Cl), which illustrates the difference in rate of methyl group transfer between [Rh](Me)$_2$ and ^{t}Bu(PNP)Rh(Me) (Figure 19). Even more prominently, transmetallation to the milder electrophile reveals the dramatic effect in switching from a *tert*-butyl phosphino complex (which gave essentially instantaneous quantitative transmetallation to (cod)Pt(Me)(TFA)) to the less sterically hindered *iso*-propyl phosphino complex.

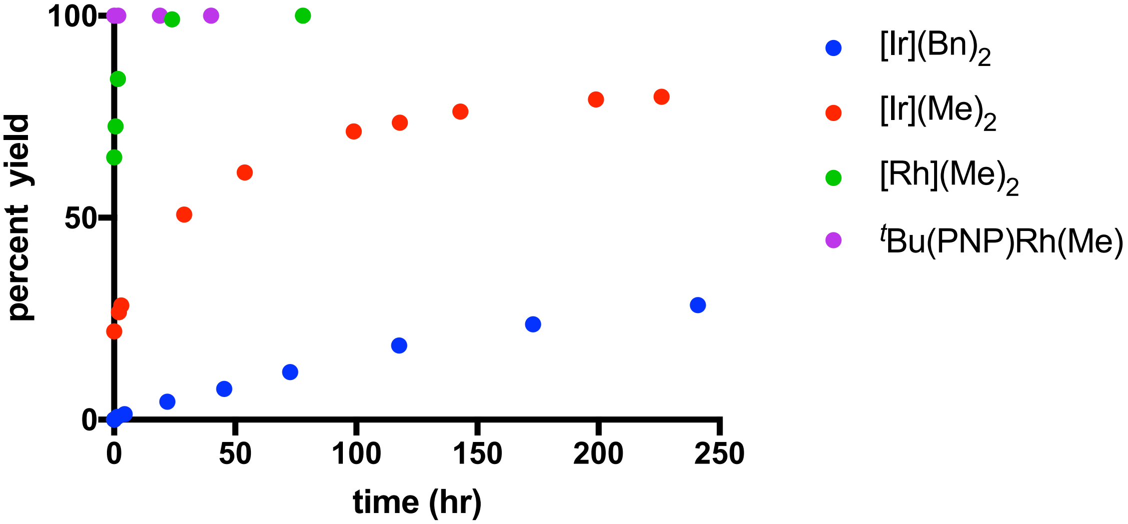

Figure 18 Comparison of reaction profiles of benzyl and methyl group transfer from various donors to (cod)Pt(Me)(TFA) at room temperature.

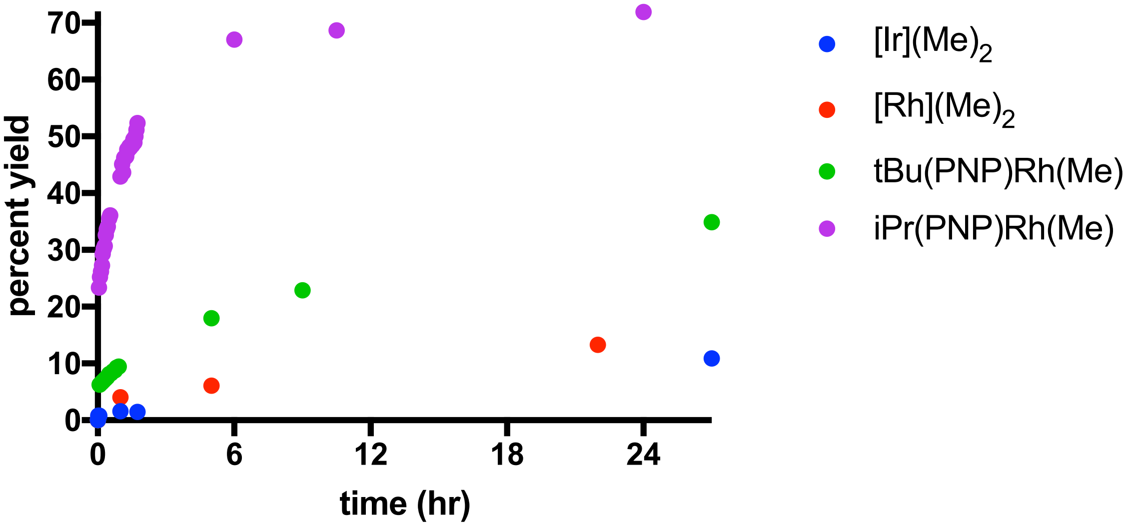

Figure 19 Comparison of reaction profiles of methyl group transfer from various donors to (cod)Pt(Me)(Cl) at room temperature.

The significant methyl transfer rate enhancements upon switching from [Ir](Me)$_2$ to [Rh](Me)$_2$, then from [Rh] to (PNP)Rh, and finally from ^{t}Bu(PNP) to ^{i}Pr(PNP) served as a fortuitous model system: although there was no guarantee that factors which accelerated methyl group transfer would also accelerate aryl group transfer, this sequence of metal and ligand modifications enabled the phenyl group transfer reaction (Figure 16). Figure 20, on the other hand, shows notable examples of organometallic complexes that did not yield observable quantities of the transmetallation product (cod)Pt(Me)(R). In particular, it is surprising that tri-butylbenzylstannane (Bu_3SnBn) did not undergo transmetallation to (cod)Pt(Me)(TFA) despite its reactivity towards transmetallation in Stille couplings. [32] The lack of reactivity of Bu_3SnBn towards (cod)Pt(Me)(TFA) demonstrates that transition metal hydrocarbyl donors possess complementary reactivity to main group organometallics employed in cross coupling reactions. If this complementary reactivity could be harnessed in a catalytic sense (ie dual catalysis, Figure 2) it could enable previously inaccessible reactivity in cross coupling methodology while eliminating the need for stoichiometric, pre-functionalized main group metal(loid) reagents.

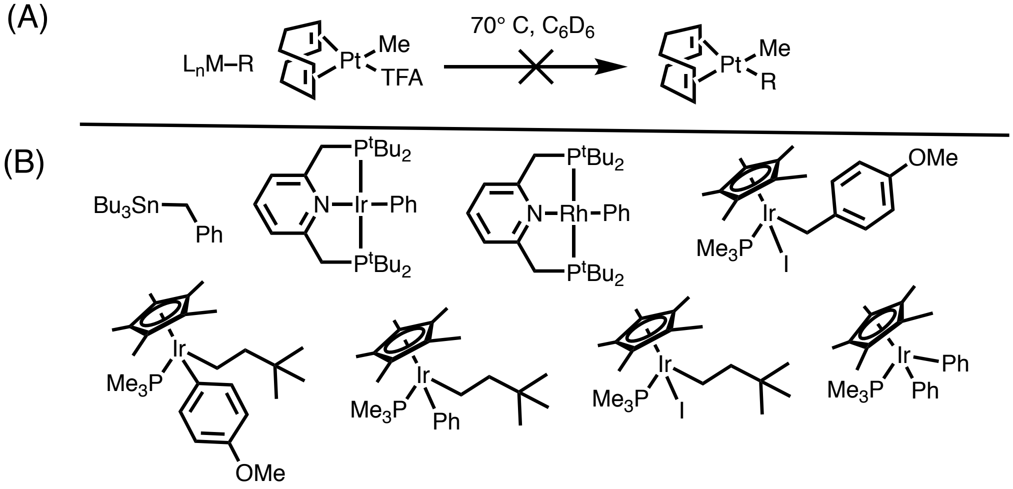

Figure 20 (A) General transmetallation reaction (B) Examples of organometallic complexes that did not afford observable quantities of the hydrocarbyl group transfer product (cod)Pt(Me)(R).

Scope of Hydrocarbyl Acceptors

The enhanced rates of group transfer from (PNP)Rh complexes offered several important advantages (detailed below) which prompted us to explore the scope of organometallic electrophiles which could be substituted by hydrocarbyl ligands via transmetallation from (PNP)Rh(R). Toward our goal of dual catalysis, the (PNP)Rh scaffold offers three major advantages: first, we expected the increased rates of transmetallation from (PNP)Rh(R) would address the presumed challenge of turnover limiting transmetallation in dual catalysis. Second, (PNP)Rh(R) complexes possess only one transferable ligand, in contrast to other reactive donors (Figure 16) that contain two potentially competitive hydrocarbyl ligands. Third, and most importantly, the unique mechanism of C-H activation on the (PNP)Rh platform by ligand deprotonation (Figure 15C) provided a simple solution to enabling turnover (C-H activation) from the products of transmetallation (Figure 9).

The majority of electrophiles tested for reactivity towards hydrocarbyl group transfer were group 10 $L_nM(R)(X)$ complexes chosen for their relevance towards cross coupling: one example, however, stands apart. When ^{i}Pr(PNP)Rh(Me) was treated with 1.2 equivalents of trimethyltin chloride (Me_3SnCl) in C_6D_6, the deep red solution immediately turned bright orange and was analyzed within 10 minutes by ^{1}H NMR to reveal complete conversion to the oxidative addition intermediate ^{i}Pr(PNP)Rh(Me)($SnMe_3$)(Cl) in 82% yield with minor conversion to ^{i}Pr(PNP)Rh(Cl) and $SnMe_4$ (Figure 22B). The presence of $^{3}J_{P\text{-}Sn}$ coupling (77 Hz) by $^{31}P\{^{1}H\}$ NMR provides strong evidence for the presence of covalent Sn-Rh bond (dative Rh→Zn bonding will be discussed in Chapter 4). Upon heating to 70 °C for one hour, the intermediate underwent reductive elimination to yield ^{i}Pr(PNP)Rh(Cl) and tetramethyltin (Figure 22A). This reactivity is notable because it offers a counter example to the generally accepted rationalization of transmetallation thermodynamics: namely, that transmetallation from main group metal(loid) nucleophiles to transition metal electrophiles is driven by the electropositivity of main group metal(loid)s and the formation of main group metal(loid) halide salts.

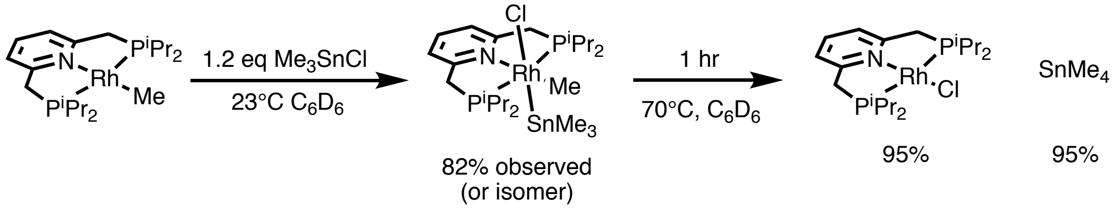

Figure 21 Sequential oxidative addition and reductive elimination to give overall methyl group transfer to trimethyltin chloride.

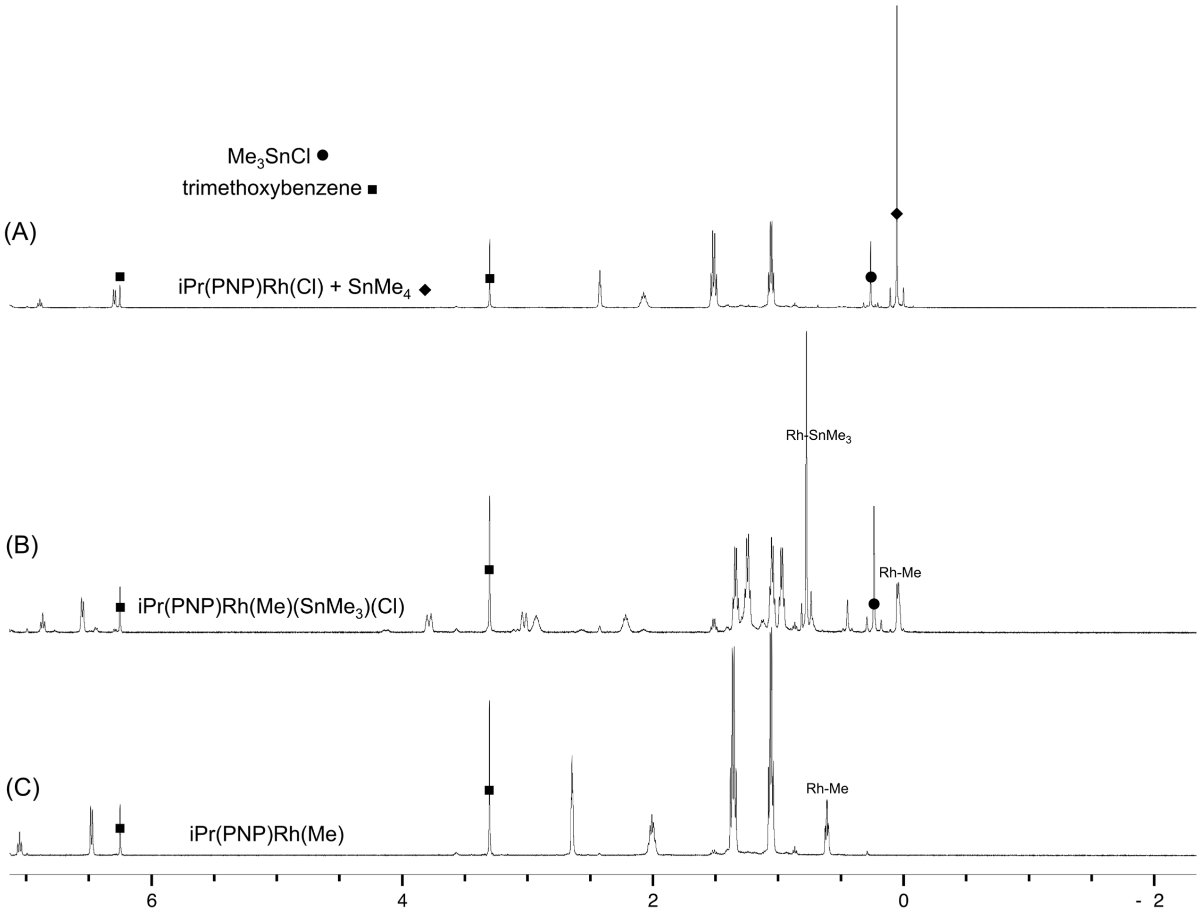

Figure 22 Stacked spectra showing (A) products (B) intermediate (C) reactants in oxidative addition of trimethyltin chloride by iPr(PNP)Rh(Me).

The observation of dative and covalent (PNP)Rh-M bonding also provides one possible framework for interpreting the enhanced reactivity of (PNP)Rh(R) complexes towards transmetallation relative to [Ir/Rh](R)$_2$ and (Cp)(NO)Mo/W(R)$_2$. Whereas the later are all coordinatively saturated three-legged piano-stool complexes, the PNP ligand enforces a square planar geometry which leaves coordinatively unsaturated Rh(I) d^8 with a high energy d_{z2} HOMO that can interact with Lewis acidic metal centers (Sn, Zn, etc). With this in mind, one might speculate that the enhanced reactivity of (PNP)Rh(R) towards transmetallation may be a consequence of (PNP)Rh complexes obviating the need for electrophile ionization (as was the case with $[Ir](R)_2$) by forming dative or covalent Rh-M intermediates, which in turn may promote ionization or simply render transmetallation unimolecular via a heterobimetallic adduct. Further kinetic studies are required to evaluate the viability of this hypothesis with metals other than tin.

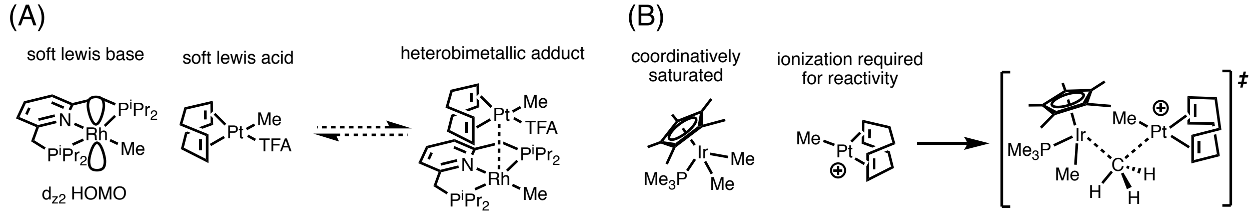

Figure 23 Speculation on the role of open coordination sites in facilitating hydrocarbyl group transfer from (PNP)Rh(R) to soft electrophiles.

The observation of transmetallation from (PNP)Rh(Me) to tin raises the possibility of an alternative approach to dual catalysis; main group metal(loid) shuttling (Figure 24). Toward this end, the viability of aryl group transfer to tin was established; however, the poor efficiency of this transformation precludes catalytic utility (Figure 25A). Moreover, in the presence of alkali metal alkoxides required for C-H activation, trimethyltin chloride undergoes rapid salt metathesis, which dramatically reduces the rate and efficiency of methyl group transfer (Figure 25B).

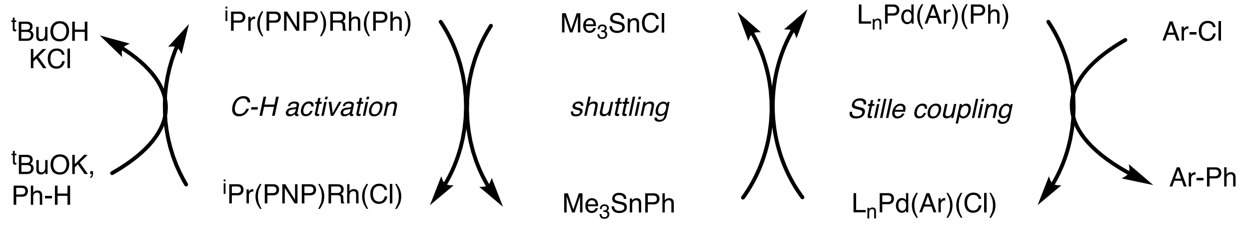

Figure 24 Proposed cycle for trimetallic catalysis via main group metal(loid) shuttling.

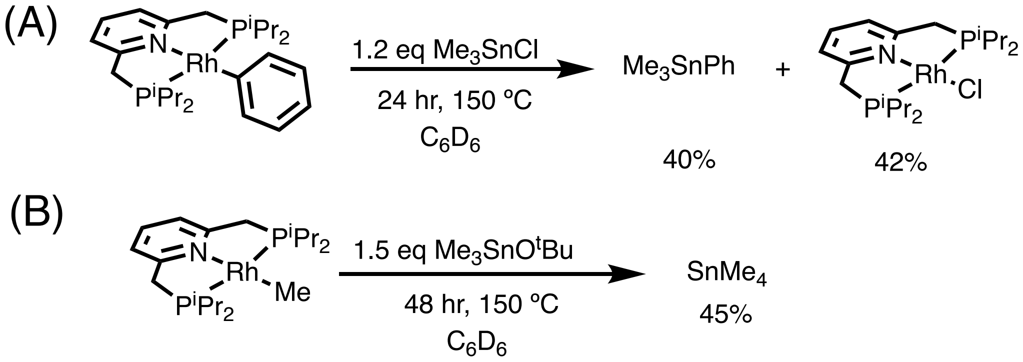

Figure 25 (A) Phenyl group transfer to trimethyltin chloride (B) Methyl group transfer to trimethyltin *tert*-butoxide.

Our exploration of organometallic electrophiles suitable for aryl group transfer from (PNP)Rh(Ph) was primarily aimed at achieving dual catalysis and thus concentrated on palladium and platinum complexes. Toward this end, after observing phenyl group transfer to (cod)Pt(Me)(TFA) (Figure 26A and B), one of the first experiments conducted was a test of the reactivity of ^{i}Pr(PNP)Rh(Ph) toward (sphos)Pd(Ar)(Cl), a state of the art cross coupling intermediate (Figure 26C). When none of the desired cross coupling product, 4-fluoro-biphenyl, was observed in this reaction, we set out to determine which features in our model complex were important for enabling aryl group transfer reactivity; specifically, the role of the metal center (Pt vs Pd), ancillary ligand (alkyl vs aryl), leaving group (TFA vs Cl), and supporting ligand (bidentate olefin vs hemilabile phosphine) (Figure 26D).

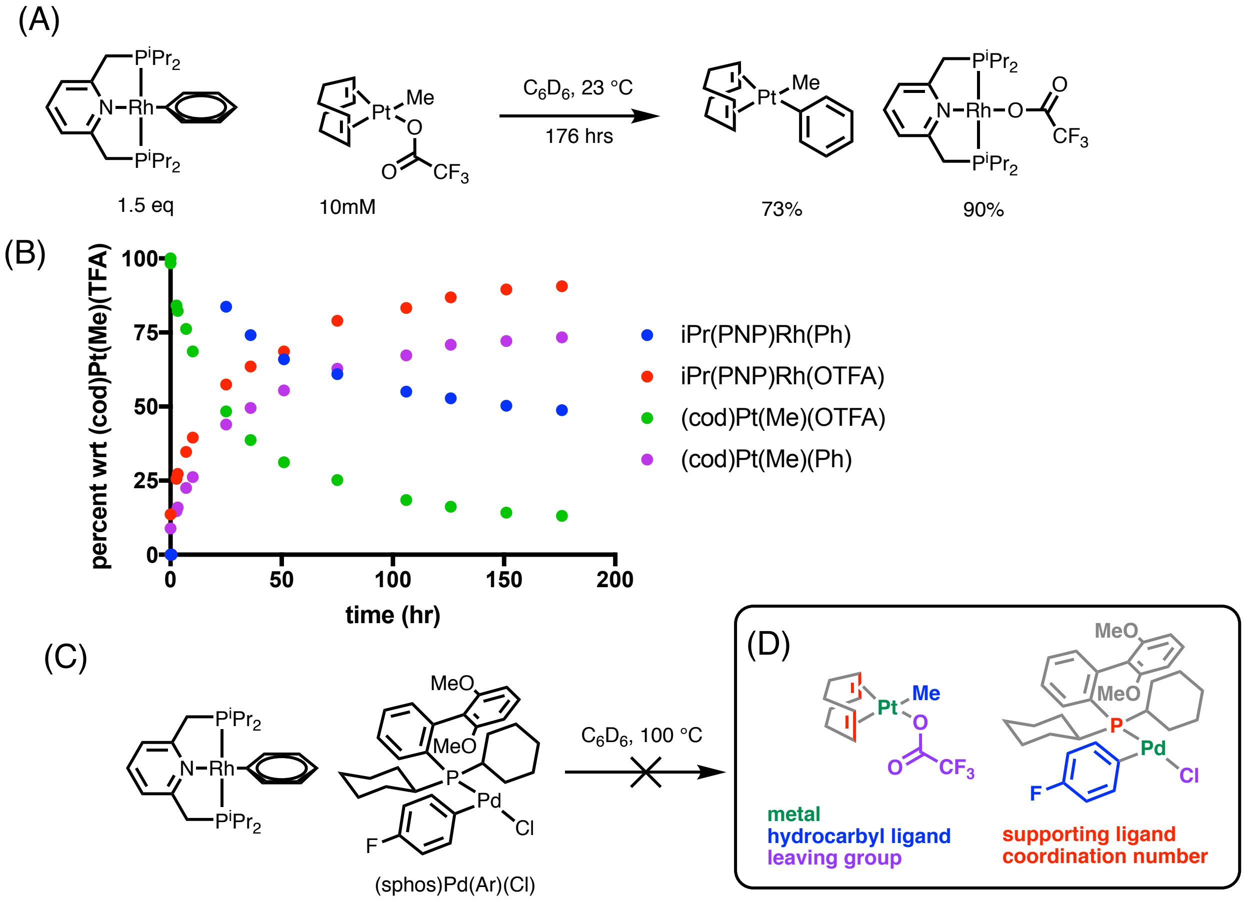

Figure 26 (A) Room temperature phenyl group transfer to (cod)Pt(Me)(TFA) (B) reaction profile for phenyl group transfer to (cod)Pt(Me)(TFA) (C) No desired product for phenyl group transfer to (sphos)Pd(Ar)(Cl) (D) key variables to explore for enabling transmetallation in dual catalysis.

Phenyl group transfer to (cod)Pt(R)(X) tolerates both methyl and aryl ancillary ligands (R) with both chloride and sulfonate leaving groups (X) (Figure 27 A-E). Transmetallation to platinum chloride complexes required heating to 70 °C to achieve yields over 50% on the timescale of days (Figure 27 A and D). Platinum sulfonate complexes reacted faster and under milder conditions with better yields than analogous chloride and trifluoroaceate complexes (Figure 27 B, C, and E). Upon extended heating yields of (cod)Pt(Me)(Ph) decreased with concomitant formation of ligand exchange products (cod)Pt(Me)$_2$ and (cod)Pt(Ph)$_2$ (Figure 27A). iPr(PNP)Rh(OTs), the rhodium product of transmetallation to (cod)Pt(Me)(OTs), underwent intramolecular oxidative C-H oxidative addition slowly at room temperature and to complete conversion with heating to 70 °C (see Chapter 4). At higher concentrations, transmetallation to (cod)Pt(Me)(OMs) gave rapid formation of an intermediate with broken C_2 symmetry that may be analogous to the oxidative addition observed with trimethyltin chloride (Figure 27B).

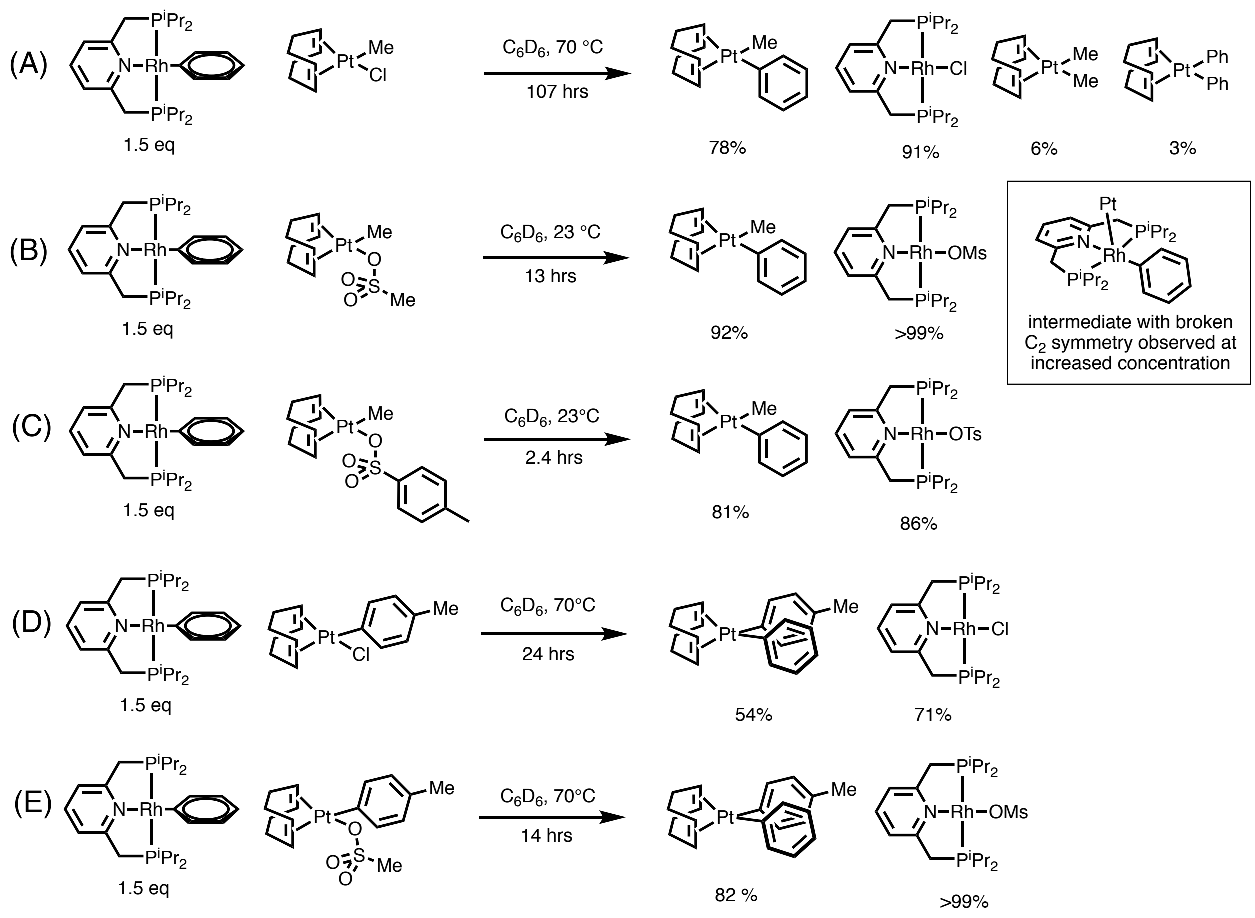

intermediate with broken C_2 symmetry observed at increased concentration

Figure 27 Phenyl group transfer from ^{i}Pr(PNP)Rh(Ph) to a variety of (cod)Pt(R)(X) complexes.

Platinum complexes served as useful models for observing stoichiometric transmetallation; we hypothesized, however, that slow reductive elimination from Pt(II) was likely preclude Pt from catalytic turnover and thus turned our attention to palladium(II) electrophiles. Group transfer to (cod)Pd(Me)(Cl) was assessed to allow for direct comparison to reactions with (cod)Pt(Me)(Cl). An excess of iPr(PNP)Rh(Me) reacted with (cod)Pd(Me)(Cl) in minutes to give low yields of the desired group transfer products and a mixture of uncharacterized byproducts (Figure 28A). Attempted phenyl group transfer did not yield the desired transmetallation or cross coupled products; however, (cod)Pd(Me)(Cl) did react rapidly with an excess of iPr(PNP)Rh(Ph) to afford a new (PNP)Rh species with broken C_2 symmetry (Figure 28B). The results in Figure 28 A and B suggest that transmetallation to palladium (II) from (PNP)Rh(R) is indeed possible, albeit susceptible to alternative reaction pathways. Given the thermal instability of (cod)Pd(Me) complexes (Figure 28C and D), we turned our attention palladium complexes more likely to support catalytic activity.

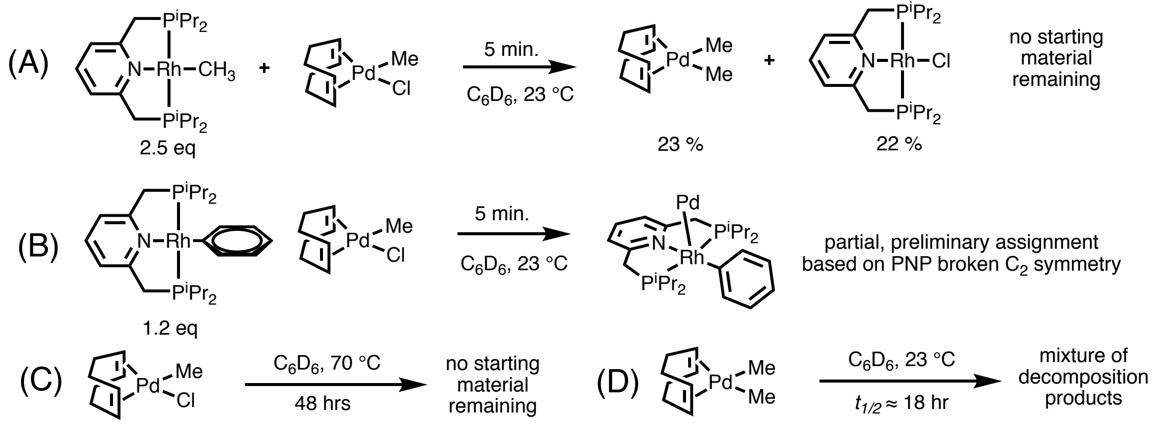

Figure 28 Transmetallation to (cod)Pd(Me)(Cl).

None of the palladium and nickel phosphine complexes (M^2) that we assessed showed any transmetallation or cross coupling reactivity in the absence of excess aryl halide, strong base, or ionizing additives (Figure 29). The lack of transmetallation between (PNP)Rh(Ph) and various M^2 complexes was confounded by the fact that reactions conducted under attempted catalytic conditions gave some amount of cross coupled product. Subsequent controls, however, revealed (PNP)Rh(Ph) reacts with aryl iodides to form biaryls and (PNP)Rh(I) (see chapter 3 for details). At elevated temperatures (PNP)Rh(Ph) also reacts with aryl chlorides and aryl triflates to form biaryls, however the majority of the (PNP)Rh(Ph) starting material decomposes to a mixture of uncharacterized products. The background reactivity of (PNP)Rh(Ph) with aryl halides is dramatically accelerated in the presence of strong base (to a lesser extent for aryl chlorides) (see chapter 3 for details). In the absence of any transition metal, aryl iodides and bromides (to a much smaller extent aryl chlorides) undergo direct arylation at elevated temperatures in aromatic solvents in the presence of potassium *tert*-butoxide.

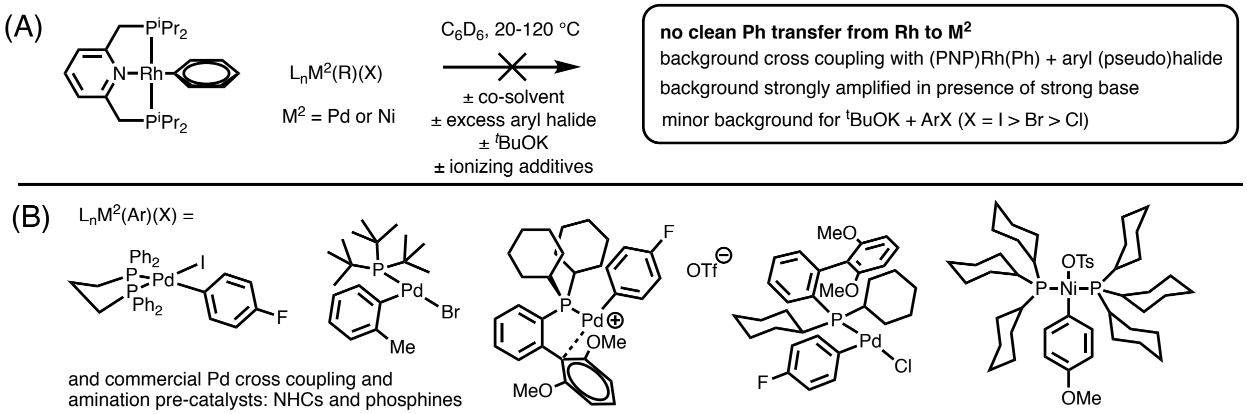

Figure 29 (A) Summary of attempted transmetallation/dual catalysis with cross coupling pre-catalysts and putative intermediates (B) scope of precatalysts and intermediates evaluated for reactivity towards transmetallation/dual catalysis.

Given the disappointing dearth of transmetallation reactivity towards palladium phosphine complexes, we turned our attention back to transmetallations to platinum complexes. Although we initially feared that platinum complexes might undergo prohibitively slow reductive elimination, those fears were apparently misplaced given a number of reports in the literature of C-C reductive elimination from platinum complexes[40-55] including a biaryl reductive elimination that proceeds at sub-ambient temperatures.[56] My only additional contribution to this work was in testing the reactivity of (dppp)Pt(ptol)(Cl), which did not undergo aryl group transfer from (PNP)Rh(Ph) at elevated temperature in THF, PhH, DCB, or DMF (Figure 30A). The rest of the excellent work in Figure 30 (B-D) was conducted by Natalie Chan.

Based on the fact that the only common feature in the our transmetallation reactions was the presence of an olefin ligand, we were encouraged to explore the reactivity of a hemi-labile phosphepine complex, which underwent transmetallation with (PNP)Rh(Ph) at a rate qualitatively similar to (cod)Pt(R)(Cl) (Figure 30C). To our surprise, the biaryl platinum complex that developed over the course of the reaction underwent reductive elimination at extended reaction times. Importantly, the organic products of this reaction were a nearly equal mixture of homo and hetero-coupled biaryls suggesting that the rate of unproductive transmetallation between two platinum centers was faster than the rate of reductive elimination. Given the synthetic challenge of obtaining useful quantities of pure (phosphepine)Pt(Ar)(Cl) we decided to test whether other hemilabile platinum (II) aryl halide complexes are suitable for transmetallation.

Noting the reactivity of a platinum complex with a hemi-labile phosphepine ligand, we wondered whether additional hemilabile phosphines would support transmetallation to Pt(II). In contrast to discouraging results with (sphos)Pd(Ar)(Cl) (Figure 26C), the platinum congener (sphos)Pt(Ar)(Cl) yielded the most promising result in this project to date (Figure 30D). Transmetallation to (sphos)Pt(Ar)(Cl) gave good conversion to the desired products with excellent selectivity for cross-coupling over homo coupling, which suggests that sphos possesses a balanced steric profile that allows (PNP)Rh(Ph) to approach while suppressing bimolecular exchange between (sphos)Pt(Ar)(Cl) complexes.

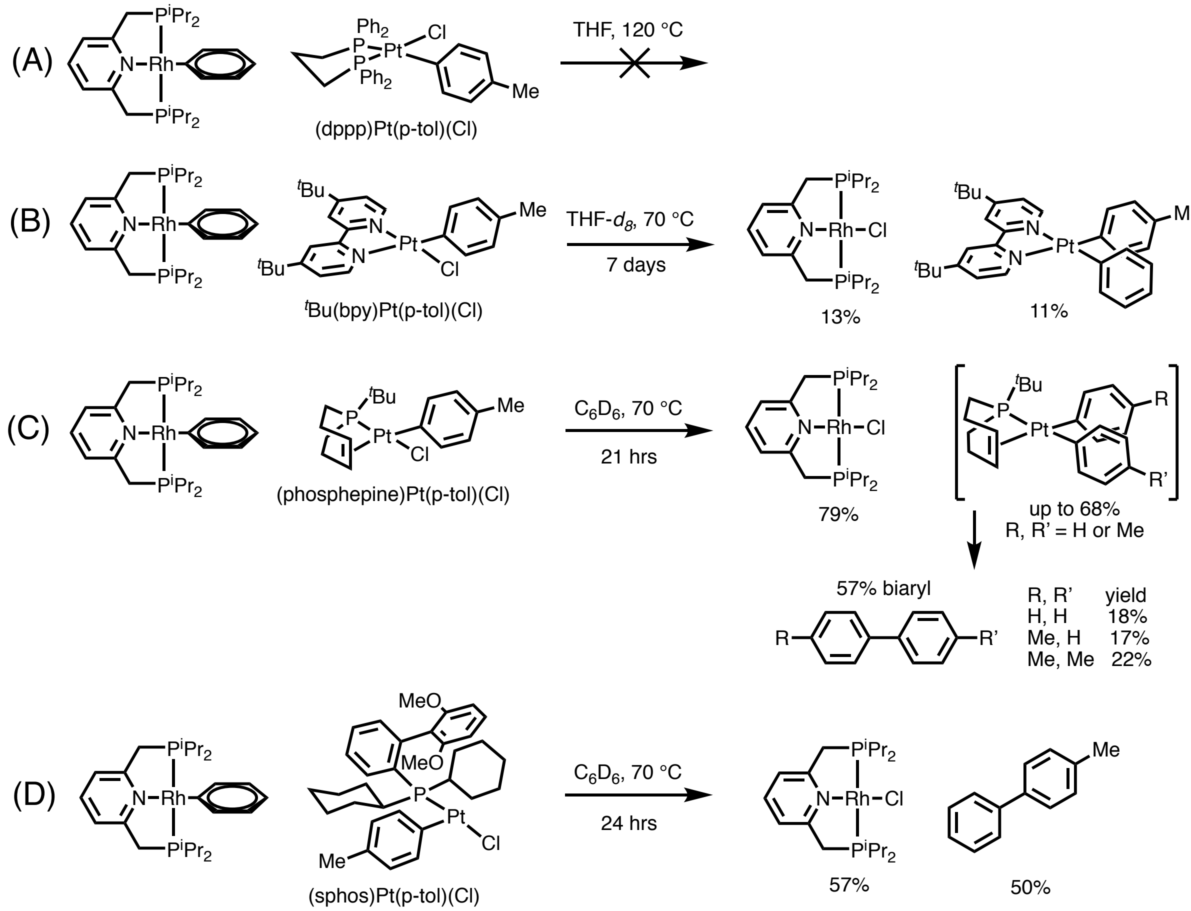

Figure 30 Transmetallation to platinum(II) complexes with various ligands.

Outlook, Obstacles, and Proposals

In developing catalytic methods by linking together stoichiometric reactions there are two distinct challenges. First, reactivity: can one combination of ligands, concentrations, additives, and solvents mediate every necessary step at a given temperature? After achieving the necessary reactivity, the more challenging prerequisite for catalysis is compatibility: do the established combination of ligands, concentrations, additives, and solvents favor the desired reactivity, or, when combined, can they follow unproductive pathways that overwhelm the desired reactivity. The result in Figure 30D nearly completes the reactivity requirements in Figure 31. The only major remaining question of reactivity is whether (sphos)Pt(0) can mediate oxidative addition of C(sp^2)-(pseudo)halides. I've taken the liberty of denoting the Pt-counter-ion as X rather than Cl in Figure 31 because Cl is essentially a worst-case scenario: in every instance that we have examined (including [Ir], [Rh], W, Mo, and (PNP)Rh) transmetallation has been slowest to platinum electrophiles with a chloride leaving group and faster with TFA, mesylate, or tosylate. In light of reports of oxidative addition of vinyl triflate to simple platinum precursors with observable reactivity as low as -40 °C,[57,58] I am confident that future researchers will be able to establish this necessary reactivity with a ligand (labeled "phos" in Figure 31) that supports oxidative addition, transmetallation, and reductive elimination.

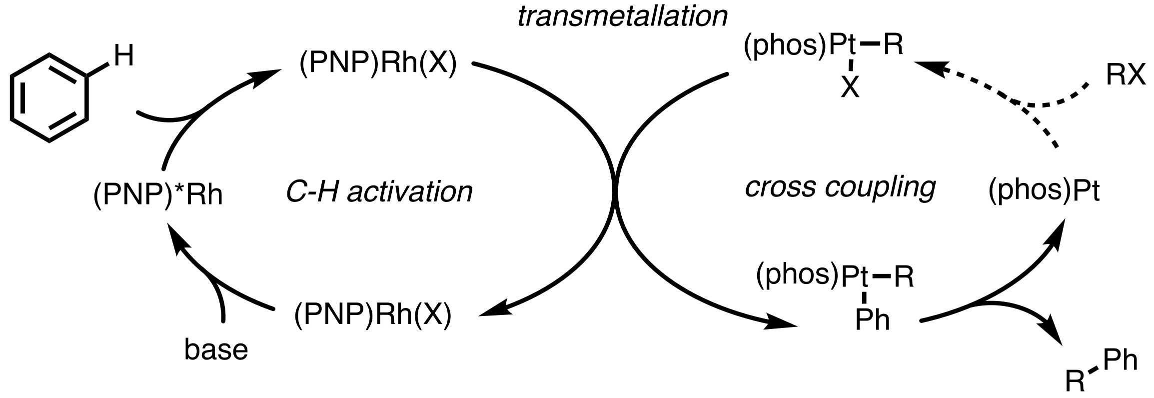

Figure 31 Summary of the reactivity observed toward dual catalysis with one remaining mode of reactivity (oxidative additon) to be established before completing the stepwise cycle.

The greatest challenge remaining in our group's work toward dual catalysis is compatibility. The glaring issue that must be addressed is finding a fully compatible base.

To date, our studies have primarily employed the two bases reported to mediate (PNP)Rh ligand deprotonation, potassium *tert*-butoxide and potassium hexamethyldisilazide. [37] Screening other bases for ligand deprotonation of (PNP)Rh(Cl) resulted in little or no C-H activation but did lead to H/D exchange at the benzylic position as observed by ${}^{2}J_{PD}$ coupling by ${}^{31}P\{{}^{1}H\}$ NMR (Figure 32A). An important breakthrough in this regard was the observation that (PNP)Rh complexes with less coordinating anions (methanesulfonate) can be deprotonated by milder bases (Figure 32B, more in chapter 3). Perhaps the foremost obstacle regarding base compatibility is the well precedented salt metathesis chemistry of group 10 metal halide complexes with alkali metal bases (Figure 32C) (for metathesis with (phosphino)Pd(Ar)(X) see[59] for (cod)Pt(Me)(Cl) see[60]).

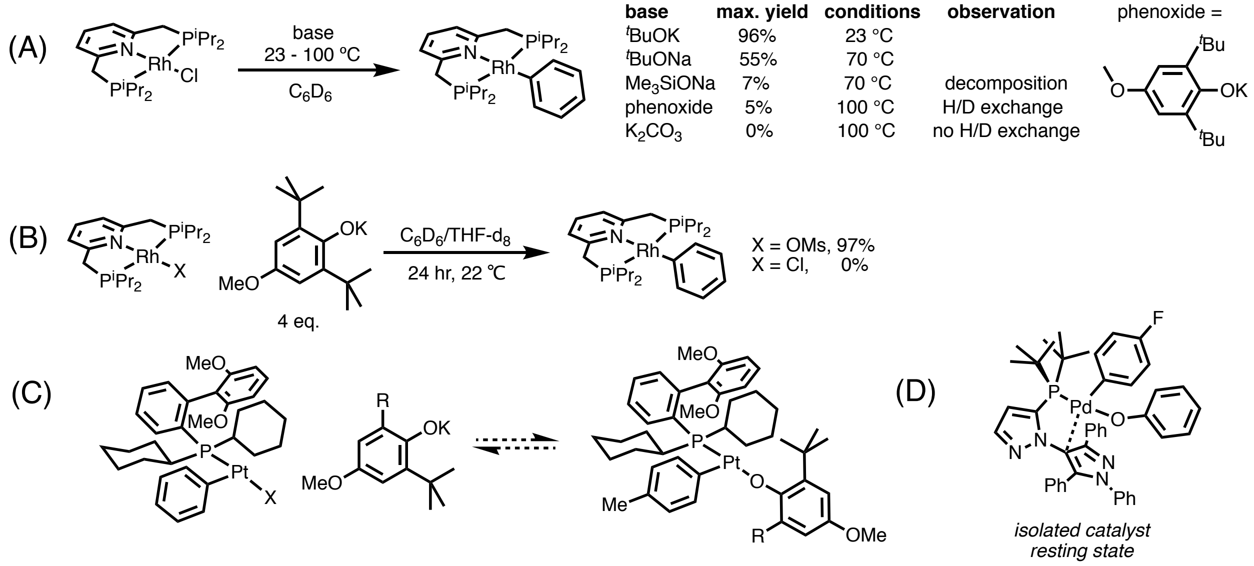

base	max. yield	conditions	observation
^{t}BuOK	96%	23 °C	
^{t}BuONa	55%	70 °C	
Me_3SiONa	7%	70 °C	decomposition
phenoxide	5%	100 °C	H/D exchange
K_2CO_3	0%	100 °C	no H/D exchange

Figure 32 Observations relevant to finding a base compatible with all aspects of dual catalysis

The observed dependence on leaving group ability in rates of transmetallation from (PNP)Rh(Ph) are not promising for transmetallation to platinum alkoxide and phenoxide complexes (Figure 27); however, these concerns about transmetallation to alkoxide and phenoxide complexes still demand experimental validation. The only example of transmetallation from (PNP)Rh(R) to a metal alkoxide was conducted with perhaps the worst possible leaving group and still gave substantial methyl group transfer under forcing conditions (Figure 25B). In future work, if any aryl group transfer to (phos)Pt(Ar)(OAr) is observed, the rate of aryl group transfer might be improved by decreasing the binding affinity of the phenoxide either by increasing the steric bulk of *ortho* substituents or adding electron withdrawing substituents (Figure 32C). Introducing electron withdrawing groups on phenoxide bases used in C-H activation (Figure 32B) will provide important insight into the pKa of (PNP)Rh(OMs). Finally, it should be noted that introducing phenoxide ligands is by no means incompatible with Pd(II) coupling chemistry: in fact, a LPd(Ar)(OPh) complex was recently characterized as the catalyst resting state in a reaction that was incompatible with strong bases (Figure 32D).[61,62]

To summarize our study of the scope of transition metal electrophiles suitable for arylation via transmetallation from (PNP)Rh(Ph): transmetallation to (cod)Pt complexes is high yielding, supports methyl and aryl ancillary ligands, and favors weakly coordinating anions (TFA, OMs, OTs) over chloride (Figure 27). Transmetallation to (cod)Pd was promising in that it showed explicit methyl group transfer from rhodium to palladium; however, the thermal instability of the reactants and products prevented further characterization (Figure 28). Attempts at transmetallation to palladium phosphine complexes gave no sign of useful transmetallation from rhodium to palladium, but revealed extensive background reactivity in the presence of strong base, both with and without transition metals (Figure 29). Natalie Chan's excellent work on hemilabile platinum phosphine complexes has revived the viability of dual catalysis with the surprising result that hemi-labile platinum phosphine complexes support transmetallation and reductive elimination. The two remaining challenges towards achieving dual catalysis are 1.) finding a platinum complex that supports oxidative addition as well as recently established transmetallation and reductive elimination 2.) finding a base that is sufficiently basic and unhindered to enable deprotonation of (PNP)Rh(OMs) and simultaneously sufficiently non-coordinating to prevent it from suppressing transmetallation to Pt(II).

The final variable to achieving non-directed C-H functionalization through dual catalysis appears now to depend squarely on establishing a base that is sufficiently basic for (PNP) ligand deprotonation and sufficiently non-coordinating to allow for transmetallation to platinum. The current state of the art in palladium catalyzed coupling of C(sp^2)-sulfonates suggests a promising future for dual catalysis. In particular, direct alkylation of phenyl methanesulfonate with acetone requires deprotonation of acetone (pKa ~26) whereas deprotonation of (PNP)Rh(OMs) proceeds smoothly with the conjugate base of 2,6-bis-*tert*-butyl-4-methoxy-phenol (pKa 4-methoxyphenol, 19). One reasonable course of action moving forward would be to first establish transmetallation to Pt complexes with ligands optimized for cross coupling of C(sp^2)-sulfonates like BrettPhos,[63] CMphos,[64,65] Mor-Dalphos,[66] and (stunningly) triphenylphosphine[57,58] (Figure 33C). After establishing transmetallation reactivity to platinum mesylates, the key challenge will be to tune phenoxide bases on (L)Pt(Ar)(OAr) with a combination of electron withdrawing groups and bulky *ortho* substituents to enable transmetallation without catastrophically suppressing PNP ligand deprotonation (Figure 33D).

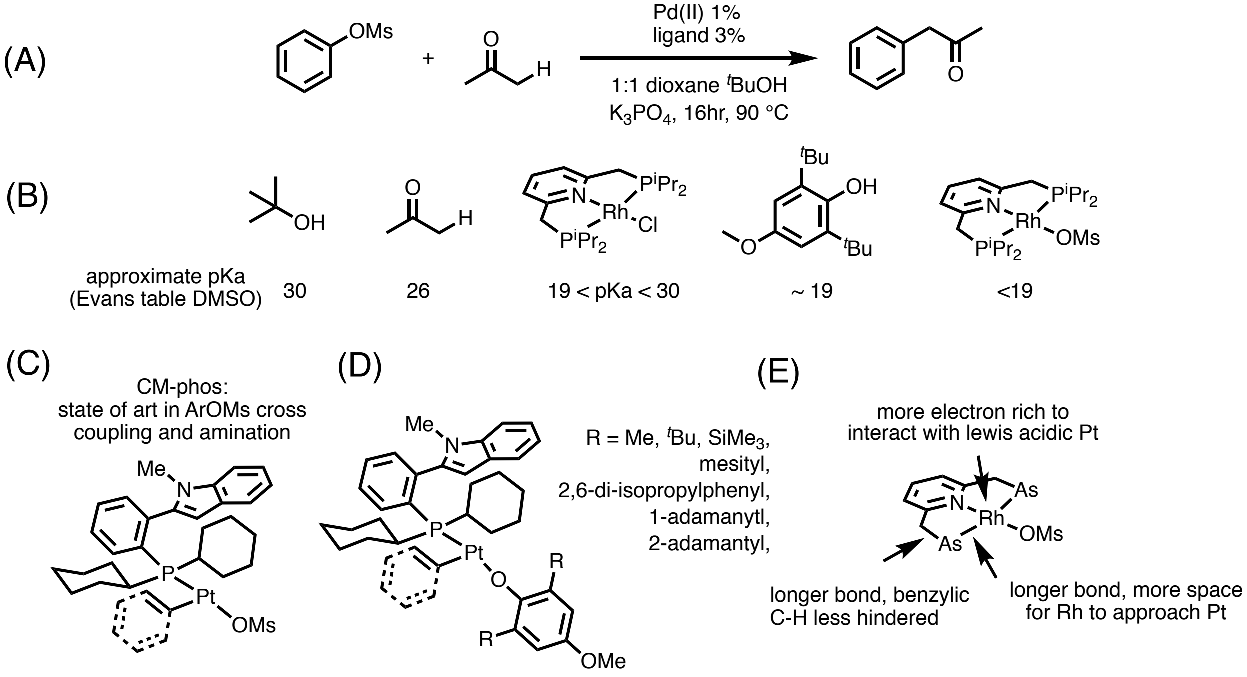

Figure 33 State of the art in direct alkylation of aryl methanesulfonates and recommendations for future work towards dual catalytic arylation of C(sp^2)-sulfonates.

Regarding potential modifications to the pincer complex: perturbations to the electronics of the pyridyl π system will necessarily benefit one form of reactivity at the expense of another. Given that we have not yet explored the limits of electron deficient phenoxides that might enable ligand deprotonation, it seems premature to focus on further acidifying the pyridyl π system, presumably at the expense of the rate of transmetallation. Instead, given that transmetallation is still prohibitively slow (one turnover would take ~1 day at 70 °C with (sphos)Pt(Ar)(Cl)) the top priority for PNP ligand modification should be synthesis of the arsine congener (Figure 33E). This modification may facilitate transmetallation both by increasing the electron density of the lewis basic rhodium center and reducing steric hindrance about the metal by expanding both the Rh-As distance and the As-C distance of the bulky isopropyl substituents.

In conclusion, significant progress has been made since Dr. Durak's seminal observation of benzyl group transfer from $[Ir](Bn)_2$ [30] and tireless development of iridium promoted palladium catalyzed direct arylation. [31] Key challenges in the project when I joined the effort were 1.) no reactivity for stoichiometric aryl group transfer, 2.) partial turnover only under difficult to control, ionizing, biphasic conditions and 3.) no clear path to enable turnover of the C-H activation catalyst. Each of these challenges has been directly resolved by our discovery of the enhanced group transfer reactivity of iPr(PNP)Rh(Ph) and its unique mechanism of C-H activation by metal ligand cooperativity which provides a clear pathway for catalyst turnover.

Experimental

Materials

Unless otherwise noted, all reagents were obtained from commercial suppliers and used without further purification. Tetrahydrofuran (THF), diethyl ether, methylene chloride (DCM), toluene (PhMe), and pentane were obtained from an Innovative Technologies solvent purification system (solvent deoxygenated by N_2 sparge and dried over alumina). Methane sulfonic acid was dried by azeotropic distillation with anhydrous toluene and then vacuum distilled. Water was degassed by bubbling with nitrogen for 1 hour. Acetone was dried over $MgSO_4$, distilled under N_2 into a Schlenk flask, and degassed by three freeze-pump-thaw cycles. Benzene-d_6 was degassed by three freeze-pump-thaw cycles in a glass tube sealed with a Kontes stopper and stored over 3 Å molecular sieves. THF-d_6 was dried over sodium/benzophenone ketyl and vacuum transferred to a glass storage vessel with a Kontes stopper. Methylene chloride-d_2 was dried over CaH_2, distilled into a Schlenk flask, and stored under N_2. Molecular sieves were activated in a Schlenk flask under vacuum (<0.05mmHg) in a sand bath set 250°C for at least 12 hours. Alumina, silica, and celite that were used in the glove box were all dried in a Schlenk flask under vacuum in a sand bath set to 280°C, 150°C, and 280°C respectively.

Complete analytical data and preparations have been reported for $[Ir](Me)_2$, [Ir](Me)(Cl), [Ir](Me)(TFA), $[Rh](Me)_2$, [Rh](Me)(Cl), $[Ir](Bn)_2$, [30] [Ir](Bn)(Cl), [Ir](Bn)(TFA), [30] (cod)Pt(Me)(Cl), (cod)Pt(Me)(TFA), [30] (cod)Pt(Me)(Bn), $(cod)Pt(Me)_2$, ^{t}Bu(PNP)Rh(Me), ^{t}Bu(PNP)Rh(Cl), [37] $(Cp)(NO)W(Bn)_2$, [67] $(Cp)(NO)Mo(Bn)_2$ [67] (Cp)(NO)W(Bn)(Cl), [68] (Cp)(NO)Mo(Bn)(Cl), [68]

General Procedures

Unless otherwise noted, all reactions and manipulations were performed under a circulating nitrogen atmosphere in an Innovative Technologies glove box, or using standard Schlenk technique. Glassware was dried in an oven set to 150 °C before use. Flash column chromatography was carried out using Silicycle 230-400 mesh silica gel. NMR spectra (^{1}H, ^{13}C, ^{19}F, and ^{31}P) were obtained using a Bruker 500 MHz spectrometer at room temperature. Chemical shifts are reported in ppm and coupling constants are reported in Hz. Products of reactions monitored by in situ NMR were confirmed by comparison to authentic material prepared by either the procedures listed above in the materials section or below in the experimental section. All benzylmagnesium chlorides were titrated under N_2 with salicylaldehyde phenylhydrazone in THF according a previously reported procedure. [69]

Benzyl magnesium chlorides were prepared by the following general procedure

Under air atmosphere, an oven-dried 100 ml 3-neck round bottom flask with stir bar, reflux condenser, and addition funnel was charged with freshly ground magnesium turnings (1.095 g, 45 mmol). The entire apparatus was then flame dried under vacuum and purged with N_2. 31.5 ml of dry Et_2O was added and the suspension stirred rapidly. 13.5 ml of dry Et_2O and one equivalent (45 mmol) of the desired benzyl chloride were added to the addition funnel. The solution of benzyl chloride was added dropwise, and the reaction mixture was heated to initiate the reaction, which then maintained reflux during addition of the remaining benzyl chloride solution. Following addition, the reaction mixture was heated to maintain reflux overnight. The final solution was cannula transferred into an oven-dried Schlenk flask and brought into a glove box under inert atmosphere, where it was titrated.

General Procedure for synthesis of Hammett study substrates $[Ir](CH_2Ar)_2$

Under an inert dry box atmosphere, a 20 ml scintillation vial containing a stir bar was charged with 200 mg of $[Ir](Cl)I_2$. The solid was suspended in dry Et_2O and stirred rapidly. 3 equivalents of the appropriate benzyl Grignard in diethylether were added dropwise, bringing the total reaction volume to 2.4 mL. The solution was stirred overnight before being diluted with an additional 2 ml Et_2O. The solution was filtered over a pad of basic alumina and eluted with additional Et_2O. The solvent was removed under vacuum, and the crude solid was purified on a column of basic alumina under air atmosphere. 4:1 hexanes:Et_2O was used as an eluent, and the first yellow band was collected and dried under vacuum. Samples were further purified by crystallization in pentane at -35°C

[Ir](CH_2-C_6H_4-4-F)$_2$

^{1}H NMR (500 MHz, C_6D_6) δ 7.10 (m, 4H), 6.88 (t, J=8.7 Hz, 4H), 3.00 (m, 2H) 2.75 (m, 2H) 1.31 (2, J_{HP}=1.7 Hz, 15H), 0.84 (d, J_{HP}=9.4 Hz, 9H)

^{13}C{^{1}H} NMR (126 MHz, C_6D_6) δ 161.17 (s), 159.26 (s), 149.05 (m), 130.31 (d, J=7.0 Hz), 114.89 (d, J=20 Hz), 92.56 (d, J=3.5 Hz), 14.18 (d, J=35 Hz), 8.97 (d, J=1.0 Hz), 0.93 (d, J=8.3 Hz)

^{31}P{^{1}H} NMR (202 MHz, C_6D_6) δ -43.60

^{19}F NMR (470 MHz, C_6D_6) δ -121.75

[Ir](CH_2-C_6H_4-3-F)$_2$

MDR01092 (5 – ^{1}H; 2 – ^{31}P; 3 – ^{19}F; 4 – ^{13}C)

^{1}H NMR (500 MHz, C_6D_6) δ 7.07 (d, J=11 Hz, 2H), 6.96 (m, 4H), 6.75 (m, 2H), 3.05 (m, 2H), 2.81 (m, 2H), 1.30 (d, J_{HP}=1.4 Hz, 15 H), 0.86 (d, J_{HP}=9.3 Hz, 9H)

^{13}C{^{1}H} NMR (126 MHz, C_6D_6) δ 164.43 (s), 162.50 (s), 156.97 (m), 128.73 (d, J=8.5 Hz), 125.03 (d, J=2.3 Hz), 115.95 (d, J=20 Hz), 109.47 (d, J=21 Hz), 92.53 (d, J=3.5 Hz), 14.18 (d, J=35 Hz), 8.89 (d, J=1.1 Hz), 1.72 (m)

$^{31}P\{^1H\}$ NMR (202 MHz, C_6D_6) δ -43.70

^{19}F NMR (470 MHz, C_6D_6) δ -115.62

[Ir](CH_2-C_6H_4-3-Me)$_2$

MDR-1-94 (3 – ^{1}H; 4 – ^{31}P; 5 – ^{13}C)

^1H NMR (500 MHz, C_6D_6) δ 7.19 (s, broad, 3H), 7.14 (m, 3H), 6.89 (d, J=7.2 Hz), 3.24 (m, 2H), 2.95 (m, 2H), 2.30 (s, 6H), 1.42 (d, J_{HP}=1.8 Hz, 15H), 0.94 (d, 9.4 Hz, 9H)

$^{13}C\{^1H\}$ NMR (126 MHz, C_6D_6) δ 153.65 (d, J=4.0 Hz), 136.33 (s), 130.59 (s), 127.60 (s), 126.80 (s), 123.68 (s), 92.62 (d, J=3.6 Hz), 21.71 (s), 14.33 (d, J=35 Hz), 9.07 (d, J=1.1 Hz), 2.32 (d, J=8.3 Hz)

$^{31}P\{^1H\}$ NMR (202 MHz, C_6D_6) δ -43.562

Synthesis of (cod)Pt(Me)(OMs)

(cod)Pt(Me)$_2$ (71.0 mg, 213 µmol) was weighed into a 20 mL vial and dissolved in 5 mL DCM. Methane sulfonic acid (41.0 mg 427, µmol) was weighed into a separate vial and dissolved in 1 mL DCM to give a 427 mM stock solution. The methane sulfonic acid stock solution (500 µL, 213 µmol, 1 eq) was added dropwise to the stirring platinum solution. The mixture was filtered over a pad of celite on a cotton plug in a glass pipette into a 20 mL vial and pumped to dryness. The white solid was suspended in 5 mL of pentane and the supernatant was removed to give 63.8 mg 72% of pure(cod)Pt(Me)(OMs). Single crystals suitable for x-ray diffraction were obtained by dissolving the entire sample in 500 µL of PhH, layering w/ 3mL Et_2O followed by 10 mL pentane, and allowing the layers to slowly diffuse together for 12 hrs at room temp and 16 hrs at -35°C.

^{1}H-NMR (C_6D_6) 0.98 (3H, s w/ Pt satellites, $J_{H\text{-}Pt}$ = 64.9 Hz) Pt-CH_3, 1.19-1.73 (8H, m) cod CH_2's, 2.76 (1H, s) OMs CH_3, 3.68 (2H, m w/ Pt satellites, $J_{H\text{-}Pt}$ = 83.2 Hz) cod CH trans to Me, 6.11 (2H, m, $J_{H\text{-}Pt}$ = 25.24 Hz) cod CH trans to OMs.

^{13}C-NMR (C_6D_6) 6.63 (s w/ Pt satellites $J_{C\text{-}Pt}$ = 636.77 Hz) Pt-CH_3, 26.99 (s w/ Pt satellites $J_{C\text{-}Pt}$ = 29.13 Hz) cod CH_2, 30.60 (s w/ Pt satellites $J_{C\text{-}Pt}$ = 26.57 Hz) cod CH_2, 39.85 (s) OMs CH_3, 77.69 (s w/ Pt satellites $J_{C\text{-}Pt}$ = 255.55 Hz) cod CH trans to Me, 114.56 (s w/ Pt satellites $J_{C\text{-}Pt}$ =29.55Hz) cod CH trans to OMs.

Synthesis of ^{t}Bu(PNP)Rh(CH_2Ph)

^{t}Bu(PNP)Rh(Cl) (45.1 mg, 87.7 µmol) was weighed into a 1 dram vial and transferred as a solid into a J. Young tube with THF-d_8 (500µL). ^{1}H and ^{31}P NMR of the starting material was taken for comparison. The tube was charged benzyl magnesium chloride (30 µL, 96.5 µmol, 0.98 M). The mixture was monitored by NMR immediately after addition and at t=1 hr, t= 8 hrs, and daily thereafter until no starting material remained (43 hrs at room temp.). By ^{31}P NMR the mixture contained two products in a 3:1 ratio in qualitatively good yield. Heating the reaction mixture favored the undesired product. The contents of the J. Young tube was poured into a 20 mL vial, the tube was washed into the vial with pentane, and the mixture solvent was removed under vacuum. The mixture was suspended in 5 mL pentane and dried in vacuo 3 times to remove any traces of THF. The crude material was extracted with 3x 500µL pentane and passed over a PTFE syringe filter into a 1 dram vial nested in a 20 mL vial and the 20 mL vial was sealed with a rubber lined cap. The mixture was stored at -35°C to allow for slow evaporation of pentane. After 2 days the supernatant was removed and dark red crystals were dried under vacuum. Only large, clean edged crystals were transferred to a tared vial to give 3.35 mg, 6.5 % of pure material. The supernatant still contained a large amount of desired product mixed with minor product and was further cooled to yield x-ray quality single crystals.

H-NMR (500 MHz, THF-d_8) 1.28 (36 H, m) ^{t}Bu, 2.85 (2H, m) Rh-CH_2 , 3.15 (4H, m) P-CH_2, 6.64 (1H, t, J=7.20 Hz) para Ph, 6.84 (2H, t, J=7.47 Hz) meta Ph, 7.03 (2H, d, J=7.55 Hz) meta pyridine, 7.25 (2H, d, J=7.50 Hz) ortho Ph , 7.50 (1H, t, J=7.55 Hz) para pyridine.

$^{13}C\{^1H\}$ NMR (126 MHz, THF-d_8) δ 161.6100 (m) pyridine C ortho to N, 132.50 (m) Ph ipso to CH_2, 130.04 (m) pyridine CH para to N overlapped with Ph CH ortho to CH_2, 126.12 (s) Ph CH meta to CH_2, 119.63 (s) Ph CH para to CH_2, 118.82 (m) pyrdine CH meta to N, 38.04 (m) PCH_2, 34.28 (m) ^{t}Bu C, 29.05 (m) ^{t}Bu CH_3, 3.50 (m) Rh-CH_2

Chapter 3: Rhodium 2,6-Bis(di-*iso*-propylphosphinomethyl)pyridine: Improved C-H Activation, Functionalization, and Catalysis

Introduction

Given our overarching goal of controlling reactive intermediates within a protein scaffold for selective C-H functionalization; our interest was piqued by the reported reactivity of the complex (PNP)Rh(Cl), which is capable of mediating room temperature C-H activation without assistance from substrate directing effects (Figure 34 A and B).[37] We hypothesized that a suitable oxidant may allow for functionalization of the activated aryl fragment with concomitant regeneration of the rhodium complex required for C-H activation (Figure 34C). Our search for suitable oxidants to enable (PNP)Rh(Ph) turnover began when we noticed unexpected reactivity between (PNP)Rh(Ph) and aryl (psdeudo)halides in control reactions while studying dual catalysis (Chapter 2). Given that C-H activation of benzene proceeds at room temperature without assistance from substrate directing effects, it was our hope that (PNP)Rh would be able to cleave all aromatic C-H bonds on simple substrates (Figure 34D). If this reactivity was achieved, we could then begin to consider strategies for incorporating these catalysts into protein scaffolds to evolve for catalyst controlled site selectivity.

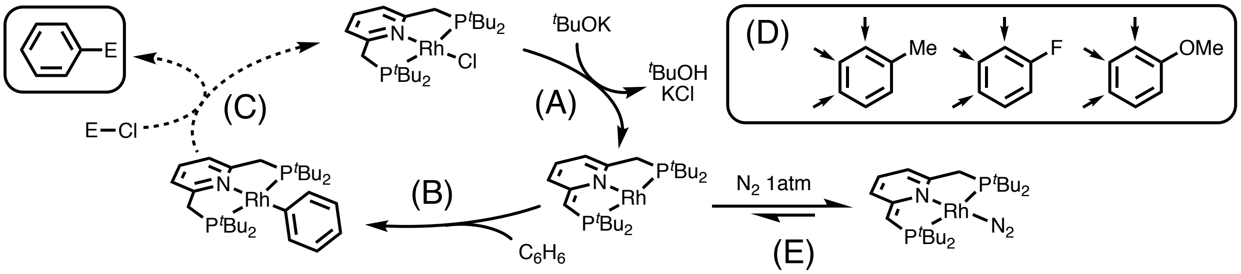

Figure 34. Reactivity of interest with (PNP)Rh complexes: (A) ligand deprotonation to give dearomatized intermediate (B) C-H activation (C) proposed functionalization of activated aromatic moiety and catalyst turnover (D) targeted reactivity (E) inhibition of reactive intermediate by nitrogen coordination.

Our approach to developing a catalytic method based on the known reactivity in Figure 34 was reported in a recent publication[70] and started by accelerating C-H activation, suppressing nitrogen inhibition (Figure 34E) and enabling the use of milder bases for C-H activation. We next turned our attention to studying the reactivity of the product of C-H activation (PNP)Rh(Ph) toward a variety of oxidants (Figure 34C). Finally, we applied our new understanding of the reactivity of (PNP)Rh(Ph) to develop a method for (PNP)Rh catalyzed arylation of aryl iodides.

C-H Activation

Given that functionalization of (PNP)Rh(Ph) depends on efficient C-H activation, we set out to optimize the ligand and conditions to improve the rate and yield of C-H activation. We hypothesized that decreasing the size of the di-alkyl phosphino groups on the PNP ligand would: (1) facilitate ligand deprotonation with bulky bases by reducing hinderance abou thte ligand C-H bond, (2) reduce nitrogen inhibition by creating a more spacious pocket around the metal center that is less able to differentiate between small

(N_2) and medium sized (C_6H_6) ligands, and (3) reduce steric clashes with approaching substrate. In line with this last point, Yehao Qiu has calculated the barrier to benzene oxidative addition at both *iso*-propyl and *tert*-butyl pincer complexes and noted that the barrier to C-H addition is 3.9 kcal/mol lower for the *iso*-propyl complex.

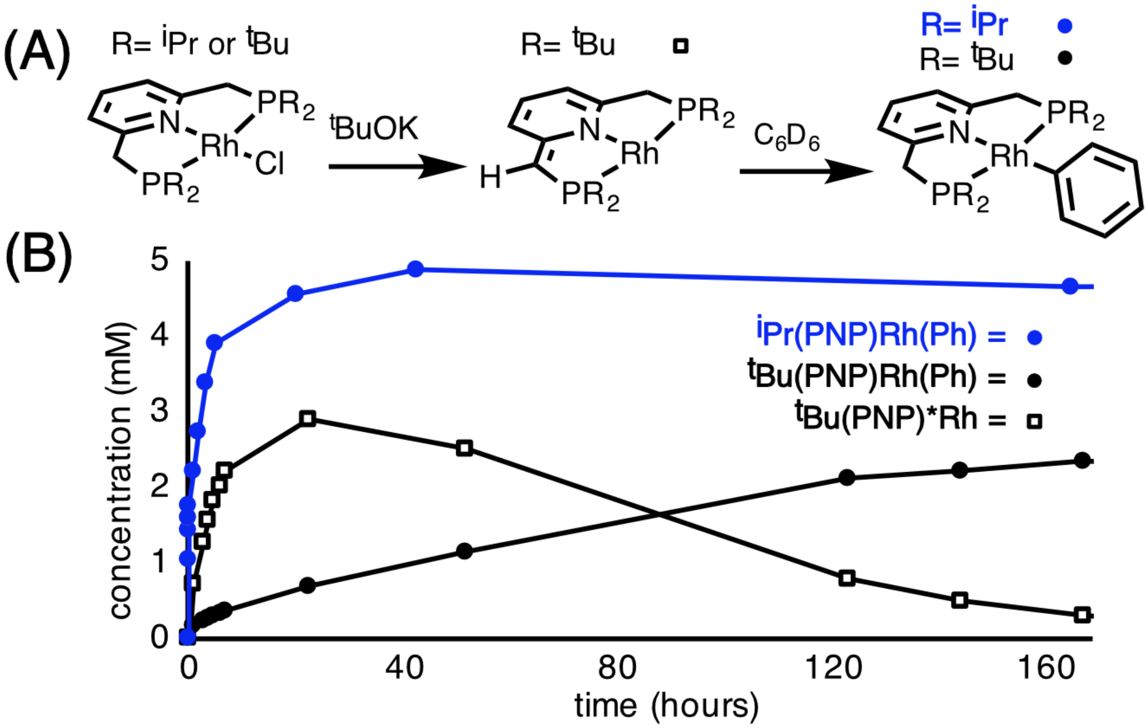

Figure 35 (A) Intermediate and product in C-H activation of (PNP)Rh(Cl) (B) Overlaid reaction profiles for side by side C-H activatons with ^{i}Pr(PNP)Rh(Cl) and ^{t}Bu(PNP)Rh(Cl).

Indeed, when 5mM solutions of ^{i}Pr(PNP)Rh(Cl) and ^{t}Bu(PNP)Rh(Cl) were treated with 1.2 equivalents of ^{t}BuOK in side by side reactions, ^{i}Pr(PNP)Rh(Cl) gave product formation at an initial rate 100 times greater than and ^{t}Bu(PNP)Rh(Cl) (101 and 0.95 μM/min respectively, Figure 35). The initial rate of starting material consumption (a lower bound for rate of ligand deprotonation) was only 7-fold faster for and ^{i}Pr(PNP)Rh(Cl) (113 vs 16 μM/min), and no build-up of dearomatized intermediate was observed during the reaction of and ^{i}Pr(PNP)Rh(Cl). These results suggest that substituting ^{t}Bu for ^{i}Pr accelerates the overall reaction by a modest increase in the rate of ligand deprotonation and a larger acceleration in C-H cleavage.

After improving the overall rate and efficiency of base promoted C-H activation, we sought to introduce additional modifications to enable the use of milder bases that would be compatible with a wider range of oxidants. At the time of our work, the only published progress toward catalytic C-H functionalization on the (PNP)Rh platform involved photo-carbonlyation of benzene with ^{t}BuOK, carbon dioxide, H_2, and tosic acid (1.3 ttn, 5 days). This reaction was fundamentally limited by the incompatibility of the base required for ligand deprotonation and the electrophile required for Rh-C cleavage. [71] We hypothesized that using a less coordinating (and weakly π donating) rhodium counter ion would afford a more positively charged rhodium center capable of withdrawing more electron density from the pyridine π system; such a modification would acidify the PNP ligand by allowing greater delocalization of the additional electron density in the dearomatized conjugate base of ligand deprotonation. To our great delight, the methane sulfonate (OMs) complex ^{i}Pr(PNP)Rh(OMs) reacted with benzene in the presence of potassium 2,6-bis(*tert*-butyl)-4-methoxy-phenolate to give the corresponding phenyl complex in excellent yield (97%), whereas ^{i}Pr(PNP)Rh(Cl) was inert under these conditions (Figure 36A). ^{i}Pr(PNP)Rh(Cl) did undergo C-H activation with phenoxide bases in low yield at elevated temperature and with higher yield in the presence of the Lewis acidic additive $Zn(OTf)_2$.

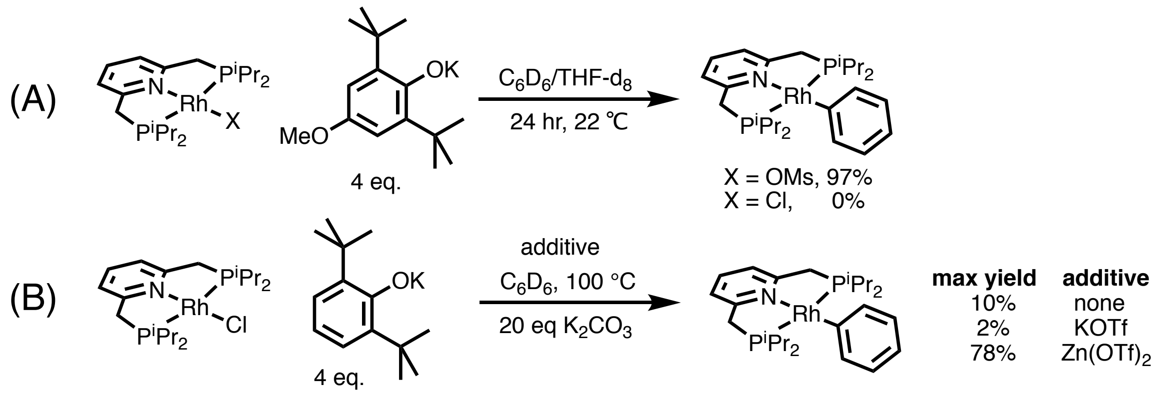

Figure 36 C-H activation with milder phenoxide base.

To our surprise, the rate and maximum yield of stoichiometric C-H activation revealed a strong dependence on alkali metal counter ion (K>Na>>Li: Figure 37A). In a separate experiment (no THF co-solvent), I observed that an N-heterocyclic carbene copper alkoxide served as a suitable base for ligand deprotonation and C-H activation (Figure 37B). In the context of our work demonstrating the metallophilicity of the (PNP)Rh scaffold towards various Lewis acids (Sn, Zn, Pt), one possible rationalization of the observed dependence on *tert*-butoxide counter ion is that PNP ligand deprotonation depends on a M-M Lewis-acid/Lewis-base interaction in which rhodium donates to the *tert*-butoxide counter ion (Figure 37C).

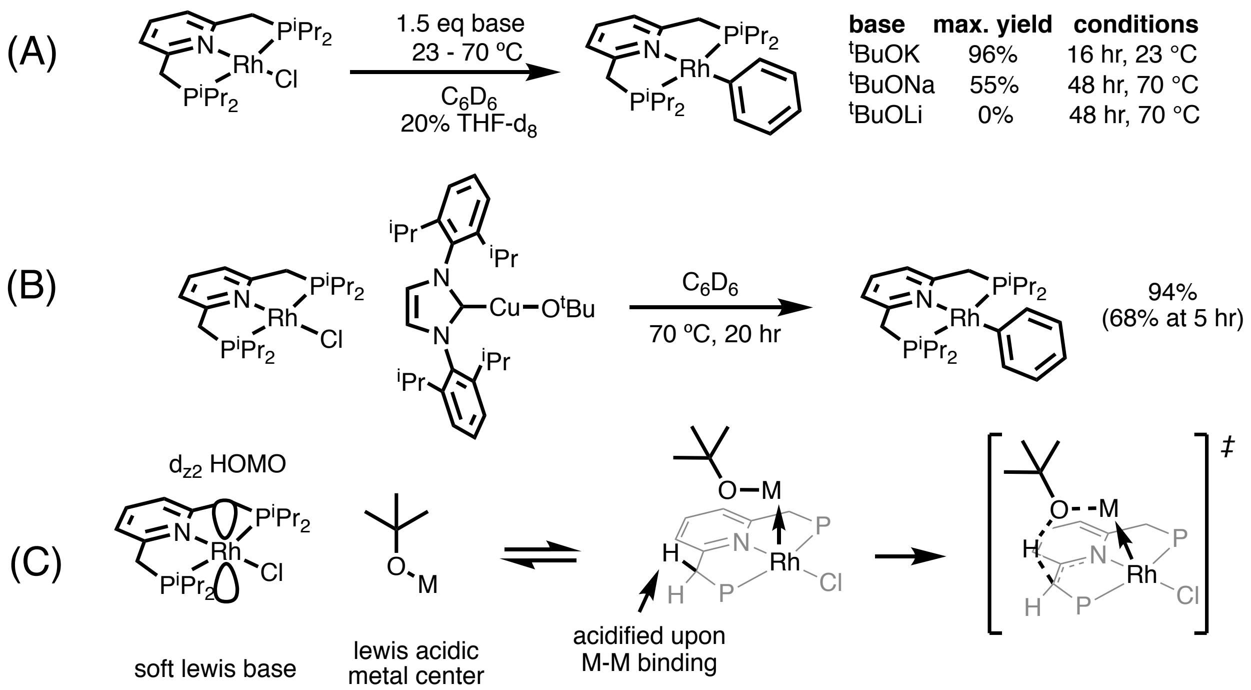

base	max. yield	conditions
^{t}BuOK	96%	16 hr, 23 °C
^{t}BuONa	55%	48 hr, 70 °C
^{t}BuOLi	0%	48 hr, 70 °C

Figure 37 Maximum yield of C-H activation with (A) varying alkali metal *tert*-butoxides and (B) N-heterocyclic carbene copper *tert*-butoxide. (C) Rationalization of observed dependence on *tert*-butoxide counter ion.

The hypothesized interaction may acidify the PNP C-H by withdrawing electron density from the pyridine π system in which the additional electron density of conjugate base is delocalized. Alternatively, such an interaction may favor larger *tert*-butoxide counter ions by extending the M-O bond distance, placing the basic oxygen center in closer proximity to the relevant C-H bond. Although weakly coordinating anions were used previously[72,73] on (PNP)Ir complexes to provide an open coordination site for Ph-H oxidative addition, we did not observe C-H activation with ^{i}Pr(PNP)Rh(OMs) in the absence of base.

In contrast to ^{i}Pr(PNP)Rh(OMs), the 4-toluene-sulfonate (OTs) complex ^{i}Pr(PNP)Rh(OTs) reacted with the *ortho* C-H bond of the weakly coordinating anion to give a Rh(III) hydrido arylsuflonate—notably, the first direct observation of C-H oxidative addition to afford a stable (PNP)Rh(III) aryl hydride (Figure 38).[74] The double addition product ^{i}Pr(PNP)Rh(H)(OTs)$_2$ (generated in the presence of excess 4-toluene-sulfonic acid), on the other hand, did not undergo ortho-metallation upon prolonged heating (Figure 38). The differential reactivity of ^{i}Pr(PNP)Rh(OTs) and ^{i}Pr(PNP)Rh(H)(OTs)$_2$ toward C-H activation underscores a salient point in catalyst design. When (PNP)Rh(Ph) is functionalized in the presence of excess arene and oxidant, the resulting (PNP)Rh(X) can access productive and unproductive pathways: namely, C-H activation or further reaction to with electrophile to generate over oxidized complexes incapable of C-H activation. As such, a key challenge in developing (PNP)Rh catalyzed C-H functionalization is finding electrophiles that react readily with (PNP)Rh(Ph) to give (PNP)Rh(X) and react negligibly with (PNP)Rh(X) relative to the rate of C-H activation.

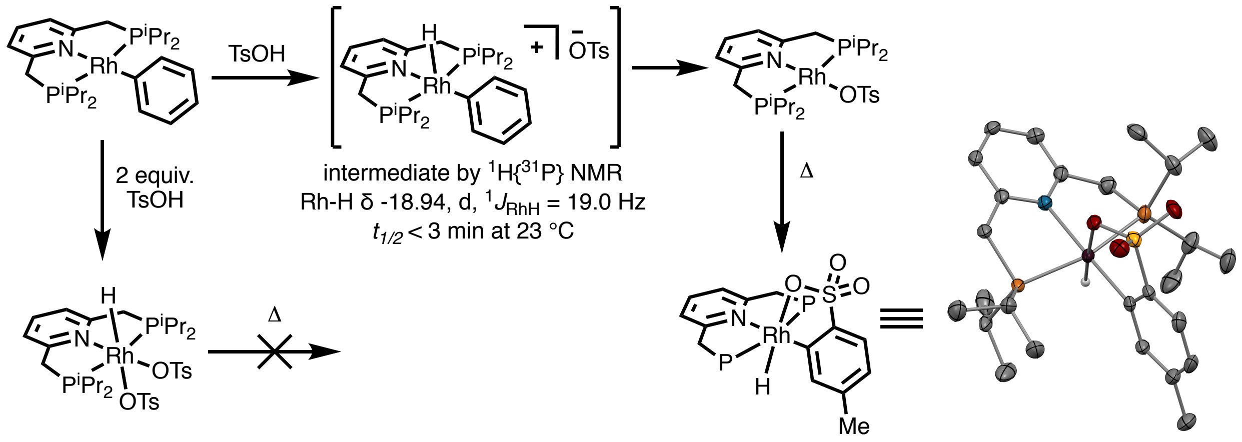
intermediate by $^1H\{^{31}P\}$ NMR
Rh-H δ -18.94, d, $^1J_{RhH}$ = 19.0 Hz
$t_{1/2}$ < 3 min at 23 °C

Figure 38 Reactivity of ^{i}Pr(PNP)Rh(Ph) with 4-toluene-sulfonic acid.

Reactivity of (PNP)Rh(Ph)

Keeping in mind the importance of balancing and oxidants that would react with (PNP)Rh(Ph) but not with (PNP)Rh(X), we sought to explore the reactivity of (PNP)Rh(Ph) toward a variety of electrophiles both to understand the basic reactivity of adducts of C-H activation and to find reagents amenable to (PNP)Rh catalyzed, non-directed C-H functionalization (Figure 39).

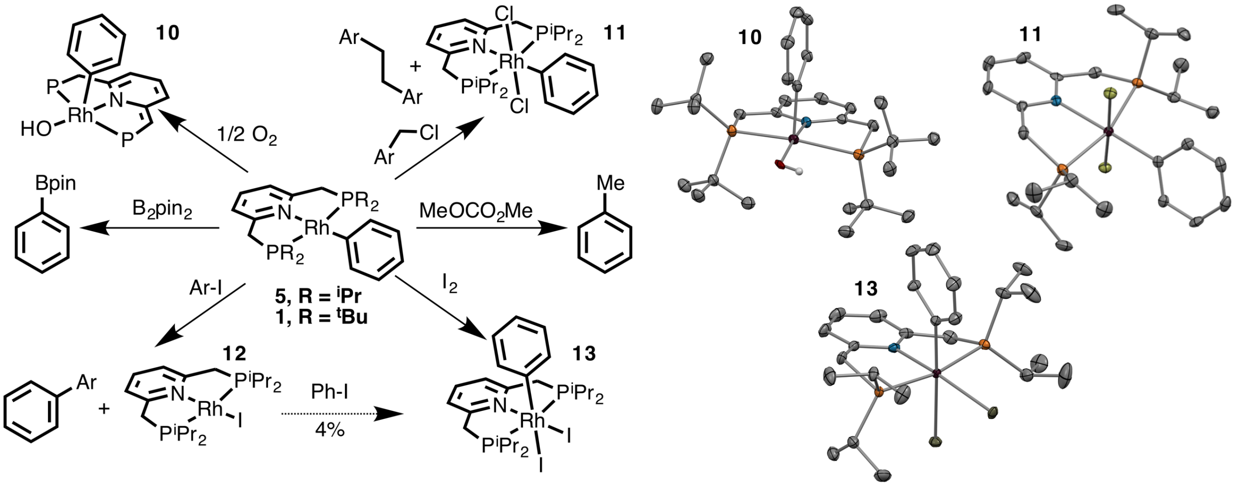

Figure 39 Reactivity of (PNP)Rh(Ph) with various electrophiles and oxidants and ORTEPS of complexes **10**, **11**, and **13** with 50% thermal ellipsoids and hydrogens omitted for clarity (except OH).

A recent report of oxidative addition of O_2 to (PNP)Ir(Ph) suggested that **1** might react with O_2 to afford dearomatized Rh(III) hydroxo complex **10**.[75] Moreover, reductive elimination of phenol from **10** would afford the requisite dearomatized complex (Figure 35A) and thereby circumvent the need for harsh exogenous bases. Complex **1** did indeed react with O_2 to give a dearomatized species consistent with complex **10** as the major product. Crystals of complex **10** suitable for x-ray diffraction were obtained, but attempts to purify and isolate complex **10** in bulk were not successful. Moreover, reductive elimination of phenol from the crude mixture was not observed with prolonged heating. In an attempt to lower the barrier to reductive elimination, we next explored the reactivity of **5** with C_{sp3}-X electrophiles. When **5** was treated with *p*-tolyl-benzylchloride, an intermediate consistent with the desired oxidative addition product was observed by ^{1}H NMR, but this compound disproportionated to complex **11** and 4,4'-dimethyl-dibenzyl rather than undergoing the desired reductive elimination. In contrast, reaction of **5** with dimethylcarbonate afforded alkylated arene (toluene) in good yield (76%).

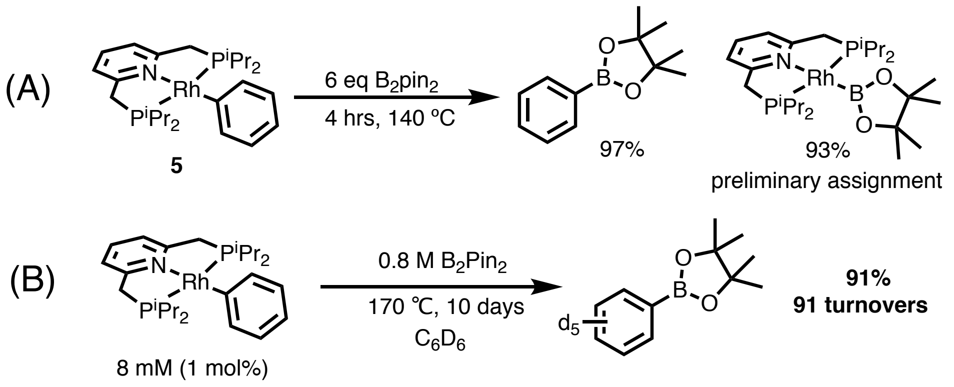

Figure 40 (A) Reaction of (PNP)Rh(Ph) with B_2Pin_2 (B) Rhodium catalyzed C-H borylation of C_6D_6 with B_2Pin_2.

^{i}Pr(PNP)Rh(Ph) reacted with B_2pin_2 at 140 °C yielding phenylboronic acid-pinacol ester in excellent yield (97%) and very clean conversion by $^{31}P\{^1H\}$ NMR to a new rhodium complex with a ^1H NMR spectrum consistent with the rhodium boryl ^{i}Pr(PNP)Rh(Bpin) (Figure 39 and Figure 40A). Notably, when ^{i}Pr(PNP)Rh(Ph) was treated with an excess of B_2pin_2 in C_6D_6, it was able to slowly catalyze 91 turnovers of C-H borylation at elevated temperatures (Figure 40B).

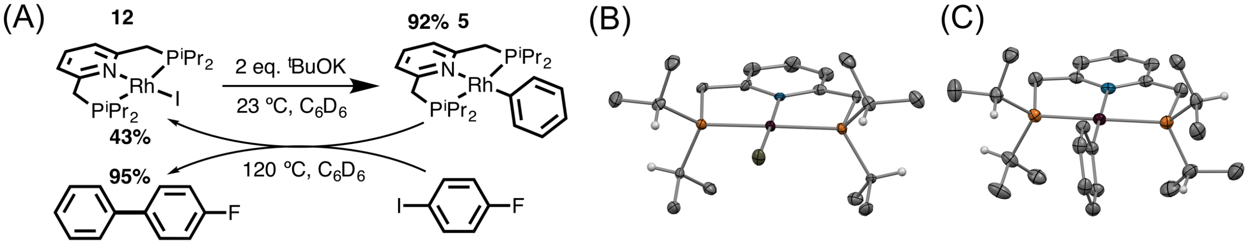

Figure 41 (A) C-H activation with complex **12** and functionalization of C-H activation adduct **5** with 4-fluoro-iodobenzene. (B) ORTEP of complex **12** with 50% thermal ellipsoids (C) ORTEP of complex **5** with 50% thermal ellipsoids.

Previous studies on oxidative addition of aryl halides to pincer complexes and on the stability of aryl halides to base led us to pursue reactions of **5** with aryl iodides (Figure

39 and Figure 41).[76-79] To our delight, **5** reacted with aryl iodides at elevated temperature (120 °C) to yield the desired biaryl product and (PNP)Rh(I) (**12**) (Figure 41). Among the electrophiles assessed in Figure 39, aryl iodides stood out as the least likely to undergo further unproductive addition to the organometallic product (PNP)Rh(X). To confirm this, we heated **12**—the product of the reaction of **5** with aryl iodides—with excess iodobenzene (Figure 39). After 40 hours at 140 °C, only 4% of unproductive oxidative addition product **13** was formed as confirmed by independent synthesis of **13** via reaction of **5** with I_2 (Figure 39). Moreover, iodo complex **12** reacted with C_6D_6 to give the desired C-H activation adduct **5** (Figure 41). In contrast to the C-H activation reactions in Figure 35, which were conducted in sealed tubes with evacuated head space to reduce N_2 inhibition, C-H activation with complex **12** was conducted under N_2 atmosphere, indicating that isopropyl ligand substitution effectively resolved the problem of N_2 inhibition. C-H activation with complex **12**, coupled with the reaction of **5** with aryl iodides as shown in Figure 41, demonstrates the feasibility of steps in the desired cycle outlined in Figure 34.

(PNP)Rh catalyzed direct arylation of aryl iodides

With an improved complex for rhodium mediated C-H activation (**3**) in hand and a deeper understanding of the reactivity of C-H activation adducts **1** and **5** in mind, we sought to determine whether these complexes were capable of catalytic C-H functionalization of simple arenes. Gratifyingly, complex **3** catalyzed direct C-H arylation of benzene with a variety of aryl iodides (Figure 42A). Control reactions revealed that in the absence of rhodium catalyst there is a minor background reaction (reported parenthetically for each reaction). Complex **3** also catalyzes arylation of several simple arenes with moderate electronic and steric variation (Figure 42B). Importantly, this system enables functionalization of all C-H bonds (ortho, meta, para, benzylic, and methoxy) in each substrate tested with only minor contributions from substituent directing effects. As noted above, the design of catalysts which can override functional group directing effects and electronic bias to give catalyst controlled selectivity first requires the development of catalysts that do not require particular functional groups to promote C-H functionalization.

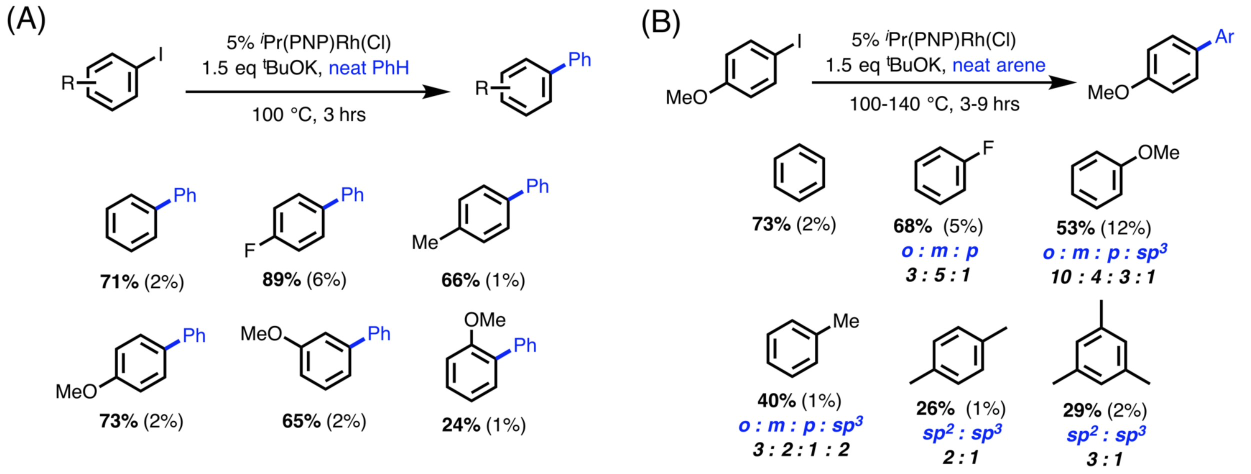

Figure 42 (A) Direct arylation of benzene with various aryl iodides: yield in bold and yield of background reaction (no Rh) in parentheses; (B) Direct arylation of various arenes with 4-iodoanisole: yield in bold and yield of background reaction (no Rh) in parentheses.

Given reports of direct arylation reactions using aryl iodides in the presence of ^{t}BuOK and an organic catalyst,[80] control reactions were conducted to compare the yield of ^{t}BuOK-mediated benzene arylation in the presence of no additives, 5 mol% ^{i}Pr(PNP)Rh(Cl), or 5 mol% of the ^{i}Pr(PNP) ligand (Figure 43A, entries 2, 4, and 5). These reactions revealed comparable and dramatically reduced yields under the latter two conditions relative to the former, indicating that the reaction is not catalyzed by demetallated ligand alone.[80] Whereas organocatalytic transformations of this type show no activity in the presence of a catalytic radical trap (TEMPO),[81] the (PNP)Rh catalyzed reaction maintained substantial activity under the same conditions (Figure 43A, entry 3). Notably, the less hindered complexes (**3** and **5**) were much more efficient precatalysts than bulkier complexes **2** and ^{t}Bu(PNP)Ir(coe)(PF$_6$)—consistent with metal centered reactivity.

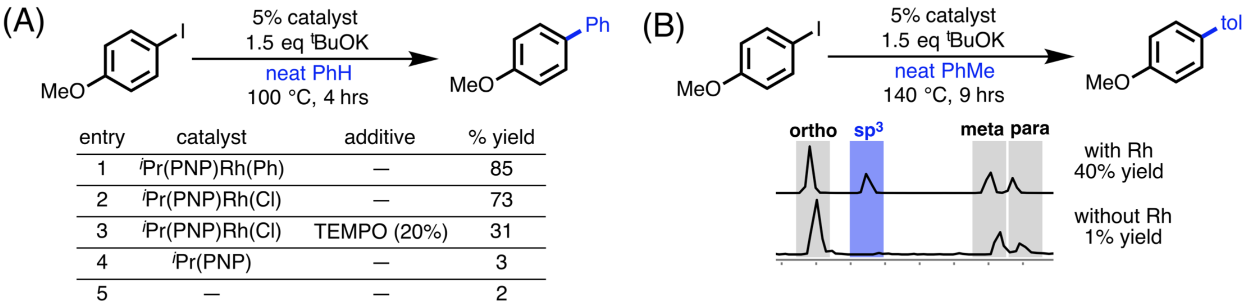

entry	catalyst	additive	% yield
1	^{i}Pr(PNP)Rh(Ph)	—	85
2	^{i}Pr(PNP)Rh(Cl)	—	73
3	^{i}Pr(PNP)Rh(Cl)	TEMPO (20%)	31
4	^{i}Pr(PNP)	—	3
5	—	—	2

Figure 43 (A) Control reactions with alternative pre-catalysts and TEMPO additive; (B) extracted ion GCMS chromatograms of toluene reaction mixtures show no sp^3 functionalization in the absence of rhodium

The sp^2 selectivity in rhodium catalyzed direct arylation is most consistent with previously reported radical based arylations (Figure 43B).[80] Notably, reactions in the presence or absence of rhodium catalyst had similar sp^2 selectivity. This finding could indicate that the rhodium complexes studied herein catalyze C-H functionalization by initiating or accelerating the background reaction, which has been proposed to proceed through radical intermediates (Figure 43B).[80,82] On the other hand, the sp^3 C-H functionalization observed for toluene, anisole, *p*-xylene, and mesitylene was not observed in the ^{t}BuOK mediated background reaction, indicating that the rhodium catalyst enables access to pathways that are not accessible to the active species in the background reaction (Figure 43B).

Conclusion

Overall, we harnessed the ability of the (PNP)Rh platform to mediate non-directed C-H activation and translated this reactivity into a catalytic system that achieved our goal of functionalizing all C-H bonds on a variety of substrates (Figure 34D and Figure 42B). This was enabled by the fact that this complex does not require directing groups to enable C-H activation and achieved by a ligand modification to dramatically enhance the rate of C-H activation and expanding our understanding of stoichiometric reactivity of the C-H activation complex (PNP)Rh(Ph) with a variety of electrophiles. Moreover, we found that key drawbacks to the (PNP)Rh platform (nitrogen inhibition and dependence on strong base) were readily mitigated by simple modifications (smaller phosphines and weakly coordinating anions, respectively). The resulting catalytic method, like others based on the PNP platform that emerged from stoichiometric reactions,[83,84] sheds new light on the reactivity of the (PNP)Rh platform in the form of unexpected sp^3 functionalization and potential catalysis of radical based transformations.

Experimental

Unless otherwise noted, all reactions and manipulations were performed under a circulating nitrogen atmosphere in an Innovative Technologies glovebox, or using standard Schlenk technique. J. Young tubes were washed with base bath (prepared with 100 g KOH, 200 mL DI H_2O, and 700 mL *iso*-propanol), followed by methanol, water, and acetone. Glassware was oven dried prior to use.

Unless otherwise noted, all reagents were obtained from commercial suppliers and used without further purification. Hydrocarbons and ethereal solvents were ketyl tested prior to use. Benzene (PhH) and C_6D_6 were dried for 48 hours over activated 4Å molecular sieves, degassed by three cycles of freeze pump thaw and transferred to fresh sieves in the glovebox. Arene solvents were dried over activated 4Å molecular sieves, degassed by three freeze-pump thaw cycles, passed over a pad of activated alumina in the glovebox and stored over activated 4Å molecular sieves. CD_2Cl_2 was dried over calcium hydride and vacuum transferred into bomb with a teflon cap. Liquid aryl halides were degassed by three cycles of freeze pump thaw and passed over pad of activated alumina in the glovebox. Acetone and acetone-d_6 were dried over 4Å molecular sieves for 24 hour, distilled, and stored over calcium sulfate. Tetrahydrofuran (THF), diethyl ether (Et_2O), dichloromethane (CH_2Cl_2), toluene (PhMe), and pentane were obtained from an Innovative Technologies solvent purification system (solvent deoxygenated by N_2 sparge and dried over two columns of activated alumina). Molecular sieves and silica were activated at 200 °C under dynamic vacuum (0.05 mm Hg) until visible water stopped condensing in a trap immersed in liquid nitrogen, then for an additional 12 hours after that. Alumina was activated at 350 °C under dynamic vacuum (0.05 mm Hg) until visible water stopped condensing in a trap immersed in liquid nitrogen, then for an additional 12 hours after that. Methane sulfonic acid (MsOH) was dried by stirring 50 mL MsOH with 2 grams of P_2O_5, heating to 100 °C for 1 hour, and distillation under vacuum. 4-toluene sulfonic acid was dried by azeotropic distillation with toluene followed by recrystallization from warm, anhydrous, benzene in the glovebox. The concentrations of Grignards were determined by titration in triplicate with salicylaldehyde phenylhydrazone.[69]

The nomenclature (PNP)* is used to indicate side arm deprotonated ligand.

As noted previously,[85] due to strong ^{31}P-^{31}P coupling in the pincer ligand, many ^1H and ^{13}C signals appear as virtual triplets (vt) and are reported as such with the apparent coupling constant noted. In $^{31}P\{^1H\}$ experiments the sweep-width of the decoupling channel is insufficient to simultaneously decouple aliphatic and hydridic ^1H resonances: as such, $^{31}P\{^1H\}$ spectra of rhodium hydrides include coupling to Rh-H.

Yields for rhodium catalyzed direct arylation and background reactions are reported as the average of three reactions run in parallel with respect to a calibration curve. Calibration curves were prepared for all non-isomeric biaryl products. Calibration curves were prepared for meta, para, and sp^3 functionalized products of toluene: the three products had response factors within 10% of each other, so for the remaining substrates, the response factor was determined for a single regio-isomer. All biaryl products that were not commercially available (Combi-Blocks) were prepared by Suzuki-Miyaura reaction to confirm their retention times by GC. Authentic standards of sp^3 functionalized positions on toluene, p-xylene, and mesitylene were prepared by a literature procedure.[86] Authentic standard of sp^3 functionalization product of anisole was prepared by a reported procedure.[87]

Literature procedures were used to prepare[Rh(coe)$_2$ (Cl)]$_2$,[88] ^{i}Pr(PNP),[89] pyrr-^{i}Pr(PNP),[84] ^{t}Bu(PNP),[90] ^{i}Pr(PNP)Rh(Cl) **3**,[91] ^{t}Bu(PNP)Rh(Cl) **2**,[92] ^{t}Bu(PNP)Rh(Ph) **2**,[93] potassium 2,6-bis(*tert*-butyl)-4-methoxy-phenolate,[94] and ^{t}Bu(PNP)Ir(coe)(PF$_6$).[72]

Synthesis of 5 ^{i}Pr(PNP)Rh(Ph)

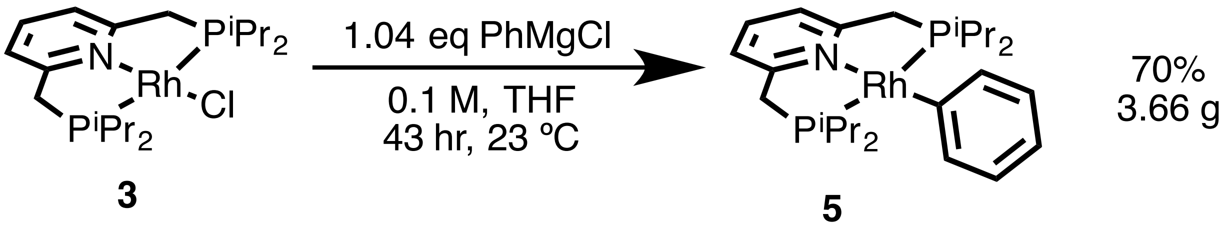

Figure 44: Synthesis of 5 ^{i}Pr(PNP)Rh(Ph)

A 500 mL round bottom flask was charged with **3** (4.778g, 10 mmol, 1 equiv.), a stir bar, and 100 mL of THF. To the deep red, stirring solution was added phenyl magnesium chloride in THF (10.4 mmol, 4.55 mL, 2.2M, 1.04 equiv.). Reaction progress was monitored by ^{31}P NMR of 50 µL aliquots dissolved in 500 µL C_6D_6. After 43 hours, all of the starting material had been consumed and the solvent was removed under reduced pressure. To remove any residual THF, the dark solid mixture was suspended in 10 mL of toluene and concentrated in vacuo. The mixture was extracted with refluxing pentane (40 mL) which filtered over a medium frit into a warm side arm flask. The mixture of product and magnesium salts in the original reaction vessel was extracted 6 times in this manner while gently warming the collection flask to prevent precipitation. Over the course of the extractions approximately half of the pentane evaporated to give a saturated solution of **5** in warm pentane. The filtrate was transferred to a 200 mL jar, sealed, allowed to cool to room temperature, and transferred to a -35 °C freezer. After 48 hours at -35 °C the supernatant was decanted to give 3.66g (70% yield) of large black-red crystals of complex **5**. Single crystals suitable for x-ray diffraction were grown by slow evaporation of pentane from the supernatant solution at -35 °C. Anal Calcd for $C_{25}H_{40}NP_2Rh$: C, 57.81; H, 7.76; N, 2.70. Found: C, 58.99; H, 8.02; N, 2.57. . Material prepared by this method gave carbon analysis outside the range viewed as establishing analytical purity (Δ1.81%). Elemental analysis and graphical ^{1}H, ^{31}P, and ^{13}C NMR data are provided to illustrate the degree of purity of the bulk material obtained by this method without additional purification.

^{1}H NMR (500 MHz, C_6D_6) δ 7.94 (d, $^3J_{HH}$ = 7.6 Hz, 2H, Rh-Ph ortho), 7.21 (t, $^3J_{HH}$ = 7.4 Hz, 2H, Rh-Ph meta), 7.01 (t, $^3J_{HH}$ = 7.6 Hz, 1H, pyr-para), 6.93 (t, $^3J_{HH}$ = 7.1 Hz, 1H, Rh-Ph para), 6.51 (d, J = 7.6 Hz, 2H, pyr-meta), 2.72 (vt, $^3J_{PH}$ = 3.3 Hz, 4H, PCH_2), 1.91 (m, 4H, ^{i}Pr CH), 1.14 (m, (doublet by ^{1}H{^{31}P} $^3J_{HH}$ = 7.1 Hz), 12H, ^{i}PrCH$_3$), 1.04 (m, (doublet by ^{1}H{^{31}P} $^3J_{HH}$ = 6.9 Hz), 12H, ^{i}PrCH$_3$).

^{31}P{^{1}H} NMR (202 MHz, C_6D_6) δ 42.64 (d, $^1J_{RhP}$ = 168.8 Hz).

^{13}C{^{1}H} NMR (126 MHz, C_6D_6) δ 167.64 (vtd, $^2J_{PC}$ = 13.5, $^1J_{RhC}$ 32.3 Hz, Rh-Ph C ipso), 161.20 (dvt, $^2J_{RhC}$ = 1.4, $^2J_{PC}$ = 6.6 Hz, pyr C-ortho), 141.11 (vt, $^3J_{PC}$ = 3.1 Hz, Rh-Ph C ortho), 130.35 (s, pyr C-para), 124.79 (m, Rh-Ph C meta), 119.13 (vt, $^3J_{PC}$ = 4.6 Hz, pyr C meta), 118.13 (vt, $^5J_{PC}$ = 1.3 Hz, Rh-Ph C para), 37.03 (vt, $^1J_{PC}$ = 5.9 Hz, PCH_2), 24.15 (dvt, $^2J_{RhC}$ = 2.9, $^1J_{PC}$ = 8.9 Hz, ^{i}Pr CH), 18.85 (vt, $^2J_{PC}$ = 3.6 Hz, ^{i}Pr CH$_3$), 17.77 (m, ^{i}Pr CH$_3$).

Synthesis of 6 ^{i}Pr(PNP)Rh(OMs)

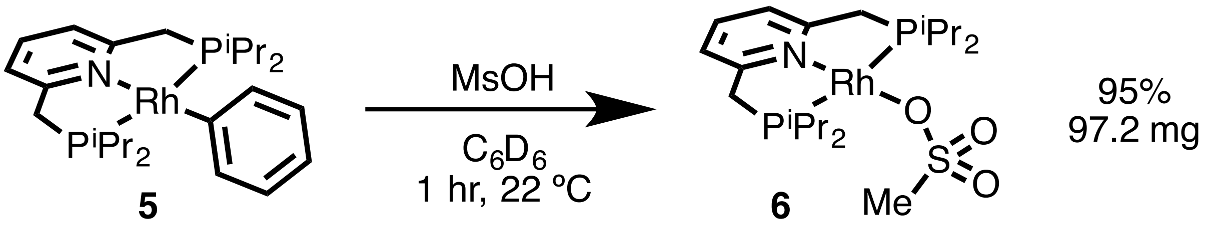

Figure 45: Synthesis of 6 ^{i}Pr(PNP)Rh(OMs)

A J. Young tube was charged with **5** (100 mg, 0.192 mmol, 1 equiv.) and 500 µL of C_6D_6. To the blackish solution was added 12.5 µL of methane sulfonic acid. The tube was capped, shaken, and analyzed by ^{1}H and ^{31}P NMR within 5 minutes of mixing. The reaction was monitored one hour later, which revealed no further reaction. The contents of the J. Young tube were poured into 10 mL of stirring pentane in a 20 mL scintillation vial at -35 °C to give an orange-red precipitate. The precipitate settled to the bottom of the vial overnight at -35 °C at which time the supernatant was decanted to give 97.2 mg (95% yield) of complex **6**. Anal Calcd for $C_{20}H_{38}NO_3SP_2Rh$: C, 44.70; H, 7.13; N, 2.61. Found: C, 46.57; H, 7.52; N, 2.78. Material prepared by this method gave carbon analysis outside the range viewed as establishing analytical purity (Δ1.87%). Elemental analysis and graphical ^{1}H, ^{31}P, and ^{13}C NMR data are provided to illustrate the degree of purity of the bulk material obtained by this method without additional purification.

^{1}H NMR (500 MHz, C_6D_6) δ 6.79 (t, $^3J_{HH}$ = 7.4 Hz, 1H, pyr para), 6.22 (d, $^3J_{HH}$ = 7.7 Hz, 2H, pyr meta), 2.76 (s, 3H, OMs-CH_3), 2.39 (vt, $^3J_{PH}$ = 3.5 Hz, 4H, PCH_2), 2.28 (m (septet by ^{1}H{^{31}P} $^3J_{HH}$ = 7.0Hz), 4H, ^{i}PrCH), 1.55 (m, (doublet by ^{1}H{^{31}P} $^3J_{HH}$ = 7.0 Hz), 12H, ^{i}PrCH_3), 1.03 (m, (doublet by ^{1}H{^{31}P} $^3J_{HH}$ = 7.0 Hz), 12H, ^{i}PrCH_3).

^{31}P{^{1}H} NMR (202 MHz, C_6D_6) δ 47.88 (d, $^2J_{RhP}$ = 148.8 Hz, 2P).

^{13}C{^{1}H} NMR (126 MHz, C_6D_6) δ 165.03 (vtd, $^2J_{PC}$ = 6.3, $^3J_{RhC}$ = 1.1 Hz, ortho pyr), 129.76 (s, para pyr), 119.38 (vtd, $^3J_{PC}$ = 5.3, $^4J_{RhC}$ = 1.2 Hz, meta pyr), 38.74 (s, OMs-CH_3), 34.49 (vtd, $^1J_{PC}$ = 6.7, $^2J_{RhC}$ = 1.5 Hz, PCH_2), 24.25 (vtd, $^1J_{PC}$ = 9.6, $^2J_{RhC}$ = 1.0 Hz, ^{i}PrCH), 19.23 (vt, $^2J_{PC}$ = 3.9 Hz, ^{i}PrCH_3), 17.70 (s (br), ^{i}PrCH_3).

Synthesis of 7 ^{i}Pr(PNP)Rh(OTs)

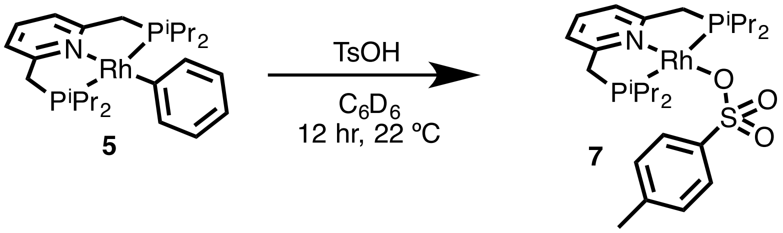

98% NMR yield
5.8 mg
68% isolated

Figure 46: Synthesis of 7 ^{i}Pr(PNP)Rh(OTs)

To a J. Young tube was added a stock solution in C_6D_6 of **5** (14 µmol, 583 µL, 24 mM, 1 equiv.) which also contained mesitylene (4.66 µmol, 8 mM) as an internal standard. To this solution was added a stock solution in C_6D_6 of 4-toluene sulfonic acid (14 µmol, 93.3 mM, 150 µL). The mixture was immediately capped, shaken, and analyzed by ^{1}H NMR which revealed conversion to **7** with concomitant elimination of benzene as the major products. However, during the first 6 minutes of the reaction, an intermediate was observed with ^{1}H and ^{31}P NMR spectra consistent with metal centered protonation (see figure below)— specifically a rhodium hydride resonance (δ -18.94, m by ^{1}H NMR, d by ^{1}H{^{31}P} NMR, $^1J_{RhH}$ = 19.0 Hz) and broken symmetry of the PCH_2 and ^{i}Pr resonances. After 12 hours at 21 °C the reaction had gone to 98% of the desired product by ^{1}H NMR with respect to mesitylene internal standard. The reaction mixture was poured into a 1 dram vial, concentrated under reduced pressure, and suspended in 1 mL of pentane. After 12 hours at -35 °C the supernatant was removed by pipette to afford 5.8 mg (68% yield) of complex **7**. The precipitated material contains several minor (PNP)Rh impurities and is estimated to be 80% pure as determined by integration of the ^{31}P NMR spectrum.

Observation of an intermediate in the synthesis of 7 *ⁱ*Pr(PNP)Rh(OTs)

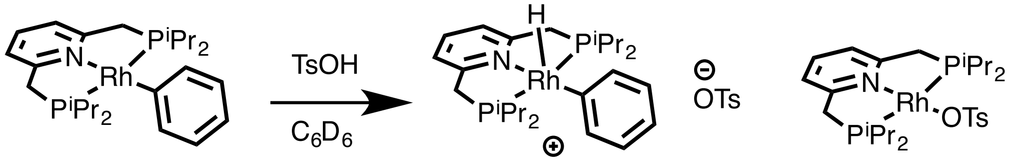

14 *μ*mol

3 min, 21 °C	**36%**	50%
6 min, 21 °C	10%	86%
12 hr, 21 °C	0%	**98%**

Figure 47: Observation of an intermediate in the synthesis of 7 *ⁱ*Pr(PNP)Rh(OTs)

^{1}H NMR (500 MHz, C_6D_6) δ 8.17 (d, $^3J_{HH}$ = 7.9 Hz, 2H, OTs CH), 6.91 (d, $^3J_{HH}$ = 7.8 Hz, 2H, pyr meta), 6.85 (t, $^3J_{HH}$ = 7.6 Hz, 1H, pyr para), 6.28 (d, $^3J_{HH}$ = 7.6 Hz, 2H, OTs CH), 2.43 (m, 4H, PCH_2), 2.27 (m, (septet by $^1H\{^{31}P\}$ $^3J_{HH}$ = 7.0 Hz), 4H, ^{i}PrCH), 1.97 (s, 3H, OTs CH_3), 1.56 (m, (doublet by $^1H\{^{31}P\}$ $^3J_{HH}$ = 7.0 Hz), 12H, $^iPrCH_3$), 1.02 (m, (doublet by $^1H\{^{31}P\}$ $^3J_{HH}$ = 6.9 Hz) 12H, $^iPrCH_3$).

$^{31}P\{^1H\}$ NMR (202 MHz, C_6D_6) δ 48.41 (d, $^1J_{RhP}$ = 147.8 Hz).

$^{13}C\{^1H\}$ NMR (126 MHz, C_6D_6) δ 165.10 (vtd, $^2J_{PC}$ = 6.4 Hz, $^3J_{RhC}$ = 1.1 Hz, pyr ortho), 143.74 (s, OTs quaternary), 138.48 (s, OTs quaternary), 130.04 (s, pyr para), 128.21 (s,OTs CH), 126.65 (s, OTs CH), 119.49 (vtd, $^3J_{PC}$ = 5.4, $^4J_{RhC}$ = 0.9 Hz, pyr meta), 34.48 (vtd, $^1J_{PC}$ = 6.9, $^2J_{PC}$ = 1.4 Hz, PCH_2), 24.26 (vt, $^1J_{PC}$ = 9.5 Hz, ^{i}PrCH), 20.74 (s, OTs CH_3), 19.32 (vt, $^2J_{PC}$ = 3.9 Hz, $^iPrCH_3$), 17.70 (s, $^iPrCH_3$).

Synthesis of 8 *ⁱ*Pr(PNP)Rh(H)(OTs)

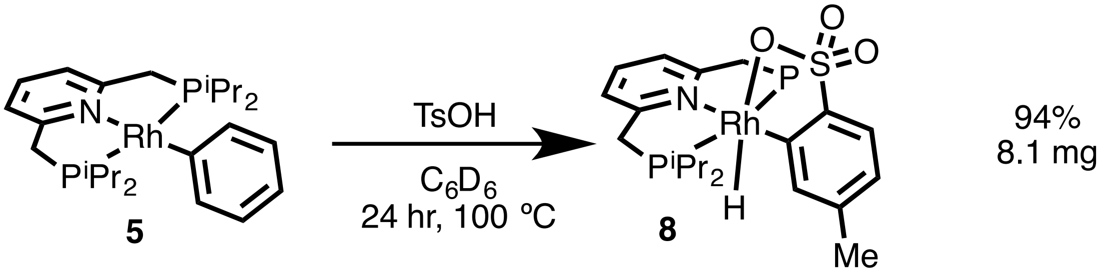

Figure 48: Synthesis of 8 *ⁱ*Pr(PNP)Rh(H)(OTs)

To a J. Young tube was added a stock solution in C_6D_6 of **5** (14 µmol, 583 µL, 24 mM, 1 equiv.) which also contained mesitylene (4.66 µmol, 8 mM) as an internal standard. To this solution was added a stock solution in C_6D_6 of 4-toluene sulfonic acid (14 µmol, 93.3 mM, 150 µL). The mixture was immediately capped, shaken, and analyzed by ^{1}H NMR which revealed conversion to **7** with concomitant elimination of benzene as the major products. After 12 hours the reaction had gone to complete conversion to complex **7**. The reaction mixture was heated to 100 °C for 12 hours, during which time a white solid precipitated from the reaction mixture. The suspension was transferred to a 1 dram vial and the supernatant removed by pipette. The precipitate was washed with diethyl ether and dried under vacuum to give 8.1 mg (94% yield) of **8** as an off-white precipitate. Anal Calcd for $C_{26}H_{42}NO_3SP_2Rh$: C, 50.90; H, 6.90; N, 2.28. Found: C, 51.09; H, 6.94; N, 2.22. **^{1}H NMR** (500 MHz, CD_2Cl_2) δ 7.68 (t, $^3J_{HH}$ = 7.7 Hz, 1H, pyr para), 7.34 (d, $^2J_{HH}$ = 7.6 Hz, 1H, pyr ortho), 7.23 (s, 1H, OTs), 7.19 (d, $^3J_{HH}$ = 7.8 Hz, 1H, OTs), 6.71 (d, $^3J_{HH}$ = 7.7 Hz, 1H, OTs), 3.73 (d br, $^2J_{HH}$ = 16.2 Hz, 2H, PCH_2), 3.49 (d br, $^2J_{HH}$ = 16.2 Hz, 2H, PCH_2), 2.93 (m, 2H, ⁱPrCH), 2.24 (m, 5H, ⁱPrCH' overlapped with OTs-CH_3), 1.10 (m, (doublet by

$^1H\{^{31}P\}$ $^3J_{HH}$ = 7.1 Hz), 6H, ^{i}PrCH$_3$), 1.05 (m, 12H, ^{i}PrCH$_3$), 0.86 (m, 6H, ^{i}PrCH$_3$), -18.65 (vtd, $^2J_{HP}$ = 12.7, $^1J_{HRh}$ = 32.4 Hz, 1H, Rh-H).

$^{31}P\{^1H\}$ NMR (202 MHz, CD_2Cl_2) δ 58.55 (td, $^2J_{PH}$ = 12.7, $^1J_{PRh}$ = 109.2 Hz).

$^{13}C\{^1H\}$ NMR (126 MHz, CD_2Cl_2) δ 161.42 (m, pyr ortho), 145.57 (s, OTs quaternary), 143.46 (m, OTs CH), 137.84 (s, pyr para), 137.08 (s, OTs quaternary), 129.80 (m, Rh-C), 124.82 (s, OTs CH), 122.14 (s, OTs CH), 120.34 (vt, $^3J_{PC}$ = 4.1 Hz, pyr meta), 38.02 (vt, $^1J_{PC}$ = 9.7 Hz, PCH$_2$), 23.54 (vt, $^1J_{PC}$ = 10.0 Hz, ^{i}PrCH), 22.82 (vt, $^1J_{PC}$ = 13.8 Hz, ^{i}PrCH), 20.99 (s, OTs-CH$_3$), 18.75 (m, ^{i}PrCH$_3$), 18.51 (s br, ^{i}PrCH$_3$), 17.73 (s br, ^{i}PrCH$_3$), 17.16 (s br, ^{i}PrCH$_3$).

Synthesis of 9 *^{i}*Pr(PNP)Rh(H)(OTs)$_2$

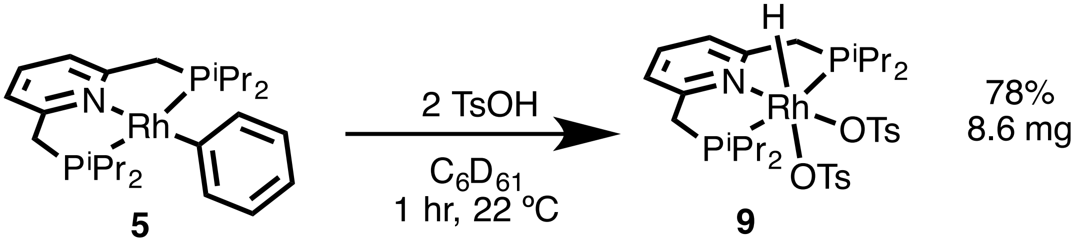

Figure 49: Synthesis of 9 ^{i}Pr(PNP)Rh(H)(OTs)$_2$

To a J. Young tube was added a stock solution in C_6D_6 of **5** (14 µmol, 583 µL, 24 mM, 1 equiv.) which also contained mesitylene (4.66 µmol, 8 mM) as an internal standard. To this solution was added a stock solution in C_6D_6 of 4-toluene sulfonic acid (28 µmol, 93.3 mM, 300 µL). The mixture was immediately capped, shaken, and analyzed by ^{1}H NMR which revealed complete conversion to **9** with concomitant elimination of benzene as the major products. The reaction was monitored again one hour later and revealed no further reaction. The reaction mixture was transferred to a 1 dram vial, concentrated in vacuo and washed with pentane, and dried under vacuum to give 8.6 mg (78% yield) of **9** as an off-white precipitate. Anal Calcd for $C_{33}H_{50}NO_6S_2P_2Rh$: C, 50.44; H, 6.41; N, 1.78. Found: C, 50.72; H, 6.49; N, 1.78.

^{1}H NMR (500 MHz, C_6D_6) δ 8.12 (d, $^3J_{HH}$ = 8.0 Hz, 2H, OTs), 8.07 (d, $^3J_{HH}$ = 8.1 Hz, 2H, OTs), 7.03 (t, $^3J_{HH}$ = 7.7 Hz, 1H, pyr para), 6.87 (d, $^3J_{HH}$ = 7.8 Hz, 2H, OTs), 6.83 (d, $^3J_{HH}$ = 8.0 Hz, 2H, OTs), 6.62 (d, $^3J_{HH}$ = 7.7 Hz, 2H, pyr meta),

4.49 (vtd, $^3J_{HP}$ = 4.4, $^2J_{HH}$ =17.0 Hz, 2H, PCH_2), 3.30 (m, (septet by $^1H\{^{31}P\}$ $^3J_{HH}$ = 7.2 Hz), 2H, ^{i}PrCH), 2.77 (vtd, $^3J_{HP}$ = 3.5, $^2J_{HH}$ = 17.1 Hz, 2H, PCH_2), 2.20 (m, (septet by $^1H\{^{31}P\}$ $^3J_{HH}$ = 7.1 Hz), 2H, ^{i}PrCH), 1.94 (s, 3H, OTs-CH_3), 1.92 (s, 3H, OTs-CH_3), 1.55 (m, (doublet by $^1H\{^{31}P\}$ $^3J_{HH}$ = 7.2 Hz), 6H, ^{i}PrCH_3), 1.47 (m, (doublet by $^1H\{^{31}P\}$ $^3J_{HH}$ = 7.0 Hz), 6H, ^{i}PrCH_3), 1.29 (m, (doublet by $^1H\{^{31}P\}$ $^3J_{HH}$ = 7.2 Hz), 6H, ^{i}PrCH_3), 0.88 (m, (doublet by $^1H\{^{31}P\}$ $^3J_{HH}$ = 6.8 Hz), 6H, ^{i}PrCH_3), -18.97 (vtd, $^2J_{HP}$ = 10.2, $^1J_{HRh}$ = 19.5 Hz, 1H,Rh-H).

$^{31}P\{^1H\}$ NMR (202 MHz, C_6D_6) δ 49.85 (dd, $^2J_{PH}$ = 9.1, $^1J_{PRh}$ 100.6 Hz, 2P).

$^{13}C\{^1H\}$ NMR (126 MHz, C_6D_6) δ 167.06 (vt br, $^2J_{CP}$ = 4.5 Hz, pyr ortho), 141.32 (s, OTs quaternary), 139.47 (s, OTs quaternary), 137.71 (s, pyr para), 128.52 (s br, OTs CH), 128.47 (s, OTs CH), 126.63 (s, OTs CH), 126.33 (s br, OTs CH), 120.59 (vt, $^3J_{CP}$ = 5.5 Hz, pyr meta), 36.01 (vt, $^1J_{CP}$ = 9.4 Hz, PCH_2), 25.87 (vt, $^1J_{CP}$ = 12.7 Hz, ^{i}PrCH), 25.49 (vt, $^1J_{CP}$ = 11.0 Hz, ^{i}PrCH), 20.72 (br, 2xOTs-CH_3), 19.03 (vt, $^2J_{CP}$ = 2.0 Hz, ^{i}PrCH_3), 18.64 (br, ^{i}PrCH_3),18.17 (br, ^{i}PrCH_3), 17.86 (br, ^{i}PrCH_3).

Synthesis of 10 ^{t}Bu(PNP)*Rh(OH)(Ph)

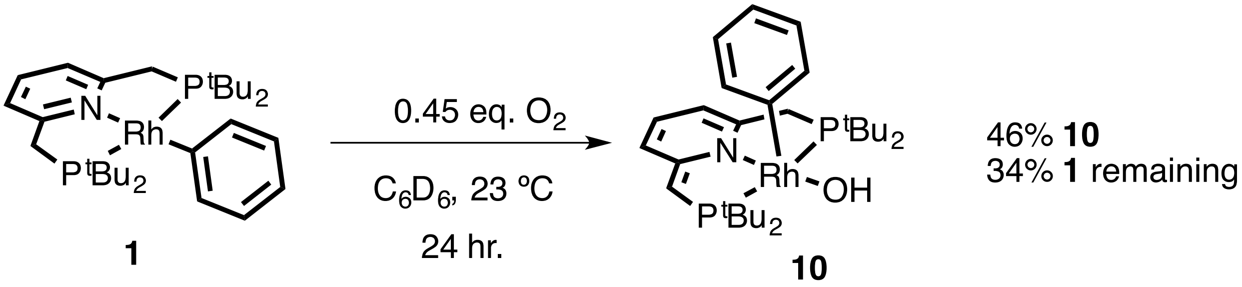

Figure 50: Synthesis of 10 ^{t}Bu(PNP)*Rh(OH)(Ph)

Following a previously reported procedure for the iridium congener[95] a J. Young tube was charged with a C_6D_6 stock solution of **1** (25 µmol, 50 mM, 500 µL) which also contained 1,3,5-trimethoxybenzene (2.5 µmol, 5 mM) as internal standard. The tube was removed from the glovebox, degassed by 3 cycles of freeze pump thaw, and sealed with the headspace under vacuum while the solution was frozen in a -78 °C bath. With the sample still in the -78 °C bath, a J. Young adaptor was removed from the vaccuum manifold and fitted with a rubber septum and the space between the septum and J. Young cap was evacuated. Immediately after the needle attached to vacuum was removed from the septum, a gas tight syringe containing O_2 gas (11.25 µmol, 250 µL, 0.45 eq) was plunged into the septum. The O_2 was immediately drawn into the evacuated space between the J. young cap and the septum. Then the J. Young cap was opened, to expose the contents of the J. Young tube (still under static vacuum) to the oxygen enriched space between the cap and septum. The sample was immersed in liquid nitrogen to condense oxygen in the J. Young tube. After 30 seconds of equilibration, the J. Young cap was sealed and the sample removed from liquid nitrogen. Upon thawing, the sample immediately changed color from dark red to dark brown (experiments with greater than 0.5 equivalents O_2 resulted in a green reaction mixture, complete consumption of starting material, and multiple rhodium containing products by ^{31}P NMR). Most of the reaction occurred in the 5 minutes between thawing the sample and acquiring the first NMR spectrum, but the yield with respect to 1,3,5-trimethoxybenzene is reported after 24 hours because of better peak shapes (likely due to paramagnetic intermediates or side reactions early in the reaction progress). Vapor diffusion of pentane into the reaction mixture afforded single crystals suitable for x-ray diffraction experiments. Unfortunately, clean bulk material for complete NMR characterization could not be obtained. Instead, complex **10** was characterized in the reaction mixture which contains highly diagnostic resonances consistent with a rhodium hydroxide complex on a dearomatized PNP ligand with an apical phenyl group: Rh-OH δ 0.32 (vt, $^3J_{PH}$ = 3.6 Hz, 1H), inequivalent benzylic PCH_2 δ 2.99 (dd, $^2J_{HH}$ = 16.2 Hz, $^2J_{PH}$ = 6.7 Hz , 1H), δ 2.58, (dd, $^2J_{HH}$ = 16.2 Hz, $^2J_{PH}$ = 8.9 Hz , 1H), one downfield PCH corresponding the deprotonated "arm" δ 3.56, (d, $^2J_{PH}$ = 4.9 Hz , 1H, obscured by impurity in spectra below, visible when impurity is consumed in the presence of 0.7 eq. O_2), and dramatically upfield and downfield shifted aromatic doublets (8.10 and 6.39 ppm) corresponding to the two ortho C-H's on the apical phenyl (note similarity to apical phenyl in complex **13**.). In the NMR spectra portion of the SI is a complete series of selective NOE experiments on the diagnostic resonances described above (mixing time 300 ms): the proton that was irradiated is emphasized with a bold circle and the protons with which it interacts are highlighted with color coded boxes. These selective NOE experiments are fully consistent with the assigned structure.

Synthesis of 11 ^{i}Pr(PNP)Rh(Ph)(Cl)$_2$

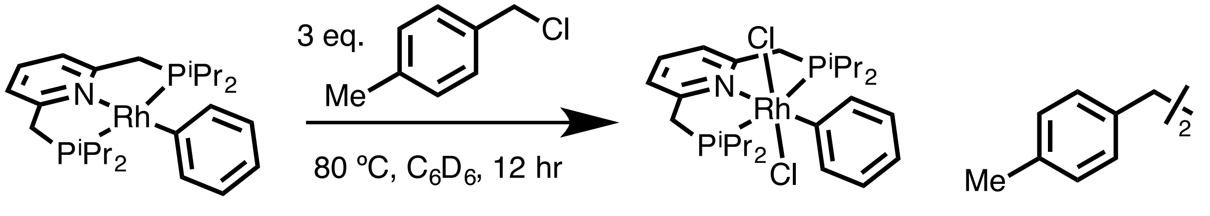

5

11
74% wrt Rh

95% wrt Rh

Figure 51: Synthesis of 11 ^{i}Pr(PNP)Rh(Ph)(Cl)$_2$

To a J. Young tube was added a stock solution in C_6D_6 of **5** (6.8 µmol, 200 µL, 35 mM, 1 equiv.) which also contained 1,3,5-trimethoxybenzene (1.4 µmol, 7 mM) as an internal standard. The solution was diluted with 250 µL of C_6D_6. To this solution was added a stock solution in C_6D_6 of 4-methyl-benzylchloride (20.4 µmol, 204 mM, 100 µL, 3 eq.). The mixture was immediately capped, shaken, and analyzed by ^{1}H and ^{31}P NMR which revealed complete consumption of **5**, major conversion to **11** and 4,4'-dimethyl-bibenzyl, and an additional (PNP)Rh product consistent with oxidative addition of benzylchloride (see section S1.5 for spectra: broken symmetry about ^{i}Pr and PCH$_2$, Rh-CH$_2$ (δ 4.20 (m by ^{1}H, d by ^{1}H{^{31}P} $^2J_{RhH}$ = 2.4 Hz), ^{31}P{^{1}H} (δ 34.35, d, $^1J_{RhP}$ = 113.0 Hz)). After 5 hours, the concentration of the intermediate had decreased and a yellow precipitate (**11**) began to form. Solution was heated to 80 °C for 12 hours which gave 74% yield of **11** and 95% of 4,4'-dimethyl-bibenzyl by ^{1}H NMR with respect to trimethoxybenzene internal standard. The product mixture was transferred to a 1 dram vial, and dichloromethane was added dropwise until the yellow precipitate dissolved. This mixture was layered with diethyl ether, which afforded yellow single crystals of **11** suitable for X-ray diffraction. The supernatant of the crystallization mixture was analyzed by GCMS which revealed a single organic product with a mass consistent with 4,4'-dimethyl-bibenzyl. Anal Calcd for $C_{25}H_{40}NP_2RhCl_2$: C, 50.86; H, 6.38; N, 2.37. Found: C, 51.93; H, 6.57; N, 2.28. Material prepared by this method gave carbon analysis outside the range viewed as establishing analytical purity (Δ1.07%). Elemental analysis and graphical ^{1}H, ^{31}P, and ^{13}C NMR data are provided to illustrate the degree of purity of the bulk material obtained by this method without additional purification.

^{1}H NMR (500 MHz, CD_2Cl_2) δ 8.06 (d, $^{3}J_{HH}$ = 7.8 Hz, 2H, Rh-Ph ortho), 7.71 (t, $^{3}J_{HH}$ = 7.7 Hz, 1H, pyr para), 7.39 (d, $^{3}J_{HH}$ = 7.4 Hz, 2H, pyr meta), 6.89 (t, $^{3}J_{HH}$ = 7.3 Hz, 2H, Rh-Ph meta), 6.83 (t, $^{3}J_{HH}$ = 7.0 Hz, 1H, Rh-Ph para), 3.92 (vt, $^{2}J_{PC}$ = 4.2 Hz, 4H, PCH_2), 2.89 (m, (septet by $^{1}H\{^{31}P\}$ $^{3}J_{HH}$ = 7.3 Hz), 4H, ^{i}PrCH), 1.32 (m, (doublet by $^{1}H\{^{31}P\}$ $^{3}J_{HH}$ = 7.2 Hz), 12H, $^{i}PrCH_3$), 1.05 (m, (doublet by $^{1}H\{^{31}P\}$ $^{3}J_{HH}$ = 7.3 Hz), 12H, $^{i}PrCH_3$).

$^{31}P\{^{1}H\}$ NMR (202 MHz, CD_2Cl_2) δ 37.02 (d, $^{1}J_{RhP}$ = 93.7 Hz).

$^{13}C\{^{1}H\}$ NMR (126 MHz, CD_2Cl_2) δ 160.88 (vt, $^{2}J_{PC}$ = 3.2 Hz, pyr ortho), 144.11 (vtd, $^{1}J_{RhC}$ = 8.6, $^{2}J_{PC}$ = 24.8 Hz, Rh-Ph ipso), 139.98 (vtd, $^{3}J_{PC}$ = 2.4, $^{2}J_{RhC}$ = 0.7 Hz, Rh-Ph ortho), 137.86 (s, pyr para), 125.05 (s, Rh-Ph meta), 121.47 (s, Rh-Ph para), 120.78 (vt, $^{3}J_{PC}$ = 4.4 Hz, pyr meta), 40.28 (vt, $^{1}J_{PC}$ = 11.4 Hz, PCH_2), 24.00 (vtd, $^{1}J_{PC}$ = 10.5, $^{2}J_{RhC}$ =1.1 Hz, ^{i}PrCH), 19.08 (s, $^{i}PrCH_3$), 18.67 (s, $^{i}PrCH_3$).

Synthesis of 12 ^{i}Pr(PNP)Rh(I)

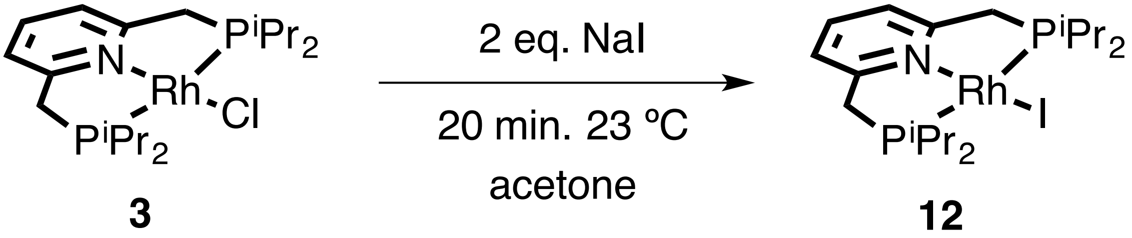

Figure 52: Synthesis of 12 ^{i}Pr(PNP)Rh(I)

To a 20 mL glass vial charged with a stir bar was added 0.5 mL acetone solution of ^{i}Pr(PNP)Rh(Cl) (72 mg, 0.15 mmol, 1 eq.) and 0.6 mL acetone solution of NaI (45 mg, 0.30 mmol, 2 eq.). After stirring at room temperature for 10 min, ^{31}P NMR analysis indicated complete consumption of ^{i}Pr(PNP)Rh(Cl). The acetone solvent was removed by vacuum. The remaining solids were suspended in a minimal amount of benzene and syringe filtered. The filtrate was then concentrated and transferred to a small vial. Vapor diffusion of pentane was used to crystalize the product, ^{i}Pr(PNP)Rh(I). Suitable elemental analysis was not obtained for complex **12**. Graphical ^{1}H, ^{31}P, and ^{13}C NMR data are provided to illustrate the degree of purity of the bulk material obtained by this method; however, the possible presence of residual sodium iodide cannot be excluded.

^{1}H NMR (500 MHz, C_6D_6): δ 6.98 (t, $^{3}J_{HH}$ = 7.8 Hz, 1H, pyr para), 6.4 (d, $^{3}J_{HH}$ = 7.69 Hz, 2H, pyr meta), 2.47 (vt, $^{2}J_{PH}$ = 3.5 Hz, 4H, PCH$_2$), 2.18 (m, (septet by ^{1}H{^{31}P} $^{3}J_{HH}$ = 6.9 Hz), 4H, ^{i}PrCH), 1.52 (m, (doublet by ^{1}H{^{31}P} $^{3}J_{HH}$ = 7.0 Hz), 12H, ^{i}PrCH$_3$), 0.97 (m, (doublet by ^{1}H{^{31}P} $^{3}J_{HH}$ = 6.9 Hz), 12H, ^{i}PrCH$_3$).

^{31}P{^{1}H} NMR (202 MHz, C_6D_6): δ 50.40 (d, $^{1}J_{RhP}$ = 139.4 Hz).

$^{13}C\{^1H\}$ NMR (126 MHz, C_6D_6) δ 163.29 (vt, $^2J_{CP}$ = 7.0 Hz, pyr ortho), 129.45 (s, pyr para), 119.69 (vt, $^3J_{CP}$ = 6.1 Hz, pyr meta), 36.57 (vt, $^1J_{PC}$ = 6.0 Hz, PCH_2), 24.18 (vt, $^1J_{PC}$ = 10.5 Hz, ^{i}Pr CH), 19.35 (t, $^2J_{PC}$ = 3.2 Hz, ^{i}Pr CH_3), 17.58 (s br, ^{i}Pr CH_3).

Synthesis of 13 ^{i}Pr(PNP)Rh(Ph)(I)$_2$

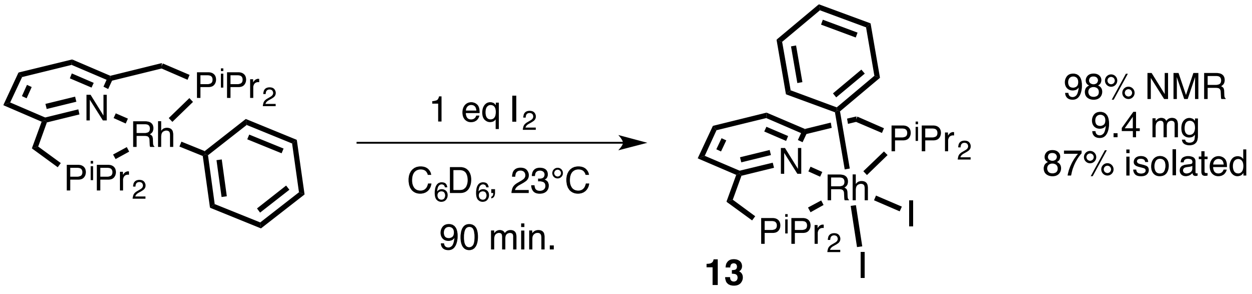

Figure 53: Synthesis of 13 ^{i}Pr(PNP)Rh(Ph)(I)$_2$

To a J. Young tube was added a stock solution in C_6D_6 of **5** (14 µmol, 500 µL, 28 mM, 1 equiv.) which also contained mesitylene (4.0 µmol, 8 mM) as an internal standard. The solution was diluted with 100 µL of C_6D_6. To this solution was added a stock solution in C_6D_6 of iodine (14 µmol, 140 mM, 100 µL). The mixture was immediately capped, shaken, and analyzed by ^{1}H NMR which revealed complete consumption of starting material, major conversion to **13**, and an additional species with a ^{1}H NMR spectrum consistent with the trans isomer of **13** ($^{31}P\{^1H\}$ NMR δ 27.94 ppm, d, $^1J_{PRh}$ = 94.2 Hz). After 90 minutes the mixture had undergone complete conversion to **13** in 98% yield by ^{1}H NMR with respect to 1,3,5-trimethoxybenzene internal standard. The reaction mixture was transferred to a 1 dram vial, concentrated in vacuo and washed with pentane, and dried under vacuum to give 9.4 mg (87% yield) of **13** as an orange solid. Graphical ^{1}H, ^{31}P, and ^{13}C NMR data are provided to illustrate the degree of degree of purity of the bulk material obtained by this method; however, the possible presence of residual iodine cannot be excluded.

^{1}H NMR (500 MHz, CD_2Cl_2) δ 8.86 (d br, $^3J_{HH}$ = 7.0 Hz, 1H, Ph ortho), 7.76 (t, $^3J_{HH}$ = 7.7 Hz, 1H, pyr para), 7.45 (d, $^3J_{HH}$ = 7.7 Hz, 2H, pyr meta), 6.94 (t br, $^3J_{HH}$ = 7.3 Hz, 1H, Ph meta), 6.89 (t, $^3J_{HH}$ = 6.9 Hz, 1H, Ph para), 6.70 (t br, $^3J_{HH}$ = 7.1 Hz, 1H, Ph meta), 5.59 (d br, $^3J_{HH}$ = 7.3 Hz, 1H, Ph ortho), 4.28 (vtd, $^2J_{HP}$ = 4.3, $^2J_{HH}$ = 17.2 Hz, 2H, PCH), 3.79 (m, (septet by ^{1}H{^{31}P} $^3J_{HH}$ = 7.3Hz), 2H, ^{i}PrCH), 3.63 (vtd, $^2J_{HP}$ = 4.0,$^2J_{HH}$ = 17.2 Hz, 2H, PCH), 2.02 (m, (septet by ^{1}H{^{31}P} $^3J_{HH}$ = 7.2Hz) 2H, ^{i}PrCH), 1.69 (m, (doublet by ^{1}H{^{31}P} $^3J_{HH}$ = 7.4 Hz), 6H, ^{i}PrCH$_3$), 1.49 (m, (doublet by ^{1}H{^{31}P} $^3J_{HH}$ = 7.3 Hz), 6H, ^{i}PrCH$_3$), 1.18 (m, (doublet by ^{1}H{^{31}P} $^3J_{HH}$ = 7.3 Hz), 6H, ^{i}PrCH$_3$), 1.13 (m, (doublet by ^{1}H{^{31}P} $^3J_{HH}$ = 7.3 Hz), 6H, ^{i}PrCH$_3$).

^{31}P{^{1}H} NMR (202 MHz, CD_2Cl_2) δ 33.56 (d, $^1J_{RhP}$ = 96.1 Hz).

^{13}C{^{1}H} NMR (126 MHz, CD_2Cl_2) δ 163.19 (vt, $^4J_{PC}$ = 4.1 Hz, pyr ortho), 145.78 (br, Ph ortho), 145.00 (vtd, $^2J_{PC}$ = 8.8, $^1J_{RhC}$ = 30.5 Hz, Ph ipso), 137.59 (s, pyr para), 132.16 (br, Ph ortho), 127.30 (br, Ph meta), 127.07 (br, Ph meta), 123.24 (s, Ph para), 122.21 (vtd, $^3J_{PC}$ = 5.1, $^4J_{RhC}$ = 0.8 Hz, pyr meta), 41.76 (vt, $^1J_{PC}$ = 10.9 Hz, PCH$_2$), 30.99 (vt, $^1J_{PC}$ = 11.7 Hz, ^{i}PrCH), 26.45 (vtd, $^1J_{PC}$ = 11.1 Hz, $^2J_{RhC}$ = 1.9 Hz, ^{i}PrCH), 21.33 (br, ^{i}PrCH$_3$), 20.28 (br, ^{i}PrCH$_3$), 19.48 (br, ^{i}PrCH$_3$), 18.77 (br, ^{i}PrCH$_3$).

Computational methodology

A description of the computational methodology is included below. All calculations were performed by Yehao Qiu. A more detailed discussion of the calculations can be found in Mr. Qiu's undergraduate research thesis. The Gaussian 09 program package[96] was used for all described calculations. Geometry optimization and frequency calculations for all reported structures were performed under the B3LYP-D3BJ/[6-31G(d,p) + Lanl2dz (for Rh)] level of theory (B3LYP-D3BJ/BS1) using an ultrafine pruned (99,590) integration grid with the corresponding Hay-Wadt effective core potential for Rh and Grimme's empirical dispersion-correction with Becke-Johnson damping for B3LYP.[97]

Bulk solvent effects were taken into consideration for geometry optimization and frequency calculations using the self-consistent reaction field polarizable continuum model (IEF-PCM) [98-100] with benzene as the solvent. Thermal corrections for Gibbs free energy (G) and enthalpy (H) were calculated at the B3LYP-D3BJ/BS1 level of theory and the free energies were corrected to a solution standard state of 1 M at 298.15 K.[101,102] The electronic energy of every B3LYP-D3BJ/BS1 optimized structure was further recalculated under the B3LYP-D3BJ/[6-311++G(d,p) + SDD (for Rh)] level of theory (B3LYP-D3BJ/BS2), with PCM model of benzene incorporated. The thermal corrections (calculated under B3LYP-D3BJ/BS1) were applied to the recalculated electronic energies to give the final Gibbs free energy and enthalpy values.

Figure 54: Images of optimized reactants, products, and transition states.

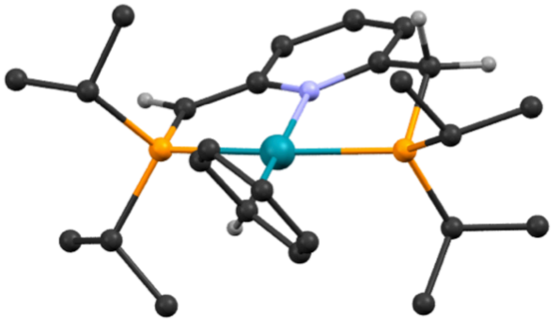

iPr(PNP)*Rh-PhH reactant

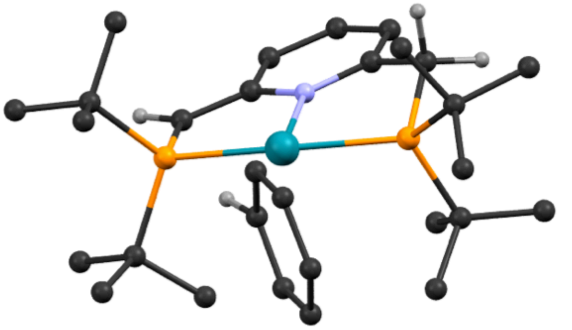

tBu(PNP)*Rh-PhH reactant

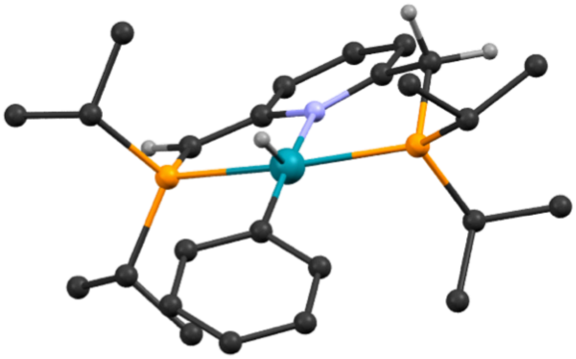

iPr(PNP)*Rh-H-Ph TS1

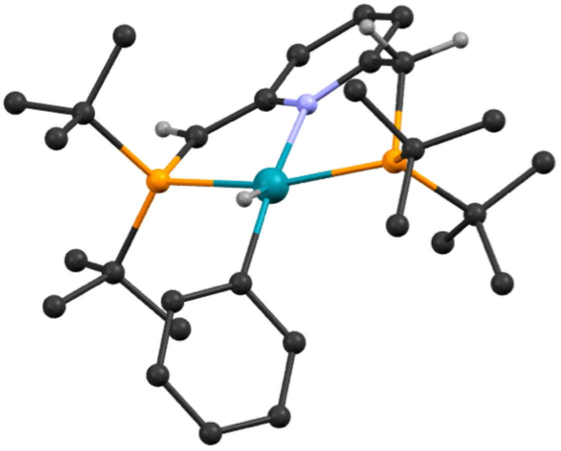

tBu(PNP)*Rh-H-Ph TS2

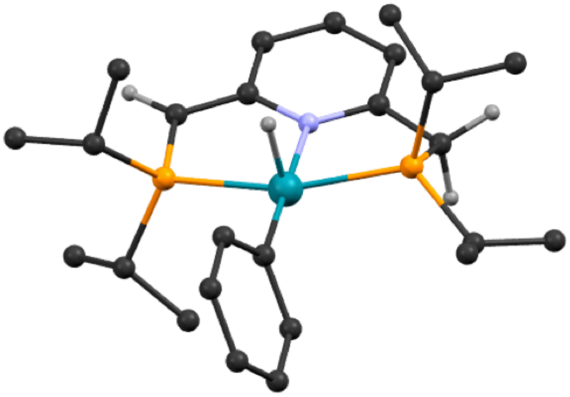

iPr(PNP)Rh(H)(Ph) product

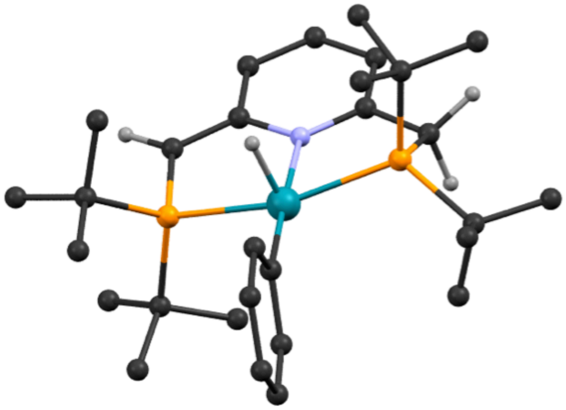

tBu(PNP)Rh(H)(Ph) product

Effect of alkali metal counter ion on stoichiometric C-H activation

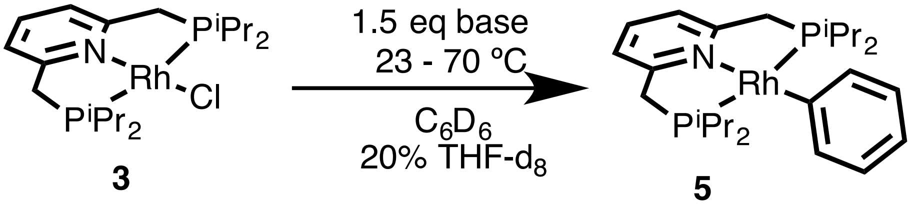

Figure 55: Effect of alkali metal counter ion on stoichiometric C-H activation

Table 3: Effect of alkali metal counter-ion on yield of stoichiometric C-H activation

time (temp)	**^{t}BuOK**	**^{t}BuONa**	**^{t}BuOLi**
2 hr (23 °C)	75%	0%	0%
16 hr (23 °C)	**96%**	8%	0%
1 hr (70 °C)	--	34%	0%
3 hr (70 °C)	--	42%	0%
16 hr (70 °C)	--	49%	0%
48 hr (70 °C)	--	**55%**	**0%**

To a medium-wall glass tube was added a C_6D_6 stock solution of ^{i}Pr(PNP)Rh(Cl) (8 µmol, 400 µL, 20 mM, 1 eq.) which also contained mesitylene (8 µmol, 1 eq.) as the internal standard. To this mixture was then added a THF-d8 stock solution of the appropriate alkali metal salt of *tert*-butoxide (12 µmol, 100 µL, 120 mM, 1.5 eq.). The medium-wall tube was immediately capped, frozen in liquid nitrogen, and flame sealed. Subsequently, the mixture was thawed and ^{1}H, ^{31}P NMR analysis was performed within 5 min. The reaction was periodically monitored during the next 24 hours and the yields reported above were determine with respect to mesitylene internal standard.

Stoichiometric C-H activation with phenolate base

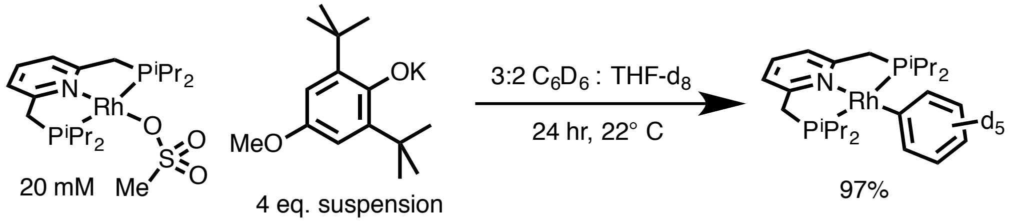

time (hrs)	yield
0.5	67%
5	91%
24	97%

Figure 56: Stoichiometric C-H activation with phenolate base

To a J. Young tube was added a stock solution in C_6D_6 of ^{i}Pr(PNP)Rh(OMs) (10 µmol, 200 µL, 50 mM, 1 equiv.) which also contained 1,3,5-trimethoxybenzene (2.0 µmol, 10 mM) as an internal standard. This solution was diluted with 100 µL C_6D_6. To this solution was added a concentrated suspension of potassium 2,6-bis(*tert*-butyl)-4-methoxy-phenolate (40 µmol, 200 mM, 200 µL). The mixture was analyzed by ^{1}H NMR at 0.5, 5, and 24 hours which revealed conversion to **5** in 67, 91, and 97% respectively. When ^{i}Pr(PNP)Rh(Cl) (**3**) was treated with potassium 2,6-bis(*tert*-butyl)-4-methoxy-phenolate, no conversion to **5** was observed.

Intermediate in reaction of ^{i}Pr(PNP)Rh(Ph) with benzyl chloride

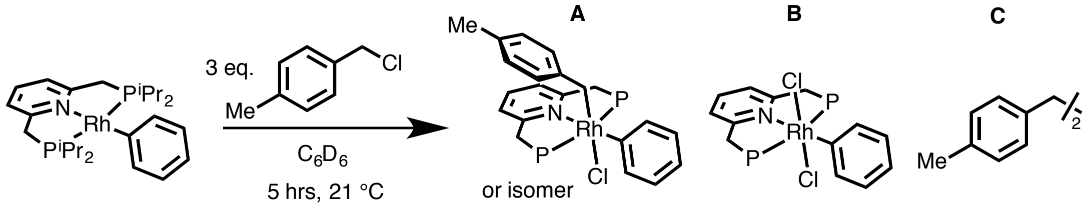

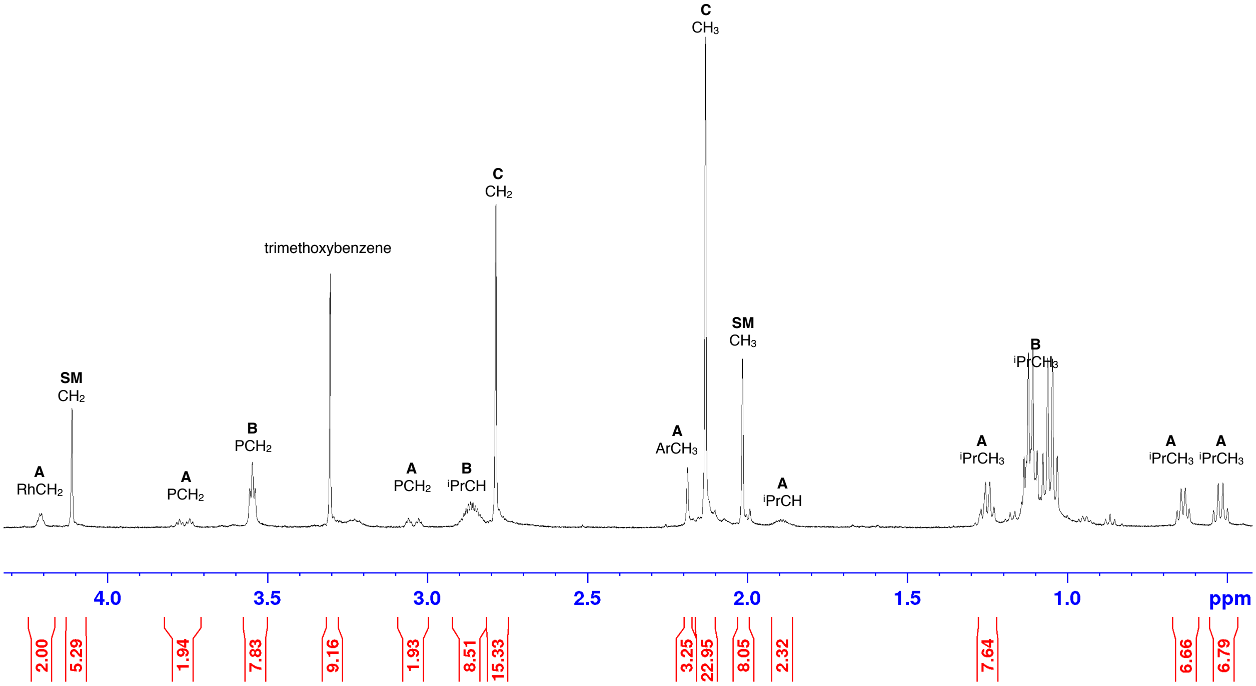

Figure 57: ^{1}H NMR of reaction of ^{i}Pr(PNP)Rh(Ph) with benzyl chloride

Reaction of ^{i}Pr(PNP)Rh(I) with iodobenzene

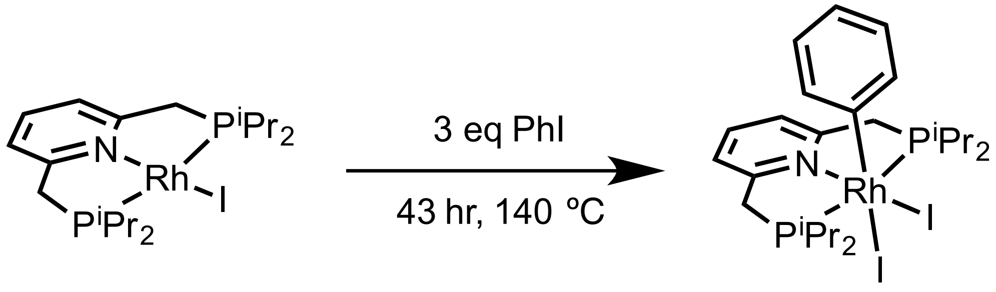

12, 75% remains

13, 4%

Figure 58: Reaction of ^{i}Pr(PNP)Rh(I) with iodobenzene

To a J. Young tube was added a stock solution in C_6D_6 of **12** (13.2 µmol, 500 µL, 26.4 mM, 1 equiv.) and 1 µL dioxane as internal standard. A preliminary ^{1}H NMR was acquired to determine the ratio of **12** to dioxane. Iodobenzene (39.6 µmol, 4.4 µL, 3 equiv.) was added to the reaction mixture and the tube was heated to 140 °C and monitored by ^{1}H and ^{31}P NMR. After 43 hours, 4% of oxidative addition product **13** had formed as determined by integration with respect to dioxane internal standard (diagnostic ^{1}H NMR resonances in C_6D_6 at 9.5 and 5.6 ppm and ^{31}P NMR at 33.64 ppm, d, $^{1}J_{RhP}$ = 96.2 Hz).

Catalytic reactions in the presence of TEMPO

Direct arylation of aryl iodides in the presence of potassium tert-butoxide and an organic catalyst are reported to have zero activity in the presence of 20 mol% TEMPO. [81] In contrast, the rhodium catalyzed reactions reported herein, maintain substantial reactivity in the presence of 20% TEMPO under similar reaction conditions.

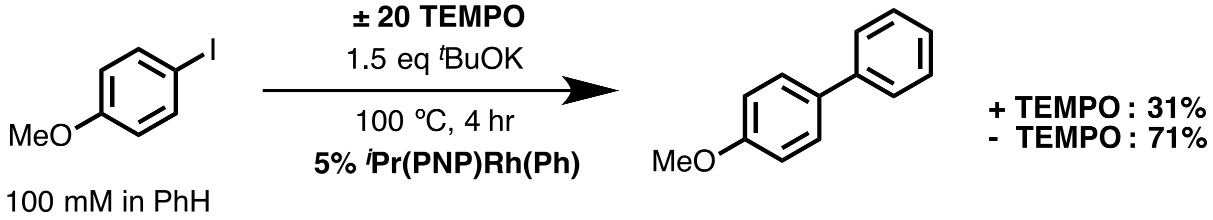

Figure 59: Catalytic reactions in the presence of TEMPO

Catalytic reactions with various (PNP)M pre-catalysts

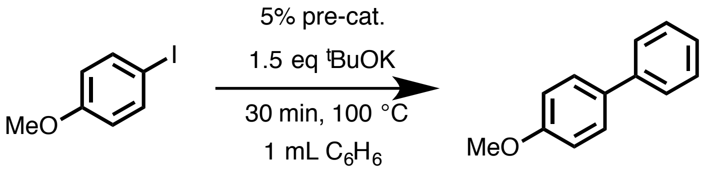

Figure 60: Reaction scheme for catalytic reactions with various (PNP)M pre-catalysts

Direct arylations were attempted with a variety of precatalysts. The reactions were conducted according to the general procedure, but were stopped early (30 minutes) to detect any major differences in initial rate.

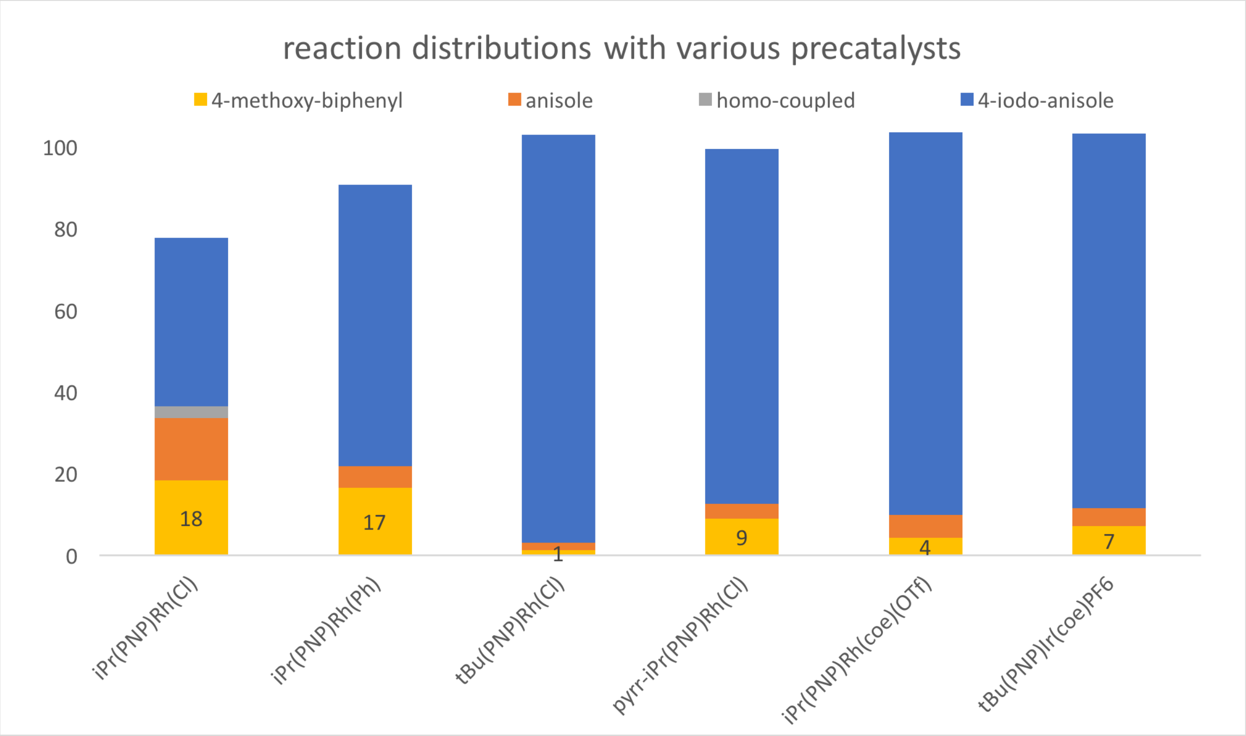

Figure 61: Product disctributions for reactions with various pre-catalysts.

Toluene product distributions with and without rhodium catalyst

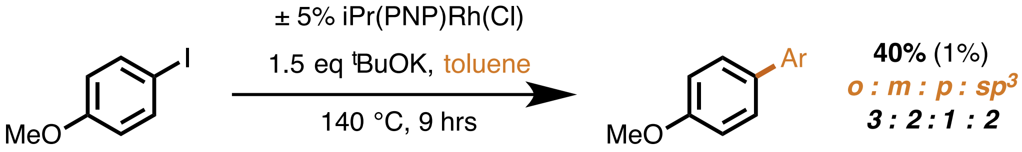

Figure 62: Toluene product distributions with and without rhodium catalyst

GCMS trace of reaction of toluene with and without Rh catalyst. Because the yield of the background reaction is so low (1%), the product mixture is difficult to see in the total ion count, but is readily apparent when the molecular ion of the product (m/z 198.1) is extracted. In extracted ion mode, it is clear that the Rh catalyze reaction contains all four regio-isomers, but the background reaction only includes the sp^2 regio-isomers.

GCMS traces of toluene reaction mixtures

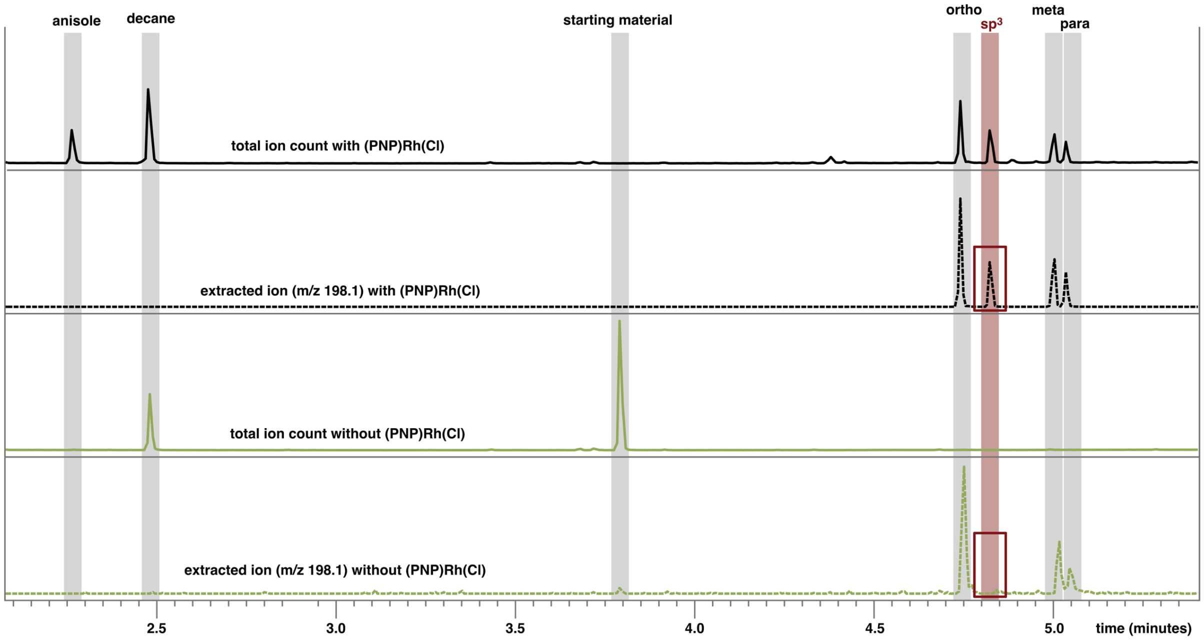

Figure 63: GCMS traces of toluene reaction mixtures

General procedure for (PNP)Rh catalyzed direct arylation of various aryl iodides

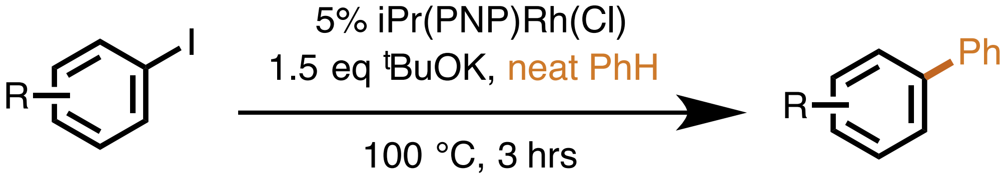

Figure 64: General procedure for (PNP)Rh catalyzed direct arylation of various aryl iodides

Six 2 mL Kimble-Chase Kontes graduated micro-vial were charged with potassium tert-butoxide (0.15 mmol, 16.8 mg, 1.5 eq.). Each the vial was added a stock solution of aryl iodide in benzene (0.1 mmol, 0.5 mL, 200 mM, 1 eq.). Three of the vials were diluted with an additional 0.5 mL of benzene (control reaction with no Rh): to the remaining three vials was added a stock solution of **5** in benzene (0.05 mmol, 0.5 mL, 10 mM, 5 mol%). Each vial was equipped with a triangular spin vane and a Kimble-Chase Kontes 15 mM nylon compression cap with a Mininert teflon lined valve. The vials were removed from the glovebox and heated for 3 hours in an aluminum heating block equilibrated to 100 °C. The vials were removed from the heating block, quenched with 1 mL of water at 4 °C. To each vial was added hexamethylbenzene as a stock solution in toluene (0.01 mmol, 200 µL, 50 mM). The vials were recapped, shaken, and their contents transferred by pipette to 3mL Chem-Elut columns. The columns were eluted by gravity with 4x3 mL ethyl acetate. An aliquot of the eluent was analyzed by GCMS and the yield of each reaction was determined by GCMS with respect to a calibration curve.

General procedure for (PNP)Rh catalyzed direct arylation with various arenes

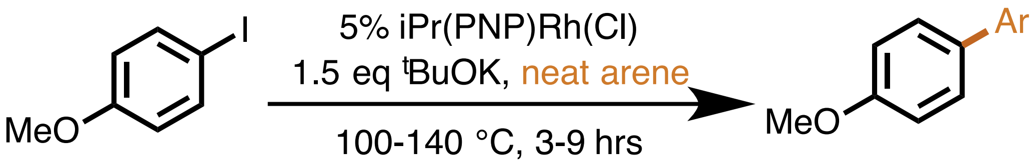

Figure 65 General reaction scheme for (PNP)Rh catalyzed direct arylation with various arenes

Six 2 mL Kimble-Chase Kontes graduated micro-vial were charged with potassium tert-butoxide (0.15 mmol, 16.8 mg, 1.5 eq.). To each the vial was added a stock solution of 4-iodo-anisole in arene solvent (0.1 mmol, 0.5 mL, 200 mM, 1 eq.). Three of the vials were diluted with an additional 0.5 mL of arene solvent (control reaction with no Rh): to the remaining three vials was added a stock solution of **5** in arene solvent (0.05 mmol, 0.5

mL, 10 mM, 5 mol%). Each vial was equipped with a triangular spin vane and a Kimble-Chase Kontes 15 mM nylon compression cap with a Mininert teflon lined valve. The vials were removed from the glovebox and heated in an equilibrated aluminum heating block. Benzene and fluorobenzene gave complete conversion in three hours at 100 °C; however, anisole, toluene, p-xylene, and mesitylene required heating to 140 °C for 9 hours to achieve complete consumption of starting material. The vials were removed from the heating block, quenched with 1 mL of water at 4 °C. To each vial was added internal standard (tetradecane for anisole and mesitylene, *n*-decane for all other arenes) as a stock solution in toluene (0.01 mmol, 200 µL, 50 mM). The vials were recapped, shaken, and their contents transferred by pipette to 3mL Chem-Elut columns. The columns were eluted by gravity with 4x3 mL ethyl acetate. An aliquot of the eluent was analyzed by GCMS and the yield of each reaction was determined by GCMS with respect to a calibration curve. The products of reaction with fluorobenzene were not separable by GCMS so their selectivity was determined by ^{19}F NMR with comparison to the chemical shifts of the independently synthesized authentic standards.

Stoichiometric reaction of 5 with dimethylcarbonate

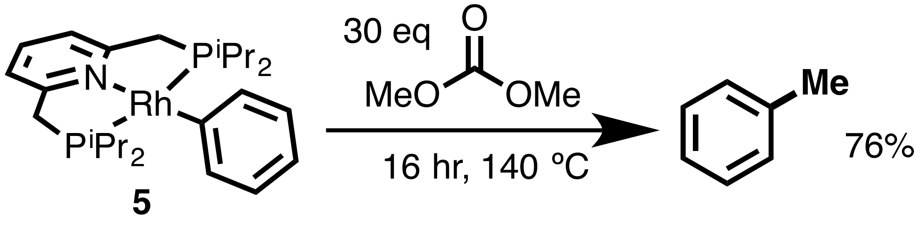

Figure 66: Stoichiometric reaction of 5 with dimethylcarbonate

To a J. Young tube was added a stock solution in C_6D_6 of **5** (7 µmol, 200 µL, 35 mM, 1 equiv.) which also contained 1,3,5-trimethoxybenzene (1.4 µmol, 7 mM) as an internal standard. To this solution was added a stock solution in C_6D_6 of dimethylcarbonate (210 µmol, 0.7M, 300 µL). The tube was sealed, heated to 140 °C, and monitored by ^{1}H and ^{31}P NMR. After 16 hours, no **5** remained and the desired methylated product (toluene) had formed in 76% yield as determined by integration with respect to 1,3,5-trimethoxybenzene internal standard. The reaction mixture was further analyzed by GCMS which confirmed the presence of toluene as the only observed organic product by comparison of the retention time and mass spectrum to a sample of toluene. There were several (PNP)Rh products of this reaction which resulted in a series of broad resonances between 56 and 66 ppm by ^{31}P NMR.

Stoichiometric reaction of 5 with B_2pin_2

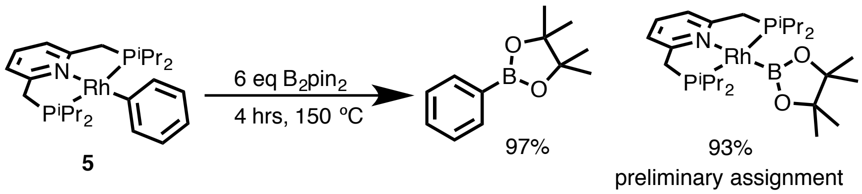

Figure 67: Stoichiometric reaction of 5 with B_2pin_2

To a J. Young tube was added a stock solution in C_6D_6 of **5** (7 µmol, 200 µL, 35 mM, 1 equiv.) which also contained 1,3,5-trimethoxybenzene (1.4 µmol, 7 mM) as an internal standard. To this solution was added a stock solution in C_6D_6 of B_2pin_2 (42 µmol, 140 mM, 300 µL). The tube was sealed, heated to 150 °C and monitored by ^{1}H and ^{31}P NMR. After 4 hours, no **5** remained and phenylboronic acid pinacol ester (PhBpin) had formed in 97% yield as determined by integration with respect to 1,3,5-trimethoxybenzene internal standard. The reaction mixture was further analyzed by GCMS which confirmed the presence of PhBpin as the only observed organic product by comparison of the retention time and mass spectrum to a sample of commercial PhBpin. The (PNP)Rh complex undergoes clean conversion to a new (PNP)Rh product. The reaction progress by ^{31}P NMR is shown below as well as the ^{1}H{^{31}P} NMR of the product with peaks consistent with the hypothesized rhodium boryl complex shown above.

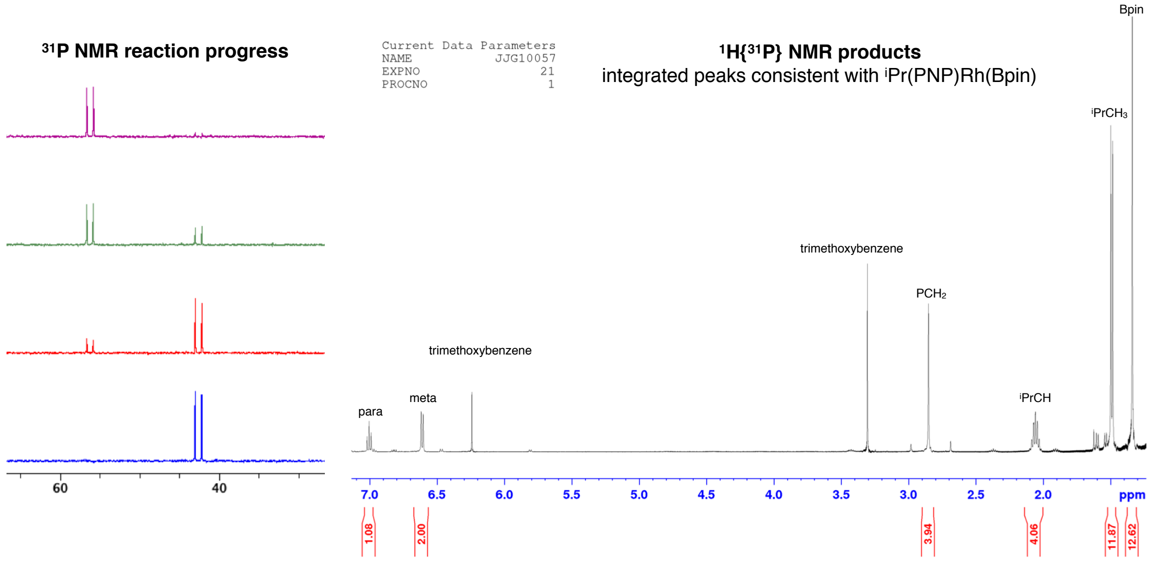

Figure 68: Product mixture from stoichiometric reaction of 5 with B_2pin_2

Catalytic reaction of 5 with B_2pin_2

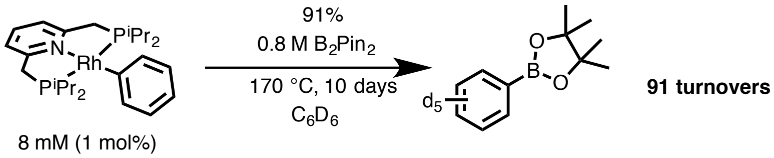

Figure 69: Catalytic reaction of 5 with B_2pin_2

To a 1 dram vial was added B_2pin_2 (0.4 mmol, 101.6 mg, 1 equiv.), a stock solution in C_6D_6 of **5** (4 µmol, 80 µL, 50 mM, 1 mol%), 1,3,5-trimethoxybenzene (4 µmol, 20 µL, 200 mM) as an internal standard, and an additional 400 µL of C_6D_6. The mixture was transferred to a medium wall NMR and connected to a Swage ultra-torr Cajon adaptor. The sample was flame sealed under active vacuum and alternately monitored by ^{1}H NMR and heated in 20 °C increments. While the reaction began to give conversion to PhBpin as low as 80 °C, practical rates were not observed until 170 °C, which still required 10 days for complete consumption of starting material, at which time the reaction had given 91% yield as determined by integration of product methyl resonance with respect to 1,3,5-trimethoxybenzene internal standard.

Stoichiometric reaction of 5 with 4-fluoro-iododbenzene

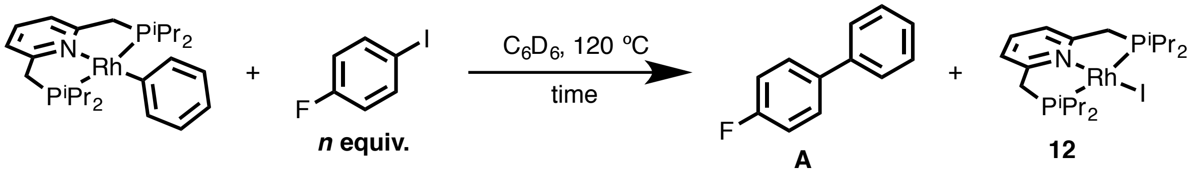

Figure 70: Stoichiometric reaction of 5 with 4-fluoro-iododbenzene

Table 4: Yields of arylations at various times and aryl iodide loadings

***n* equiv**	1.5	1.5	1.5	3	3	3	9	9	9
time (hr)	1.5	3.5	12	1.5	3.5	12	1.5	3.5	12
% yield A	31	52	70	52	89	95	74	77	84
% yield 12	20	35	48	36	46	43	47	46	48

To a J. Young tube was added a stock solution in C_6D_6 of **5** (14 µmol, 500 µL, 28 mM, 1 equiv.) which also contained mesitylene (4 µmol, 8 mM) as an internal standard. To this solution was added a stock solution in C_6D_6 of 4-iodo-fluorobenzene (14**n* µmol, 1M, 14**n* µL, *n* eq., where "*n*" refers to the number of equivalents indicated above). The reaction mixture was heated to 120 °C and monitored periodically. The yields of both the organic and rhodium products were determined by ^{1}H NMR with respect to mesitylene internal standard and are reported in the table above.

Notably, there is a second rhodium product that accounts for much of the mass balance in these reactions, which has diagnostic ^{1}H and ^{31}P resonances consistent with subsequent oxidative addition of aryl iodide to **12** to give Rh(III) products like **13** (^{1}H doublets at 9.5 and 5.6 ppm consistent with two ortho C-H's on apical Rh-aryl and ^{31}P doublet at 33.61 ppm with $^1J_{RhP}$ = 96.7Hz: compare to **13** which has ^{1}H doublets at 9.5 and 5.6 ppm and ^{31}P 33.64 ppm, d, $^1J_{RhP}$ = 96.2 Hz). Thus, we hypothesize that in the absence of base, complex **12** reacts with excess aryl iodide to give Rh(III), but in the presence of base (catalytic conditions) this unproductive reactivity is mitigated by fast C-H activation at **12** to regenerate ^{i}Pr(PNP)Rh(Ph) (**5**).

Stoichiometric C-H activation of C_6D_6 with ^{i}Pr(PNP)Rh(I) 12

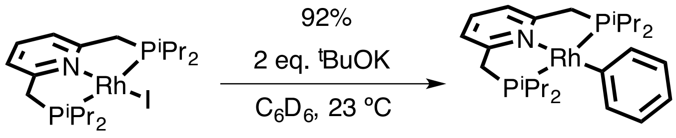

time	%P	%SM
5 min	7	93
20 min	16	82
2 hr	53	48
21 hr	87	11
29 hr	92	10

Figure 71: Stoichiometric C-H activation of C_6D_6 with ^{i}Pr(PNP)Rh(I) 12

To a J. Young tube was added a stock solution in C_6D_6 of **12** (9.12 µmol, 120 µL, 76 mM, 1 equiv.) which also contained 1,3,5-trimethoxybenzene (1.8 µmol, 15 mM) as an internal standard. This solution was diluted with 280 µL C_6D_6. To this solution was added a stock solution of potassium *tert*-butoxide (19 µmol, 95 mM, 200 µL, 2 eq). The mixture was analyzed by ^{1}H NMR monitored over 29 hours after which, no further reaction occurred. The yield of product and amount of starting material remaining at the observed time points are reported above with respect to 1,3,5-trimethoxybenzene internal standard.

Chapter 4: Characterization and Theoretical Investigation of a Transition State Analog for Proton Transfer During C-H Activation by a Rhodium Pincer Complex

Foreword

In this chapter, we present the synthesis, characterization, and bonding analysis of a putative isolobal transition state analogue. A comparative analysis of the bonding interactions in the calculated transition state and the observed transition state analogue validate our hypothesis that the transition state is indeed isolobal to the isolated analogue. Notably, the transition state of interest was dismissed in a prior publication in favor of alternatives transition states with lower calculated barriers. Reevaluation of the energies of the proposed transition states in the context of the relevant rate equations indicates that the previously dismissed transition state is the most relevant under the prescribed reaction conditions. This work was conducted in collaboration with Natalie Chan, Dr. Alexander Filatov, Dr. Rahul Khade, Yehao Qiu, and Prof. Yong Zhang (*in the Department of Chemistry and Chemical Biology, Stevens Institute of Technology, Hoboken, NJ). A manuscript is in preparation.

Introduction

In stable molecules, the identification of novel bonding interactions starts with the observation of unique structural features (contracted interatomic distances, unexpected geometries, etc.) followed by rigorous characterization using quantum chemical calculations and comparison of the experimental and computed structures. Bonding interactions in transition states, on the other hand, are less amenable to this cooperative back and forth between experiment and theory because the geometries of transition states cannot be experimentally observed for any but the simplest of reactions. Insight into bonding interactions in a transition state structures therefore relies entirely on computational methods. Specifically, several possible transition state structures are calculated and analyzed based on experimental outcomes, calculated energies, and chemical intuition. The element of human judgement in determining which calculated geometries merit further analysis, however, limits our understanding of transition state bonding to the bonding interactions present in structures with geometries that conform to our current understanding of molecular structure and bonding. In contrast to structural studies of stable molecules, which can reveal unexpected geometries that spark new insights into how atoms and molecules interact, our understanding of bonding in transition states is limited to the concepts that can be derived from analysis of transition state geometries that match our observations in stable molecules. Therefore, a strategy for directly observing unusual transition state geometries, which could then be subjected computational bonding analysis, would provide a first step toward the cooperative back and forth between observation and computation that has driven our current understanding of bonding interactions.

Transition state analogues are stable molecules designed to mimic the van der Waals geometry and electrostatic potential surfaces of transition states.[103] Based on the large effective binding constants calculated for enzymes and transition states for the reactions that they catalyze, it was hypothesized and subsequently demonstrated that transition state analogues can be exquisite enzyme inhibitors.[104-107] Bonding in transition state analogues is, however, necessarily different than that in the corresponding transition states because the later are non-equilibrium species.[103]

Whereas transition state analogues mimic structure but not necessarily bonding, the isolobal analogy was put forward to describe bonding similarities between structurally diverse molecular fragments.[108] Specifically, Hoffmann defined two fragments as being isolobal "if the number, symmetry properties, approximate energy, and shape of the frontier orbitals and the number of electrons in them are similar-not identical, but similar".[108] Combining these two concepts, one arrives at the idea of isolobal transition state analogues–stable compounds that mimic the geometry and orbital interactions in a transition state. The structural characterization of such compounds, in parallel with comparative analysis of the calculated bonding interactions in the transition state and transition state analogue, provides a model for the type of synergistic feedback between observation and computation that can both motivate and validate our understanding of the unique geometries and bonding interactions present in transition states.[109,110]

Background

Our group and others have been investigating the reactivity of 2,6-bis(di-*t*-butyl-phosphinomethyl)pyridine (PNP) complexes due to their ability to mediate challenging bond activations via metal ligand cooperativity.[38,39,70,111-114] In particular, (PNP)Rh complexes are capable of cleaving aromatic C-H bonds at room temperature without the assistance of directing groups (Figure 2A).[37,73] This reactivity is uniquely enabled by deprotonation of the benzylic methylene in the PNP ligand (e.g. **1** to **2**), which leads to charge delocalization between the benzylic site and rhodium. In a remarkable example of metal ligand cooperativity, the increased electron density on rhodium promotes C-H cleavage via greater donation to the substrate C-H σ* orbital to generate Rh(III) hydride **3**.[115] After C-H oxidative addition, the deprotonated methylene acts as a base and reductant by accepting a proton to give Rh(I) complex **4**.[37] The metal to ligand proton transfer has been proposed to proceed via transition state **5** (Figure 2B and Figure 76).[116,117] Herein, we describe the synthesis and characterization of heterobimetallic complex, **6**, which has similar C_{benzyl}-Z-Rh connectivity to **5**, where Z = H or ZnPh for **5** and **6**, respectively. We reasoned that, if the LUMOs of the bridging Z ligands (4s and 1s, respectively) are similar (but not identical), **6** would constitute an isolobal analogue for transition state **5** (Figure 1C).[108,118-121]

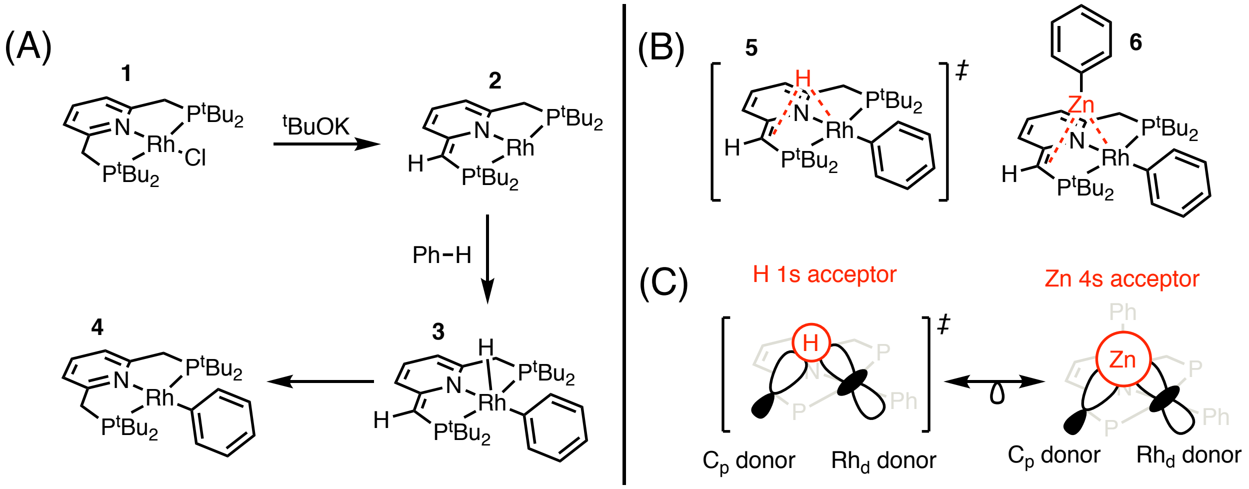

Figure 72. (A) Mechanism of C-H activation via metal ligand cooperation; (B) Transition state **5** and transition state analogue **6**; (C) Representation of hypothesized isolobal relationship between bridging fragments in **5** and **6**.

Synthesis and Characterization of the Transition State Analogue

Complex **6** was prepared by heating **4** with diphenylzinc at 70 °C for 18 hours (Figure 73A). We originally isolated **6** as a byproduct of a previously reported procedure for synthesis of **4**.[93,122] The purest batch of material we were able to obtain was contaminated by 2% biphenyl and 4% compound **4**. The solid-state structure of **6** was determined by single crystal X-ray diffraction (Figure 73B). The contracted C1-C2 interatomic distance (C1-C2 1.44Å vs C3-C4 1.51Å) is consistent with partial double bond character and supports the assigned dearomatized structure.[123] The most notable structural feature of **6** is the zinc fragment which bridges between C1 and Rh.[120,121,124-127] The C1-Zn distance (2.20Å) is greater than the sum of the covalent radii (1.98Å)[128] and the geometry about C1 is distorted away from sp^3 and most closely resembles an sp^2 carbon with a lone pair localized in a p orbital donating to Zn (C2-C1-Zn 89°, P1-C1-Zn 87°, P1-C1-C2 114°). The long C1-Zn distance positions Zn in proximity to rhodium (Rh-Zn 2.52Å) and within the sum of Rh and Zn covalent radii (2.64Å).[128] The structure of **6** in solution was determined by multinuclear NMR, COSY, and NOESY. The most diagnostic features of the $^1H\{^{31}P\}$ NMR spectrum are the three resonances corresponding corresponding to the protons on C1 and C4 which clearly indicate the complex is dearomatized (C1, no $^2J_{HH}$ coupling) and that the two faces of the molecule (with respect to the original P-Rh-N plane) are not equivalent (C4, $H^a \neq H^b$).

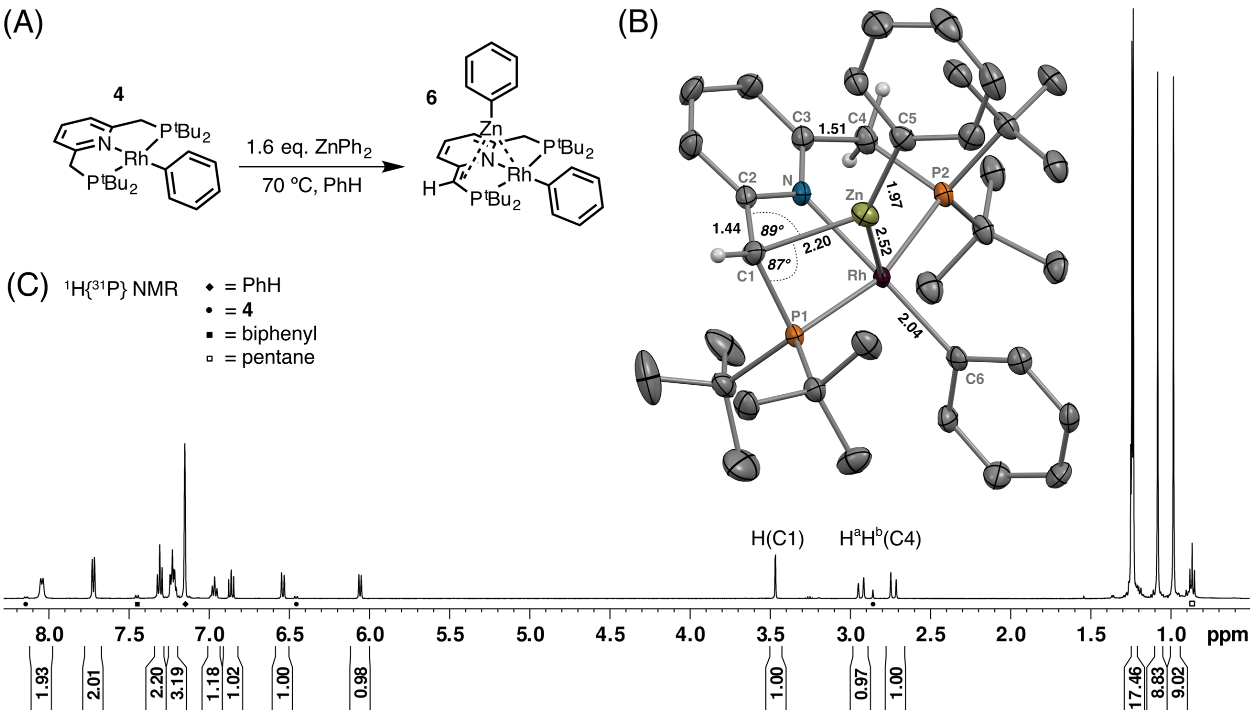

Figure 73 (A) Synthesis of **6** (B) ORTEP of compound **6** with 50% thermal ellipsoids and non-essential hydrogens omitted for clarity (C) $^1H\{^{31}P\}$ NMR of compound **6** in C_6D_6.

Comparative Analysis of Bonding in Transition State and Analogue

To compare bonding between the C_{benzyl}-Z-Rh fragments in compound **6** and transition state **5**, the structures of both compounds were optimized using density functional theory calculations. The calculated structure of **6** agreed well with the observed solid state geometry. The structure of **5** was also similar to the previously calculated transition state of the iridium congener.[116] The calculated wave functions of these compounds were analyzed using the quantum theory of atoms in molecules (QTAIM), which holds that bonded atoms are linked by a bond path (a vector defined by maximal electron density, $\rho(\mathbf{r})$) and that on the bond path lies a bond critical point (BCP) at which the first derivative of $\rho(\mathbf{r})$ is zero.[129-131] Importantly, the topological features of $\rho(\mathbf{r})$ and the Laplacian of this value, $\nabla^2\rho(\mathbf{r})$, offer insight into the nature of bonding interactions.[130] As shown in Figure 74, bond paths and BCPs between C$\cdots$Z and Rh$\cdots$Z (Z = H and Zn) were successfully located, indicating that the Rh$\cdots$H, Rh$\cdots$Zn, C$\cdots$H, and C$\cdots$Zn interactions are bonding in nature. Based on their positive $\nabla^2\rho(\mathbf{r})$ values and negative total energy densities, H(**r**)'s, bonding between these atoms can be classified as electrostatic with partial covalence (Table 1). These data suggest that this transition state analogue **6** bears qualitatively similar bonding features with **5**.

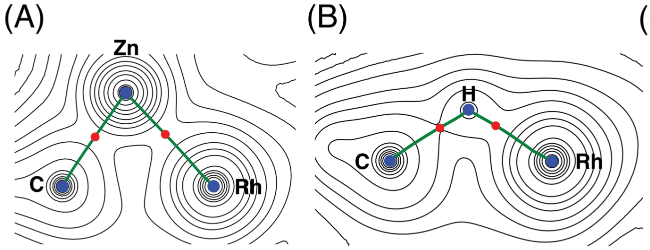

(C)

Complex	Bond	R (Å)	ρ(r) (au)	$\nabla^2\rho$(r) (au)	H(r)(au)
5	Rh$\cdots$H	1.742	0.10277	0.03316	-0.0489
6	Rh$\cdots$Zn	2.582	0.04897	0.06868	-0.0172
7[b]	Preagostic C-H...M	2.3~3.0	0.01~0.03	0.03~0.07	-0.001 ~0.001
8[c]	Agostic C-H...M	1.8~2.3	0.04~0.05	0.15~0.25	n/a
9[d]	M-H	1.4~1.9	0.13~0.16	0.01~0.2	n/a

Figure 74 Contour line diagram of $\nabla^2\rho(\mathbf{r})$ for (A) complex **6** in the Rh-Zn-C plane and (B) transition state **5** in the Rh-H-C plane. Green lines connecting atoms in blue are bond paths and red circles are bond critical points. (C) Selected bond critical point properties: [a]See experimental section for full list of properties. [b]Data are for M…H preagostic and hydrogen bonding (HB) interactions from Ref.[132] [c]Geometric data and AIM results are from Ref.[133] and Ref.[134] respectively. [d]Geometric and QTAIM data for metal hydrides are from Ref[135] and Ref [136,137] [138] respectively.

Charge density may also be used to assess bonding strength in similar systems, with stronger bonds usually having larger $\rho(\mathbf{r})$ and shorter bond distance.[139] This allows for comparison of **5** to other complexes in which a hydrogen atom interacts with a transition metal, including metal hydrides and complexes that exhibit hydrogen bonding,[140] preagostic, or agostic interactions.[141] The $\rho(\mathbf{r})$ data in Table 1 show that the Rh$\cdots$H interaction in **5** has greater charge density at the BCP than typical M$\cdots$H interactions and is more similar to a metal hydride, consistent with relatively little M-H bond cleavage in the metal to ligand proton transfer transition state. The magnitude of the charge density at the BCP for the Rh$\cdots$Zn interaction in **6** is less than that for the Rh$\cdots$H interaction in **5**–

perhaps due to the larger atomic radius of Zn. Overall, however, the topology of the charge density at the BCPs between Rh-Z and C-Z indicates similar bonding in **5** and **6**. In light of the similar geometry and bonding about the bridging C_{benzyl}-Z-Rh fragments in **5** and **6**, we sought to assess whether the orbital interactions that stabilize the unusual geometry of **6** are similar to those that enable metal ligand cooperativity in transition state **5**. In particular, we aimed to computationally evaluate the hypothesis—introduced qualitatively in Figure 2C—that the bridging zinc fragment in **6** is isolobal to the bridging proton in **5** by virtue of the analogous LUMOs in the bridging ligands, 4s and 1s for Z = ZnPh and H, respectively. Key interactions of the bridging fragments in **5** and **6** were therefore assessed using second order natural bond orbital (NBO) perturbation theory to identify stabilizing donor-acceptor pairs of NBOs (Figure 75).[142]

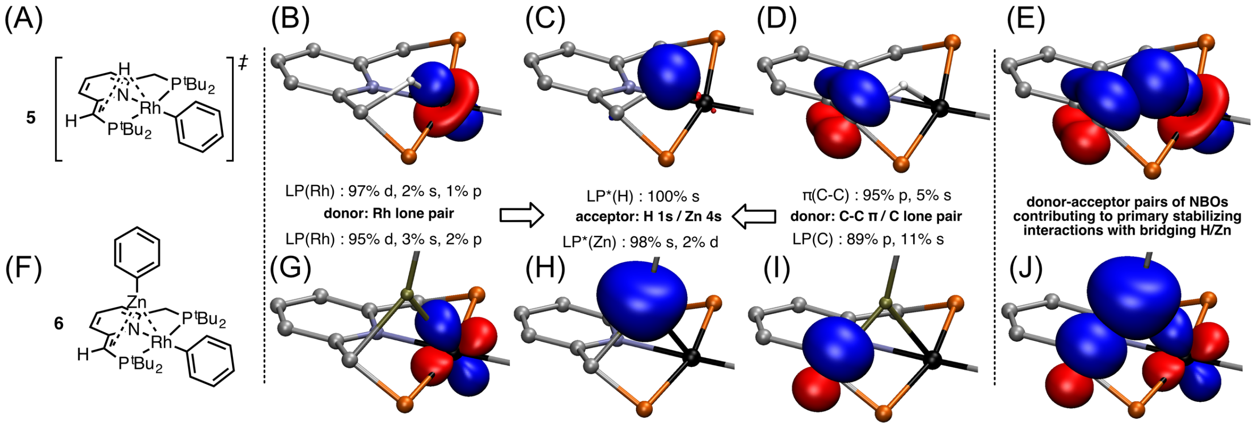

Figure 75 Summary of stabilizing donor acceptor pairs from second order NBO perturbation theory (A) representation of transition state **5** (B) Donor NBO in **5**, 4d(Rh) (C) Acceptor NBO in **5**, 1s(H) (D) Donor NBO in **5**, π(C-C) (E) Overlaid NBO donors and acceptor that contribute to stabilizing the bridging proton in **5** (F) representation of transition state analog **6** (G) Donor NBO in **6**, 4d(Rh) (H) Acceptor NBO in **6**, 4s(Zn) (I) Donor NBO **6**, 2p(C) (J) Overlaid NBO donors and acceptor that contribute to stabilizing the bridging Zn in **6** .

The bridging fragments in both **5** and **6** are stabilized by two major donor-acceptor interactions. In transition state **5** a rhodium d orbital donates to the 1s orbital on the bridging hydrogen: 4d(Rh) → 1s(H) (Figure 75B → C). The second stabilizing pair in transition state **5** involves donation from a π(C-C) bonding NBO on the dearomatized ligand to the LUMO of the bridging proton: π(C-C) → 1s(H) (Figure 75D → C). These donor-acceptor interactions to the bridging hydrogen in transition state **5** are overlaid in Figure 75E. In complex **6**, a rhodium d orbital donates to the empty non-bonding orbital on the bridging Zn: 4d(Rh) → 4s(Zn) (Figure 75G → H). The second stabilizing pair in complex **6** involves donation from a lone pair localized in a primarily p orbital on the deprotonated ligand to the LUMO of the bridging ZnPh: 2p(C) → 4s(Zn) (Figure 75I → H). These donor-acceptor interactions to the bridging ZnPh fragment in transition state analog **6** are overlaid in Figure 75J.

As hypothesized above, this analysis is consistent with an isolobal relationship between the NBOs localized on the bridging fragments in **5** and **6** that contribute to the largest stabilizing interactions on those fragments. Specifically, in both interactions (and in both structures) the acceptor is an s type NBO localized on the bridging atom; namely, a low occupancy 1s type NBO on H^+ in **5** and a low occupancy 4s type NBO on $PhZn^+$ in **6**. The four NBOs which donate into bridging s-type NBOs, on the other hand, are somewhat varied. It is worth noting, however, that despite the variation in their composition, all four donor NBOs interact with the bridging acceptors with the same (σ) symmetry.

Discussion of Alternate Metal to Ligand Proton Transfer Pathways

Alternatives pathways for metal to ligand proton transfer were explored in a prior publication using density functional theory.[116] The paper posits that one or two bridging water molecules may facilitate metal to ligand proton transfer (Figure 76). The claim is made based on lower calculated barriers to proton transfer in the presence of one or two bridging water molecules. The authors do not, however, comment on the fact that rates are the products of rate constants and concentrations. Given that water is present in low concentrations in nominally anhydrous benzene, one should expect that a water dependent pathway may become negligible under the reaction conditions.

Metal to ligand proton transfer is thought to be a fast step after rate limiting oxidative addition; in this case, it is not possible to kinetically determine the effect of water on the rate of metal to ligand proton transfer. To offer a more complete sense of the dominant reaction pathways over a range of water concentrations, an analysis of the relevant rate equations is given below.

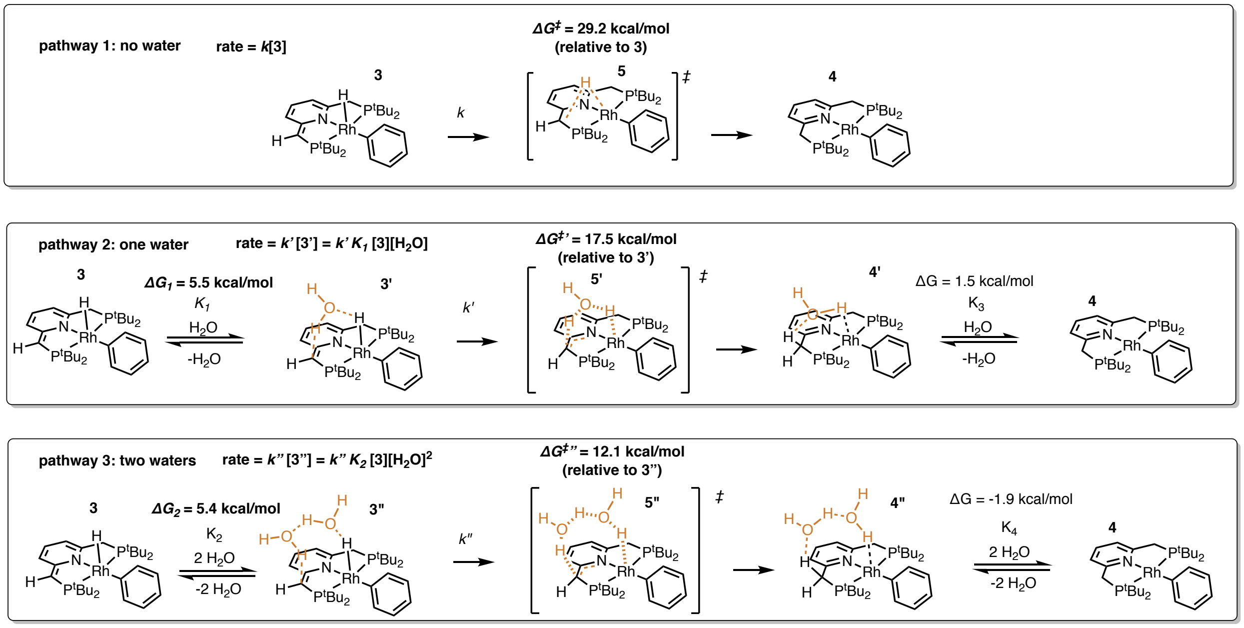

Figure 76 Three possible pathways for metal to ligand proton transfer, labeling of their associated rate constants and equilibrium constants, and DFT calculated energies of the relevant species.

By assuming rapid pre-equilibrium between the reactant **3** and water bound complexes (**3'** and **3"**) the rates of all three pathways can be written as follows:

Equation 1: $rate_{0water} = k[\mathbf{3}]$

Equation 2: $rate_{1water} = K_1 k'[\mathbf{3}][\mathrm{H_2O}]$

Equation 3: $rate_{2water} = K_2 k''[\mathbf{3}][\mathrm{H_2O}]^{\mathbf{2}}$

The calculated ΔG_1 *and* ΔG_2 of water binding can be used with equation 4 to determine K_1 and K_2.

Equation 4: $\Delta G^0 = -RT\ln(\mathrm{K}_{eq})$

The calculated $\Delta G^{\ddagger}$ of each elementary reaction can be used with equation 5 to determine *k*, *k'*, and *k"*.

Equation 5: $k = \frac{\kappa k_B T}{h} e^{-\frac{\Delta G^{\ddagger}}{RT}}$

After determining K_1, K_2, *k*, *k'*, and *k"* from ΔG_1, ΔG_2, $\Delta G^{\ddagger}$, $\Delta G^{\ddagger}{}'$, and $\Delta G^{\ddagger}{}''$, respectively; we can plot the rate of each pathway as a function of [H_2O] by setting [**3**] to an arbitrary low value. (Because the concentration of **3** is a constant across equations 1-3 it will not affect which of the three pathways is dominant at a given [H_2O].) By arbitrarily setting [**3**] = 100 nm and plotting the rate of all three pathways as a function of [H_2O] spanning from 0.001-1.0 ppm we obtain Figure 77. This range of water concentrations was chosen because it represents the concentration of water in benzene when dried for 24 hours by a variety of standard dessicants: for example benzene dried for 24 hours over alumina, sieves, and silica has been reported to contain 0.006, 0.03, and 0.3 ppm of water, respectively.[143] This analysis suggests that under rigorously anhydrous conditions, which were used in this work, direct metal to ligand proton transfer dominates, whereas moderately dry benzene enables contributions from zero, one and two water pathways to the overall transformation.

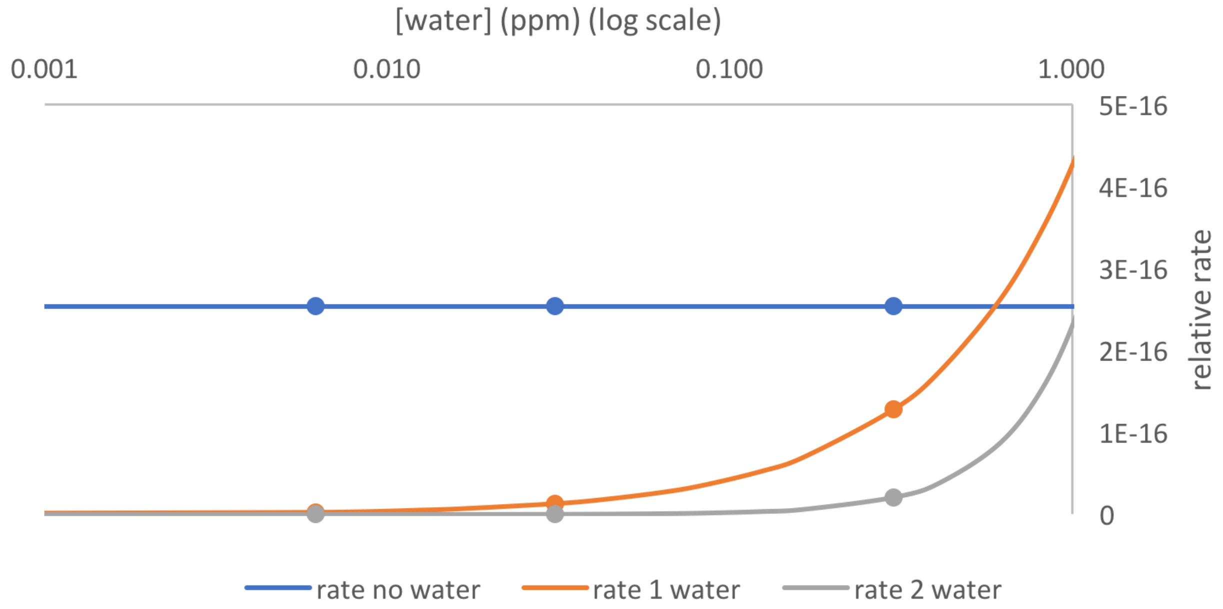

Figure 77 Plot of rates of 0, 1, and 2 water pathways for proton transfer from 0.001-1.0 ppm H_2O based on DFT calculated energies of water binding and proton transfer: colored circles indicate the relative rates of each pathway in benzene dried by alumina, sieves, and silica from left to right respectively.[143]

Conclusion

Structural characterization of **6** and analysis of bonding in both this complex and isolobal transition state **5** revealed that the same type of orbital interactions that stabilize the unusual geometry of **6** also lower the energy of transition state **5** and, in so doing, enable otherwise inaccessible C-H activation reactivity via metal ligand cooperativity. Moreover, isolobal substitution of H in transition state **5** for ZnPh in **6** appears to warp the energy landscape of the latter such that it lies in an energetic well rather than at a saddle point (Figure 78). The idea of an isolobal transition state analogue builds upon the two seminal concepts for which it is named, which, together, provide a framework for conceptualizing and illustrating the stabilizing orbital interactions that occur in transition states.

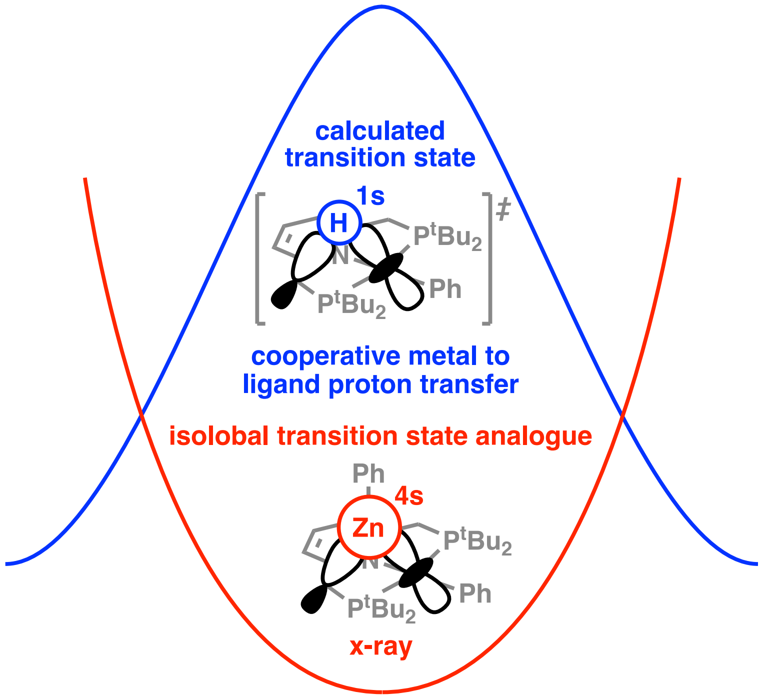

Figure 78 Substitution of an isolobal fragment distorts the energy surface about a transition state from a saddle point to an energetic well.

In this work, structural characterization an isolobal transition state analogue, in parallel with computational analysis of bonding in the transition state and the analogue, provides a model for the type of synergistic feedback between observation and computation that can both motivate and validate our understanding of the unique geometries and bonding interactions present in transition states. Reevaluation of several proposed pathways revealed that the previously dismissed transition state for direct metal to ligand proton transfer is the most favorable of the calculated pathways under the prescribed reaction conditions. This new understanding of metal-ligand cooperativity underscores the value of structural characterization for its ability to surprise and generate new hypotheses which are tested and provide unforeseen chemical insights.

Experimental

Methods and Materials

Unless otherwise noted, all reactions and manipulations were performed under a circulating nitrogen atmosphere in an Innovative Technologies glovebox, or using standard Schlenk technique. J. Young tubes were washed with base bath (prepared with 100 g KOH, 200 mL DI H_2O, and 700 mL *iso*-propanol), followed by methanol, water, and acetone. Glassware was oven dried prior to use.

Unless otherwise noted, all reagents were obtained from commercial suppliers and used without further purification. Hydrocarbons and ethereal solvents were ketyl tested prior to use. Benzene (PhH) and C_6D_6 were dried for 48 hours over activated 4Å molecular sieves, degassed by three cycles of freeze pump thaw and transferred to fresh sieves in the glovebox. Pentane was obtained from an Innovative Technologies solvent purification system (solvent deoxygenated by N_2 sparge and dried over two columns of activated alumina). Molecular sieves were activated at 200 °C under dynamic vacuum (0.05 mm Hg) until visible water stopped condensing in a trap immersed in liquid nitrogen, then for an additional 12 hours after that. The concentrations of Grignard reagents were determined by titration in triplicate with salicylaldehyde phenylhydrazone.[69]

As noted previously,[85] due to strong ^{31}P-^{31}P coupling in the pincer ligand, many ^{1}H and ^{13}C signals appear as virtual triplets (vt) and are reported as such with the apparent coupling constant noted. (https://www.chem.wisc.edu/areas/reich/chem605/)

The nomenclature (PNP)* is used to indicate side arm deprotonated ligand.

Literature procedures were used to prepare $[Rh(coe)_2(Cl)]_2$,[88] *t*Bu(PNP),[90] *t*Bu(PNP)Rh(Cl),[92] *t*Bu(PNP)Rh(OTf),[93] and *t*Bu(PNP)Rh(Ph).[93]

Synthesis and Characterization

*t*Bu(PNP)*Rh(Ph)(ZnPh) was prepared by two different methods, which are described below. Both methods give the same product (by NMR spectroscopy) with varying degrees of purity and reproducibility. Neither method gave analytically pure material, but material of >90% purity (by ^{1}H NMR spectroscopy) was obtained by Method 1. Notably, while method 1 gave the purest material in a single run, method 2 gave a more reproducible means of obtaining *t*Bu(PNP)*Rh(Ph)(ZnPh). Complete graphical NMR data are provided in the NMR spectra section to support the identity and purity of complex **6** as prepared by method 1.

Method 1: Synthesis of ^{t}Bu(PNP)*Rh(Ph)(ZnPh) from $[Rh(coe)_2(Cl)]_2$

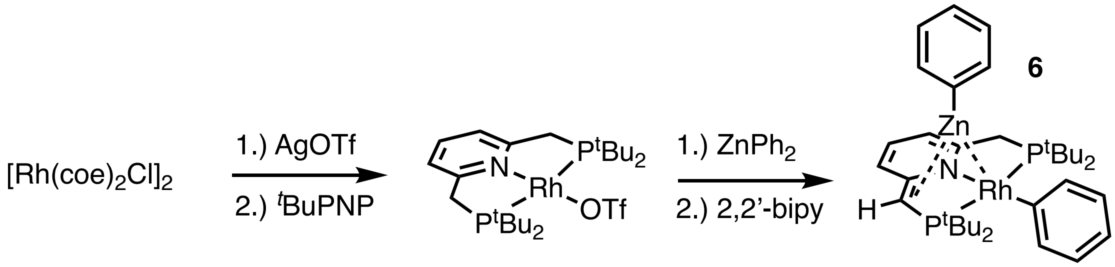

Figure 79: Method 1: Synthesis of ^{t}Bu(PNP)*Rh(Ph)(ZnPh) from $[Rh(coe)_2(Cl)]_2$

*t*Bu(PNP)*Rh(Ph)(ZnPh) was prepared by a modified procedure for preparation of *t*Bu(PNP)Rh(Ph).[93] To a 25 mL Schlenk flask was added $[Rh(coe)_2Cl]_2$ (326 mg, 0.454 mmol, 1.0 equiv.), silver trifluoromethanesulfonate (234.6 mg, 0.912 mmol, 2.01 equiv.), and a stir bar. The flask was sealed, removed from the glovebox, and evacuated and refilled three times under argon. 10 mL of degassed THF was transferred via cannula into the Schlenk flask and the orange solution with grey precipitate was stirred at room temperature for 10 minutes. The solution was transferred and the solid was washed with an additional 3x4 mL THF via cannula filtration into a 100 mL Schlenk flask containing ^{t}Bu(PNP) (358.6 mg, 0.908 mmol, 2.0 equiv.) under argon. The solution turned deep red/orange and was stirred for 10 minutes at room temperature at which time the solvent was removed under reduced pressure. The orange, nitrogen-sensitive solid was washed with degassed pentane (3x10 mL) under argon. The Schlenk flask was brought into the glovebox and charged with diphenylzinc (600 mg, 2.73 mmol, 3.0 equiv/Rh). The flask was sealed with a septum, removed from the glovebox and charged with 60 mL of benzene. The septum was replaced with a glass stopper under argon and the flask was degassed under argon by three cycles of freeze pump thaw. The mixture was heated to 60 °C for 17 hours during which time it turned dark brown. 2,2'-bipyridine (426.4 mg, 2.73, 3.0 equiv./Rh) was added under argon and the solvent was removed under reduced pressure. The brown solid was extracted with 10x5 mL warm pentane in the glove box, filtered, concentrated under reduced pressure, and dissolved in 0.5 mL benzene. Vapor diffusion of pentane into the concentrated benzene solution yielded 188 mg (29%) of complex **6** contaminated with 4% ^{t}Bu(PNP)Rh(Ph) and 2% biphenyl as determined by ^{1}H NMR. The supernatant of this mixture was cooled to -35 °C to afford single crystals suitable for x-ray diffraction.

^{1}H NMR (500 MHz, C_6D_6) δ 8.04 (d br, ${}^{3}J_{HH}$ = 6.9 Hz, 2H, Rh-Ph ortho), 7.72 (d, ${}^{3}J_{HH}$ = 6.6 Hz, 2H, Zn-Ph ortho), 7.31 (t, ${}^{3}J_{HH}$ = 7.4 Hz, 2H, Zn-Ph meta), 7.23 (m, 3H, Rh-Ph meta overlapped with Zn-Ph para), 6.97 (t, ${}^{3}J_{HH}$ = 7.2 Hz, 1H, Rh-Ph para), 6.86 (t, ${}^{3}J_{HH}$ =

7.7 Hz, 1H, pyr para), 6.54 (d, $^3J_{HH}$ = 8.2 Hz, 1H, pyr meta), 6.06 (d, $^3J_{HH}$ = 7.2 Hz, 1H, pyr meta'), 3.47 (m, (^{1}H{^{31}P} d, $^3J_{RhH}$ = 1.1 Hz), 1H, dearomatized PCH), 2.93 (m, (^{1}H{^{31}P} d, $^2J_{HH}$ = 16.7 Hz), 1H, PCH_2), 2.73 (m, (^{1}H{^{31}P} d, $^2J_{HH}$ = 16.7 Hz), 1H, PCH_2'), 1.24 (m, 18H, overlapped ^{t}Bu's), 1.08 (m, (^{1}H{^{31}P} s), 9H, ^{t}Bu), 0.98 (m, (^{1}H{^{31}P} s), 9H, ^{t}Bu).

^{13}C{^{1}H} NMR (126 MHz, C_6D_6) δ 170.92 (vt br, $^2J_{PC}$ = 3.2 Hz, pyr ortho), 164.32 (vtd, $^2J_{PC}$ = 10.6, $^1J_{RhC}$ = 34.0 Hz, Rh-Ph ipso), 159.49 (vt br, $^2J_{PC}$ = 3.3, pyr ortho), 150.92 (m br, Zn-Ph ipso), 141.84 (s br, Rh-Ph ortho), 137.89 (s, Zn-Ph ortho), 134.27 (s, pyr para), 127.31 (s, Zn-Ph meta), 126.60 (s, Zn-Ph para), 125.46 (s, Rh-Ph meta), 119.80 (s, Rh-Ph para), 112.37 (vt, $^3J_{PC}$ = 5.0 Hz, pyr meta), 108.90 (vt, $^3J_{PC}$ = 4.6 Hz, pyr meta'), 49.43 (m br, PCH), 42.92 (m br, ^{t}Bu quaternary), 36.66 (dd, $^2J_{RhC}$ = 5.9, $^1J_{PC}$ 8.3 Hz, PCH_2), 35.31 (m, overlapped ^{t}Bu quaternary), 34.54 (m, ^{t}Bu quaternary), 31.10 (vt, $^2J_{PC}$ = 2.9 Hz, ^{t}Bu CH_3), 29.63 (vt, $^2J_{PC}$ = 2.2 Hz, ^{t}Bu CH_3), 29.00 (vt, $^2J_{PC}$ = 3.5 Hz, ^{t}Bu CH_3), 28.70 (vt, $^2J_{PC}$ = 3.3 Hz, ^{t}Bu CH_3).

^{31}P{^{1}H} NMR (202 MHz, C_6D_6) δ 60.92 (m).

Method 2: Synthesis of ^{t}Bu(PNP)*Rh(Ph)(ZnPh) from ^{t}Bu(PNP)Rh(Ph)

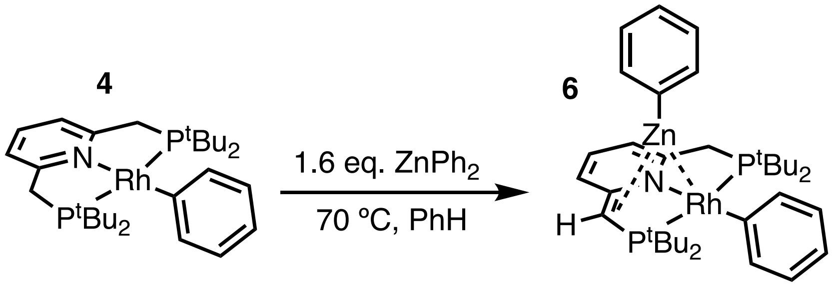

Figure 80: Method 2: Synthesis of ^{t}Bu(PNP)*Rh(Ph)(ZnPh) from ^{t}Bu(PNP)Rh(Ph)

To a 25mL resealable glass tube equipped with a stir bar was added ^{t}Bu(PNP)Rh(Ph) (209 mg, 0.363 mmol, 1.0 equiv.), diphenylzinc (128 mg, 0.581 mmol, 1.6 equiv.), and 7.25 mL benzene. The bomb was sealed with a teflon lined stopper, removed from the glovebox, and heated to 70 °C for 1 hour at which time a 50 μL aliquot was dissolved in 500 μL of C_6D_6 to check the reaction progress by ^{1}H NMR. After 18 hours at 70 °C another 50 μL aliquot was analyzed by ^{1}H NMR and the reaction was determined to be complete. The reaction mixture was transferred to a 20mL vial, concentrated to 2mL under reduced pressure, and layered with 10 mL pentane. After 12 hours at room temperature the mixture was transferred to a -35°C freezer. After 24 hours at -35°C, the mixture was filtered and the supernatant was concentrated under reduced pressure to afford 167 mg of material contaminated with residual diphenylzinc shown in Figure 82.

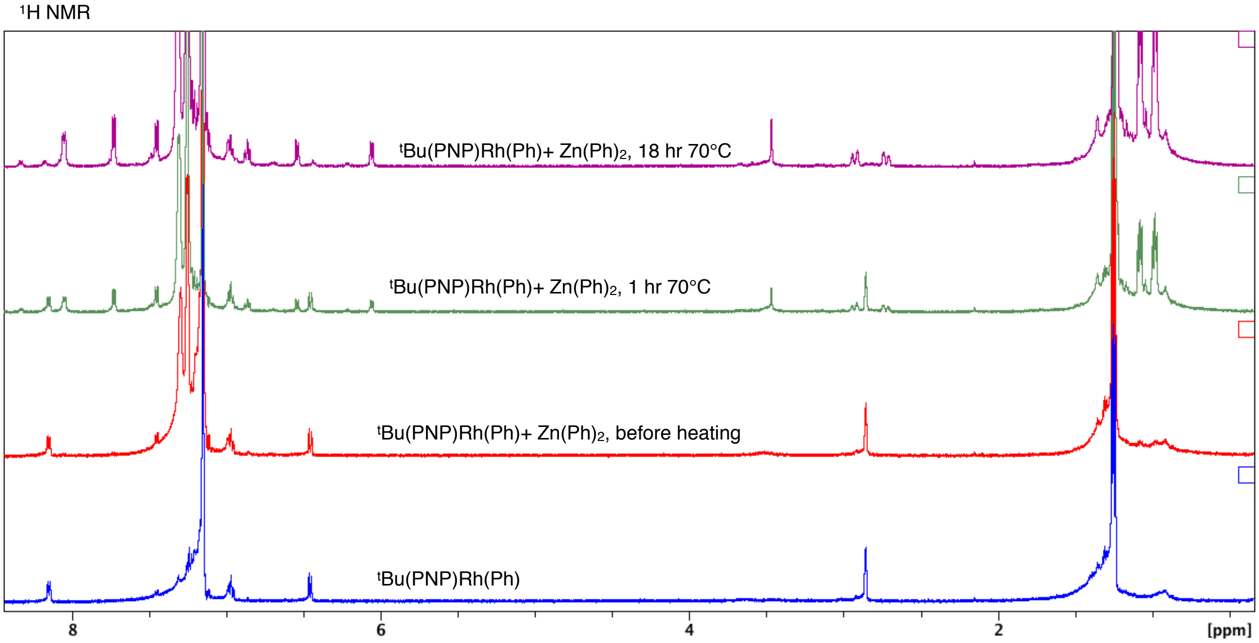

Figure 81: Monitoring reaction progress of method 2 by ^{1}H NMR.

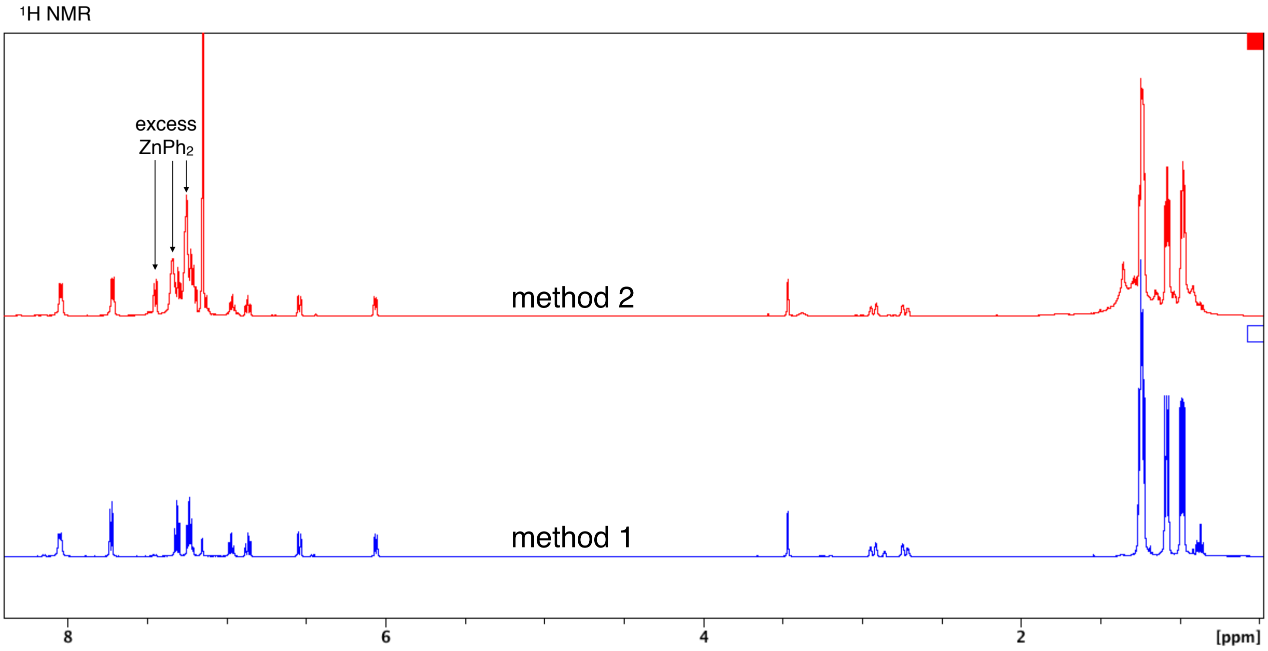

Figure 82 Comparison ^{1}H NMR of material prepared by method 1 and method 2.

Synthesis of S1 ^{i}Pr(PNP)Rh(Ph)(ZnCl$_2$) (Natalie Chan)

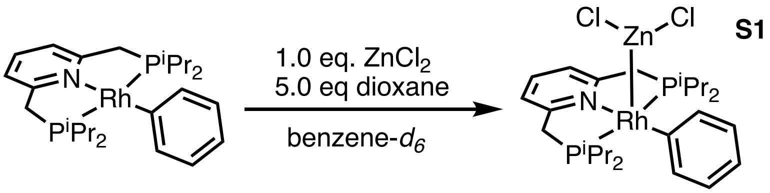

Figure 83 Synthesis of ^{i}Pr(PNP)Rh(Ph)(ZnCl$_2$) by Natalie Chan

A J. Young tube was charged with ZnCl$_2$ (5 µmol, 100 µL, 50 mM in THF, 1 equiv.). The tube was capped and THF was removed from the tube *in vacuo* on a Schlenk line. To the dried ZnCl$_2$ was added ^{i}Pr(PNP)*Rh(Ph) (5 µmol, 100 µL, 50 mM in C$_6$D$_6$, 1 equiv.), dioxane (25 µmol, 2.1 µL, 5 equiv.) and C$_6$D$_6$ (400 µL). The tube was capped and shaken up. The reaction turned from dark red to a light brown upon shaking. The tube was analyzed by ^{31}P, ^{1}H, ^{1}H{^{31}P} NMR within 2 minutes of mixing. The reaction was monitored two hours later, which revealed full conversion of the [Rh] starting material. The reaction yielded 96% of **S1** by ^{1}H NMR integration with respect to an internal standard. The contents of the J. Young tube was poured into a 20 mL scintillation vial. Volatiles were removed *in vacuo*. The orange crude product was dissolved in minimal amount of hot benzene and filtered through a 20 μm syringe filter into a 1-dram shell vial. Vapor diffusion of pentane into the concentrated benzene solution afforded single crystals of **S1** suitable for x-ray diffraction.

^{1}H NMR (500 MHz, C_6D_6) δ 8.13 (d, $^3J_{HH}$ = 7.4 Hz, 2H, Rh-Ph ortho), 7.24 (t, $^3J_{HH}$ = 7.4 Hz, 2H, Rh-Ph meta), 7.03 (t, $^3J_{HH}$ = 7.6 Hz, 1H, Rh-Ph para), 6.96 (t, $^3J_{HH}$ = 7.2 Hz, 1H, pyr para), 6.67 (d, $^3J_{HH}$ = 7.6 Hz, 2H, pyr meta), 3.68 (m, (doublet by ^{1}H{^{31}P}, $^2J_{HH}$ = 17.4 Hz), 2H, P-CH_2), 2.84 (m, (doublet by ^{1}H{^{31}P}, $^2J_{HH}$ = 17.5 Hz), 2H, P-CH_2), 2.18 (m, 2H, ^{i}Pr-H), 2.09 (m, 2H, ^{i}Pr-H), 1.27 (dd, $^3J_{HH}$ = 8.4 Hz, $^2J_{PH}$ = 24.1 Hz, 6H, ^{i}Pr-CH_3), 0.90 (dd, $^3J_{HH}$ = 7.8 Hz, $^2J_{PH}$ = 22.6 Hz, 6H, ^{i}Pr-CH_3), 0.82 (dd, $^3J_{HH}$ = 7.6 Hz, $^2J_{PH}$ = 22.3 Hz, 6H, ^{i}Pr-CH_3), 0.71 (dd, $^3J_{HH}$ = 6.4 Hz, $^2J_{PH}$ = 19.6 Hz, 6H, ^{i}Pr-CH_3).
^{31}P{^{1}H} NMR (202 MHz, C_6D_6) δ 40.02 (d, $^1J_{Rh\text{-}P}$ = 123.9 Hz, 2P).

Computational Methodology

The Gaussian 09 program package[96] was used for all described calculations. Geometry optimization and frequency calculations for all reported structures were performed under the B3LYP-D3BJ/[6-31G(d,p) + Lanl2dz (for Rh and Zn)] level of theory (B3LYP-D3BJ/BS1) using an ultrafine pruned (99,590) integration grid with the corresponding Hay-Wadt effective core potential for Rh and Zn and Grimme's empirical dispersion-correction with Becke-Johnson damping for B3LYP.[97] Frequency calculations were performed on all reported structures to ensure that each minimum-energy structure has no imaginary frequencies and each transition state (TS) structure has precisely one imaginary frequency.

Bulk solvent effects were taken into consideration for geometry optimization and frequency calculations using the self-consistent reaction field polarizable continuum model (IEF-PCM) [98-100] with benzene as the solvent. Thermal corrections for Gibbs free energy (G) and enthalpy (H) were calculated at the B3LYP-D3BJ/BS1 level of theory and the free energies were corrected to a solution standard state of 1 M at 298.15 K.[101,102] The electronic energy of every B3LYP-D3BJ/BS1 optimized structure was further recalculated under the B3LYP-D3BJ/[6-311++G(d,p) + SDD (for Rh) + 6-311G(d,p) (for Zn)] level of theory (B3LYP-D3BJ/BS2), with PCM model of benzene incorporated. The thermal corrections (calculated under B3LYP-D3BJ/BS1) were applied to the recalculated electronic energies to give the final Gibbs free energy and enthalpy values.

All BCP properties were calculated by using the AIM2000 program[144] from the wavefunctions generated from using the same method and basis set in single point energy and NBO calculations, except for Rh, an all-electron basis set DGDZVP in Gaussian 09 was used.

Table 5: Comparison of solid state and DFT optimized geometries

	Rh-Zn (Å)	C1-Zn (Å)	C1-C2 (Å)	∠C1ZnRh (°)	∠C2C1Zn (°)	∠P1C1Zn (°)
x-ray	2.518	2.203	1.428	79.37	88.56	86.56
optimized	2.582	2.273	1.454	77.53	92.41	87.86
∣Δ∣	0.064	0.070	0.026	1.84	3.85	1.30

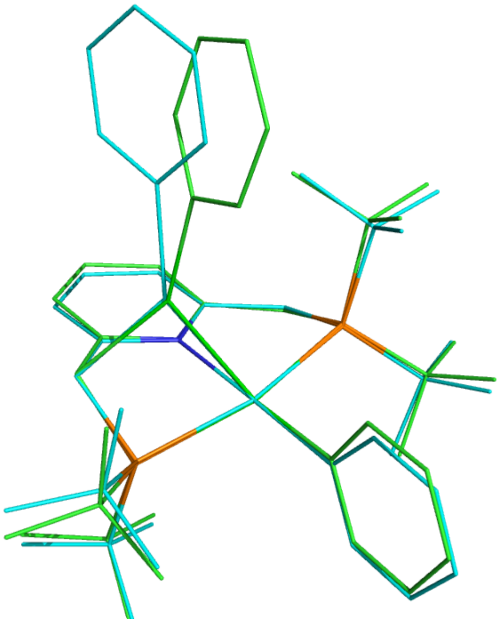

Figure 84: Overlaid line drawings of structure determined by x-ray diffraction (cyan) and optimized by density functional theory (green).

Chapter 5: C-H Activation and Functionalization with Amino Acid Complexes of Palladium(II)

Foreword

Mono-protected amino acid (MPAA) ligands are used in a number of palladium catalyzed C-H functionalization reactions. Herein, we report the synthesis and detailed characterization of a series of MPAA complexes prepared via cyclopalladation of dimethylbenzylamine in the presence of MPAAs. The isolated complexes exist as μ-carboxylato (MPAA) bridged dimers and feature potential M-M cooperativity and secondary sphere hydrogen bonding interactions. Selective MPAA coordination and relay of stereochemistry, previously suggested to uniquely result from κ^2-(*N*,*O)* MPAA coordination, are both observed. The isolated MPAA complexes undergo C-C and C-X (X=Cl, Br, I) bond formation when treated with electrophiles used for catalytic C-H functionalization. Stoichiometric iodination of MPAA palladacycles was found to proceed via a dinuclear palladium species with one equivalent of iodine, and the isolated complexes also served as viable precatalysts for catalytic C-H functionalization. Together, these results provide a number of insights into the reactivity of Pd-MPAA complexes relevant to C-H bond functionalization. This work has been published and was conducted in collaboration with Alexander Filatov, Brandon Haines, and Djamaladdin Musaev.

Introduction

One of the foremost challenges in transition metal catalyzed C-H functionalization has been the development of catalysts that selectively modify one C-H bond in the presence of others with similar steric and electronic properties.[2,3,8,145-147] Palladium catalyzed transformations that exploit the ability of Lewis basic functional groups within a substrate to coordinate to the metal catalyst and thus confer site selectivity to C-H bond cleavage (activation) have long proven particularly useful in this regard.[4,148,149] In combination with this approach, mono-*N*-protected amino acid (MPAA) ligands have been found to accelerate[150,151] and impart enantioselectivity[152-157] to several Pd(II)-catalyzed C-H functionalization reactions.[158]

Numerous approaches, including DFT calculations,[159-163] mass spectrometry,[164,165] and steady state kinetics[150,166] have been used to investigate the mechanism(s) by which MPAA ligands affect Pd(II)-catalyzed C-H functionalization. These studies have concluded that MPAA-promoted, Pd(II)-catalyzed C-H bond functionalization proceeds via a N-H cleavage and subsequent C-H activation mechanism.[161] The proposed active catalyst is generated by κ^2-(*N*,*O*) coordination of MPAA to Pd(II) (Figure 85) followed by deprotonation of the *N*-protected amide. Concerted metallation-deprotonation (CMD)[167-171] of the substrate C-H bond by either the *N*-protecting group[165] of the MPAA ligand or an external base[159] could then occur. κ^2-(*N*,*O*) binding of the MPAA ligand is thought to enforce a rigid structure capable of relaying chirality from the MPAA to a prochiral substrate in the CMD transition state.[164] With the development of this mechanistic paradigm, it has become widely accepted that the active catalysts are monomeric κ^2-(*N*,*O*) Pd(II)MPAA complexes.

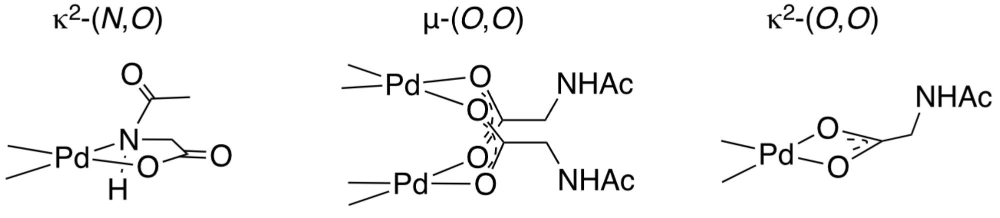

Figure 85. Three potential modes for coordination of the MPAA *N*-acetylglycine to Pd(II)

Notably, however, no Pd(II)MPAA intermediates in these reactions have been rigorously characterized in solution or by X-ray diffraction. To shed light on the nature of MPAA coordination to Pd(II) and to understand the impact that MPAA coordination has on the nuclearity and stoichiometric reactivity of these complexes, we sought to isolate and characterize Pd(II)MPAA complexes analogous to those invoked for catalysis. Such complexes would also serve as models to specifically probe and understand individual steps of proposed catalytic cycles and guide the design of new and more effective ligands for C-H functionalization catalysis.

Synthesis of MPAA Complexes via Ligand Exchange

Putative κ^2-(*N*,*O*) binding of MPAA ligands to Pd(II) during catalytic C-H functionalization was first proposed[157] in the literature based on the previously reported[172] synthesis of **1**, Pd(dmba)(NAc-Gly) (Figure 86A, dmba = *N*,*N*-dimethylbenzylamine, NAc-Gly = *N*-acetyl-glycine). Indeed, we obtained a good yield (71%) of a complex consistent with the ^{1}H and ^{13}C NMR data reported for **1** by following this procedure. The κ^2-(*N*,*O*) MPAA coordination in **1** was originally assigned based on analogy to the corresponding unprotected glycine complex.[172] To gain further confidence in this assignment, we determined the structure of the isolated product by single-crystal X-ray analysis. The structure observed in the solid state is the μ^2-(*O*,*O*) MPAA-bridged dimer complex **2** (Figure 86B and C) instead of the reported κ^2-(*N*,*O*) complex **1**.

To address the possibility that this dimer may only exist in the solid state, a solution of **2** was analyzed by ^{1}H NMR, NOESY, and ESI-MS—all of which are consistent with a dimeric MPAA-bridged palladium complex. An initial indication of a dimeric complex in solution is the large upfield shift in one of the inequivalent benzylic resonances (H^a) and *N*-methyl resonances (Me^a) relative to the precursors $[Pd(dmba)(Cl)]_2$ and Pd(dmba)(acac) (acac = acetylacetonate) (Figure 86A and E). This large upfield shift is consistent with proximity to the ring current of an aromatic π-system—as one would expect for the carboxylate bridged dimer **2**—and is strikingly similar to the ^1H NMR of known acetate bridged dimer **4** $[Pd(dmba)(OAc)]_2$ (Figure 86E).[173-175] The most direct evidence for the existence of **2** as a dimer in solution is the presence of an NOE between the aromatic C-H ortho to palladium with the upfield NMe^a and while the downfield resonance NMe^b has no such NOE (Figure 86D).

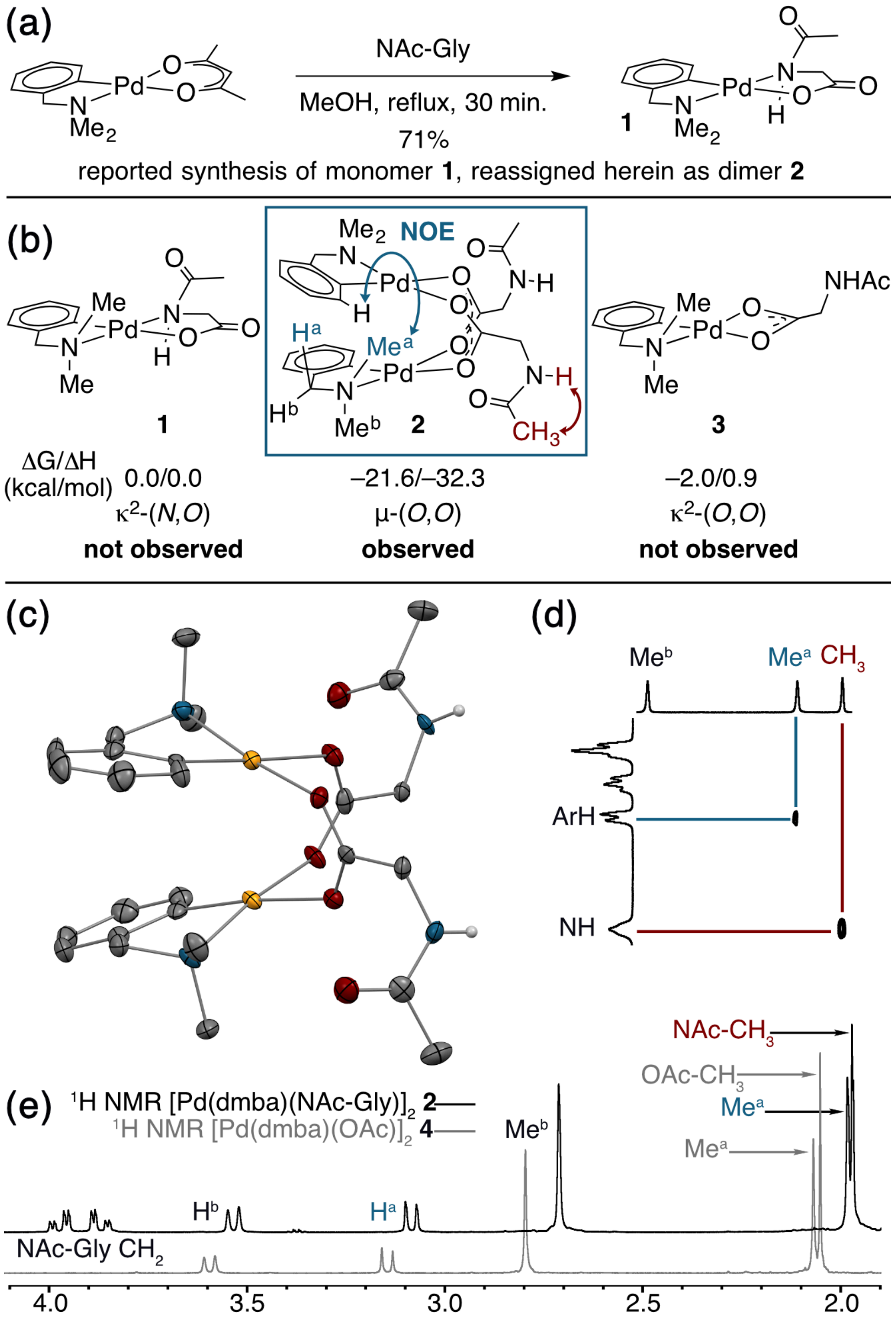

Figure 86 (a) Previously reported synthesis of **1**, which is herein reassigned as complex **2**. (b) Relative calculated energies (ΔG/ΔH) of **1**, **2**, and **3** with observed NOEs noted on **2**; (c) ORTEP diagram of **2** with 50% ellipsoids; in structures throughout yellow=Pd, red=O, blue=N, grey=C, white=H, and green=halogen; (d) Portion of ^{1}H NOESY spectrum with diagnostic cross peaks; (e) Overlaid ^{1}H NMR spectra of MPAA complex **2** with acetate complex **4** offset by 0.1 ppm for clarity.

DFT calculations[176] were conducted to gain further insight into the stability of the dimeric structure of **2** (Figure 86B). Good agreement between the calculated and crystal structures of **2** is observed; for example, the Pd-Pd distances in the two structures are 2.95 and 2.99 Å, respectively (See SI for full structural analysis). Moreover, the free energy/enthalpy of dimerization ($\Delta G_{dimer}/\Delta H_{dimer}$) for **2** (*i.e.* energy of the reaction 2(**1**) $\rightarrow$**2**) is calculated to be -21.6/-32.3 kcal/mol (Figure 86B). This finding shows that the dimeric structure **2** is significantly more stable than that of two putative monomers (**1**). Calculations also indicate that the κ^2-(*N*,*O*) coordination mode of NAc-Gly in **1** is less stable than the κ^2-(*O*,*O*) binding mode (**3**) by 2.0 kcal/mol, suggesting that the proposed κ^2-(*N*,*O*) coordination mode may not be the most stable monomer complex. We also located a μ-(*N*,*O*) dimer structure with dmba and NAc-Gly, **2**-μ-(*N*,*O*), that is higher in energy than **2** by 16.0 kcal/mol. These results show, for the first time, that widely used MPAA ligands can stabilize dimeric, μ-(*O*,*O*) carboxylate-bridged Pd(II)MPAA complexes directly analogous to widely-studied acetate-bridged palladacycles.[177-182]

Synthesis of MPAA Complexes by C-H Activation

To determine if **2** could also be prepared via cyclopalladation of dmba in the presence of MPAA, an equimolar mixture of palladium acetate, dmba, and NAc-Gly was stirred at room temperature in methanol. Analysis of the crude reaction mixture revealed **2** as the major product despite the presence of a 2:1 excess of acetate:MPAA, indicating selective coordination of MPAA over acetate. Complete conversion of dmba was observed overnight, and a 57% isolated yield of **2** was obtained after crystallization. These conditions were used to prepare MPAA-bridged complexes **6a-d** (NAc-Gly, NAc-

Ala, NAc-Leu, NAc-Ile) from trifluoromethyl dmba derivative **5a** (F_3C-dmba) in 62-91% yield by ^{19}F NMR (Figure 87).

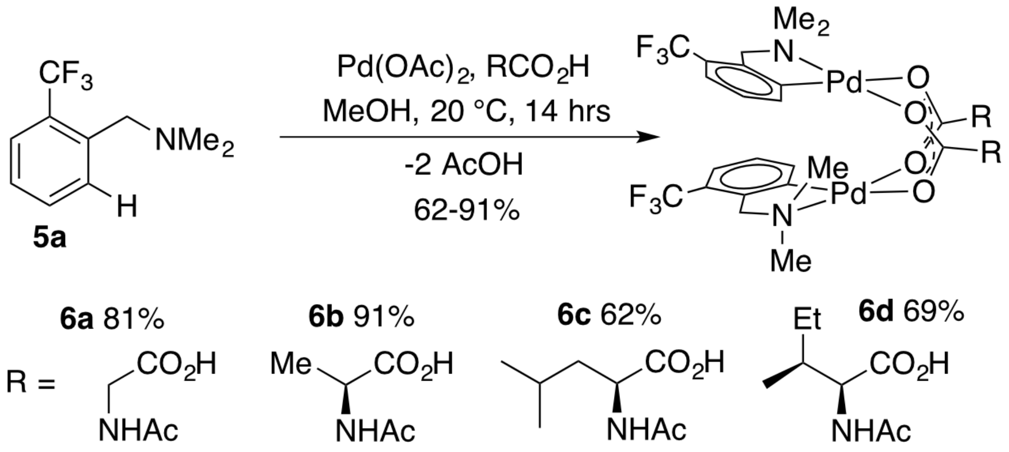

Figure 87. Synthesis and ^{19}F NMR yields of carboxylate bridged dmba dimers **6a**-**d**.

DFT calculations performed for **6a-d** and their acetate-bridged analogue, **9**, are consistent with these experimental findings. In all cases, the formation of carboxylate-bridged dimers, $[(dmba)Pd(MPAA)]_2$, from separated monomers is calculated to be highly exergonic: $\Delta G_{dimer}/\Delta H_{dimer}$ = -18.5/-35.9, -18.5/-36.7, -21.0/-39.0 -21.5/-39.6 and -17.3/-33.1 kcal/mol for **6a**, **6b**, **6c**, **6d** and **9**, respectively. These computational data demonstrate that all studied MPAAs form more stable dimeric complexes than their acetate analogs. Furthermore, the stability of $[(dmba)Pd(MPAA)]_2$ relative to the corresponding monomers increases with increasing size of the MPAA ligand side chain (i.e., **6c**/**6d**>**6a**/**6b**). Similar to our previous findings for acetate-bridged Pd(II) complexes, however, it is expected that the stability of MPAA-bridged complexes will depend on the nature of substrate directing group, MPAA, and environment (solvent, additives, etc).[183]

Characterization of Dimeric Pd(II)MPAA Complexes

Single crystal X-ray diffraction studies of **6a**-**c** confirms that each of these complexes exists as a carboxylate-bridged dimer in the solid state. However, detailed mechanistic studies are not possible without an understanding of structure in solution: though solid state structures can provide insight, solution structures and aggregation states must be determined independently[184,185]. Pulse gradient spin-echo (PGSE) experiments were conducted to assess the nuclearity of the MPAA complexes in solution.[186,187] The molecular volume of the monomeric acac complex **7** was benchmarked at 1.0 and the dimeric acetate and chloride bridged complexes (**8** and **9**) gave molecular volumes of 1.9 and 2.4 relative to **7**, indicating the ability of PGSE experiments to differentiate monomeric from dimeric Pd(dmba) complexes (Figure 88). Under the same conditions, the MPAA complexes **6a-d** all gave relative molecular radii greater than the dimeric control complexes (3.9-4.8) consistent with dimeric MPAA complexes in solution.

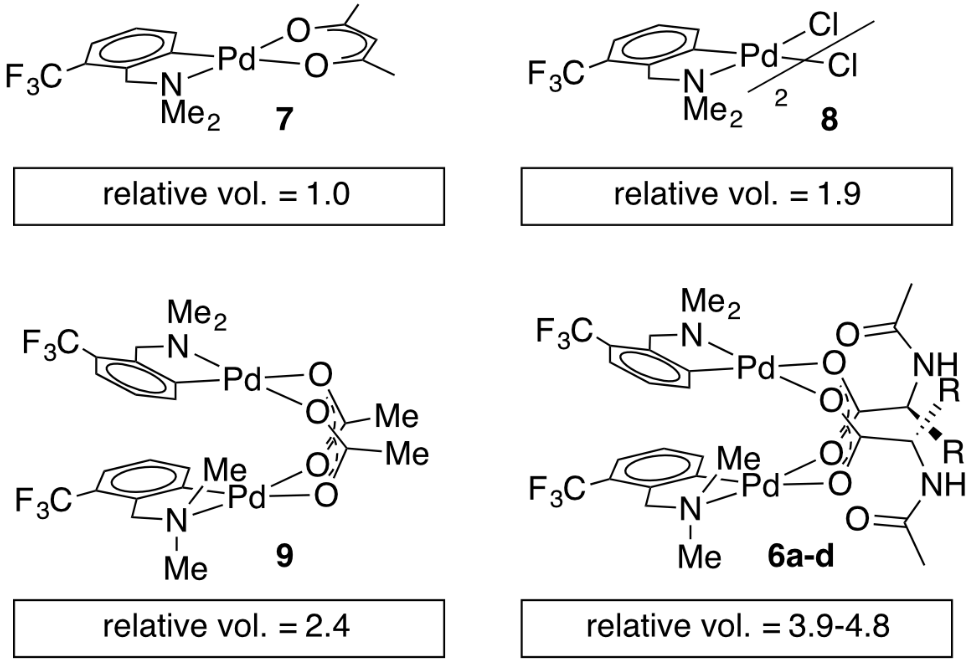

7

relative vol. = 1.0

8

relative vol. = 1.9

9

relative vol. = 2.4

6a-d

relative vol. = 3.9-4.8

Figure 88 Relative molecular volumes approximated from diffusion coefficients obtained by pulse gradient spin-echo NMR.

The dimeric nature of complexes **6a**-**d** in solution is further supported by their ^{1}H NMR and NOESY spectra, which display the same diagnostic features as the acetate bridged complexes **4** and **9** (Figure 86E and Figure 88, respectively). Specifically, upfield shifts due to magnetic anisotropy and NOE cross peaks with upfield-shifted resonances were observed.

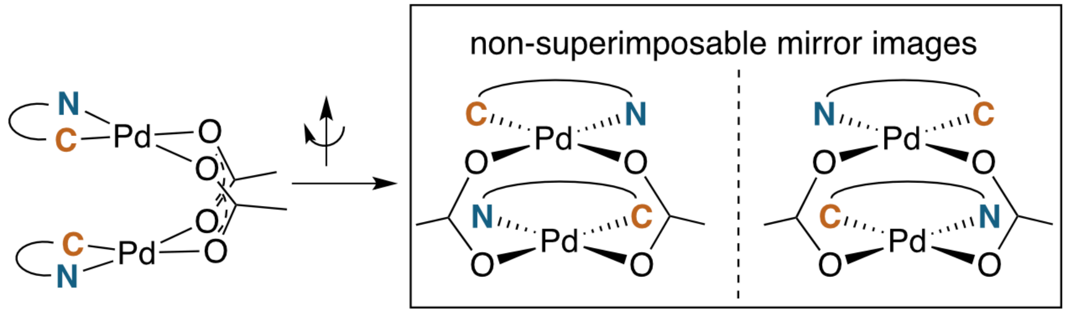

Figure 89 Chirality of bridged palladacycles

A noteworthy feature of carboxylate bridged palladacycles is the chirality of the stacked square planar coordination spheres (Figure 89). As expected for an achiral ligand, all of the NAc-Gly complexes crystallize as racemic mixtures with both enantiomers present in the unit cell. When an additional stereogenic unit is introduced to the MPAA (**6b-d)**, the chirality of the complex gives rise to two diastereomers, which are present in an approximately equal ratio for **6b-d** and are differentiable by NMR as illustrated inFigure 90. It is interesting to note that, despite a nearly 10 Å separation of the CF_3 substituents and the stereogenic centers of the MPAA ligands, the extent of diastereotopic differentiation of ^{19}F NMR appears to be correlated with the size of the MPAA side chain (Δδ= 4.5, 15, and 26 Hz for R = Me (**6b**), *i*-Bu (**6c**), and *sec*-Bu (**6d**).

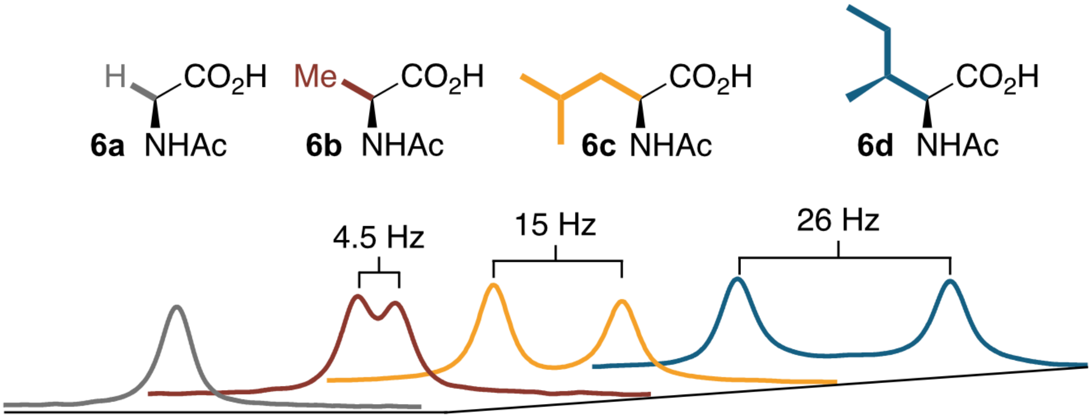

Figure 90: ^{19}F NMR of **6a**-**d** show correlation between diastereotopic differentiation and size of MPAA side chain.

Assessing Monomer Dimer Equilibrium

To address the possibility that other species (e.g., κ^2-(*N*,*O*) monomer) may be in equilibrium with the observed MPAA-bridged dimers, a crossover experiment was conducted which revealed rapid equilibration of homodimers to a statistical mixture of hetero and homodimers (Figure 91, Figure 92, and Figure 93).[182] Rapid crossover at room temperature is consistent with a small equilibrium concentration of monomeric MPAA complex capable of rapidly recombining with other free monomers in solution. This rapid equilibrium was further assessed by ^{19}F EXSY experiments which revealed $\Delta G^{\ddagger}_{exchange}$ = 19.2 kcal/mol at 21 °C.[188] The observed $\Delta G^{\ddagger}_{exchange}$ is greater than the calculated ΔG_{dimer} of **6a** (18.5 kcal/mol) and thus compatible with an exchange pathway proceeding through high energy monomeric intermediates.

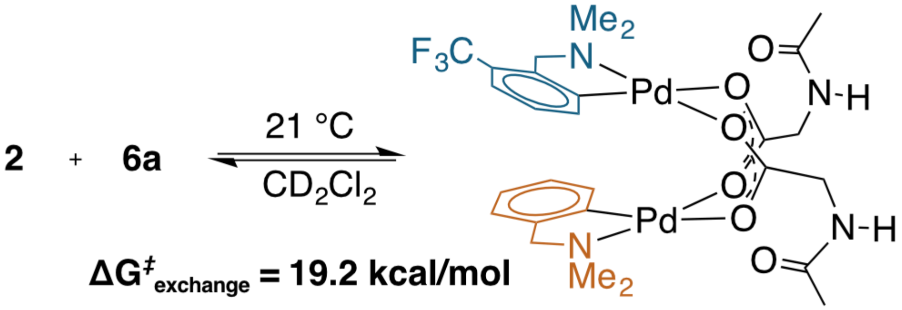

Figure 91 Crossover experiment with MPAA bridged dimers 2 and 6a reveals rapid exchange.

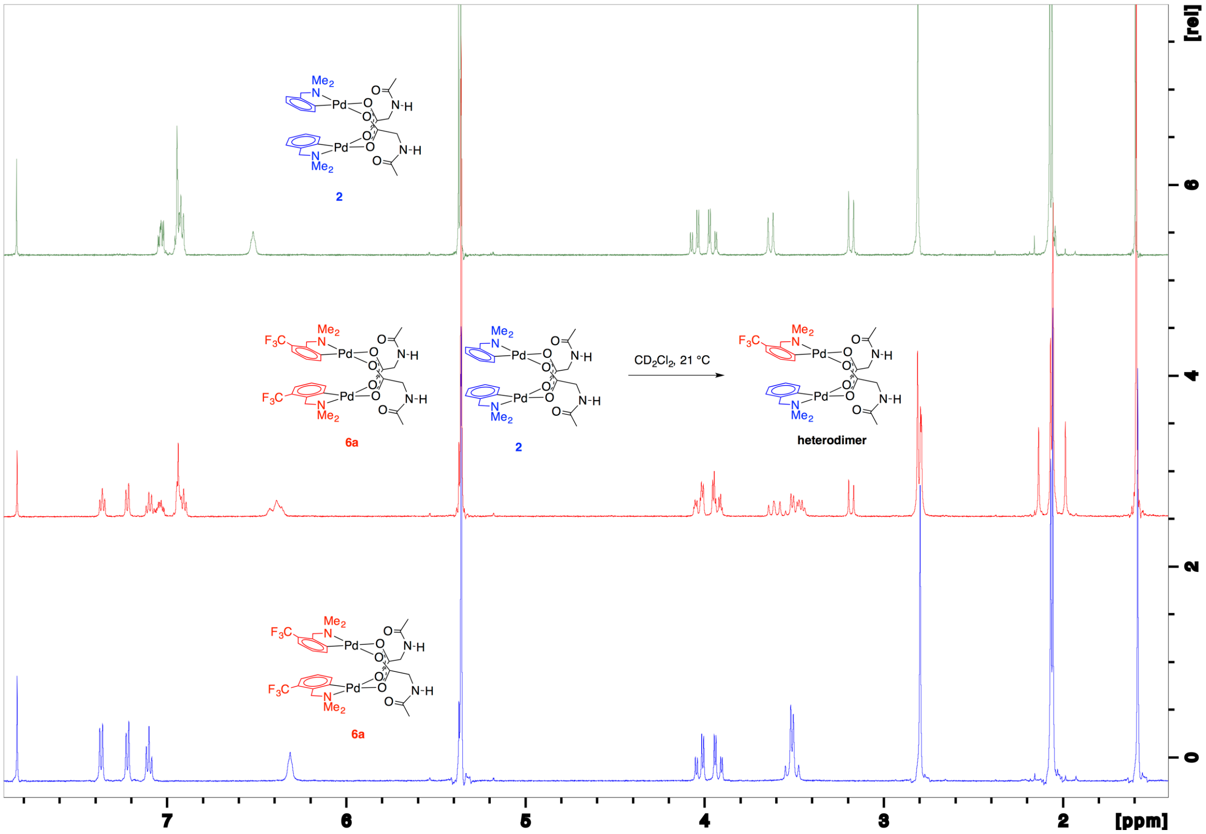

Figure 92 ^{1}H NMR of HOMO dimers **6a** and **2** compared to equilibrium mixture of homo and heterodimers.

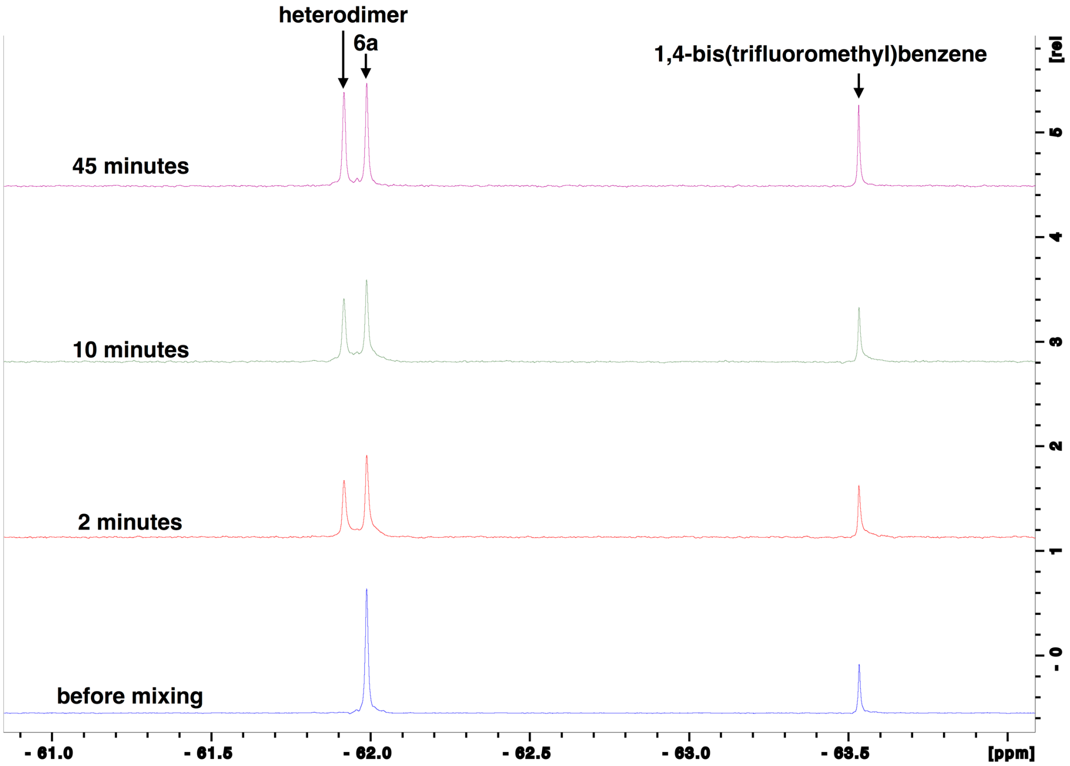

Figure 93 ^{19}F NMR of reaction progress of equilibration homo and heterodimers.

The rapid exchange of homodimers to equilibrium mixtures of homo and heterodimers enabled analysis by the method of continuous variation (MCV) which has proven especially powerful for characterizing the structure and aggregation state of complex mixtures in solution and confirmed the dimeric nature of **2** and **6a** in solution (Figure 94).[189] Complexes **6a** and **6b** were further characterized by variable temperature ^{1}H NMR (233-353K), variable concentration ^{19}F NMR (3-39 mM), and variable concentration UV-vis (0.02-0.5 mM) to shed light on the coordination mode of the putative monomeric species involved in the equilibrium shown in Figure 91. Across this range of conditions, there was no observable monomer or any other species in equilibrium with the characterized dimeric (MPAA)Pd-complexes. Attempts to observe monomeric

(MPAA)Pd-complexes by trapping with excess of amine substrate revealed no change in the ^{1}H and ^{19}F spectra of **6a** with up to 100 equivalents of **5a**. Collectively, these results as well as the DFT-calculated dimerization energies are consistent with the existence of high energy monomer complexes in rapid equilibrium with the observed MPAA-bridged dimer complexes.

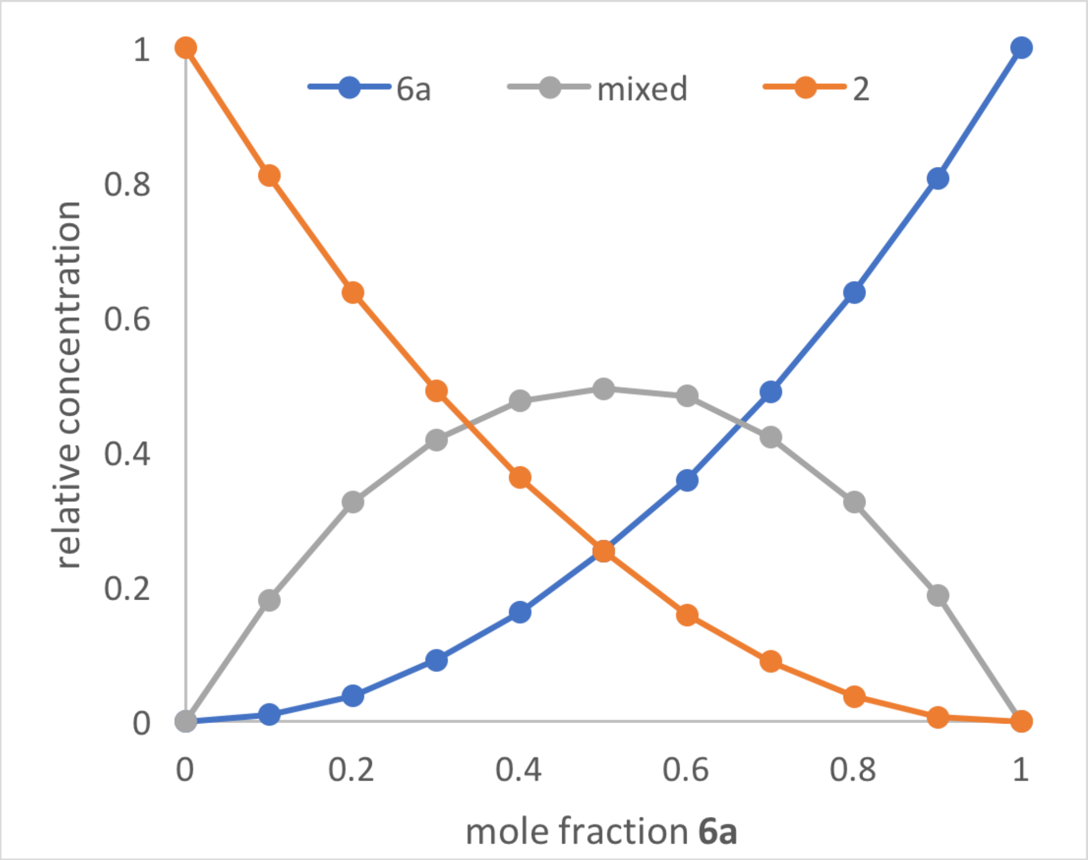

Figure 94 Job plot characteristic of a statistical ensemble of dimers

Effect of MPAA on Rate of Cyclopalladation

As noted above, C-H activation of dmba with palladium acetate gives selective formation of MPAA- over acetate-bridged di-palladium products, which have been extensively characterized in stoichiometric studies and as catalytic intermediates.[177-182]

This selectivity could result from more favorable binding of MPAA relative to acetate or faster cyclometallation by a Pd/MPAA species relative to $Pd(OAc)_2$. Cyclopalladation of CF_3-dmba to afford discrete MPAA complexes (**6a**-**d**) provides a unique model system to study the impact of MPAA on cyclopalladation rates. Initial rates for the reaction shown in Figure 95 were similar in the presence and absence of NAc-Ala and sodium acetate (NaOAc). These results suggest that kinetic effects are not responsible for the selective coordination of MPAA over acetate in compounds **6a**-**d**. Previous studies have suggested that observed rate enhancements in MPAA catalyzed C-H functionalization are the result of MPAA ligands lowering the barrier to C-H cleavage. However, MPAA accelerated C-H cleavage has not yet been directly confirmed in stoichiometric reactions, and in the system studied here, a rate effect does not account for selective MPAA coordination.

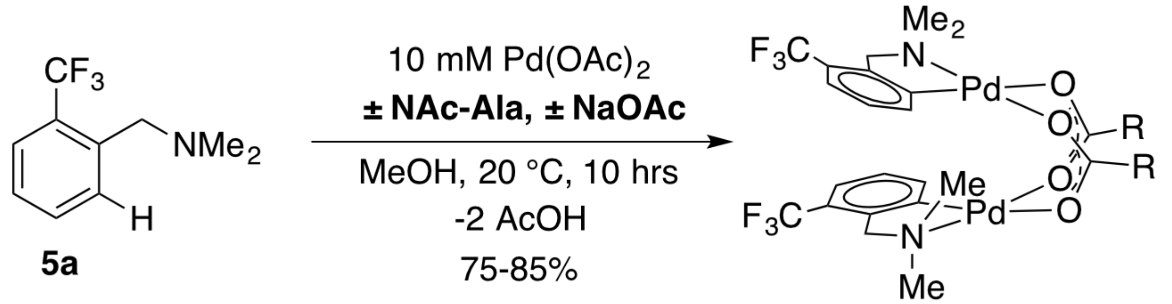

initial rate = 0.65 ± 0.03 mmol/min. ± MPAA and/or base

Figure 95. MPAA and carboxylate bases showed no effect on the rate of cyclopalladation of 5a

Pd(II)-MPAA Binding Affinity

To determine whether thermodynamic factors are responsible for selective MPAA coordination during the formation of **6a**-**d**, carboxylate exchange reactions were conducted using AcOH, NAc-Gly, NAc-Ala, and NAc-Ile (Figure 96). In forward and reverse reactions involving NAc-Gly, an equilibrium mixture containing approximately 5%

acetate-bridged complex **9** was observed.[190] In contrast, when **9** was equilibrated with NAc-Ala and NAc-Ile, the bulkier MPAA's drove the equilibrium to <1% complex **9**. Poor solubility of NAc-Gly and overlapping chemical shifts of NAc-Ala and NAc-Ile complexes precluded quantitative evaluation of the binding affinities of MPAAs and acetate. Qualitatively however, our experiments show that NAc-Gly, NAc-Ala, and NAc-Ile selectively displace acetate and suggest that NAc-Ala and NAc-Ile have a greater binding affinity than NAc-Gly (see supporting information S1.8 for ^{1}H and ^{19}F NMR of MPAA/OAc equilibrium mixtures). Thus, while these are structurally similar to acetate bridged dimers, differential binding strength leads to selective coordination of MPAAs, which can carry stereochemical information.

observed binding OAc << NAc-Gly < NAc-Ala, NAc-Ile

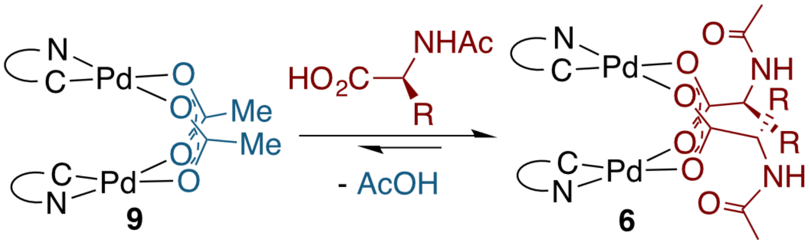

9 **6**

calculated energy of carboxylate exchange

	OAc	NAc-Gly	NAc-Ala	NAc-Ile
ΔG =	0.0	-4.0	-7.5	-9.8
ΔH =	0.0	-6.5	-7.7	-11.0

Figure 96. Competitive carboxylate binding equilibria.

To better understand bridging carboxylate binding affinity, we extended our DFT studies to examine ligand exchange equilibria ($\Delta G_L/\Delta H_L$) between acetate and MPAA ligands as defined by the equation: **9** + 2 MPAA → **6a**/**6b**/**6d** + 2 AcOH (Scheme 4).[191] The ligand exchange equilibrium was found to favor coordination of the MPAA ligands in the dimer complex, where $\Delta G_L/\Delta H_L$ = -4.0/-6.5, -7.5/-7.7 and -9.8/-11.0 kcal/mol for **6a**,

6b, and **6d**, respectively. The thermodynamic preference for MPAA binding relative to acetate is consistent with the results of a previous study on carboxylate-bridged palladium(II) dimers, in which we found that electron-withdrawing groups on bridging carboxylates stabilize the dimer relative to separated monomers by increasing interaction energy between the Pd-center and ligands (*i.e.* via the Pd-OCO bonding motif).[183] Thus, both experimental and computational results suggest bridging carboxylate binding affinity follows the trend acetate< NAc-Gly< NAc-Ala, NAc-Ile.

Substrate Scope of C-H Activation

To assess whether substrates used in C-H functionalization reactions catalyzed by Pd(II)/MPAA mixtures can form dimeric complexes analogous to **6a-d**, 1 mM methanol solutions of $Pd(OAc)_2$, NAc-Ala, and substrate were analyzed by ESI-MS after 30 minutes of mixing (Figure 97A).[157,192,193] The substrate dmba (in **11**) was studied to confirm that reaction mixtures afforded similar mass spectra to the isolated complex **2**. The substrates 2-pyridyl-diphenylmethane[157] (in **12**) and dimethylamino-ferrocenyl-methane[192,193] (in **13**) were also evaluated because both have been used in enantioselective Pd(II)/MPAA catalyzed C-H functionalization. Moreover, the former was the subject of computational,[161] synthetic,[161] and mass spectrometry[164] experiments aimed at understanding the impact of MPAA ligands on catalysis, and the latter was used in stoichiometric enantioselective cyclopalladation reactions with MPAA additives.[194-197] Thus, while these substrates cannot, of course, represent the full scope Pd(II)/MPAA catalyzed C-H functionalization due to the sensitivity of these reactions to different directing groups,[198] they are structurally similar to dmba, which we have studied in depth, and both have been used for stoichiometric model studies[161,164,194-197] and catalysis.[157,192,193]

As expected, the di-palladium ion **11** (with dmba substrate) was observed. While ions consistent with monomeric cyclopalladated (MPAA)Pd-complexes were previously reported for 2-pyridyl-diphenylmethane[164], we observe ions consistent with both monomeric and dimeric Pd species (**12**) for this substrate[157,199] and for dimethylamino-ferrocenyl-methane[192,193,200] (**13**) (Figure 97). The observed di-palladium ions are analogous to those observed in the MS of isolated, characterized carboxylate-bridged dimers **2**, **4**, **6a**-**d** and **9**. Moreover, di-palladium ions **11-13** had a higher intensity than those corresponding MPAA to monomeric complexes. For all three substrates, the palladium-containing ion with the greatest intensity is the cyclopalladated substrate with no ancillary ligands (or a fragment thereof).

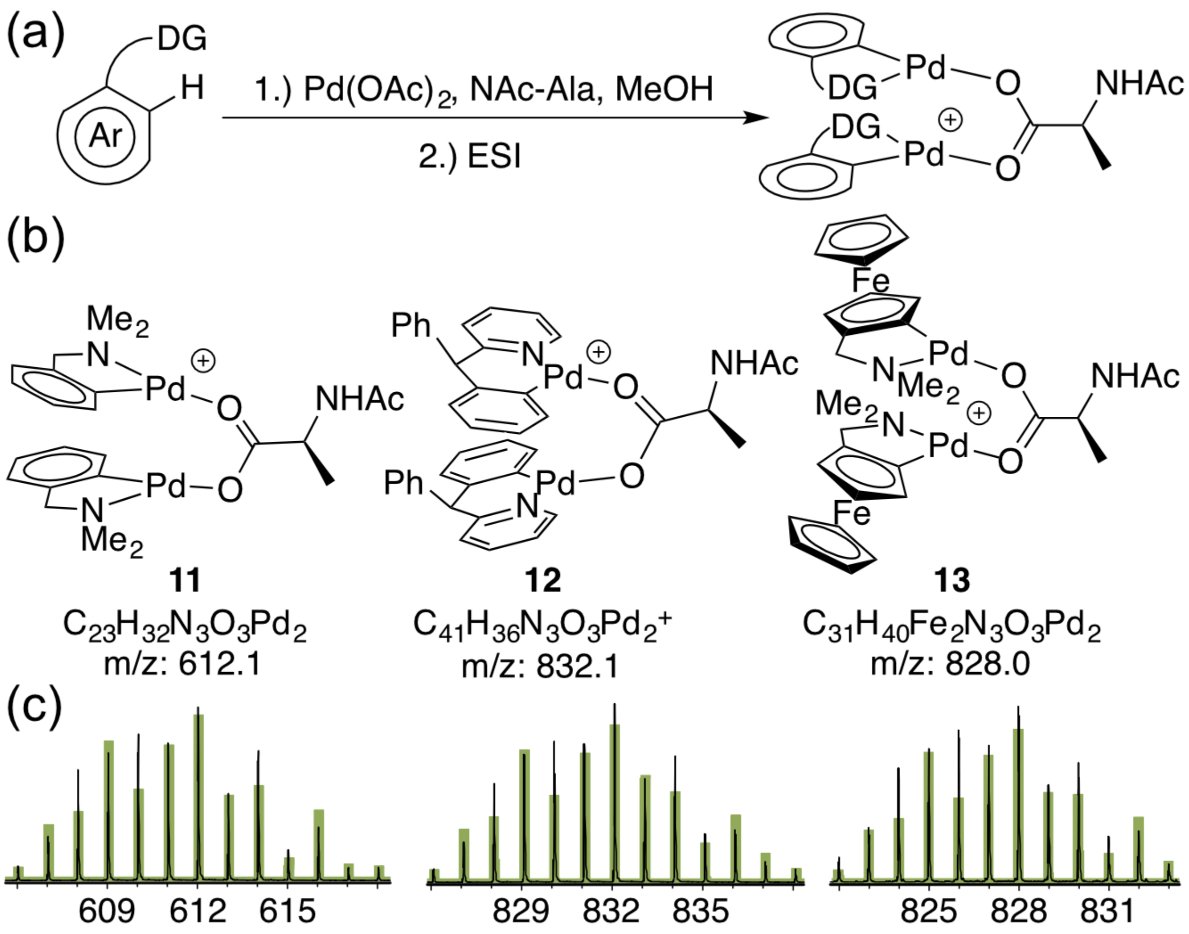

Figure 97 (a) Reaction conditions to generate MPAA complexes for analysis by ESI-MS; (b) Ions for di-palladium MPAA complexes (- 1 MPAA) (c) Observed isotope patterns for ions **11-13** (black) and overlaid theoretical isotope patterns (green) from ESI-MS analysis of reactions in (a).[201]

Given the observation of ions consistent with di-palladium substrate complexes by MS, we sought to determine whether di-palladium complexes are also present in the absence of substrate.[202] While a previous report[165] noted the monomeric species Pd(MPAA)$^+$ under such conditions, we found that 2 mM acetonitrile solutions of Pd(OAc)$_2$ and MPAA (NAc-Gly, NAc-Ala, and NAc-Leu) contain an ion corresponding to the dimeric complex Pd$_2$(MPAA)$_2^+$ in addition to Pd(MPAA)$^+$ in ratios dependent on fragmentor voltage. These results suggest that MPAA-bridged di-palladium species can form both in the absence and presence of multiple substrates used in enantioselective C-H functionalization under conditions similar to those used in the preparation of dimeric MPAA-bridged palladacycles **6a**-**d**.

We have also calculated the $\Delta G_{dimer}/\Delta H_{dimer}$ values for cyclopalladated carboxylate bridged Pd/MPAA species with 2-pyridyl-diphenylmethane[199] and 2-benzylpyridine[203] substrates, as well as with acetonitrile (i.e., no substrate). In all cases, we find that the dimer is favored over the separated two. As in our previous study, these calculations show that the nature of substrate can have a large impact on the thermodynamic stability of dimeric complexes.[183] For example, calculations show that the additional phenyl substituent of 2-(diphenylmethyl)pyridine stabilizes the corresponding cyclopalladated dimer complex relative to that derived from 2-benzylpyridine. The presented calculations are consistent with the experimental data showing that MPAA-bridged dimeric complexes can form with a wide range of substrates relevant for C-H functionalization.

Reactivity of MPAA Complexes Toward Electrophiles

The facile formation of dimeric Pd(II)MPAA complexes **2** and **6a**-**d**, along with the observation by MS and the calculated energies of analogous complexes with substrates used in catalysis, suggests that MPAA-bridged complexes could form under conditions relevant to catalytic C-H functionalization. The reactivity of **2** and **6b** toward electrophiles used in MPAA-facilitated C-H functionalization was therefore assessed. Both complexes underwent reaction with Michael acceptors,[150,204] hypervalent iodine oxidants,[205] and elemental halogens[152,206] to give C-C and C-X (X= Cl, Br, I) bond formation as illustrated in Figure 98.[207]

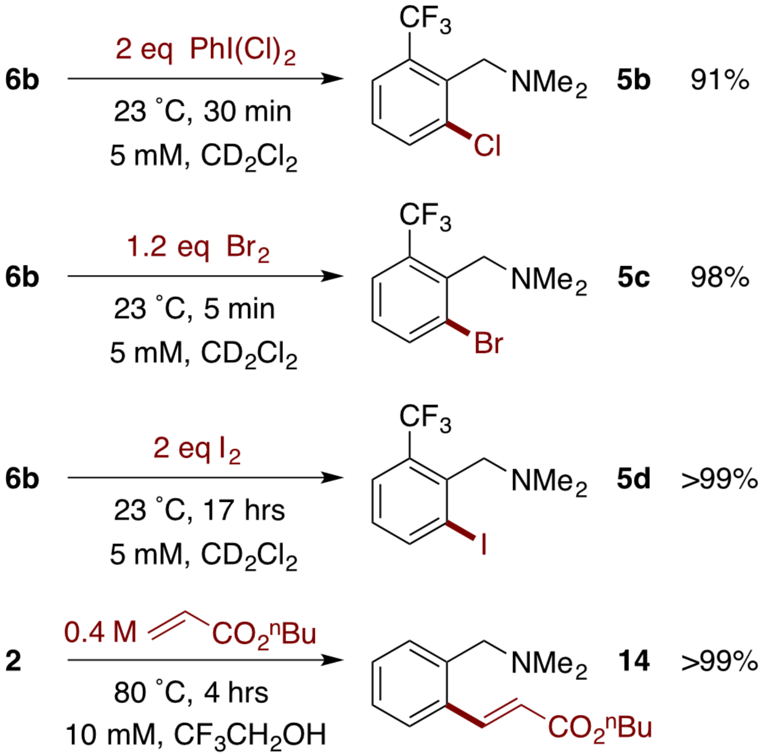

Figure 98. Representative reactions of cyclopalladated MPAA complexes with electrophiles.

To determine whether **6b** reacts with electrophiles as a dimer or perhaps via a monomeric intermediate, a kinetic analysis of the reaction of **6b** with I_2 was performed as an example— though **6b** may react differently with other electrophiles (Figure 99). An early control revealed that catalytic amounts of exogenous iodide (tetrabutylammonium iodide, Bu_4NI) led to substantial changes in the reaction profile and rate of iodination of **6b** (Figure 99B). To minimize interference from iodide generated over the course of the reaction, kinetics were analyzed by initial rates. The initial rate of iodination of **6b** is proportional to the initial concentration of **6b** (first order) indicating reaction of **6b** as a dimer, rather than a high energy monomeric intermediate (Figure 99C). Initial control experiments revealed that iodination of **6b** in the presence of increasing, catalytic amounts of exogenous iodide (0.033-0.53 equiv, Bu_4NI) exhibits saturation behavior

(Figure 99D). Thus, to avoid interference from iodide generated over the course of the iodination reaction, the order with respect to iodine was determined in the presence of a saturating concentration of Bu_4NI (53 mol%). Under these conditions, initial rate analysis indicated that the reaction was first order in iodine from 3-39 mM (Figure 99E). These results are consistent with a reaction of iodine with the dimer **6b** in the rate limiting transition structure, rather than reaction at a monomeric intermediate. Additional data and discussion of iodination in the absence of exogenous iodide are presented in the supporting information.

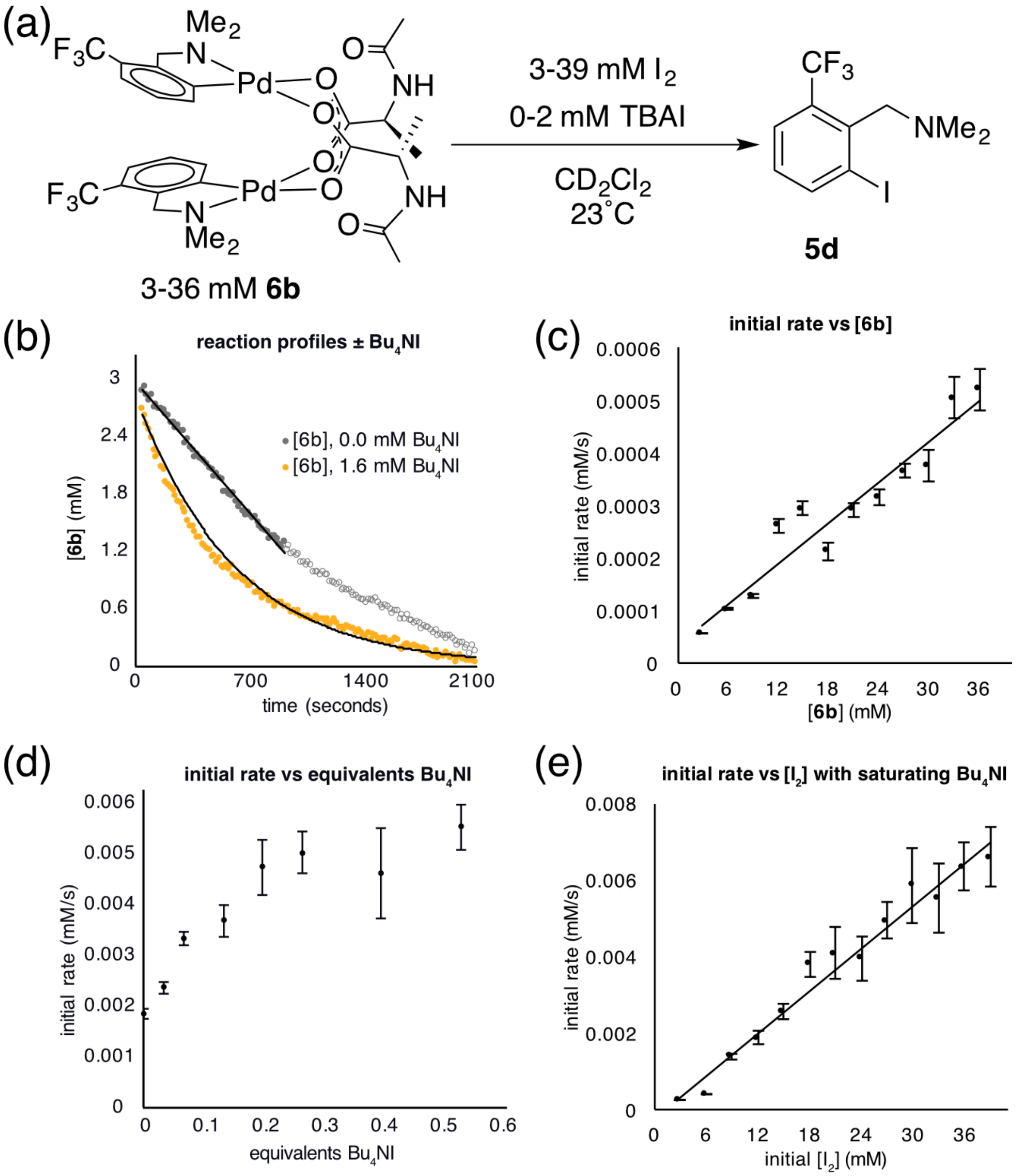

Figure 99 (a) Iodination of cyclopalladated MPAA complex **6b**; (b) Overlaid reaction profiles of iodination of **6b** in the presence and absence of Bu_4NI with an exponential fit in the presence of Bu_4NI and a linear fit for zero order portion in the absence of Bu_4NI; (c) Plot of initial rate of iodination of **6b** versus initial concentration **6b** (d) Plot of initial rate of iodination of **6b** versus equivalents of exogenous iodide; (e) Plot of initial rate of iodination of **6b** versus initial concentration of I_2 showing first order kinetics in I_2 under saturating Bu_4NI conditions.

Observation of C-H Activation from MPAA Palladacycles

While studying the reactivity of Pd(II)/MPAA complexes toward electrophiles, we found that cyclopalladated substrates with a C-H bond *ortho* to the directing group can undergo subsequent C-H activation chemistry. This reactivity affords a unique opportunity to study C-H activation in MPAA complexes with well-defined, di-palladium reactants and products. For example, combining **2** and iodobenzene dichloride led to the formation of chlorinated Pd(II)MPAA complexes **15a** and **15b** (Figure 100). This constitutes the first report of an MPAA-ligated palladacycle reacting to give discrete Pd(II)MPAA products.

Further investigation into the reaction of **2** with iodobenzene dichloride revealed the presence of chloride bridged dimers **16a**, and **16b**, which could result from carboxylate/chloride metathesis between **15a**-**b** and HCl generated *in-situ* (Figure 100). The MPAA- and chloride-bridged di-palladium products crystallized as needles and blocks, respectively, and could be separated manually. The mono-and di-chlorinated dimers co-crystallized, however, leading to partial occupancy of the chlorinated positions in the structures shown in Figure 5c and 5d. Treating **2** with excess iodobenzene dichloride led to chlorination and C-H activation of both dmba ligands and complete metathesis with chloride to give 75% **16b** and 22% **16a**, which reacted further with excess oxidant to give partial conversion to dichlorinated dmba **17** (Figure 100B and E). The dichlorinated compound (**17**) was protonated by HCl generated in situ and co-crystallized as a chloro-palladate salt (Figure 100E).

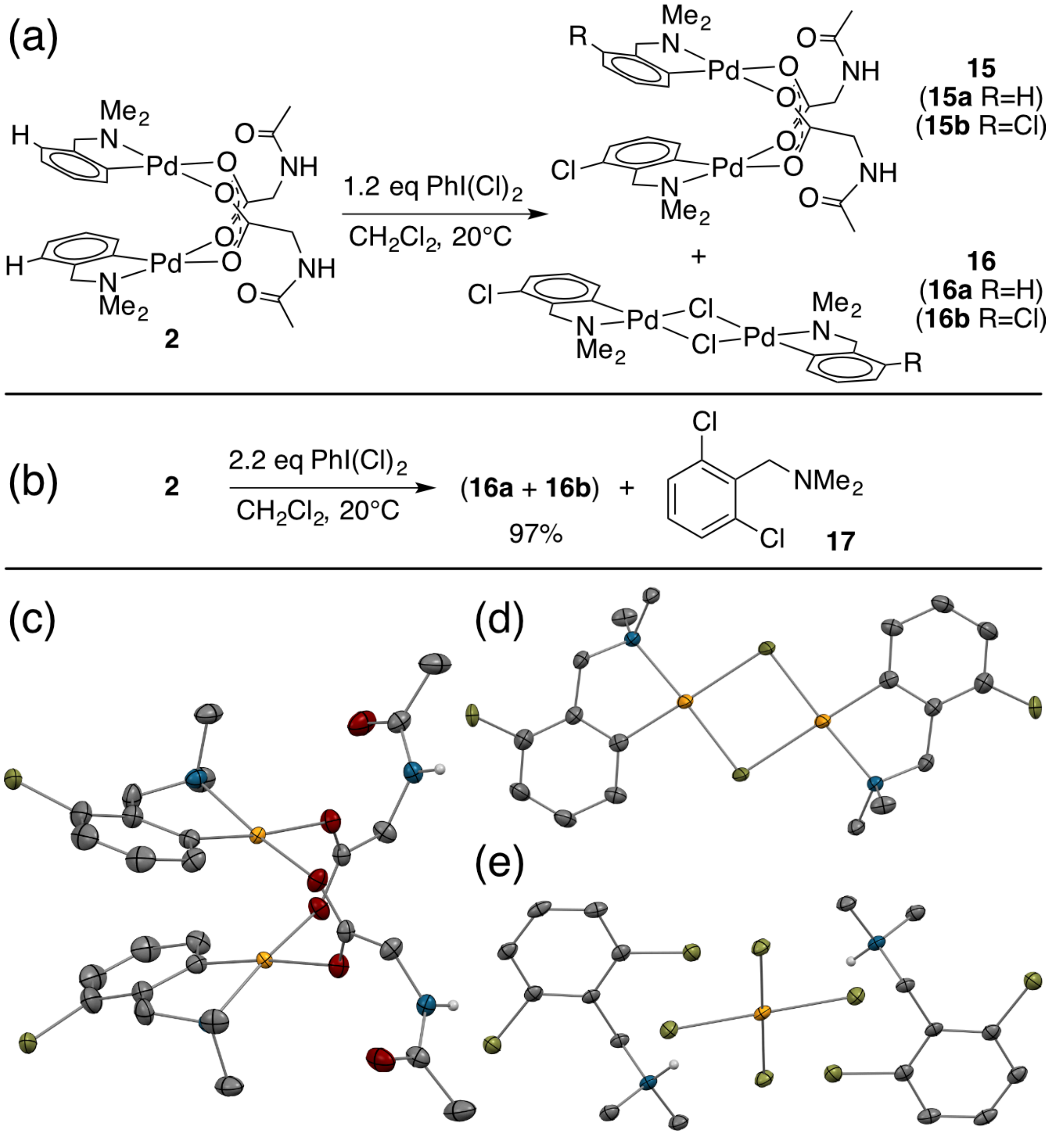

Figure 100. (a) Sequential chlorination and C-H activation of **2**; (b) chlorination of **2** with excess iodobenzene dichloride; (c) ORTEP of co-crystallized C-H activation products **15a** and**15b**: chlorines are disordered over both positions in dimer and were refined at 50% chemical occupancy; (d) ORTEP of co-crystallized C-H activation products **16a** and **16b**: chlorines are disordered over both positions in dimer and were refined at 20% chemical occupancy; (e) ORTEP of product of dmba dichlorination (**17**) co-crystallized with chloro-palladate.

The observation of stoichiometric C-H cleavage and Pd-C functionalization starting from dimeric MPAA-bridged Pd(II) complexes raises the possibility that both C-H activation and C-H functionalization could proceed via dimeric complexes. We envisioned that DFT calculations could provide further insight into potential reaction mechanisms, the nuclearity of potential intermediates (Pd(II)MPAA dimer or monomer), and factors controlling cyclopalladation and Pd-C bond functionalization for the F_3C-dmba model complexes examined.

Computational Analysis of Cyclopalladation of Dimeric and Monomeric Pd(II)/MPAA Complexes.

Several computational studies have established cyclopalladation pathways for monomeric Pd(II)MPAA complexes[159-165], and we previously studied the effect of acetate-bridged dimeric Pd(II) complexes on cyclopalladation,[183] but a similar study on dimeric MPAA-bridged Pd(II) complexes has not yet been reported. Here, we investigate the mechanisms of cyclopalladation of $[Pd(II)(\kappa\text{-}N\text{-}F_3C\text{-dmba})(\kappa\text{-OAc})(\mu\text{-NAc-Gly})]_2$ (**18-D**)[208] and its monomer (**21-M**) complex (where **-D** and **-M** signify dimeric and monomeric species, respectively). The free energy surface for cyclopalladation of the lowest energy (F_3C-dmba)Pd(II)/NAc-Gly dimer and monomer systems are shown inFigure 101. Prior to C-H activation, the monomer-dimer equilibrium for the (F_3C-dmba)Pd(II)/NAc-Gly system (i.e., 2 (**21-M**) $\rightarrow$ **18-D**) is $\Delta G_{dimer}/\Delta H_{dimer} = -3.3/-13.5$ kcal/mol, which is much smaller than that calculated for the cyclopalladated products **6a-d**. This is attributed to the strong hydrogen bonding interaction between NAc-Gly and OAc in **21-M**. As shown in Figure 6, the overall free energy barrier (relative to **18-D**) for the dimer pathway ($\Delta G^\ddagger/\Delta H^\ddagger$ =

23.2/20.3 kcal/mol) is significantly lower than that for the monomer pathway ($\Delta G^{\ddagger}/\Delta H^{\ddagger}$ = 41.7/52.1 kcal/mol). In addition, the dimer pathway has the larger driving force (again relative to the lowest reactant, **18-D**) of $\Delta G/\Delta H$ = -15.6/-15.5 kcal/mol compared to the monomer pathway, which is unfavorable by $\Delta G/\Delta H$ = 7.2/23.9 kcal/mol.

In both pathways, the C-H activation transition state requires an open coordination site on Pd to form the new Pd-C bond. Dissociation of one of the bridging MPAA ligands from **18-D**, which is thermodynamically unfavorable by $\Delta G/\Delta H$ = 20.3/18.7 kcal/mol, leads to formation of an intermediate (**19-D**) that undergoes C-H activation with a small intrinsic barrier of 2.9 kcal/mol (**TS1-D**).[209] Therefore, for the dimer pathway, cyclopalladation occurs via two sequential concerted-metallation-deprotonation (CMD) steps (at the transition states **TS1-D** and **TS2-D**) with $\Delta G^{\ddagger}/\Delta H^{\ddagger}$ = 23.2/20.3 and 19.0/18.3 kcal/mol energy barriers, respectively. Thus, the first cyclopalladation facilitates the second step of the reaction. On the other hand, formation of **22-M** on the monomer pathway is unfavorable by $\Delta G/\Delta H$ = 25.2/38.7 kcal/mol and the intrinsic barrier for C-H activation is 16.5 kcal/mol. These results show that the dimer stabilizes the C-H activation reactant and transition state relative to the monomer. It is unlikely that only one factor is responsible for such a large difference in the dimer and monomer barriers ($\Delta\Delta G^{\ddagger}$ = 13.6 kcal/mol). Instead, we attribute the acceleration in the dimer to several additive or cooperative effects including decreased *trans* effect from the bridging carboxylate to the formed Pd-C bond, intramolecular hydrogen bonding, as well as Pd-Pd and dispersive interactions between the monomer fragments.

In summary, cyclopalladation of the (F_3C-dmba)Pd(II)/MPAA dimer is calculated to be kinetically and thermodynamically favored over the monomer, indicating that the calculations generally support C-H cleavage/cyclopalladation via the dimer pathway. Notably, previous DFT studies of MPAA promoted C-H cleavage have evaluated energies of monomeric transitions states relative to monomeric MPAA reactants without commenting on possible dimeric pathways to C-H cleavage.[159-165] When the full potential energy surface is analyzed, as in Figure 101, it is apparent that assessing only the intrinsic barrier to C-H cleavage (i.e., **22-M** → **TS-M**, where $\Delta G^{\ddagger} = 16.5$ kcal/mol) neglects the fact the reactant in this step (**22-M**) is higher in energy than any of the intermediates or transition states on the dimer pathway. This illustrates the importance of assessing the energies of transformations involving monomeric and dimeric pathways relative to a common energetic reference when evaluating possible mechanisms for MPAA induced rate acceleration in C-H functionalization.

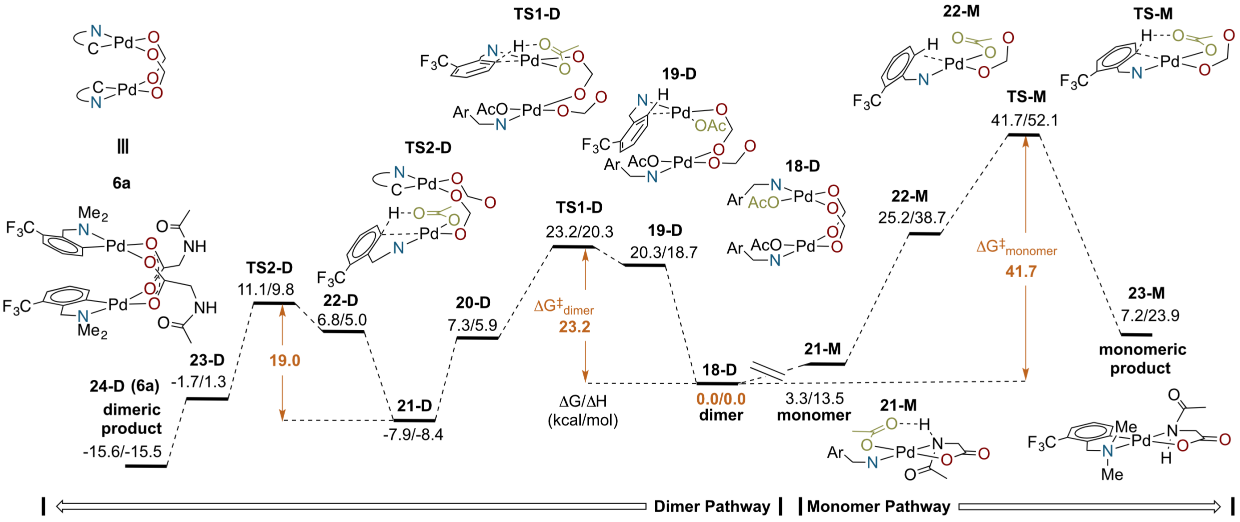

Figure 101. Energy surfaces (ΔG/ΔH) for mononuclear and dinuclear C-H cleavage: carboxylate oxygens of NAc-Gly shown in red relevant acetate for CMD highlighted in green, and all complexes except **6a** truncated for clarity, see above **6a** for key.

Computational Analysis of Pd-C Bond Iodination in Cyclopalladated MPAA Dimer and Monomer Complexes.

We previously reported that C-H iodination catalyzed by Pd(II) systems proceeds via a redox-neutral electrophilic cleavage (EC) mechanism as opposed to a Pd(II)/Pd(IV) oxidative addition and reductive elimination sequence.[210] As illustrated in Figure 102, the EC pathway is initiated by coordination of I_2 to the Pd(II) center as a Z-type ligand.[211] In the transition state, C-I bond formation and I-I bond cleavage occur in a concerted fashion without formal oxidation of the Pd(II). We also examined the effect of the nuclearity of the reactive Pd(II) species on the EC barrier and found that the reaction is faster with the acetate-bridged dimer than with the corresponding monomer.[210] The experimental observation of iodide dependent rate enhancements during the iodination of the MPAA-bridged dimer **6b** (*vide supra*) led us to investigate the effect of iodide on the reaction of **6a** with I_2 through the EC pathway. We hypothesized that coordination of iodide *trans* to the reactive, Z-type I_2 would activate the I-I bond and create a more nucleophilic palladate leading to acceleration of the electrophilic iodination process. [180,212]

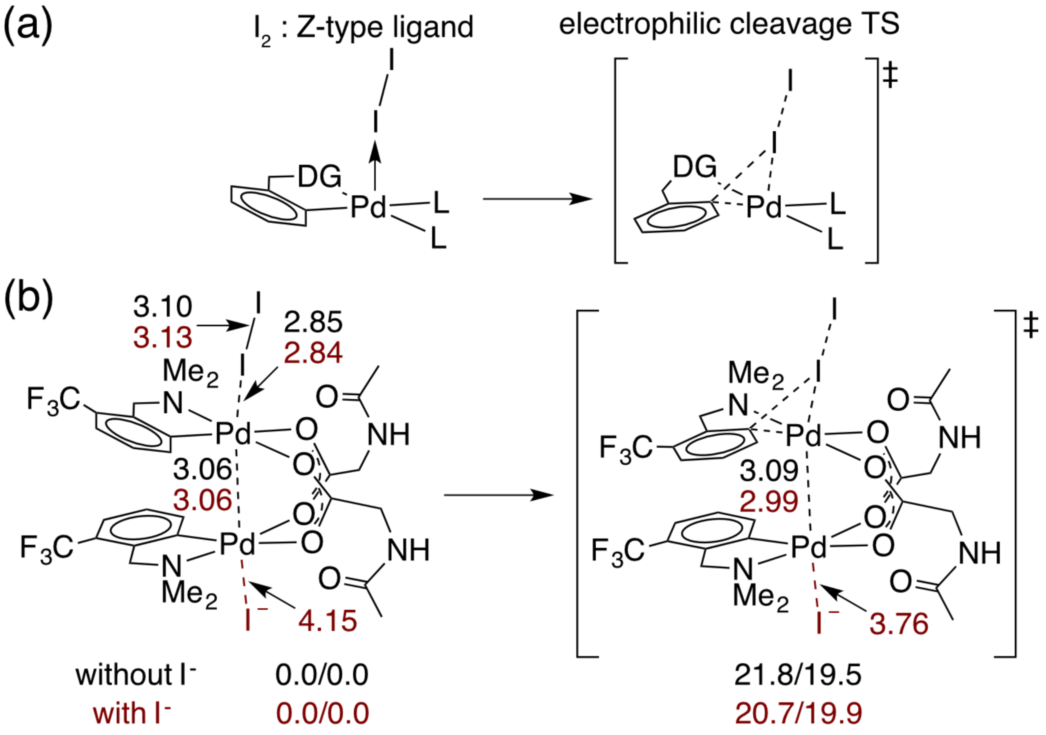

Figure 102**.** (a) General reaction pathway for the redox-neutral electrophilic cleavage (EC) mechanism for C-I bond formation; (b) Results from DFT calculations showing how iodide generated during the reaction accelerates EC with **6a** and I_2

Indeed, the free energy barrier ($\Delta G^{\ddagger}{}_{EC}$) for iodination with iodide is calculated to be slightly lower than the corresponding barrier without iodide (20.7 and 21.8 kcal/mol, respectively). Careful examination of the geometric features of the reactants and transition states show in Figure 102 provides some insight into how iodide may accelerate the EC pathway: 1) The I-I bond is slightly elongated in the presence of iodide (3.13 and 3.10 Å with and without iodide, respectively) indicating that I_2 is more activated,[210] and 2) In the transition state, the Pd-Pd distance decreases in the presence of iodide (2.99 and 3.09 Å with and without iodide, respectively) indicating that the iodide facilitates participation of the second Pd center in the transition state. [110,213,214] From these computational results and the experiments presented above, it is reasonable to conclude MPAA-bridged Pd(II) complexes react with I_2 as dimeric complexes (not monomeric intermediates); furthermore, exogenous iodide accelerates iodination and may do so by the formation of more nucleophilic iodopalladate.

MPAA Complexes as Pre-catalysts

Based on our extensive characterization of stoichiometric C-H activation and Pd-C functionalization involving the dimeric, MPAA-bridged Pd(II) complexes outlined above, we sought to determine whether these complexes are also viable precatalysts for catalytic C-H functionalization reactions. Indeed, alkenylation of dmba was catalyzed with the same rate whether **2** or Pd(II)/NAc-Gly was used as the precatalyst (Figure 103). However, similar to the stoichiometric C-H activations discussed above—in which selective MPAA coordination modified the complex's secondary coordination sphere, but did not afford rate enhancements—MPAA additives also did not accelerate catalytic C-H functionalization relative to palladium(II) acetate. These experiments thus confirm that MPAA bridged Pd dimer complexes can generate catalysts active for C-H functionalization, but they do not shed light the nuclearity or coordination mode of the active catalyst.

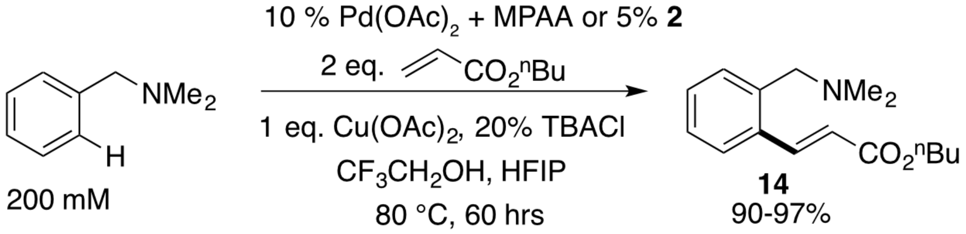

Figure 103. Pre-catalyst 2 catalyzes olefination of dmba at the same rate as mixtures of Pd(OAc)$_2$ / NAc-Gly.

On the other hand, examining the catalytic competence of isolated, structurally characterized Pd(II)MPAA complexes provides a concrete starting point for determining the nuclearity and coordination mode of intermediates in catalytic C-H functionalization reactions. Given the range of substrates and conditions used in reactions catalyzed by Pd(II)/MPAA mixtures and the potential impact of these differences on the coordination chemistry of complexes involved in catalysis, a detailed understanding of different coordination modes, such as those reported in this work, is essential. Importantly, however, characterizing the structure and reactivity of Pd(II)MPAA complexes with substrates relevant to catalysis is only a prerequisite to the loftier goal of understanding the molecular origins the rate acceleration and enantioselectivity afforded by MPAA ligands. The initial experiments summarized above using model complex **2** do not specifically implicate dimeric MPAA complexes in catalysis. On the other hand, further kinetic analysis of catalytic C-H functionalization reactions, informed by the structural characterization herein, provides a means to probe this possibility.

Summary and Conclusion

Since the discovery that MPAA ligands can accelerate and confer enantioselectivity to C-H functionalization reactions, experimental and computational studies have been conducted to understand the molecular origins of these ligand effects. Prior to our work, the structure and reactivity of discrete Pd(II)MPAA complexes remained poorly characterized. The extensive synthetic, spectroscopic, and computational studies reported herein reveal—for first time—an unprecedented class of dimeric MPAA-bridged palladacycles that are analogous to catalytically relevant acetate bridged dimers and that form selectively from mixtures of Pd(II), MPAA, and dmba derivatives. While our work focused on dmba model complexes, MS and computational analysis of analogous complexes generated from substrates used in catalysis suggests that dimeric, MPAA-bridged palladacycles could be relevant beyond dmba substrates.

Our combined experimental and computational results show that structural features of putative Pd(II)MPAA complexes inferred from catalytic outcomes, including selective MPAA coordination and relay of stereochemistry, are observed in dmba model complexes. This finding indicates that such features do not, by themselves, necessitate κ^2-(*N*,*O*) MPAA coordination to Pd(II) during catalysis. Selective formation of dimeric, MPAA-bridged complexes from MPAA/acetate mixtures results from greater MPAA binding affinity to Pd(II) relative to acetate. Diastereotopicity in bound dmba ligands results from relay of stereochemistry from distal MPAA side chains, but further experiments using substrates with prochiral C-H bonds will be required to determine if this phenomenon is relevant to enantioselective catalysis.

In addition to these observations, C-H activation of dmba in dimeric, MPAA-bridged complexes is calculated to be kinetically and thermodynamically favored over a monomeric pathway. Coordination of MPAA to Pd(II) in a κ^2-(*N*,*O*) fashion is also not predicted to provide access to lower barrier pathways to C-H cleavage in dmba, consistent with our experimental observation that MPAA does not influence the rate of dmba cyclopalladation. On the other hand, calculations indicate that the relative stability of different Pd(II)MPAA dimer complexes is substrate and ligand specific, such that different complexes and reaction pathways could dominate for different reactions or under different conditions.

Despite their stability with respect to carboxylate exchange and calculated monomer-dimer equilibrium, the dmba model complexes studied undergo both Pd-C functionalization and subsequent C-H cleavage reactions relevant to C-H functionalization chemistry. A detailed kinetic analysis of stoichiometric iodination revealed that MPAA-bridged palladacycles react as dimers rather than as putative monomeric intermediates. This analysis is consistent with previous calculations showing a lower barrier to iodination at a dimeric palladacycle than the corresponding monomeric complex.[210]

In addition to their stoichiometric reactivity, dimeric MPAA-bridged palladacycles are competent precatalysts in palladium catalyzed C-H functionalization. Thus, the structure and reactivity of the complexes reported herein provide a starting point for understanding the role of MPAA ligands in catalysis. For example, MPAA bridged palladacycles project hydrogen bond donors and acceptors into the secondary coordination sphere of the Pd centers and create the potential for cooperative metal-metal interactions. Given reports[213,215-218] of these features in catalytic mechanisms, these structural studies open the possibility of a range of additional mechanisms by which MPAA ligands might impact C-H functionalization. Alternatively, MPAA complexes could serve as stable, off-cycle catalyst reservoirs. Ongoing studies by our groups will focus on delineating possible roles of MPAA-bridged palladacycles in C-H functionalization catalysis. These fundamental studies will, in turn, provide a framework for designing improved ligands and discrete catalysts for more advanced applications.

Experimental

All commercially available reagents were used as received unless otherwise noted. Mono-protected amino acids were purchased from Chem-Impex. Thallium acetylacetonate (acac) was purchased from Strem. Palladium(II) acetate was purchased from Pressure Chemical. 2-(trifluoromethyl)pheny acetic acid was purchased from TCI. 2-(trifluoromethyl)benzyl bromide was purchased from Matrix Scientific. *N*,*N*-dimethylbenzylamine was purchased from Acros. 1,4-bis(trifluoromethyl)benzene were purchased from Alfa-Aesar. Iodobenzene dichloride was prepared by a reported procedure.[219]

All preparative reactions were conducted under air with solvents stored in air except where noted. In instances where anhydrous solvents were used, they were obtained from an Inert solvent purification system (1 hour sparge with nitrogen followed by passage over two columns of activated alumina). CD_2Cl_2 and $CDCl_3$ were dried by stirring over CaH_2 under nitrogen overnight followed by vacuum transfer into a Teflon sealed container and three cycles of freeze pump thaw. NMR tube reactions were set up in an inert atmosphere glovebox under circulating nitrogen either in a J. Young tube or an NMR tube with a rubber septum.

NMR spectra were acquired on a Bruker DRX-500 MHz spectrometer at ambient temperature unless otherwise specified. Chemical shifts are reported in ppm and coupling constants are reported in Hz. MPAA complexes with chiral MPAA's exist as nearly equal mixture of diastereomers in solution. Each of these mixtures had several baseline separated ^{1}H and ^{13}C resonances which enabled assignment of the connectivity of the

MPAA and substrate fragments; however, the absolute stereochemistry each of the diastereomers could not be assigned by NMR. As such, each ^{1}H and ^{13}C signal is annotated by its connectivity rather than absolute stereochemistry in the spectra and chemical shifts listed below and more upfield of the two diastereomeric resonances is labeled with an apostrophe in the naming scheme below. Moreover, each annotated spectra is accompanied by a chemdraw representation of one of the two diastereomers for simplicity.

All NMR tube kinetics reactions were set up in dried degassed solvents in an inert atmosphere glovebox with stock solutions prepared in volumetric flasks and dispensed with gas tight syringes. In order to obtain kinetic data as near to the start of the reaction as possible, samples were prepared without palladium inside the glovebox, one sample was removed from the glovebox with a gas tight syringe containing the appropriate volume of the palladium stock solution. The sample was brought to the NMR spectrometer, locked, shimmed, ejected from the spectrometer, injected with the palladium stock solution through a rubber septum, shaken vigorously, lowered into the spectrometer, and data acquisition began as soon as a stable lock signal was obtained (typically less than 40 seconds after injection).

Synthesis of $[Pd(dmba)(OAc)]_2$ (4)

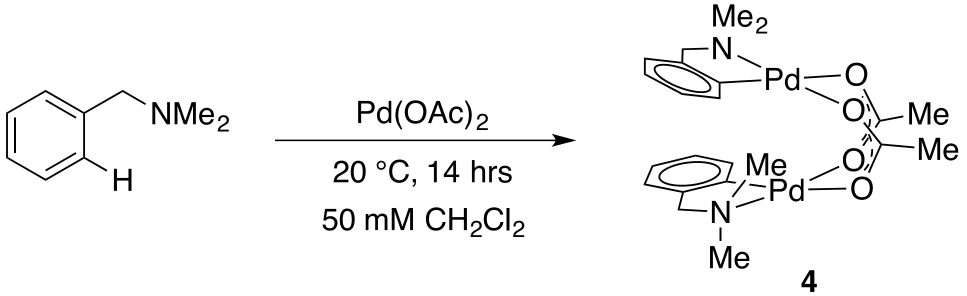

4

Figure 104: Synthesis of $[Pd(dmba)(OAc)]_2$ (4)

4 $[Pd(dmba)(OAc)]_2$ was prepared by a reported procedure[220] to give yellow crystals which matched the reported ^1H NMR of **4** $[Pd(dmba)(OAc)]_2$.

Jones, T. C.; Nielson, A. J.; Rickard, C. E. *Australian Journal of Chemistry* **1984**, *37*, 2179.

Synthesis of $[Pd(dmba)(Cl)]_2$ (S1)

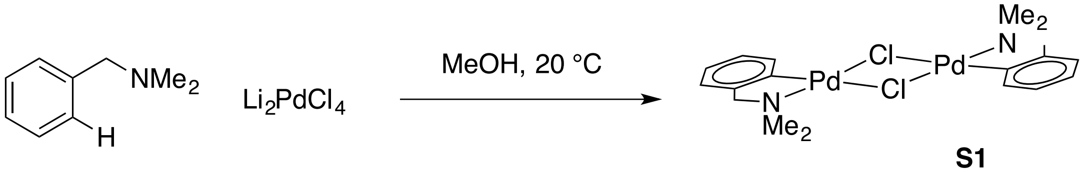

S1

Figure 105: Synthesis of $[Pd(dmba)(Cl)]_2$ (S1)

S1 $[Pd(dmba)(Cl)]_2$ was prepared by a reported procedure[221,222] to give a yellow powder which matched the ^1H NMR of **S1** $[Pd(dmba)(Cl)]_2$.

Cope, A. C.; Friedrich, E. C. J. Am. Chem. Soc. 1968, 90 (4), 909.

Pfeffer, M. Inorganic Syntheses 1989, 26, 211.

Synthesis of Pd(dmba)(acac) (S2)

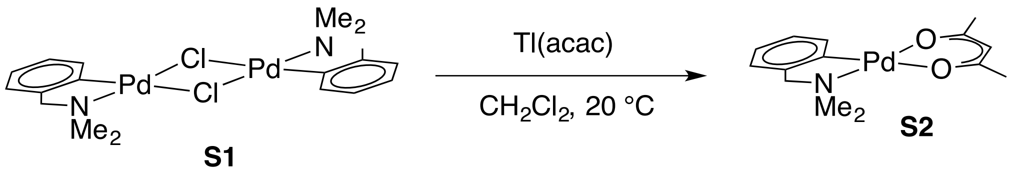

S2

Figure 106: Synthesis of Pd(dmba)(acac) (S2)

S2 Pd(dmba)(acac) was prepared by a reported procedure[172] to give a yellow powder which matched the ^{1}H NMR o**f S2** Pd(dmba)(acac).

Diaz-de-Villegas. Journal of Organometallic Chemistry 1995, 490, 35.

Synthesis of [Pd(dmba)(NAc-Gly)]$_2$ (2) from S1

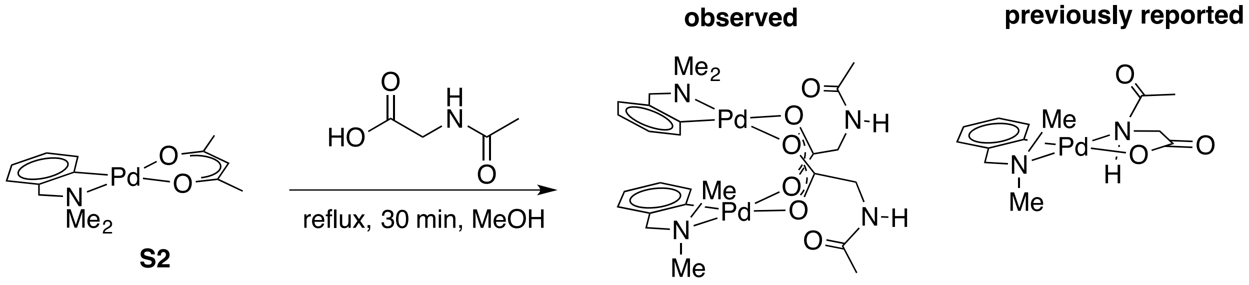

S2

2, 71%

1

Figure 107: Synthesis of [Pd(dmba)(NAc-Gly)]$_2$ (2) from S1

Complex **2** was prepared by a known procedure,[172] in which the products were assigned as the monomeric complex **1.** When the procedure was repeated, a complex with ^{1}H and ^{13}C NMR spectra matching those reported in the literature was obtained, but extensive characterization revealed that the structure in solution is **2**. Single crystals of complex **2** were obtained vapor diffusion of diethyl ether in to a concentrated of **2** in CH_2Cl_2 at 4 °C.

Diaz-de-Villegas. Journal of Organometallic Chemistry 1995, 490, 35.

Synthesis of 2 by C-H activation

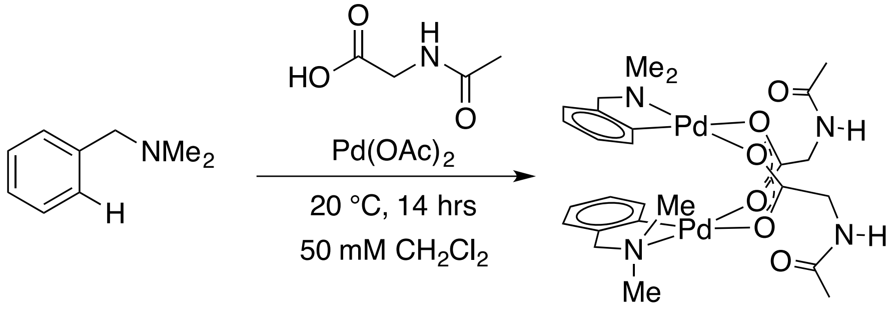

2, 57%

Figure 108: Synthesis of 2 by C-H activation

A 20 mL scintillation vial was charged with NAc-Gly (0.65 mmol, 76.1 mg, 1 equiv.), a stir bar, and 10 mL of methanol. The solution was stirred until the MPAA dissolved completely. To the MPAA solution was added solid Pd(OAc)$_2$ (0.65 mmol, 150 mg, 1 equiv.) and a solution of dmba (90 mg, 0.65 mmol, 1 equiv.) in 3 mL MeOH. The orange suspension gradually turned to a yellow solution and developed the smell of acetic acid. The solution was stirred for 14 hours at room temperature after which a 200 µL aliquot was concentrated in vacuo and to analyzed by ^{1}H NMR which revealed complete consumption of starting material and a 3:1 mixture of the desired product and a mixed MPAA/acetate complex. The remaining methanol solution was concentrated in vacuo and suspended in 3 mL toluene to azeotropically remove residual acetic acid in vacuo. The yellow solids were washed on a medium frit with 3x3mL diethyl ether to remove any remaining free acetic acid. The yellow solids were washed through the frit with 5x2 mL CH$_2$Cl$_2$ to remove any NAc-Gly. The CH$_2$Cl$_2$ solution was concentrated to 5mL, layered with 10 mL of diethyl ether, and stored over night at 4 °C. Decanting the supernatant afforded yellow solids that were not pure, but enriched in **2** by ^{1}H NMR. The enriched yellow solids were washed over a 1 cm pad of celite in a Pasteur pipette with 5x1 mL CH_2Cl_2, layered with 10 mL diethyl ether, and stored over night at 4 °C. The supernatant was decanted to afford 55.4 mg (23% yield) of pure **2** which matched the reported ^1H and ^{13}C NMR. The supernatant was concentrated by slow evaporation and layered with diethyl ether to afford an additional 77.1 mg of pure material to give a total of 132.5 mg (57% yield).

Synthesis of [Pd(CF_3-dmba)(OAc)]$_2$ (9)

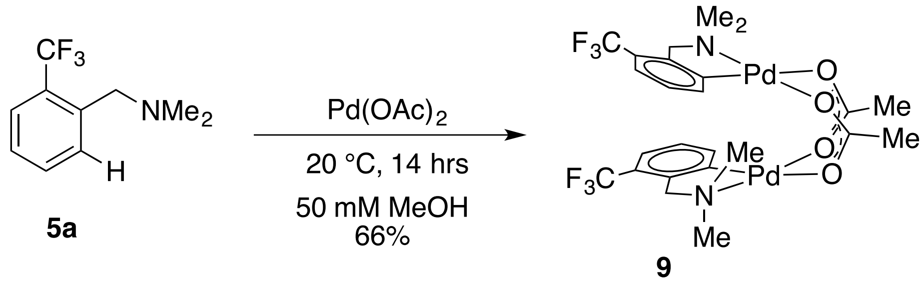

Figure 109: Synthesis of [Pd(CF_3-dmba)(OAc)]$_2$ (9)

Pd(OAc)$_2$ (112 mg, 0.5 mmol, 1 equiv.) was weighed into a 20 mL scintillation vial, dissolved in 10 mL CH_2Cl_2, and treated with CF_3-dmba (**5a**) (101 mg, 92 µL, 0.5 mmol, 1 equiv.) at 20 °C. After 14 hours, the solvent was removed under reduced pressure, and the solids filtered over a pad of celite with diethyl ether 3x3mL, which was allowed to evaporate to ca. 1 mL under ambient conditions and layered with 5 mL pentane. After 14 h at 4 °C, the supernatant was decanted to afford 112 mg (66 % yield) of yellow crystals of [Pd(CF_3-dmba)(OAc)]$_2$ (**9**). **^{1}H NMR (500 MHz, CD_2Cl_2)** δ 2.06 (s, 6 H, NMe toward π face), 2.07 (s, 6 H, OAc-CH_3), 2.78 (s, 6 H, NMe away from π face), 3.48 (m, 4 H, benzylic CH_2), 7.08 (t, J=7.70 Hz, 2 H, meta to Pd), 7.28 (d, J=7.60 Hz, 2 H, ortho to Pd), 7.34 (d, J=7.65 Hz, 2 H, para to Pd). **^{13}C NMR (126 MHz, CD_2Cl_2)** δ 24.25 (s, OAc-CH_3), 51.12 (s, NMe toward π face), 52.55 (s, NMe away from π face), 70.11 (s, benzylic CH_2), 121.47 (m, CH para to Pd), 124.01 (q, J=273.36 Hz, CF_3), 124.08 (q, J=32.59 Hz, ipso to CF_3), 124.72 (s, CH meta to Pd), 135.83 (s, CH ortho to Pd), 143.73 (s, aromatic quaternary), 146.59 (s, aromatic quaternary), 180.88 (s, OAc-$\underline{C}O_2$). **^{19}F NMR (470 MHz, CD_2Cl_2)** δ -61.917

Synthesis of [Pd(CF$_3$-dmba)(NAc-Gly)]$_2$ (6a)

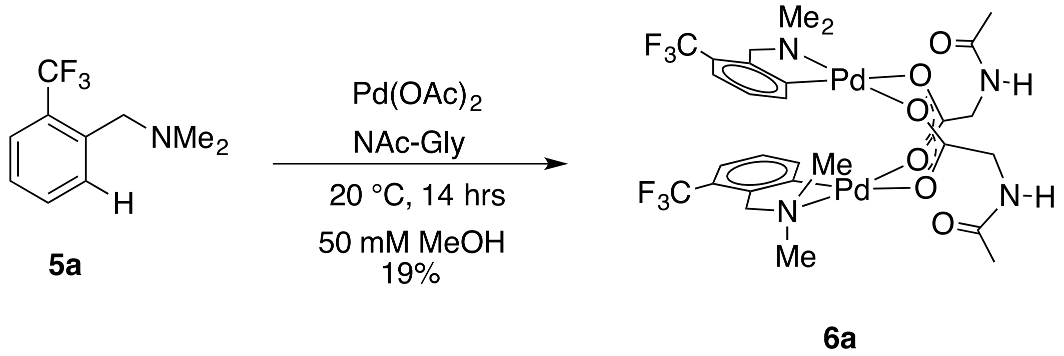

Figure 110: Synthesis of [Pd(CF$_3$-dmba)(NAc-Gly)]$_2$ (6a)

A 20 mL scintillation vial was charged with NAc-Gly (0.65 mmol, 76.1 mg, 1 equiv.), a stir bar, and 10 mL of methanol. The solution was stirred until the MPAA dissolved completely. To the MPAA solution was added solid Pd(OAc)$_2$ (0.65 mmol, 150 mg, 1 equiv.) and a solution of CF$_3$-dmba (132 mg, 0.65 mmol, 1 equiv.) in 3 mL MeOH. The orange suspension gradually turned to a yellow solution and developed the smell of acetic acid. The solution was stirred for 14 hours at room temperature after which a 200 µL aliquot was concentrated in vacuo and to analyzed by ^{19}F NMR which revealed complete consumption of starting material and 81% conversion to the desired product **6a** and 19% of mixed MPAA/ acetate complex **10**. Methanol was removed under a stream of nitrogen. The yellow solids were suspended in diethyl ether and transferred to a medium porosity frit where they were washed with 3x3mL diethyl ether to remove any free acetic acid. The yellow solids were washed through the frit with 5x2 mL 50:50 PhMe:CH$_2$Cl$_2$ to remove any NAc-Gly. The yellow PhMe:CH$_2$Cl$_2$ solution was layered with 5 mL diethyl ether, and stored over night at -35 °C. Decanting the supernatant afforded 53 mg (19% yield) of pure **6a**. Further crystallization of the precipitate resulted in material contaminated with 5-20%

of the mixed acetate MPAA complex **10**. Single crystals were grown from a concentrated solution of **6a** in CH_2Cl_2 layered with an equal volume of styrene oxide at -35 °C.

^{1}H NMR (500 MHz, CD_2Cl_2) δ 2.06 (s, 6 H, NAc-CH_3), 2.07 (s, 6 H, NMe toward π face), 2.80 (s, 6 H, NMe away from π face), 3.51 (m, 4 H, benzylic CH_2's), 3.94 (dd, J_{NH}=5.40, J_{HH}=17.79 Hz, 2 H, NAc-Gly $C\underline{H^A}H^B$), 4.05 (dd, J_{NH}=5.40, J_{HH}=17.79 Hz, 2 H, NAc-Gly $CH^A\underline{H^B}$), 6.38 (t, J_{NH}=5.40, 2 H, NH), 7.10 (t, J=7.72 Hz, 2 H, CH meta to Pd), 7.22 (d, J=7.15 Hz, 2 H, CH ortho to Pd), 7.37 (d, J=7.70 Hz, 2 H, para to Pd). **^{13}C NMR (126 MHz, CD_2Cl_2)** δ 22.92 (s, NAc-CH_3), 44.00 (s, Gly-CH_2), 51.50 (s, NMe toward π face), 52.72 (s, NMe away from π face), 70.29 (s, benzylic CH_2), 121.95 (m, CH para to Pd), 123.87 (q, J=273.39 Hz, CF_3), 124.31 (q, J=31.57 Hz, ipso to CF_3), 125.10 (s, CH meta to Pd), 135.53 (s, CH ortho to Pd), 143.65 (s, C aromatic quaternary), 145.44 (s, C aromatic quaternary), 169.77 (s, NAc-Gly $\underline{C}$(O)N),178.97 (s, NAc-Gly $\underline{C}O_2$). **^{19}F NMR (470 MHz, CD_2Cl_2)** δ -62.1103

Treating mixtures of **6a** and **10** in acetone with with an excess of aqueous lithium chloride generally afforded good conversion to the chloride bridged dimer **8**.[223]

Hiraki, K.; Fuchita, Y.; Pfeffer, M. 6-Membered Cyclopalladated Complexes of 2-benzylpyridine; Inorganic Syntheses, Vol 28, pp 208-211, 1989.

Synthesis of [Pd(CF$_3$-dmba)(NAc-Ala)]$_2$ (6b)

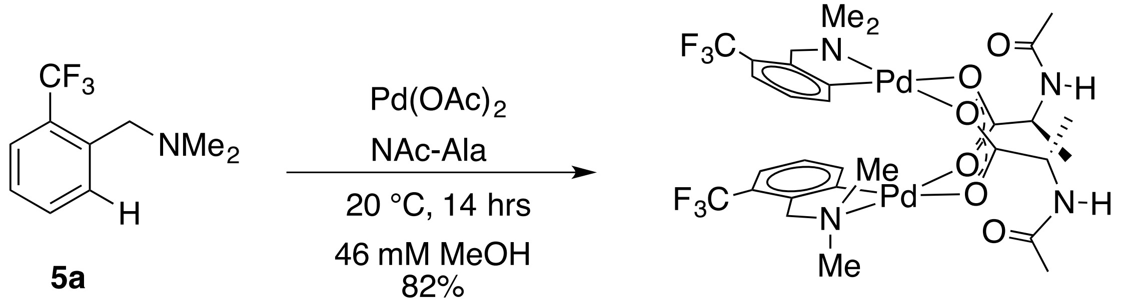

5a

6b

Figure 111: Synthesis of [Pd(CF$_3$-dmba)(NAc-Ala)]$_2$ (6b)

A 200 mL round bottom flask was charged with NAc-Ala (2.29 mmol, 300 mg, 1 equiv.), a stir bar, and 40 mL of methanol. The solution was stirred until the MPAA dissolved completely. To the MPAA solution was added solid Pd(OAc)$_2$ (2.20 mmol, 514 mg, 1 equiv.) and a solution of CF$_3$-dmba (2.29 mmol, 465 mg, 1 equiv.) in 10 mL MeOH. The orange suspension gradually turned to a yellow solution and developed the smell of acetic acid. The solution was stirred for 14 hours at room temperature after which a 200 µL aliquot was concentrated in vacuo and to analyzed by ^{19}F NMR which revealed complete consumption of starting material and 91% conversion to the desired product **6b**. Methanol was removed under a stream of nitrogen. The yellow solid was filtered over a medium porosity frit with 4x3 mL CH$_2$Cl$_2$. The yellow solution was allowed to slowly evaporate to ca. 5 mL and crystallized by slow diffusion of diethyl ether (5 mL) at -35 °C to give 825 mg (82% yield) of **6b**. Single crystals suitable for x-ray diffraction were grown by slow evaporation of a 5 mM solution of **6b** in acetonitrile under ambient conditions.

^{1}H NMR (500 MHz, CD$_2$Cl$_2$) δ 1.33 (t, J=6.55 Hz, 6 H, Ala CH$_3$ + Ala CH$_3$'), 2.00 (s, 3 H, NAc CH$_3$'), 2.04 (s, 3 H, NAc CH$_3$), 2.05 (s, 3 H, NMe upfield'), 2.07 (s,1 3 H, NMe upfield), 2.81 (s, 3 H, NMe downfield’), 2.81 (s, 3 H, NMe downfield), 3.53 (m, 4 H, benzylic CH_2 + benzylic CH_2'), 4.39 (m, 1 H, Ala methine'), 4.45 (m, 1 H, Ala methine), 6.24 (d, J=7.00 Hz, 1 H, NH'), 6.28 (d, J=6.75 Hz, 1 H, NH), 7.09 (m, 2 H, CH meta to Pd + CH meta to Pd'), 7.17 (d, J=7.60 Hz, 1 H, CH ortho to Pd'), 7.24 (d, J=7.75 Hz, 1 H, CH ortho to Pd), 7.37 (d, J=7.75 Hz, 2 H, CH para to Pd + CH para to Pd'). **^{13}C NMR (126 MHz, CD_2Cl_2)** δ 18.87 (s, Ala CH_3'), 18.99 (s, Ala CH_3), 23.05 (s, NAc CH_3 + NAc CH_3'), 50.69 (s, Ala CH'), 50.72 (s, Ala CH), 51.51 (s, NMe toward π face + NMe toward π face'), 52.75 (s, NMe away from π face'), 52.79 (s, NMe away from π face), 70.26 (s,1 benzylic CH_2 + benzylic CH_2'), 121.81 (m, CH para to Pd + CH para to Pd'), 123.91 (q, J=273.27 Hz, CF_3 + CF_3'), 124.25 (q, J=31.26 Hz, C ipso to CF_3'), 124.27 (q, J=31.38 Hz, C ipso to CF_3), 124.96 (s, CH meta to Pd'), 125.02 (s, CH meta to Pd), 135.55 (s, CH ortho to Pd'), 135.65 (s, CH ortho to Pd), 143.65 (s, quaternary aromatic), 143.68 (s, quaternary aromatic), 145.77 (s, quaternary aromatic), 145.84 (s, quaternary aromatic), 168.96 (s, C(O)N'), 169.00 (s, C(O)N), 181.73 (s, CO_2'), 181.79 (s, CO_2) **^{19}F NMR (470 MHz, CD_2Cl_2)** δ -61.975 (s), -61.986 (s).

Synthesis of [Pd(CF_3-dmba)(NAc-Leu)]$_2$ (6c)

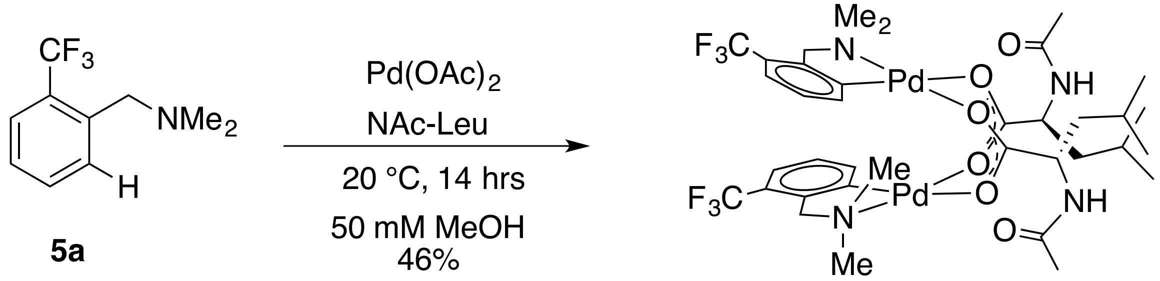

5a

6c

Figure 112: Synthesis of [Pd(CF_3-dmba)(NAc-Leu)]$_2$ (6c)

A 20 mL scintillation vial was charged with NAc-Leu (0.5 mmol, 86.5 mg, 1 equiv.), a stir bar, and 8 mL of methanol. The solution was stirred until the MPAA dissolved completely. To the MPAA solution was added solid $Pd(OAc)_2$ (0.5 mmol, 112 mg, 1 equiv.) and a solution of CF_3-dmba (102 mg, 0.5 mmol, 1 equiv.) in 2 mL MeOH. The orange suspension gradually turned to a yellow solution and developed the smell of acetic acid. The solution was stirred for 14 hours at room temperature after which a 200 µL aliquot was concentrated in vacuo and to analyzed by ^{19}F NMR which revealed complete consumption of starting material and 62% conversion to **6c**. Methanol was removed under a stream of nitrogen and the yellow solid filtered through a medium porosity frit with benzene (4x 3 mL). The yellow benzene solution was concentrated to c.a. 5 mL under a stream of nitrogen and layered with 5 mL of pentane. After 14 h of slow diffusion of pentane into the benzene solution, the supernatant was decanted and the solids washed with pentane to afford 106 mg (46%yield) **6c**. Single crystals suitable for x-ray diffraction were grown by layering 1 mL of 10 mM **6c** in CH_2Cl_2 with 1 mL PhMe followed by 2 mL n-heptane.

NMR (500 MHz, CD_2Cl_2) δ 0.98 (m, 12 H, Leu CH_3's), 1.51 (m, 4 H, Leu CH_2's), 1.68 (m, 2 H, Leu CH's), 2.00 (s, 3 H, NAc CH_3'), 2.04 (s, 3 H, NMe toward π face'), 2.07 (s, 3 H, NAc CH_3), 2.07 (s, 3 H, NMe toward π face), 2.78 (s, 3 H, NMe away from π face'), 2.80 (s, 3 H, NMe away from π face), 3.52 (m, 4 H, benzylic CH_2 + benzylic CH_2'), 4.44 (m, 1 H, Leu Hα'), 4.53 (m, 1 H, Leu Hα), 5.95 (d, J=8.55 Hz, 1 H, NH'), 6.04 (d, J=8.35 Hz, 1 H, NH), 7.10 (m, 3 H, CH ortho to Pd' + CH's meta to Pd), 7.28 (d, J=7.45 Hz, 1 H, CH ortho to Pd), 7.35 (d, J=7.50 Hz, 2 H, CH para to Pd + CH para to Pd') **^{13}C NMR (126 MHz, CD_2Cl_2)** δ 21.59 (s, Leu CH_3'), 22.91 (s, Leu CH_3), 22.94 (s, Leu CH_3), 23.04 (s, NAc CH_3'), 23.06 (s, NAc CH_3), 25.00 (s, Leu CH'), 25.02 (s, Leu CH), 42.41 (s, Leu CH_2'), 42.47 (s, Leu CH_2), 51.54 (s, NMe toward π face'), 51.60 (s,NMe toward π face), 52.68 (s, NMe away from π face'), 52.74 (s, NMe away from π face), 53.39 (s, Leu Cα'), 53.43 (s, Leu Cα), 70.27 (s, benzylic CH_2'), 70.29 (s, benzylic CH_2'), 121.74 (m, CH para to Pd + CH para to Pd'), 123.92 (q, J=273.34 Hz, CF_3'), 123.93 (q, J=273 Hz, CF_3), 124.15 (q, J=31.38 Hz, C ipso to CF_3'), 124.22 (q, J=31.10 Hz, C ipso to CF_3'), 124.82 (s, CH meta to Pd'), 124.98 (s, CH meta to Pd), 135.48 (s, CH ortho to Pd'), 135.84 (s, CH ortho to Pd), 143.61 (s, aromatic quaternary), 143.73 (s, aromatic quaternary),145.91 (s, aromatic quaternary), 146.02 (s, aromatic quaternary), 169.23 (s, C(O)N'),169.25 (s, C(O)N), 181.87 (s, CO_2'),181.90 (s, CO_2) **^{19}F NMR (470 MHz, CD_2Cl_2)** δ -61.944, -61.976

Synthesis of [Pd(CF$_3$-dmba)(NAc-Ile)]$_2$ (6d)

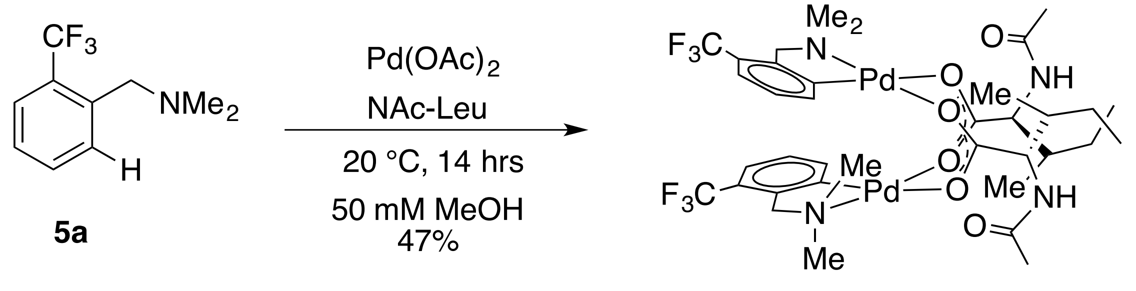

5a

6d

Figure 113: Synthesis of [Pd(CF$_3$-dmba)(NAc-Ile)]$_2$ (6d)

A 20 mL scintillation vial was charged with NAc-Ile (0.5 mmol, 86.5 mg, 1 equiv.), a stir bar, and 8 mL of methanol. The solution was stirred until the MPAA dissolved completely. To the MPAA solution was added solid Pd(OAc)$_2$ (0.5 mmol, 112 mg, 1 equiv.) and a solution of CF$_3$-dmba (102 mg, 0.5 mmol, 1 equiv.) in 2 mL MeOH. The orange suspension gradually turned to a yellow solution and developed the smell of acetic acid. The solution was stirred for 14 hours at room temperature after which a 200 µL aliquot was concentrated in vacuo and to analyzed by ^{19}F NMR which revealed complete consumption of starting material and 69% conversion to **6d**. Methanol was removed under a stream of nitrogen and the yellow solids were suspended in 2 mL diethyl ether. The suspension was transferred to a medium porosity frit and washed 2x 2 mL diethyl ether to remove residual acetic acid (note, the diethyl ether filtrate contains a substantial quantity of **6d**). The yellow solids on the frit were washed into a separate flask with 5 x 1 mL CH$_2$Cl$_2$ and precipitated by slow diffusion with 10 mL pentane at room temperature to afford 103.2 mg (47% yield) of **6d**.

^{1}H NMR (500 MHz, CD_2Cl_2) δ 0.89 (m, 6H, Ile Me + Me'), 0.95 (m, 6H, Ile Et-CH_3 + Et-CH_3'), 1.18 (m, 2H, Ile Et-CH^a_2 + Et-CH^a_2'), 1.44 (m, 2H, Ile Et-CH^b_2 + Et-CH^b_2'), 1.87 (m, 2H, Ile CH + CH'), 2.01 (s, 3H, NAc-CH_3'), 2.03 (s, 3H, NMe' toward π face), 2.04 (s, 3H, NMe toward π face), 2.06 (s, 3H, NAc-CH_3), 2.78 (s, 3H, NMe' away from π face), 2.81 (s, 3H, NMe away from π face), 3.55 (m, 4H, benzylic CH_2's), 4.40 (dd, J=5.0, 8.9 Hz, 1 H, Ile Hα'), 4.47 (dd, J=5.0, 8.9 Hz, 1 H, Ile Hα), 6.13 (t, J=8.9 Hz, 1H, NH'), 6.21 (t, J=8.9 Hz, 1H, NH), 7.09 (m, 3H, CH's meta to Pd + CH ortho to Pd'), 7.29 (d, J=7.40 Hz, 1H, CH ortho to Pd), 7.36 (d, J=7.45 Hz, 1H, CH para to Pd + CH para to Pd') **^{13}C NMR (126 MHz, CD_2Cl_2)** δ 11.48 (s, Ile Et-CH_3'), 11.49 (s, Ile Et-CH_3), 15.40 (s, Ile Me'), 15.43 (s, Ile Me), 23.12 (s, NAc-CH_3'), 23.13 (s, NAc-CH_3), 25.17 (s, Ile Et-CH_2'), 25.21 (s, Ile Et-CH_2), 38.20 (s, Ile-CH'), 38.25 (s, Ile-CH), 51.47 (s, NMe' toward π face), 51.71 (s, NMe' toward π face), 52.77 (s, NMe' + NMe away from π face), 59.13 (s, Ile Cα'), 59.31 (s, Ile Cα), 70.22 (s, benzylic CH_2'), 70.35 (s, benzylic CH_2), 121.82 (m, CH para to Pd + CH para to Pd'), 123.90 (q, J=273.57 Hz, CF_3 + CF_3'), 124.21 (q, J=32.0 Hz, C ipso to CF_3'), 124.31 (q, J=31.4 Hz, C ipso to CF_3), 124.85 (s, CH meta to Pd'), 124.99 (s, CH meta to Pd), 135.46 (s, CH ortho to Pd'), 135.82 (s, CH ortho to Pd), 143.54 (s, C aromatic quaternary), 143.68 (s, C aromatic quaternary), 145.73 (s, C aromatic quaternary), 145.77 (s, C aromatic quaternary), 169.04 (s, C(O)N'), 169.08 (s, C(O)N), 180.44 (s, CO_2'), 180.59 (s, CO_2) **^{19}F NMR (470 MHz, CD_2Cl_2)** δ -61.932, -61.967

Synthesis of [Pd(CF_3-dmba)(Cl)]$_2$ (8)

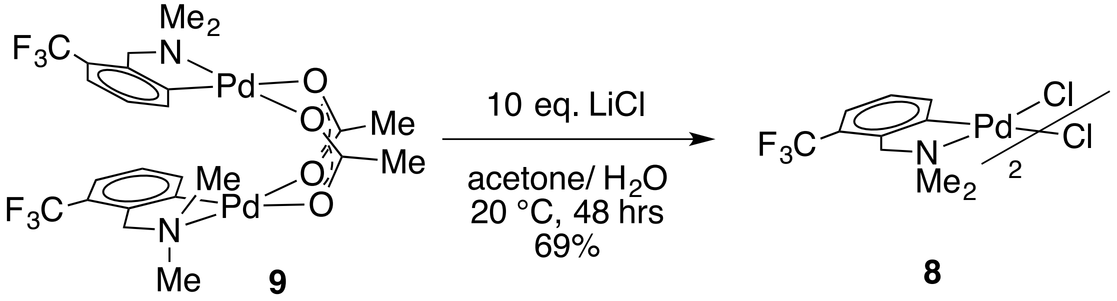

9 **8**

Figure 114 :Synthesis of [Pd(CF_3-dmba)(Cl)]$_2$ (8)

Chloride bridged dimer **8** was prepared by modification of a known procedure.[224] In 100 mL round bottom flask was with a magnetic stir bar, **9** (0.5 mmol, 382 mg, 1 equiv.) was dissolved in 20 mL acetone. The acetone solution was treated with 10 mL of aqueous lithium chloride (5.0 mmol, 212 mg, 10 equiv.) and flask was sealed with a rubber septum. After two days at room temperature, acetone was removed under reduced pressure to afford a yellow solid which was washed with 3x10 mL water. The yellow solid was washed through a medium porosity frit with diethyl ether, which was concentrated to c.a. 3 mL under a stream of nitrogen and layered with pentane to afford 475 mg (69% yield) of **8** as a mixture of two isomers (as has been previously noted for analogous chloride bridged dmba palladacycles).[224]

^{1}H NMR (500 MHz, CD_2Cl_2) δ 2.89 (s, 6 H), 2.90 (s, 6 H), 4.14 (m, 4 H), 7.04 (t, J=7.75 Hz, 2 H), 7.34 (d, J=7.70 Hz, 2 H), 7.40 (m, 2 H) **^{13}C NMR (126 MHz, CD_2Cl_2)** δ 52.86 (s), 53.05 (s), 70.98 (s), 71.21 (s), 121.82 (q, J=5.12 Hz), 123.98 (q, J=273.21 Hz), 124.13 (q, J=31.19 Hz), 124.91 (s), 125.03 (s), 136.76 (s), 137.09 (s), 144.06 (m), 145.38 (s) **^{19}F NMR** (470 MHz, CD_2Cl_2) δ -61.646 (s), -61.682 (s)

Milani, J.; Pridmore, N. E.; Whitwood, A. C.; Fairlamb, I. J. S.; Perutz, R. N. Organometallics 2015, 34 (17), 4376.

Synthesis of Pd(CF_3-dmba)(acac) (7)

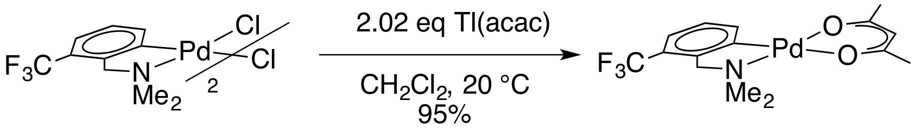

8

7

Figure 115: Synthesis of Pd(CF_3-dmba)(acac) (7)

The acac complex **7** was prepared by modification of a known procedure.[172] In an inert atmosphere glove box, a 20 mL scintillation vial equipped with a magnetic stirrer was dissolved complex **8** (306 mg, 0.445 mmol, 1 equiv.) in 5 mL CH_2Cl_2. To this solution was added solid thallium acetonylacetonate (0.898 mmol, 273 mg, 2.02 equiv.). A white solid precipitated immediately and the suspension was stirred for 1 hour after which the suspension was passed over a medium porosity frit, washed with CH_2Cl_2 3x 3 mL and concentrated under reduced pressure to afford **7** 345 mg (95% yield).

^{1}H NMR (500 MHz, CD_2Cl_2) δ 2.01 (s,3 H), 2.05 (s,3 H), 2.87 (s,6 H), 4.10 (s,2 H), s,1 H), 7.11 (t, J=7.63 Hz, 1 H), 7.32 (d, J=7.70 Hz, 1 H), 7.53 (d, J=7.65 Hz, 1 H) **^{13}C NMR (126 MHz, CD_2Cl_2)** δ 27.22 (s), 27.77 (s), 51.85 (s), 71.16 (q, J=2.05 Hz), 99.92 (s), 121.18 (q, J=5.34 Hz), 123.38 (q, J=30.56 Hz), 124.48 (q, J=271.15 Hz), 134.66 (m), 144.09 (m), 148.98 (s), 186.26 (s), 188.45 (s) **^{19}F NMR (470 MHz, CD_2Cl_2)** δ -61.541

Synthesis of CF_3-dmba (5a)

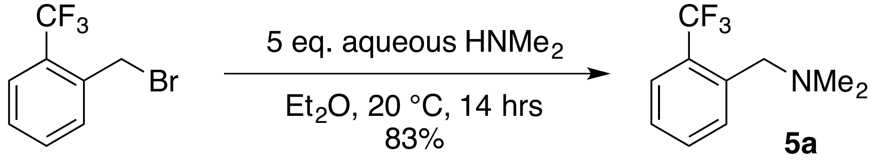

Figure 116: Synthesis of CF_3-dmba (5a)

5a was prepared by a previously reported procedure with minor modification.[225] To a 500 mL round bottom flask equipped with a magnetic stir bar was added the benzylic bromide (100.4 mmol, 24g, 1 equiv.) and 100 mL diethyl ether. To the ethereal solution was added aqueous dimethylamine (502 mmol, 56.5g (40 wt%), 5 equiv.). The heterogeneous mixture was stirred for 14 h at room temperature, after which the organic phase was separated and extracted 3 times with 10 wt% aqueous citric acid. The combined aqueous phases were treated with 15 wt% aqueous sodium hydroxide and extracted 3 times with diethyl ether. The ethereal extracts were concentrated under reduced pressure and the clear liquid was further purified by short path distillation (0.08 mmHg, 60 °C) into a receiving flask cooled to -10 °C to afford 16.86g (83% yield) of **5a**.

^{1}H NMR (**500 MHz, CD_2Cl_2**) δ 2.31 (s, 6H, NMe_2), 3.64 (s, 2H, CH_2), 7.39 (t, J=7.63 Hz, H^c), 7.59 (t, J=7.58 Hz, H^b), 7.68 (d, J=7.85 Hz, H^d), 7.85 (d, J=7.80 Hz, H^a) **^{13}C NMR (126 MHz, CD_2Cl_2)** δ 45.29 (s, NMe_2), 59.51 (q, J=1.72 Hz, CH_2), 124.63 (q, J=271.19 Hz, CF_3), 125.50 (q, J=5.89 Hz, CH ortho to CF_3), 126.65 (s, CH para to CH_2), 128.22 (q, J=29.97 Hz, C ipso to CF_3), 130.52 (s, CH ortho to CH_2), 131.78 (m, CH para to CF_3), 138.69 (q, J=1.47 Hz, C ipso to CH_2) **^{19}F NMR** (470 MHz, $CDCl_3$) δ -59.04

Tayama, E.; Kimura, H. Angew. Chem. Int. Ed. 2007, 46 (46), 8869.

Synthesis of Cl-CF$_3$-dmba (5b)

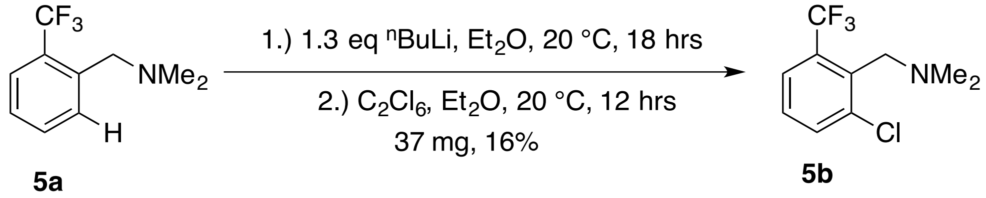

Figure 117: Synthesis of Cl-CF$_3$-dmba (5b)

A 25 mL round bottom flask equipped with a magnetic stir bar and septum was evacuated and refilled with nitrogen 3 times. To the flask, under nitrogen, was added **5a** (1 mmol, 203 mg, 1 equiv.) and 2.5 mL anhydrous diethyl ether. To the ethereal solution, n-butyl lithium (1.3 mmol, 0.845 mL (1.54M), 1.3 equiv.) was added drop-wise. The mixture was stirred under nitrogen for 18 hours at room temperature. Hexachloroethane (1.3 mmol, 308 mg, 1.3 equiv.) was added drop-wise under nitrogen as a solution in 5 mL anhydrous diethyl ether. The mixture was stirred for 12 hours under nitrogen and quenched under air with 2 grams of silica gel slurried in 5 mL of diethyl ether. The volatiles were removed under reduced pressure and the solids were loaded onto a silica gel column. Eluting with a gradient from 1-5% diethyl ether in hexanes gave two pure fractions which were combined and concentrated to give **5b** 37 mg (16% yield).

^{1}H NMR (500 MHz, CDCl$_3$) δ (s, 6H, NMe$_2$), 3.70 (s, 2H, CH$_2$), 7.34 (t, J=8.0 Hz, CH meta to CF$_3$), 7.61 (d, J=8.0 Hz, CH para to CF$_3$ + CH ortho to CF$_3$) **^{13}C NMR (126 MHz, CDCl$_3$)** δ 45.33 (s, NMe$_2$), 56.38 (s, CH$_2$), 123.82 (q, J=274.71 Hz, CF$_3$), 124.79 (q, J=6.05 Hz, CH ortho to CF$_3$), 128.19 (s, CH meta to CF$_3$),131.47 (q, J=29.73 Hz, C ipso to CF$_3$), 133.68 (s, CH para to CF$_3$), 136.04 (s, aromatic C quaternary),138.16 (s, aromatic C quaternary) **^{19}F NMR (470 MHz, CDCl$_3$)** δ -57.26

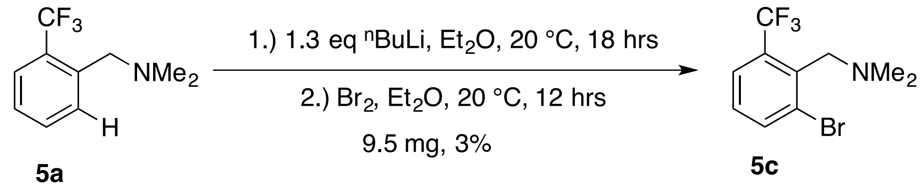

Figure 118: Synthesis of Br-CF_3-dmba (5c)

A 25 mL round bottom flask equipped with a magnetic stir bar and septum was evacuated and refilled with nitrogen 3 times. To the flask, under nitrogen, was added **5a** (1 mmol, 203 mg, 1 equiv.) and 2.5 mL anhydrous diethyl ether. To the ethereal solution, n-butyl lithium (1.3 mmol, 0.845 mL (1.54M), 1.3 equiv.) was added drop-wise. The mixture was stirred under nitrogen for 18 hours at room temperature. Bromine (1.3 mmol, 208 mg, 67µL, 1.3 equiv.) was added drop-wise under nitrogen. The mixture was stirred for 12 hours under nitrogen, quenched with 1 mL water, and acidified with 5 mL 2M HCl. The aqueous fraction was basified with 2M NaOH and extracted 3x with 5 mL diethyl ether. To the ethereal extracts was added 2g of celite and the solvent was removed under reduced pressure. The celite pad was loaded on a silica gel column which was eluted with a gradient from 1-10% diethyl ether in hexanes. Three pure fractions were obtained as assayed by GCMS and were combined to give **5c** 9.5 mg (3% yield).

^{1}H NMR (500 MHz, $CDCl_3$) δ 2.31 (s, 6H, NMe_2), 3.70 (s, 2H, CH_2), 7.25 (t, J=7.9 Hz, 1 H), 7.66 (d, J=7.9 Hz, 1 H), 7.82 (d, J=7.9 Hz, 1 H) **^{13}C NMR (126 MHz, $CDCl_3$)** δ 45.17 (s, NMe_2), 58.55 (s, CH_2), 123.44 (q, J=32.12 Hz, C ipso to CF_3), 123.70 (q, J=280.88 Hz, CF_3), 125.41 (q, J=6.02 Hz, CH ortho to CF_3), 128.37 (s, aromatic C quaternary), 128.69 (s, aromatic C quaternary), 128.81 (s, aromatic C quaternary), 137.20 (s, aromatic CH) **^{19}F NMR (470 MHz, $CDCl_3$)** δ -57.12

Synthesis of I-CF_3-dmba (5d)

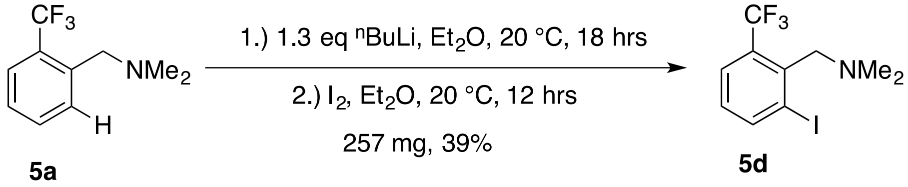

Figure 119 Synthesis of I-CF3-dmba (5d)

A 25 mL round bottom flask equipped with a magnetic stir bar and septum was evacuated and refilled with nitrogen 3 times. To the flask, under nitrogen, was added **5a** (2 mmol, 406 mg, 1 equiv.) and 5 mL anhydrous diethyl ether. To the ethereal solution, n-butyl lithium (2.6 mmol, 1.69 mL (1.54M), 1.3 equiv.) was added drop-wise. The mixture was stirred under nitrogen for 18 hours at room temperature. Iodine (2.6 mmol, 660 mg, 1.3 equiv.) was added drop-wise under nitrogen as a solution in 5 mL anhydrous diethyl ether. The mixture was stirred for 12 hours under nitrogen and quenched under air with 2 grams of silica gel suspended in 5 mL of diethyl ether. The volatiles were removed under reduced pressure and the solids were loaded onto a silica gel column. Eluting with a 5% triethylamine in hexanes gave two pure fractions which were combined and concentrated to give **5d** 257 mg (39% yield).

^{1}H NMR (500 MHz, $CDCl_3$) δ 2.29 (s, 6H, NMe_2), 3.64 (s, 2H, CH_2), 7.05 (t, J=7.9 Hz, 1 H), 7.67 (d, J=7.9 Hz, 1 H), 8.12 (d, J=7.9 Hz, 1 H) **^{13}C NMR (126 MHz, $CDCl_3$)** δ 44.80 (s, NMe_2), 61.93 (d, J=1.48 Hz, CH_2), 104.27 (q, J=4.1 Hz, aromatic quaternary), 123.72 (q, J=275.04 Hz, CF_3), 125.97 (q, J=6.10 Hz, CH ortho to CF_3), 128.39 (s,1 CH meta to CF_3), 130.56 (q, J=29.82 Hz, C ipso to CF_3), 140.06 (s, aromatic quaternary), 144.27 (d, J=1.01 Hz, CH para to CF_3) **^{19}F NMR (470 MHz, $CDCl_3$)** δ -56.94

Iodination

To an NMR tube was added a stock solution in CD2Cl2 of 6b (7.5 mM, 500 µL, 3.75 µmol), followed by a stock solution in CH2Cl2 of S1.3 (30 mM, 50 µL, 1.5 µmol), followed by a stock solution in CH2Cl2 of iodine (37.5 mM, 200 µL, 7.5 µmol, 2 equiv.). The tube was capped, shaken, and left at room temperature for 17 h at which time it was analyzed by 19F NMR and the concentration of the desired product was determined with respect to S1.3. The formation of the 5d was confirmed by spiking independently synthesized 5d into the mixture. GCMS analysis of the reaction mixture showed one major product which had the same m/z and retention time as independently synthesized 5d.

Bromination

To an NMR tube was added a stock solution in CD_2Cl_2 of **6b** (7.5 mM, 500 µL, 3.75 µmol), followed by a stock solution in CH_2Cl_2 of **S1.3** (30 mM, 50 µL, 1.5 µmol), followed by a stock solution in CH_2Cl_2 of bromine (22.5 mM, 200 µL, 4.5 µmol, 1.2 equiv.). The tube was capped, shaken, and left at room temperature for 17 h at which time it was analyzed by ^{19}F NMR and the concentration of the desired product was determined with respect to **S1.3**. GCMS analysis of the reaction mixture showed one major product which had the same m/z and retention time as independently synthesized **5c**.

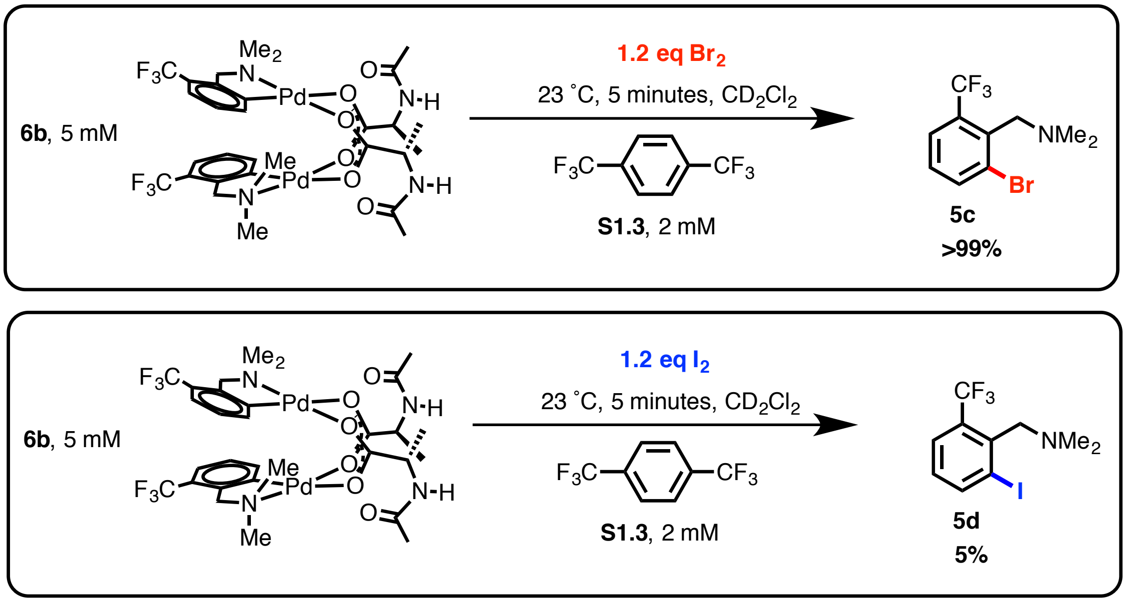

Figure 120 Reaction conditions for relative rates of iodination and bromination

To an NMR tube was added a stock solution in CD_2Cl_2 of **6b** (7.5 mM, 500 µL, 3.75 µmol) followed by a stock solution in CH_2Cl_2 of **S1.3** (30 mM, 50 µL, 1.5 µmol). The tube was sealed with a rubber septum, brought to the NMR spectrometer, locked, and shimmed. The sample was ejected from the spectrometer, and through the rubber septum was injected a stock solution in CH_2Cl_2 of X_2 (X=Br or I) (22.5 mM, 200 µL, 4.5 µmol, 1.2 equiv.). The sample was shaken and lowered into the spectrometer immediately. The reaction was monitored by ^{19}F NMR at 15 second intervals over 20 minutes the concentration of the desired products was determined with respect to **S1.3**.

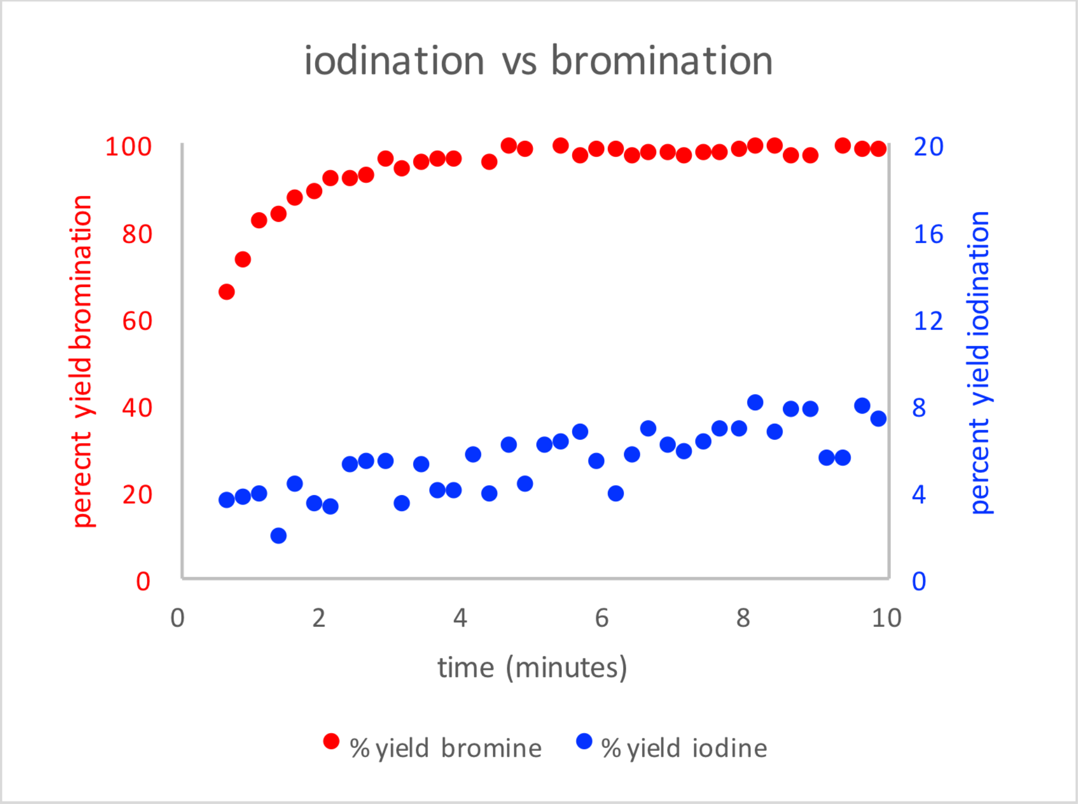

Figure 121 Reaction profiles for iodination and bromination, note separate axes

Chlorination with two equivalents iodobenzenedichloride

To an NMR tube was added a stock solution in CD_2Cl_2 of **6b** (7.5 mM, 500 µL, 3.75 µmol), followed by a stock solution in CH_2Cl_2 of **S1.3** (30 mM, 50 µL, 1.5 µmol), followed by a stock solution in CH_2Cl_2 of iodobenzene dichloride (37.5 mM, 200 µL, 7.5 µmol, 2 equiv.). The tube was capped, shaken, and left at room temperature for 30 minutes at which time it was analyzed by ^{19}F NMR and the concentration of the desired product was determined with respect to **S1.3**. GCMS analysis of the reaction mixture showed one major product which had the same m/z and retention time as independently synthesized **5b**.

Chlorination with five equivalents iodobenzenedichloride

To an NMR tube was added a stock solution in CD_2Cl_2 of **6b** (7.5 mM, 500 µL, 3.75 µmol), followed by a stock solution in CH_2Cl_2 of **S1.3** (30 mM, 50 µL, 1.5 µmol), followed by a stock solution in CH_2Cl_2 of iodobenzene dichloride (93.75 mM, 200 µL, 18.75 µmol, 5 equiv.). The tube was capped, shaken, and left at room temperature for 30 minutes at which time it was analyzed by ^{19}F NMR and the concentration of the desired product was determined with respect to **S1.3**. Further monitoring of the reaction mixture revealed decreasing concentration of **5b** and a new species developing. The mixture was transferred to a 1 dram vial and left uncapped overnight. Slow evaporation of CH_2Cl_2 afforded singled crystals of a know coordination polymer with the formula $PdCl_2$ + HCl + $HNMe_2$.

Olefination in trifluoroethanol

MPAA complex **2** (10 µmol, 7.1 mg, 1 equiv.) was weighed into a 1 mL vial and transferred as a solid into an NMR tube with a J. Young cap, vial was washed with two 250 µL portion of trifluoroethanol. Internal standard1,2,4,5-tetrachloro-benzene (10 µmol, 2.15 mg, 1 equiv.) was added to the NMR tube in the same way. n-Butyl acrylate (400 µmol, 51.3 mg, 57 µL, 40 equiv.) was added by gas tight syringe. The J. Young cap was sealed and the tube placed in an 80 °C oil bath. The reaction was monitored hourly, but precipitation of Pd black led to poor line shapes. After 4 hours, the sample was removed from the oil bath, transferred to a 20 mL scintillation vial and the volatiles were removed under reduced pressure. The reaction mixture was dissolved in $CDCl_3$ and the yield of **14** was determined by ^{1}H NMR (which matched the spectrum for this compound reported in the literature, see ref. 16) by integration of the most downfield proton with respect to internal standard.

Olefination in 1,2-dichloroethane

MPAA complex **2** (10 µmol, 7.1mg, 1 equiv.) was weighed into a 1 mL vial and transferred as a solid into an NMR tube with a J. Young cap, vial was washed with two 250 µL portion of 1,2-dichloroethane. Internal standard 1,2,4,5-tetrachloro-benzene (10 µmol, 2.15 mg, 1 equiv.) was added to the NMR tube in the same way. n-Butyl acrylate (400 µmol, 51.3 mg, 57 µL, 40 equiv.) was added by gas tight syringe. The J. Young cap was sealed and the tube placed in an 80 °C oil bath. The reaction was monitored hourly, but precipitation of Pd black led to poor line shapes. After 42 hours, the sample was removed from the oil bath, transferred to a 20 mL scintillation vial and the volatiles were removed under reduced pressure. The reaction mixture was dissolved in $CDCl_3$ and the yield of **14** was determined by ^{1}H NMR by integration of the most downfield proton with respect to internal standard.

Chapter 6: Mono-Protected Amino Acid Ligands Accelerate Enantioselective C-H Activation and Palladium Catalyzed C-H Olefination via Bimetallic Transition States

Preface

This work was conducted in collaboration with Brandon Haines and Djamaladdin Musaev at the Cherry L. Emerson Center for Scientific Computation, Emory University. A manuscript of this work is in preparation. The full computational and experimental methods will be included in the supporting information of the published manuscript.

Introduction

Mono-protected amino acid (MPAA) ligands have enabled remarkable advances in palladium-catalyzed C-H functionalization as a result of their ability to enhance reaction rates and to impart enantioselectivity to a range of transformations.[158,205,226-231] Pioneering efforts in enantioselective cyclopalladation (Figure 122A)[194] and C-H functionalization (Figure 122B)[232] leveraged chelate assistance to achieve site selectivity; however, subsequent studies have shown that Pd-MPAA mixtures can catalyze C-H functionalization even on substrates lacking directing groups (Figure 122C).[233] This non-directed reactivity holds great promise for the design of catalysts that mimic enzymatic C-H functionalization. Specifically, if a Pd-MPAA catalyst could be constrained within a supramolecular scaffold, then catalyst selectivity could be controlled via non-covalent interactions in the secondary coordination sphere.[9,12,234-239] Developing such hybrid catalysts, however, requires a detailed understanding of the discrete Pd-MPAA complexes involved in catalysis.

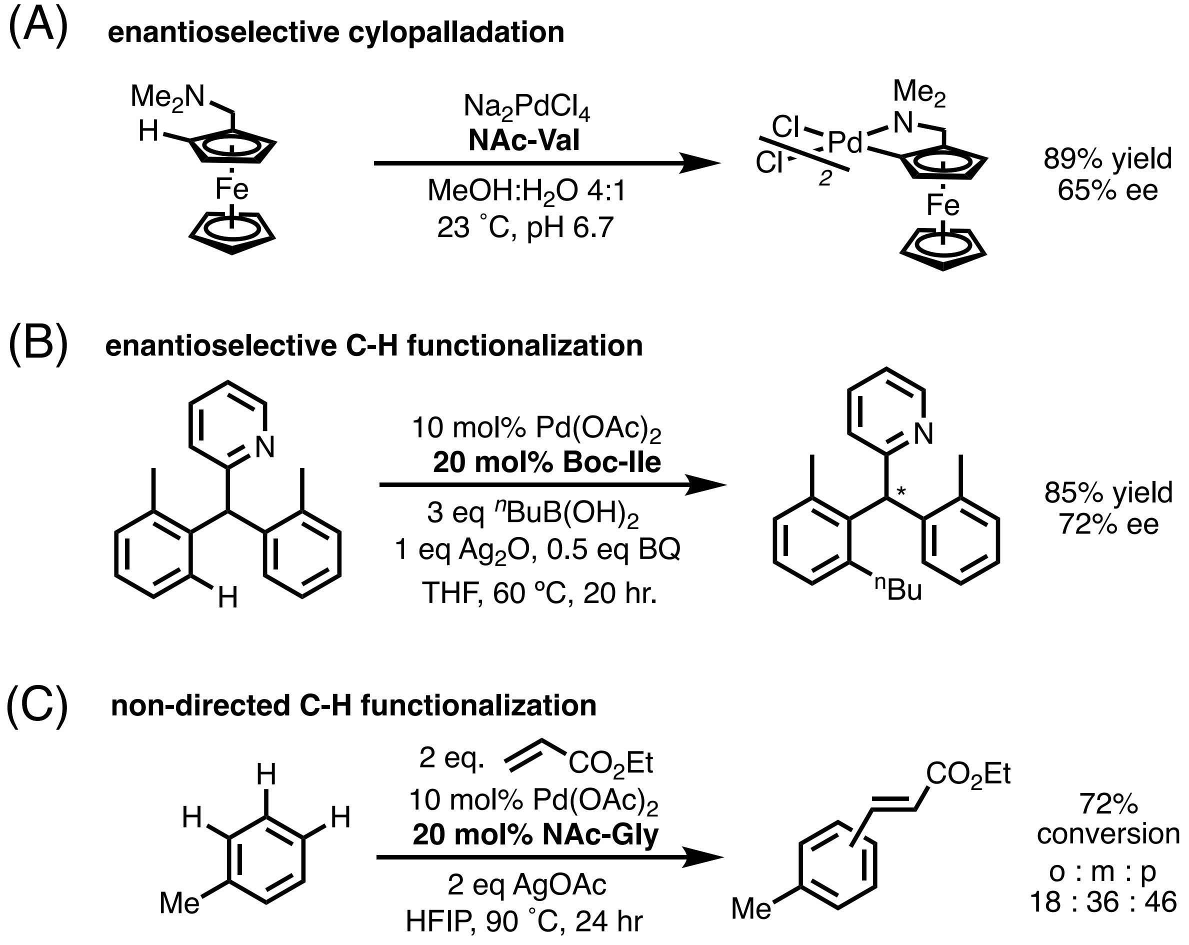

Figure 122. (A) MPAA induced, enantioselective cyclopalladation;[194] (B) Pd-MPAA catalyzed enantioselective C-H functionalization;[232] (C) Pd-MPAA catalyzed non-directed C-H functionalization.[233]

Despite the many exciting developments in Pd-MPAA methodology and several experimental and computational studies aimed at understanding these reactions, the structural basis of Pd-MPAA catalysis remains unclear in most cases. In a notable exception to this trend, a recent kinetic and spectroscopic study of MPAA-accelerated C-H iodination reactions proposed a model featuring Pd(IV) intermediates with di-anionic κ^2-(N,O)-bound MPAA ligands (Figure 123B).[152,154,240,241] No detailed experimental studies on the structure of Pd(II)-MPAA catalysts have been reported. Given this structural ambiguity, mechanistic models of Pd-MPAA catalysis generally defer to the widely-held notion that MPAA ligands coordinate monomeric intermediates by mono or di-anionic chelation (Figure 123C and B, respectively).

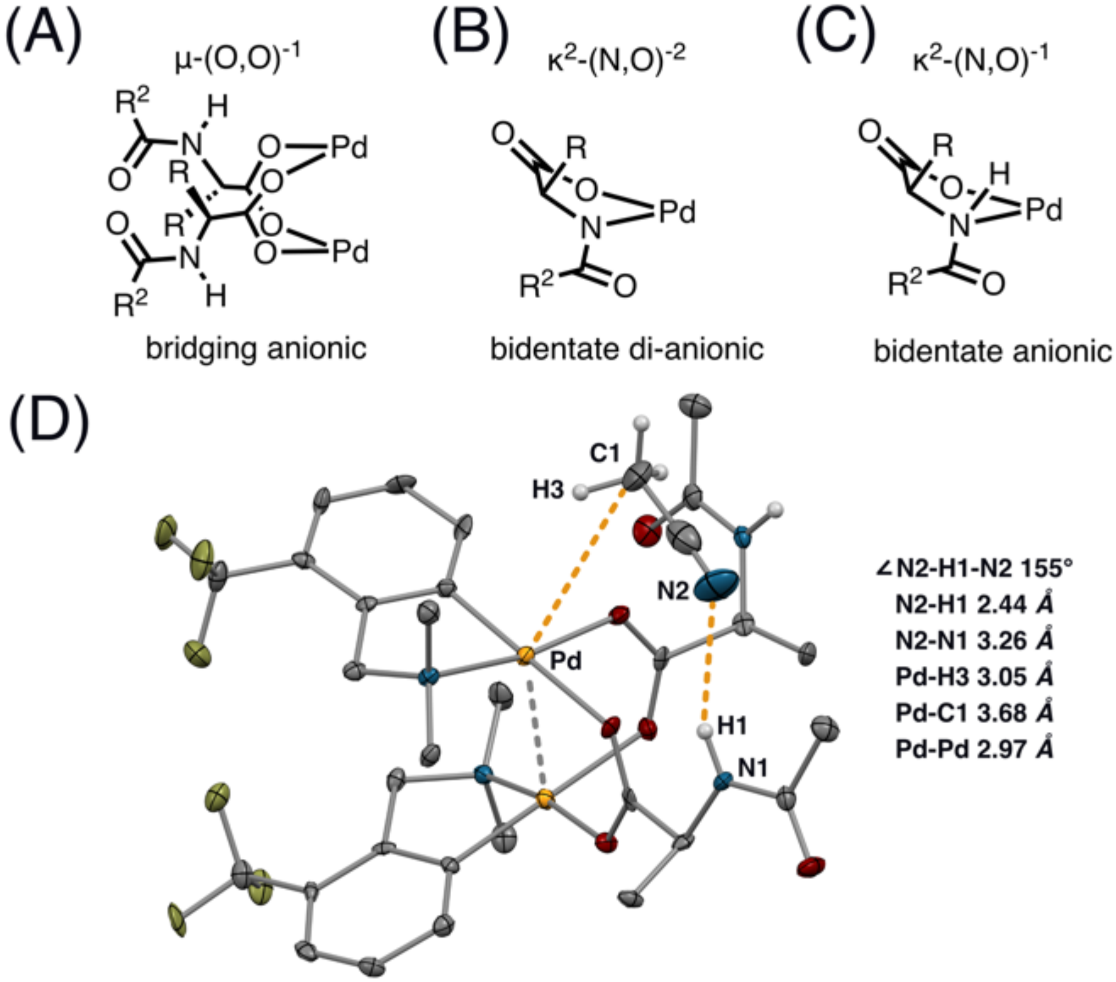

Figure 123 (A) MPAA bridged dimers observed in model palladacycles; (B) bidentate di-anionic MPAA coordination observed in Pd(IV) catalysis; (C) originally proposed bidentate anionic coordination;[242] (D) hydrogen-bonding interactions in the secondary coordination sphere of a previously reported MPAA palladacycle.[243]

Interestingly, bidentate MPAA coordination was originally proposed[232] based on a mischaracterized model from the literature[242] that was later shown by our groups to be a MPAA-bridged μ-(O,O) dimer (Figure 123A).[243] Our study more generally demonstrated that *N*,*N*-dimethybenzylamine (dmba) palladacycles generated in the presence of different MPAAs exist as carboxylate-bridged dimers (Figure 123A) in both the solid state and in solution.[243] The solid state structures of these complexes (Figure 123D), in conjunction with reports that metal-metal bonding may lower barriers involving di-palladium catalysts,[180,181,213,214,244-247] led us to hypothesize that Pd-MPAA catalysts might benefit from bimetallic cooperativity or secondary sphere hydrogen bond catalysis (Figure 123D). Isolated dimeric MPAA-bridged Pd complexes proved to be kinetically competent pre-catalysts and were observed as both the reactants and products of stoichiometric cyclopalladation.[243] This study did not, however, address the transition state of cyclopalladation leading to the observed dimers, the nuclearity of the active catalyst in MPAA promoted C-H functionalization, or the mechanisms by which MPAA ligands accelerate and enable enantioselective C-H functionalization. Insights into these questions of fundamental reactivity are essential for understanding MPAA rate acceleration and for defining discrete (pre)catalyst structures that could be incorporated into supramolecular scaffolds.

To determine whether bimetallic species contribute to the rate acceleration and enantioselectivity observed in Pd-MPAA catalysis, we transitioned from studying dmba palladacycles to related, prochiral substrates since enantioselective functionalization of these compounds provides a convenient readout (ee) of contributions from MPAA ligands on catalysis (Figure 124). Since the seminal report of MPAA-promoted enantioselective cyclopalladation[194] (Figure 122A), *N,N*-dimethylaminomethyl-ferrocene (dmaf) has been employed in numerous Pd-MPAA catalyzed enantioselective C-H functionalization reactions[192,193,248-251] and has served as a model substrate for computational[164] and synthetic[196,197,252-254] studies of MPAA-induced, enantioselective cyclopalladation.[255-258]

In light of its broad impact in the field of Pd-MPAA catalysis, dmaf was chosen as a substrate to study the species and pathways through which MPAA ligands promote activity and selectivity (igure 74A). To complement our studies of Pd-MPAA catalyzed C-H *functionalization*, the kinetics of MPAA-accelerated C-H *activation* of benzhydryl-pyridines (bhp, **3**) were also examined (Figure 124B). These studies establish the importance of bimetallic intermediates ($Pd_2MPAA_1X_1$, where X=acetate or MPAA and exerts minimal energetic influence) in MPAA-accelerated C-H functionalization and provide insight into the mechanisms by which MPAA ligands enhance the activity and selectivity of Pd(II) catalysts for C-H activation and functionalization. Beyond these insights into fundamental reactivity, this work sets the stage for the design of catalysts that exploit the non-directed reactivity of Pd-MPAA intermediates to selectively functionalize remote C-H bonds via outer sphere molecular recognition.[2,6,259-262]

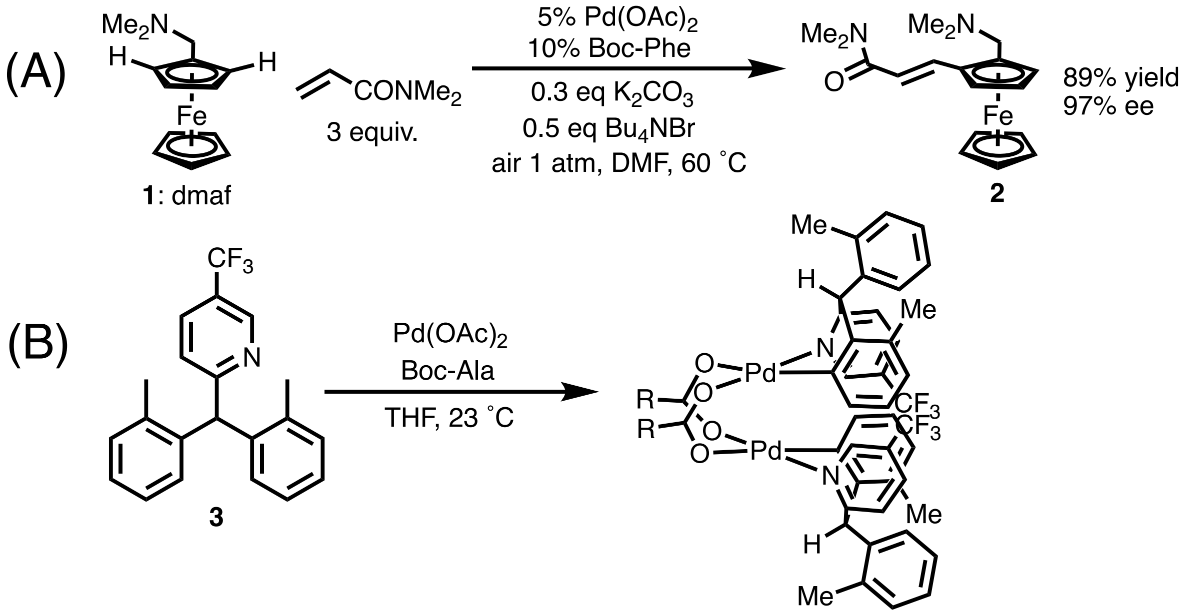

Figure 124. Reactions studied in this work: (A) Pd-MPAA catalyzed, enantioselective C-H olefination of dmaf and (B) enantioselective cylopalladation of bhp.

Structure and Speciation of dmaf Palladacycles

A detailed study of the structure and speciation of relevant MPAA-palladacycles served as a starting point for investigating the role of MPAA ligands in palladium catalyzed C-H functionalization. As in our previous work, single crystal x-ray diffraction (SXRD) revealed that dmaf palladacycles exist as carboxylate-bridged dimers in the solid state for complexes $[Pd(dmaf)(OAc)]_2$ (**4**) and $[Pd(dmaf)(NAc\text{-}Gly)]_2$ (**5**, Figure 125A), similar to those reported previously.[243] Both **4** and **5** crystallize as racemic, homo-chiral dimers with matched planar chirality between both dmaf ligands and axial chirality about the bimetallic unit (Figure 125A, *MSS* and *PRR*, the stereodescriptors M/P and R/S are used throughout to differentiate axial and planar chirality, respectively).

Characterization of these complexes in solution commenced with the acetate-bridged complex $[Pd(dmaf)(OAc)]_2$ (**4**) because acetate is present under catalytic conditions (from $Pd(OAc)_2$) and may contribute to background reactivity (*vide infra*) by competing with MPAA to coordinate the active catalyst. The solution structure of **4** at concentrations and temperatures used for catalysis in dimethylformamide (DMF) matches the solid-state structure as determined by diagnostic shielding due to magnetic anisotropy and corresponding NOE correlations. The presence of one diastereomer by ^{1}H NMR (*MSS* + *PRR*) is in sharp contrast to the chloride bridged dimer (a statistical ensemble of stereoisomers)[252] and illustrates the ability of bridging carboxylate ligands to enforce a rigid chiral environment composed of three complimentary stereogenic units. The bimetallic nature of **4** in DMF was confirmed using the structural method of continuous variation (MCV).[189] Mixtures of AA (**4**) and BB (**6**) with constant total concentration and varying ratios gave rise to a third species (AB), the concentration of which was maximized at a ratio of 1:1 A:B (Figure 125B and C). The speciation observed in Figure 125C is characteristic of an ensemble of dimers and supports the spectroscopic evidence which indicate that [Pd(dmaf)(OAc)]$_2$ (**4**) exists as an acetate bridged dimer in DMF solution. Beyond demonstrating the aggregation state of **4** in solution, MCV provides additional insight into the stereochemistry of dimeric palladacycles with bridging carboxylate ligands; specifically, the exclusive formation of one heteroaggregate (AB) diastereomer illustrates that, even with one stereogenic unit removed (relative to **4**), the axial chirality of the bimetallic unit diligently differentiates the planar chirality of the dmaf substrate.

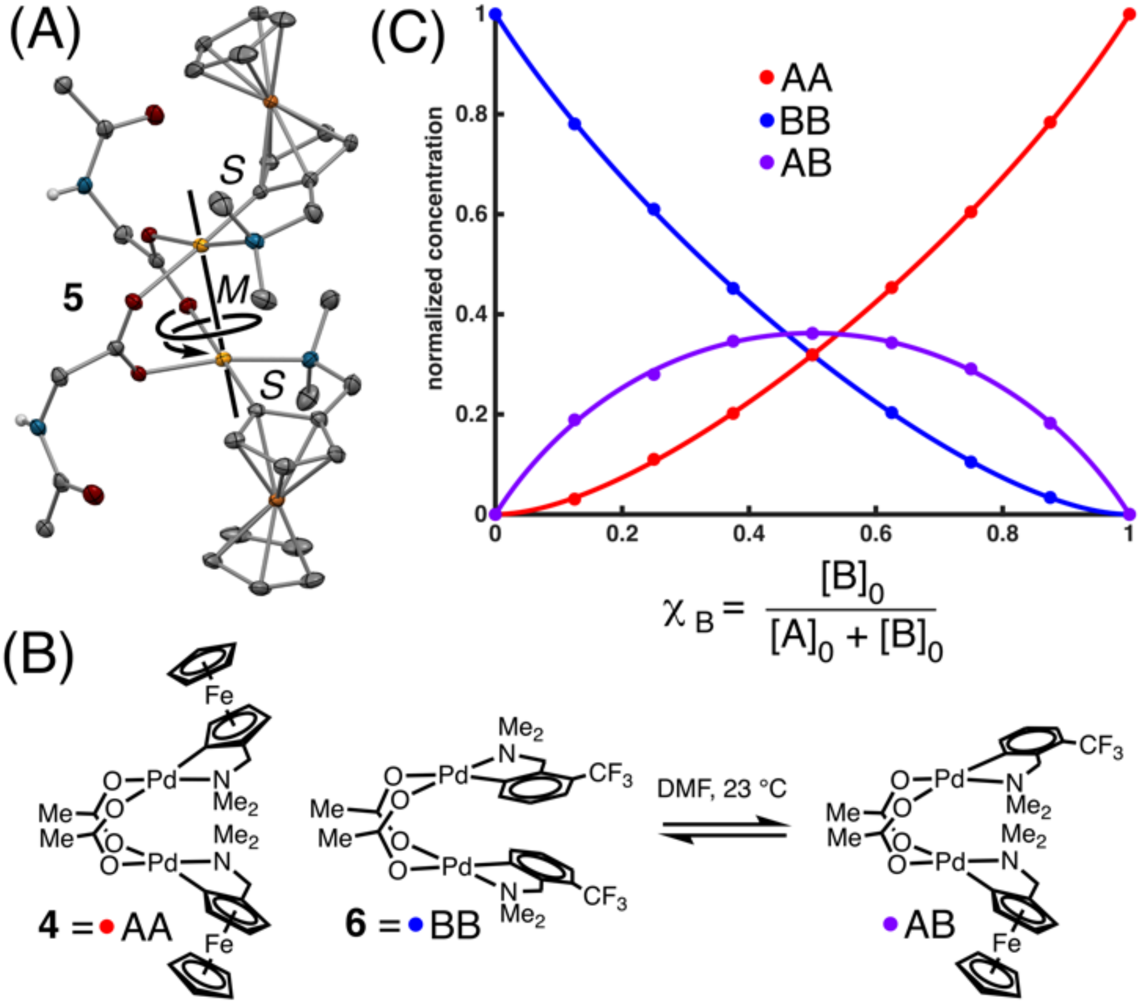

Figure 125. (A) Solid state structure of $[Pd(dmaf)(NAc\text{-}Gly)]_2$ (**5**) (*SSM* enantiomer shown, chiral axis drawn for clarity); (B) ensemble of dimers observed by structural method of continuous variation (C); distribution observed by structural MCV with parametric fits to model an ensemble of dimers.[189]

We next sought to evaluate how MPAA ligands modulate the structure and speciation of dmaf palladacycles in solution. Similar to our previous work,[243] titration of L-Boc-Ala into a DMF solution of **4** revealed diastereomeric Pd_2MPAA_1 complexes at low MPAA loading that were subsequently consumed to form diastereomeric Pd_2MPAA_2 complexes at higher MPAA loading (Figure 126, throughout, stereodescriptors L/D distinguish MPAA central chirality from dmaf planar chirality).[263] The MPAA N-H resonances were the best resolved peaks in the ensemble, however, all four MPAA complexes also revealed diagnostic, upfield N-Me resonances suggesting that the entire ensemble exists as dimers in DMF. Although chirality at the organometallic fragment (Pd_2dmaf_2) was sufficiently differentiating to resolve the secondary sphere N-H chemical shifts, the energetic difference between diastereomers upon MPAA binding was negligible as demonstrated by their equal populations within each pair of diastereomers (Pd_2MPAA_2 and Pd_2MPAA_1). Notably, resolution of bimetallic enantiomers does not depend on the planar chirality of dmaf substrates; rather, as a consequence of the axial chirality of the bimetallic unit. When the titration was conducted with racemic Boc-Ala, identical $Pd_2MPAA_1OAc_1$ diastereomers formed; however, Pd_2MPAA_2 diastereomers were accompanied by additional species with broken C_2 symmetry, consistent with mixed Pd_2(*L-Ala*)(*D-Ala*).In addition to the observed speciation and diagnostic N-Me shielding, the dimeric nature of these complexes was confirmed with pulse gradient spin echo experiments (PGSE) on the products of titrations with Boc-Gly, Boc-Ala, and Boc-Phe, which were then compared to the isolated dimer **4** and an isolated, monomeric dmaf-palladacycle.

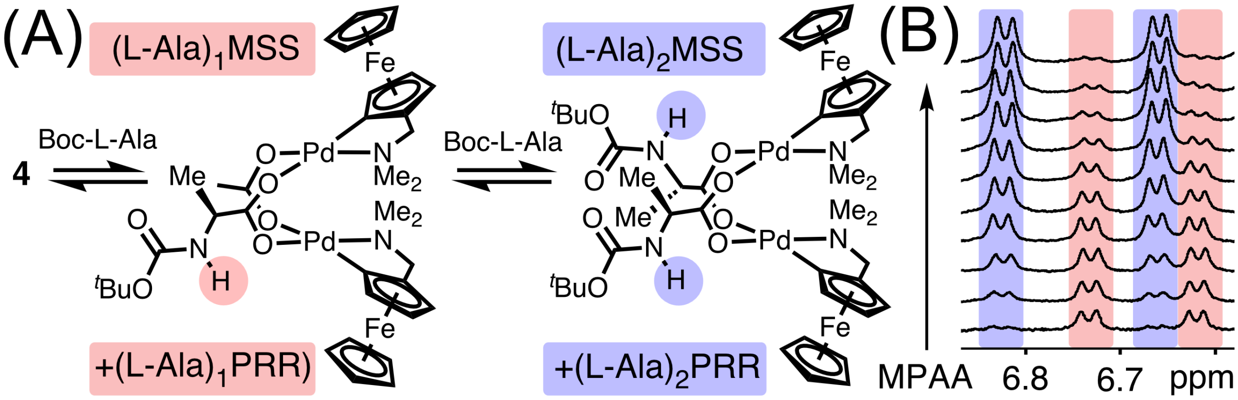

Figure 126: (A) Titration of MPAA into a DMF solution of **4** gives an ensemble of MPAA palladacyles; (B) ^{1}H NMR spectra of MPAA titration reveals sequential substitutions giving rise to diastereomeric bimetallic species bearing one (red) and two (blue) MPAA ligands.

Although dmaf palladacycles exist as carboxylate-bridged bimetallic species in DMF, a bridge-splitting equilibrium with the monomer **7** takes places in the presence of excess dmaf (Figure 127). At the same temperature and concentration used in catalysis, complex (**7**) accounts for approximately half of the total palladium loading as assessed by ^{1}H NMR. The stoichiometry of the bridge splitting complex was confirmed with MCV and is consistent with the bridge splitting equilibria observed with isolated dimers[224,264] and in systems with bimetallic active catalysts.[180,244]

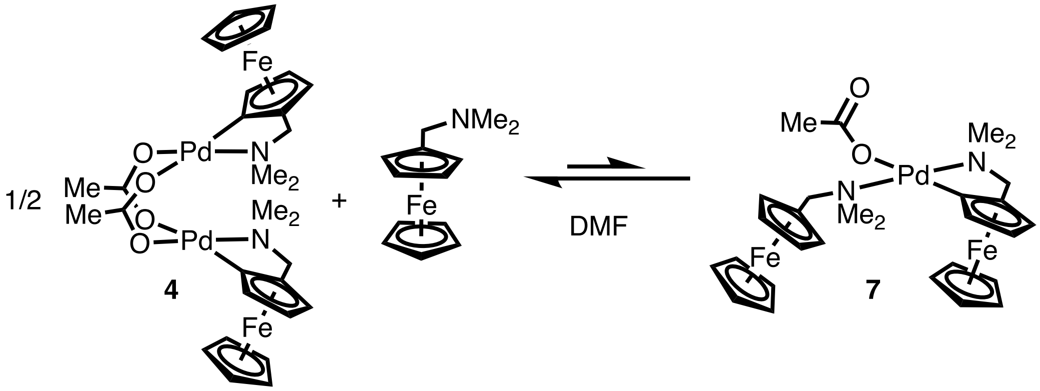

Figure 127: Bridge splitting equilibrium observed in the presence of excess dmaf.

Steady State Kinetics of dmaf Olefination

Building on our understanding of major species present Pd(II)/MPAA solutions, kinetic analysis of Pd-MPAA catalyzed dmaf functionalization was next pursued to shed light on the nature of the active catalyst(s) in these transformations. Importantly, our previous study revealed that MPAA ligands can coordinate Pd(II) to form chiral dimeric MPAA-bridged palladacycles without significantly influencing the rates of (achiral) dmba cyclopalladation or functionalization. To identify the steps that are kinetically relevant and those that are accelerated by MPAA ligands, it was therefore essential to identify a dmaf functionalization reaction that was either accelerated or rendered enantioselective (or both) by MPAA ligands.

Dehydrogenative olefination of dmaf was well suited for kinetic studies. Formation of enantioenriched products indicated the involvement of the MPAA ligand in catalysis and data acquisition was expedited by the operational simplicity of reactions conducted open to air (O_2 terminal oxidant, Figure 124A).[193,265,266] The reaction was further optimized for mechanistic analysis by omission of bromide additives, which were not needed to achieve high levels of enantioinduction. The standard reaction conditions for kinetic analysis are shown in Figure 128A. The absolute chirality of the major product enantiomer (*S*) was determined by SXRD (Figure 128B), and major enantiomer formation was quantified using chiral stationary phase supercritical fluid chromatography (SFC). Under standard conditions, Pd/MPAA mixtures provide marked acceleration of pro-*S* C-H functionalization relative to palladium(II) acetate alone (Figure 128C), meaning that both reaction rate and product enantioselectivity could be used to probe the effect of MPAA ligands on catalysis. Acetate-bridged palladacycle **4** also forms a kinetically competent catalyst in the presence of MPAA, suggesting that it undergoes facile ligand exchange with MPAA. Ligand exchange was confirmed under catalytic conditions by monitoring the rapid change in ee when a reaction is initiated with D-MPAA and subsequently spiked with L-MPAA.[241] Together, these studies highlighted the utility of dmaf olefination for kinetic analysis, but catalyst degradation observed during reaction progress kinetic analysis[267,268] necessitated analysis by initial rates.[269]

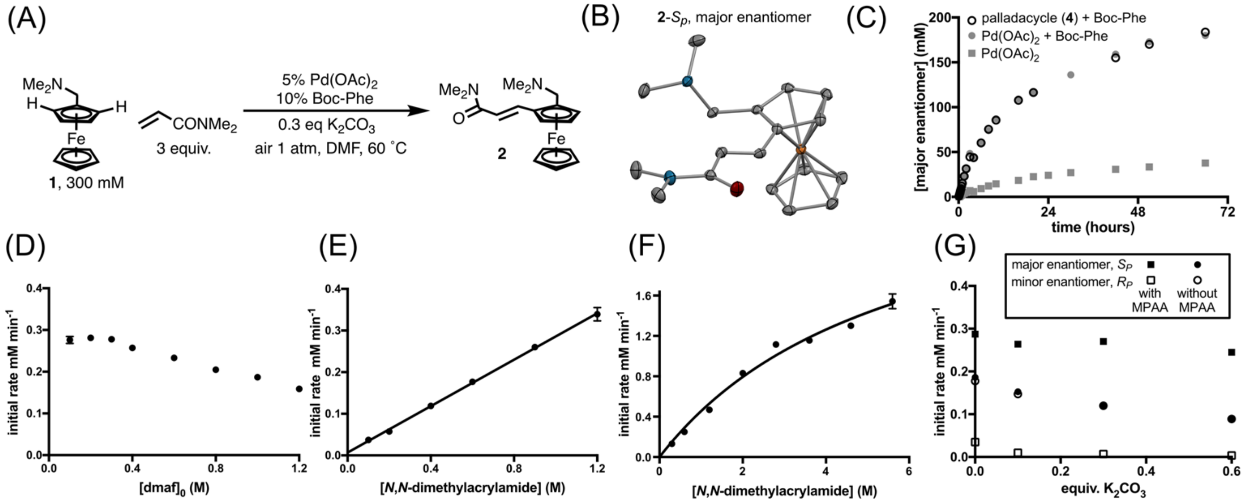

Figure 128: (A) Standard reaction conditions for kinetic studies; (B) absolute chirality of major enantiomer (S_p) as determined by SXRD: ORTEP with 40% thermal ellipsoids; (C) palladacycle **4** is a kinetically competent precatalyst for MPAA-accelerated formation of major enantiomer; (D) inverse order in dmaf; (E) first order in *N*,*N*-dimethylacrylamide (0.1-1.2M), fit to y=mx+b; (F) saturation behavior in *N*,*N*-dimethylacrylamide at high concentration, fit to Michaelis-Menten equation y=mx/(x+b); (G) slightly inverse order in K_2CO_3 with modest selectivity for suppression of the racemic background reaction.

Initial rate data were used to determine the order of each reaction component in dmaf olefination, and thus the extent to which each component contributes to the rate of Pd-MPAA turnover in this reaction (Figure 128D-G). The reaction is zero order in dmaf under the standard reaction conditions (0.1-0.3 M), but an inverse concentration dependence becomes apparent at higher dmaf loading (0.4-1.2M, Figure 128D). Zero order in dmaf indicates that dmaf association does not contribute to turnover limitation of the Pd-MPAA catalyst, while inverse order indicates an additional dmaf dependent process that inhibits turnover. If one assumes that the active catalyst is a Pd-MPAA dimer, then the latter can be rationalized by our finding that dmaf promotes dimer dissociation to generate monomer **7** and thus driving Pd off cycle (Figure 127). The reaction is first order in *N,N*-dimethyl-acrylamide from 0.1-1.2M, indicating that olefin insertion contributes to limiting the rate of Pd-MPAA turnover (Figure 128).[270-275] At higher olefin loadings, the reaction displays saturation kinetics, consistent with reversible olefin binding prior to insertion (Figure 128).[276]

In the presence of MPAA, K_2CO_3 has little effect on the rate of Pd-MPAA turnover (Figure 128G, black squares). If the role of K_2CO_3 were to deprotonate the MPAA N-H to generate di-anionic MPAA chelates, then K_2CO_3 should be necessary for MPAA induced rate acceleration and should have little effect on the background reaction. On the contrary, major enantiomer formation was similarly accelerated by MPAA (relative to Pd(II) acetate alone) in the absence of K_2CO_3 and at all K_2CO_3 loadings investigated (Figure 128G, filled squares > filled circles). The fact that added base provides no selective acceleration of the MPAA promoted reaction suggests that the role of K_2CO_3 in these reactions is not to deprotonate the MPAA N-H; instead, increasing K_2CO_3 loading appears to suppress the racemic reaction (Figure 128G, circles). This K_2CO_3 dependent suppression practically eliminates minor enantiomer formation in the MPAA-catalyzed reaction (Figure 128G, empty squares), thereby improving enantioselectivity.

Kinetic Isotope Effects in dmaf Olefination

The steady state kinetics of dmaf olefination demonstrate that the rate of Pd-MPAA turnover is controlled by olefin insertion and not by dmaf association or a K_2CO_3 dependent process: to gain insight into whether C-H activation contributes to the rate of Pd-MPAA turnover, we turned to a study of deuterium kinetic isotope effect (KIE) experiments.[277-282] In the absence of MPAA ligand, dmaf olefination revealed a primary KIE (k_H/k_D = 3.91 ± 0.40, Figure 129A). In the presence of MPAA ligand, on the other hand, a small KIE was observed in the rates of formation of both major and minor enantiomers (k_H/k_D = 1.17 ± 0.03 and 1.47 ± 0.20, respectively; Figure 129B). Notably, the rate of minor enantiomer formation is expected to have larger KIE (relative to major enantiomer) if some portion of the minor enantiomer is formed through the racemic pathway (KIE 3.91). These data indicate that MPAA ligands contribute to catalysis by accelerating C-H activation.

The potential energy surface in Figure 129C illustrates a scenario consistent with the observed rates and KIEs. The primary KIE observed without MPAA shows that C-H cleavage is turnover limiting in the background reaction (Figure 129C, black curve). The fact that MPAA significantly decreases the KIE for both major and minor enantiomer suggests that MPAA lowers the barrier of both product forming pathways such that they are no-longer turnover limiting (Figure 129C, red and blue curves). Olefin insertion is depicted as turnover limiting for the Pd-MPAA pathways because of the observed rate dependence on olefin concentration (Figure 129E); however, our experiments do not preclude the possibility of additional slow steps in the catalytic cycle (e.g. *β*-elimination or

O_2 redox chemistry). The MPAA dependent decrease in KIE of the minor enantiomer reveals an interesting scenario in which a ligand that lowers the barrier to C-H activation suppresses formation of the corresponding product. This outcome is consistent with selectivity determining C-H activation via partitioning between low barrier pathways from a common intermediate (***I***, Figure 129C) after a turnover limiting step.

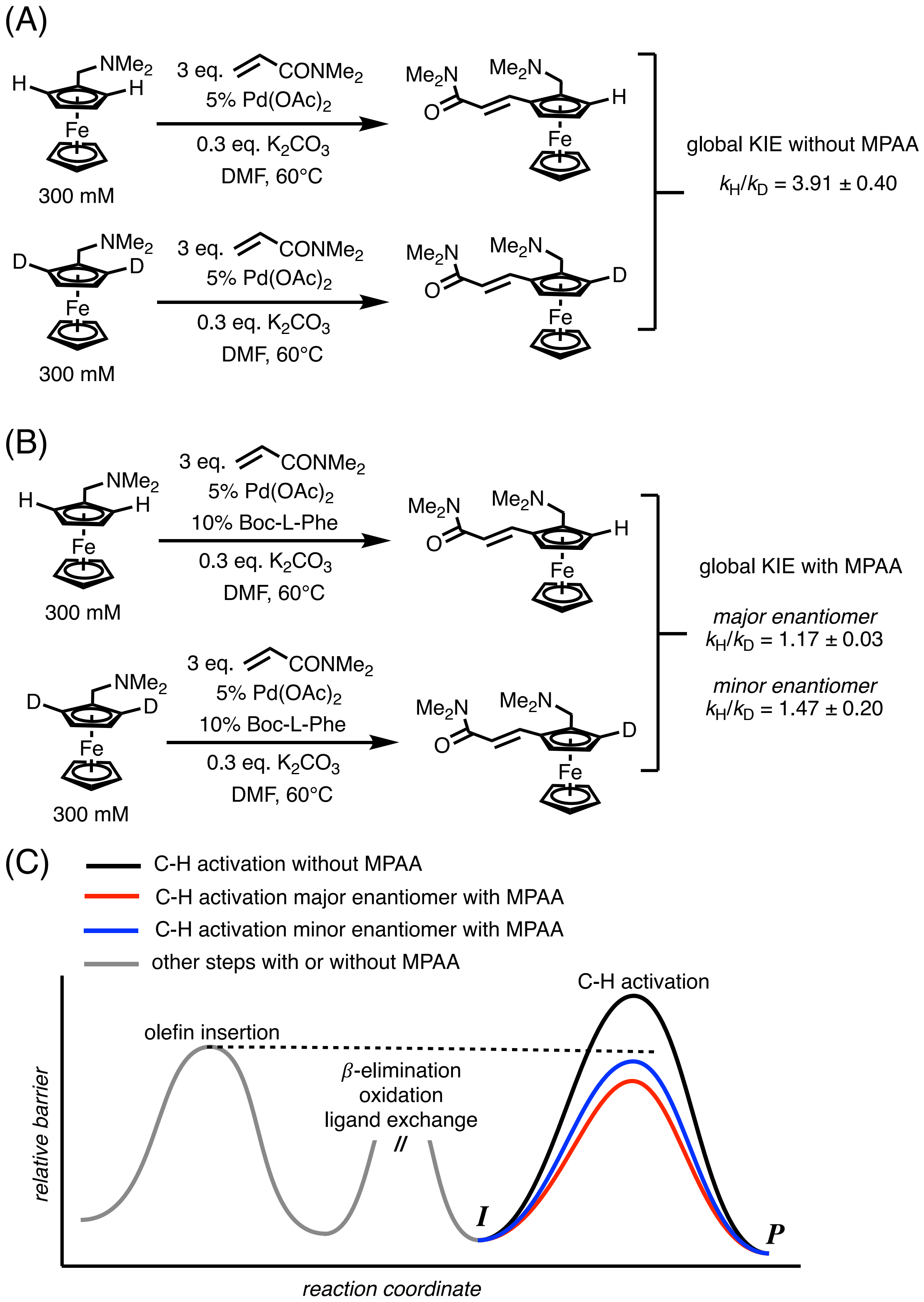

Figure 129 (A) Global KIE in the racemic reaction without MPAA; (B) global KIE of major and minor enantiomer in MPAA-accelerated reaction; (C) potential energy surface summarizing how MPAA ligands change the rate limiting step in dmaf olefination.

Catalyst Stoichiometry in dmaf Olefination

The KIE experiments presented above demonstrate that MPAA ligands change the turnover limiting step by lowering the barrier to C-H activation. Given this insight, we next sought to identify the species responsible for MPAA accelerated C-H activation. Our study of dmaf palladacycle reactivity toward MPAA ligands suggests that sequential ligand substitution gives rise to ensembles of $Pd_2MPAA_1OAc_1$ and Pd_2MPAA_2 complexes. In our previous work, we observed a related Pd_2MPAA_1 ion by high resolution mass spectrometry (Figure 130A,B). Moreover, a plot of ee versus MPAA loading revealed ee is maximized around an overall catalyst loading of Pd_2MPAA_1, suggesting that reduced C-H activation barriers may be controlled by a single MPAA ligand bridging a bimetallic catalyst with the second bridging ligand (OAc or MPAA) exerting minimal influence (Figure 130C). We further hypothesized that essential features of MPAA catalysis could be achieved through a $Pd_2MPAA_1X_1$ complex, which, in principle, could benefit from both bimetallic cooperativity and secondary sphere hydrogen bond catalysis (Figure 123D).

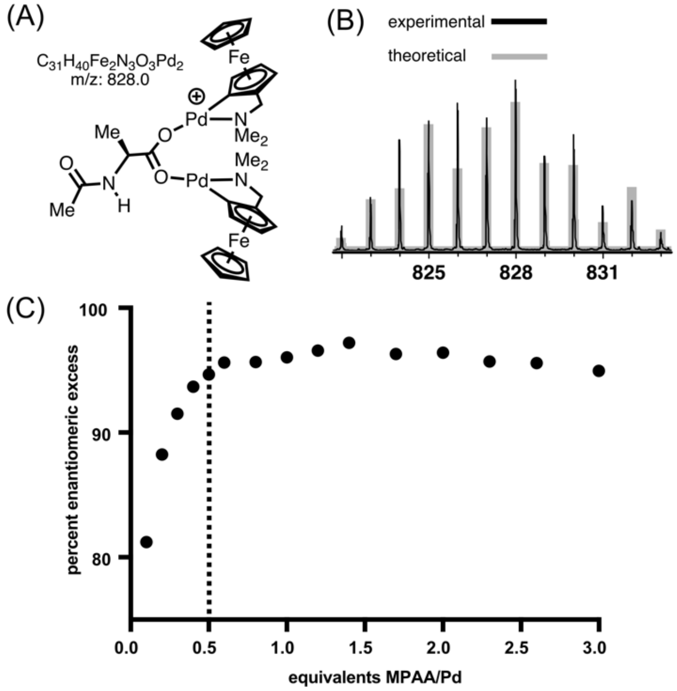

Figure 130: (A) Plot of enantiomeric excess versus MPAA loading (dashed line indicates reaction with overall catalyst loading Pd_2MPAA_1; (B) Pd_2MPAA_1 ion observed by high resolution mass spectrometry; (C) experimental and theoretical isotope patterns for the observed Pd_2MPAA_1 ion.

A non-linear effect (NLE) experiment was conducted to assess the presence of species containing more than one chiral ligand in catalysis. A small, systematic positive deviation from linearity was observed in a plot of $e.e._{MPAA}$ versus $e.e._{product}$. Notably, the small rate suppression from heteroaggregate is much more apparent in plots of ee_{MPAA} versus rate. The small magnitude of the observed NLE is consistent with our hypothesis that the second bridging ligand (X) in $Pd_2MPAA_1X_1$ plays a minor role in determining the rate and selectivity of Pd-MPAA catalysts.

To test our hypothesis that MPAA-accelerated C-H activation is achieved through a species with the stoichiometry $Pd_2MPAA_1X_1$, we sought to determine the kinetic order of MPAA ligand. Reactions conducted with 0-1.5 equivalents of MPAA ligand (with respect to palladium) accelerated formation of the major enantiomer with rate acceleration approaching saturation with much less than one MPAA ligand per palladium (Figure 131A). This observation qualitatively supports the $Pd_2MPAA_1X_1$ hypothesis; however, plotting initial rates versus MPAA loading does not provide a simple kinetic order in MPAA because it reflects competing contributions from two mechanisms (Figure 131B , Equation 6, and Equation 7).

Equation 6: $initial\ rate\ major\ enantiomer\ = k_1[\mathrm{Pd-OAc}] +\ k_2[\mathrm{Pd-MPAA}]$

Equation 7: $initial\ rate\ minor\ enantiomer\ = k_1[\mathrm{Pd-OAc}] +\ k_3[\mathrm{Pd-MPAA}]$

Considering the model in Figure 131B, the data in Figure 131A can be divided into three distinct regimes. Regime *i* consists of the rates of major and minor enantiomer formation in the absence of MPAA and defines the background reaction (k_1). Regime *ii* (from 0.01-0.5 equivalents MPAA per Pd) reveals competing contributions from background (k_1) and MPAA dependent pathways in the formation of major and minor enantiomers (k_2 and k_3, respectively). Finally, in regime *iii* (MPAA loadings greater than 0.5 equivalents MPAA per Pd) the Pd-MPAA pathway is nearly saturated and the background reaction is largely suppressed, giving rise to 4.6-fold increase in the rate of formation of major enantiomer and a 10-fold decrease in the rate of formation of minor enantiomer relative to the background reaction.

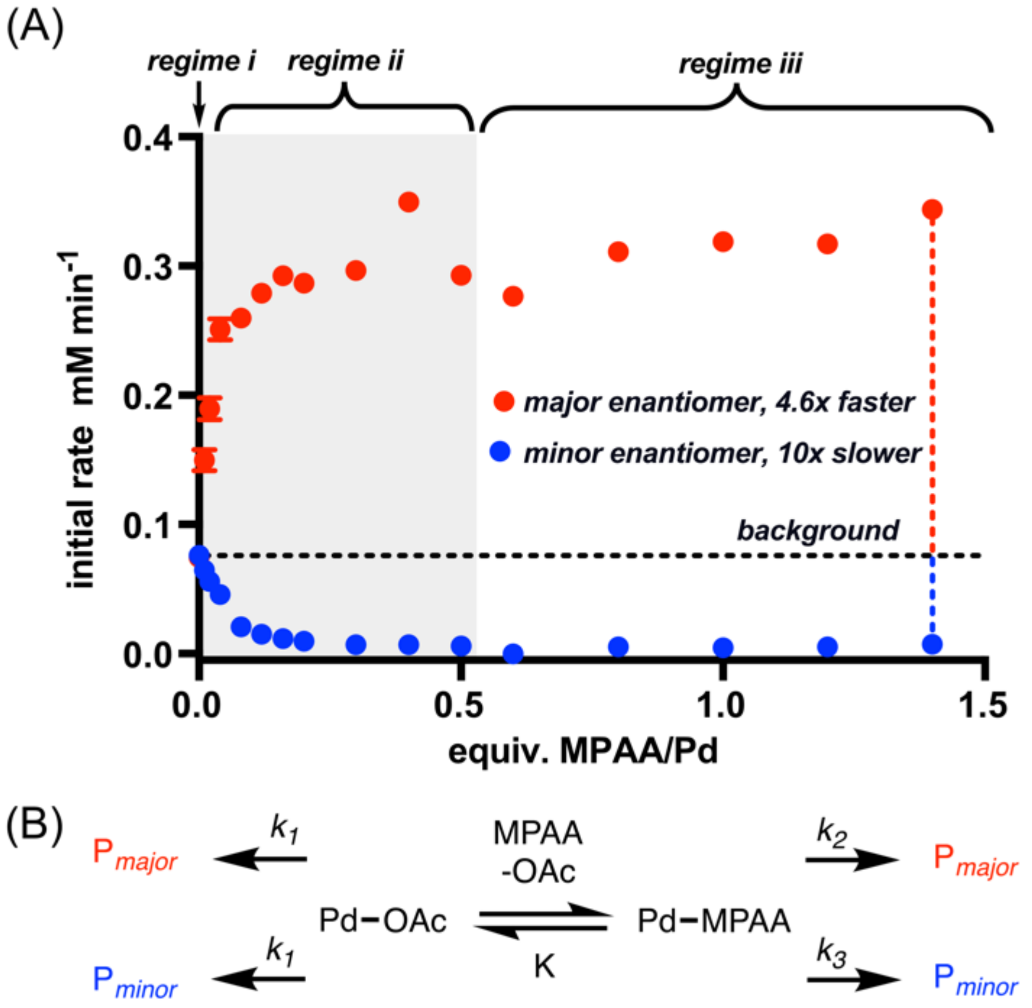

Figure 131: (A) plot of initial rate of major and minor enantiomer formation versus MPAA loading; (B) a simplified, minimal model of product forming pathways.

Thus, although maximal rate acceleration around 0.5 MPAA per Pd is qualitatively consistent with our hypothesis; the two experimental observables (rates of major and minor enantiomers) are insufficient to conclusively determine the rate constants and catalyst stoichiometries of (at least) three pathways. Such an approach would require quantification of each component in the ensemble of Pd-complexes and large quantities of highly accurate kinetic data to model the absolute stoichiometry (Pd_2MPAA_2 versus Pd_1MPAA_1) of the complexes that achieve MPAA accelerated C-H activation. Given the complexity of the ensembles of palladium species that can form in solution, it is fortunate that our qualitative observations point to a hypothesis that is readily tested without complete characterization of the ensemble of resting states; namely, that a species with a distinct *relative* stoichiometry (Pd_2MPAA_1) achieves MPAA-accelerated C-H activation. Toward this end, the kinetic method of continuous variation provides a relatively simple experimental means to probe optimal transition state stoichiometry in ligand accelerated catalysis.

Kinetic MCV Demonstrates Pd_2MPAA_1 Accounts for Rate Acceleration

The method of continuous variation (MCV) is well suited for determining the relative stoichiometry of molecular association. Whereas MCV is most frequently used to assess binding equilibria with spectroscopic observables (and thus reactant/product stoichiometry), MCV can be applied to any molecular association with an experimental observable that is linearly dependent on the concentration of the associated species. In the case of ligand-accelerated, steady-state catalysis, the relevant response is rate (and thus transition state stoichiometry).[189] Relevant applications of kinetic MCV to probe transition state stoichiometry can be found in mechanistic studies of organometallic catalysis,[283-287] enzymology,[288-292] olefin polymerization,[293,294] and, most frequently, synthetic models of metalloenzymes.[295-311]

The optimal stoichiometry of the MPAA-accelerated transition state was therefore probed using kinetic MCV by plotting the initial rate of major enantiomer formation versus mole fraction MPAA ($\chi_{MPAA} = [MPAA]_0/([MPAA]_0+[Pd(OAc)_2]_0)$) and fitting those data to Equation 8, which accounts for the two reactions that contribute to major product formation. The relative stoichiometry of palladium with respect to MPAA is represented in Equation 8 by the variable *a*. To reduce the number of adjustable parameters, *b* was determined independently ($b = 1.5$).[283,284] Non-linear least squares curve fitting of the data in Figure 132 to equation 3 gives a best fit $a = 2.03 \pm 0.13$ (constrained to b=1.5). The dashed lines in Figure 132 show the relatively poor fit when the stoichiometry is constrained to 1:1 Pd:MPAA. The best fit for the relative stoichiometry of palladium (a = 2) confirms the hypothesis, outlined above, that MPAA- accelerated C-H activation is achieved by a complex with the relative stoichiometry Pd_2MPAA_1.

Equation 8: $initial\,rate\,major\,enantiomer\ =\ m(\chi_{MPAA})(\chi_{Pd})^{a}\ +\ n(\chi_{Pd})^{b}$

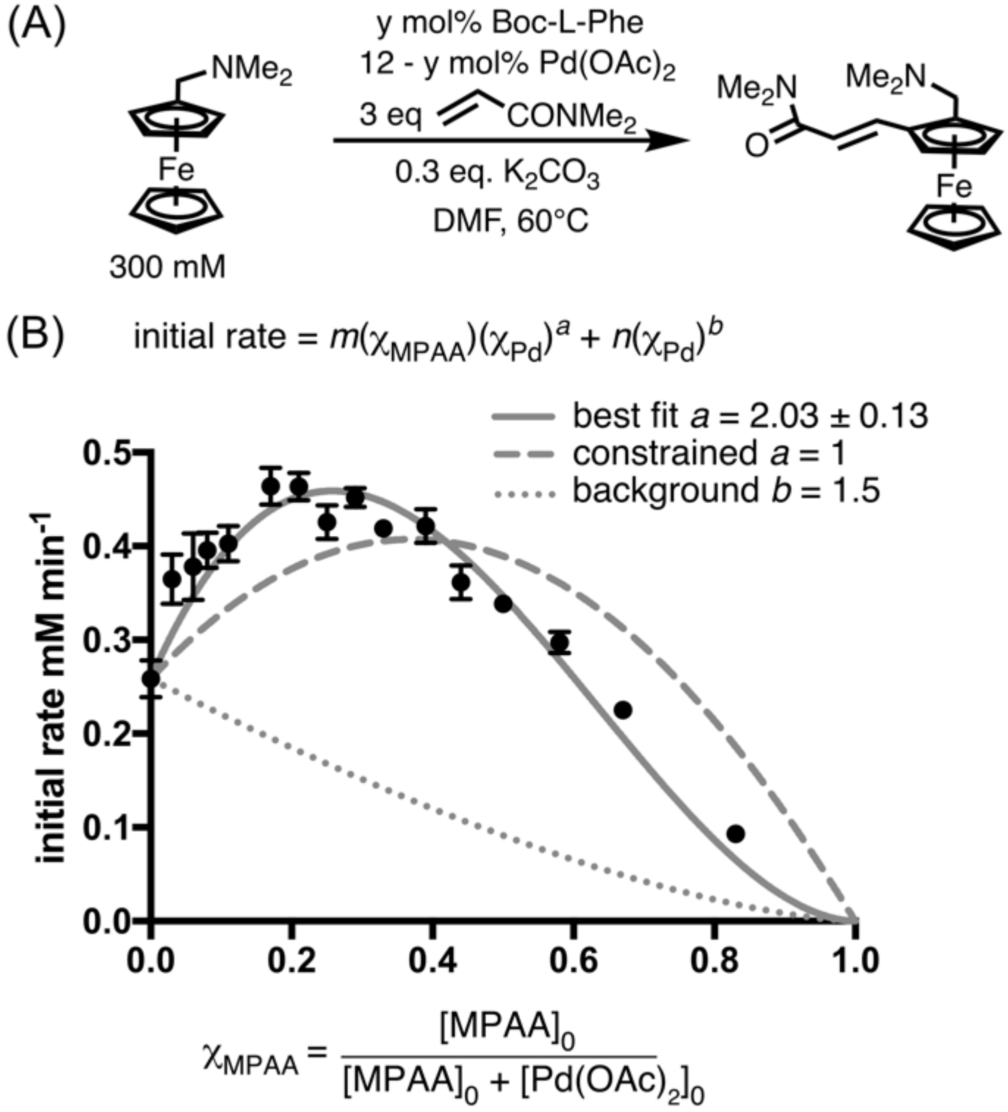

Figure 132: (A) Reaction conditions for kinetic method of continuous variation; (B) plot of initial rate of formation of major enantiomer versus χ_{MPAA} with fits to equation 3.

Computational Evaluation of MPAA Accelerated Cyclopalladation

Structural and kinetic analysis of enantioselective dmaf olefination indicate that a bimetallic catalyst($Pd_2MPAA_1X_1$) lowers the barrier to C-H activation. To corroborate this conclusion, we sought to assess whether computational models of dmaf cyclopalladation in the presence of MPAA ligands would reproduce key experimental findings from this reaction. Specifically, a viable model must account for: (1) selective pro-S C-H activation, (2) MPAA-accelerated activation of both enantiotopic C-H bonds relative to acetate, (3) cyclopalladation via a bimetallic pathway, and (4) enantioselectivity from a single MPAA ligand per bimetallic unit. A model capable of addressing these observables would also allow evaluation experimentally elusive details of MPAA accelerated C-H activation, including the hypothesis (derived from analysis of solid state structures) that MPAA ligands enable rate acceleration and enantioinduction via secondary sphere hydrogen bond catalysis.

Similar to our previous report,[243] the calculated energy surfaces indicate the bimetallic pathway is strongly favored both kinetically and thermodynamically. Both C-H activation steps on the bimetallic pathway feature a high energy intermediate in which one bridging ligand dissociates from one face of the bimetallic unit to form an open coordination site for cyclopalladation. The calculated barriers of the pro-S and pro-R C-H activation transition states accurately predict the *S* chirality of the major product ($\Delta\Delta G^{\ddagger}$ = 4.5kcal/mol). The calculated energy surfaces also reflect MPAA-accelerated activation of both enantiotopic C-H bonds relative to the acetate pathway ($\Delta G^{\ddagger acetate}$ = 29.3, $\Delta G^{\ddagger R\text{-}MPAA}$ = 27.3, and $\Delta G^{\ddagger S\text{-}MPAA}$ = 22.8 kcal/mol). The lowest energy transition states for C-H activation via $Pd_2MPAA_1OAc_1$ reproduce the absolute chirality of major reaction product ($\Delta\Delta G^\ddagger$ = 3.6kcal/mol). The calculated energy surfaces account for the experimental observables listed above and were therefore used to assess the stabilizing interactions responsible for MPAA-accelerated C-H activation.

The lowest energy $Pd_2MPAA_1OAc_1$ transition state for pro-S C-H activation is shown in Figure 133 and illustrates a key structural feature that was observed in all the lowest energy pro-S cyclopalladation transition states, secondary sphere-hydrogen bonding of the bridge ruptured MPAA ligand to the acetate participating in concerted metallation deprotonation. This stabilizing interaction features one MPAA ligand spanning two distinct palladium centers in a bimetallic unit and thereby offers a possible molecular interpretation for the mechanism by which $Pd_2MPAA_1X_1$ accelerates C-H activation. To probe possible contributions from hydrogen-bonding in MPAA catalysis, cyclopalladation transition states with MPAA ligands in various positions and conformations were compared for the both the major and minor enantiotopic C-H bonds and subsequently compared to the acetate only pathway. This analysis revealed that the lowest energy pathways include secondary sphere hydrogen bonding interactions, but that MPAA-dependent barrier lowering (relative to acetate only) is still observed when the MPAA is constrained to preclude such interactions. Hydrogen bonding interactions were consistently observed in the lowest energy transition states to pro-S cyclopalladation with L-MPAA ligands (Figure 133). Secondary sphere interactions were also present in some (but not all) of the lowest barrier pro-R transitions states and were achieved at the expense of additional clashes and distortions about the bimetallic unit. Taken together, our investigation into possible contributions from secondary sphere hydrogen bond catalysis suggest that such interactions are responsible for some (but not all) of the MPAA dependent decrease in the barrier to activation of both enantiotopic C-H bonds and that hydrogen bonding may selectively stabilize the transition state for C-H activation of the major enantiomer.

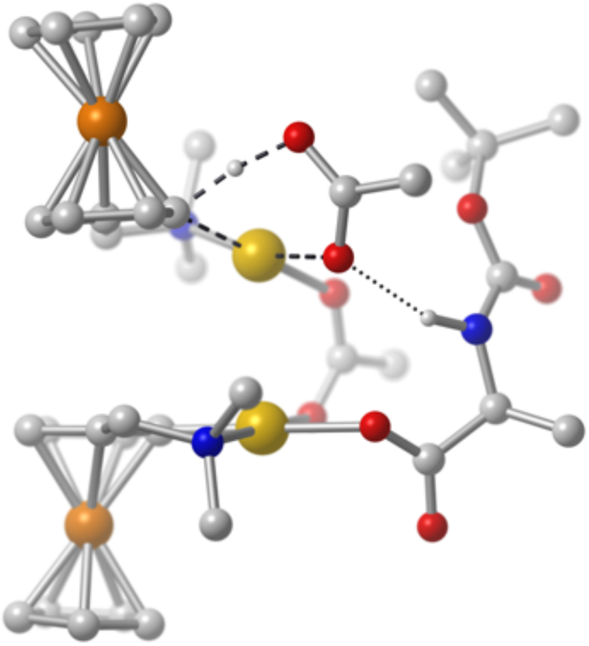

Figure 133: Secondary sphere hydrogen bonding interactions participate in C-H activation of the favored, enantiotopic C-H bond, (L-MPAA)MS(pro-S).

As a preliminary test of the computational model of secondary sphere hydrogen bond catalysis, rates and selectivities were compared for reactions conducted with Boc-NH-Phe, Boc-NMe-Phe, and no MPAA (Figure 134). The experimental results qualitatively agree with each of the predictions from the computational model: non-H-bonding ligands accelerate catalysis relative to acetate, meanwhile H-bonding ligands accelerate catalysis further and give rise to selectivity for the major enantiomer.

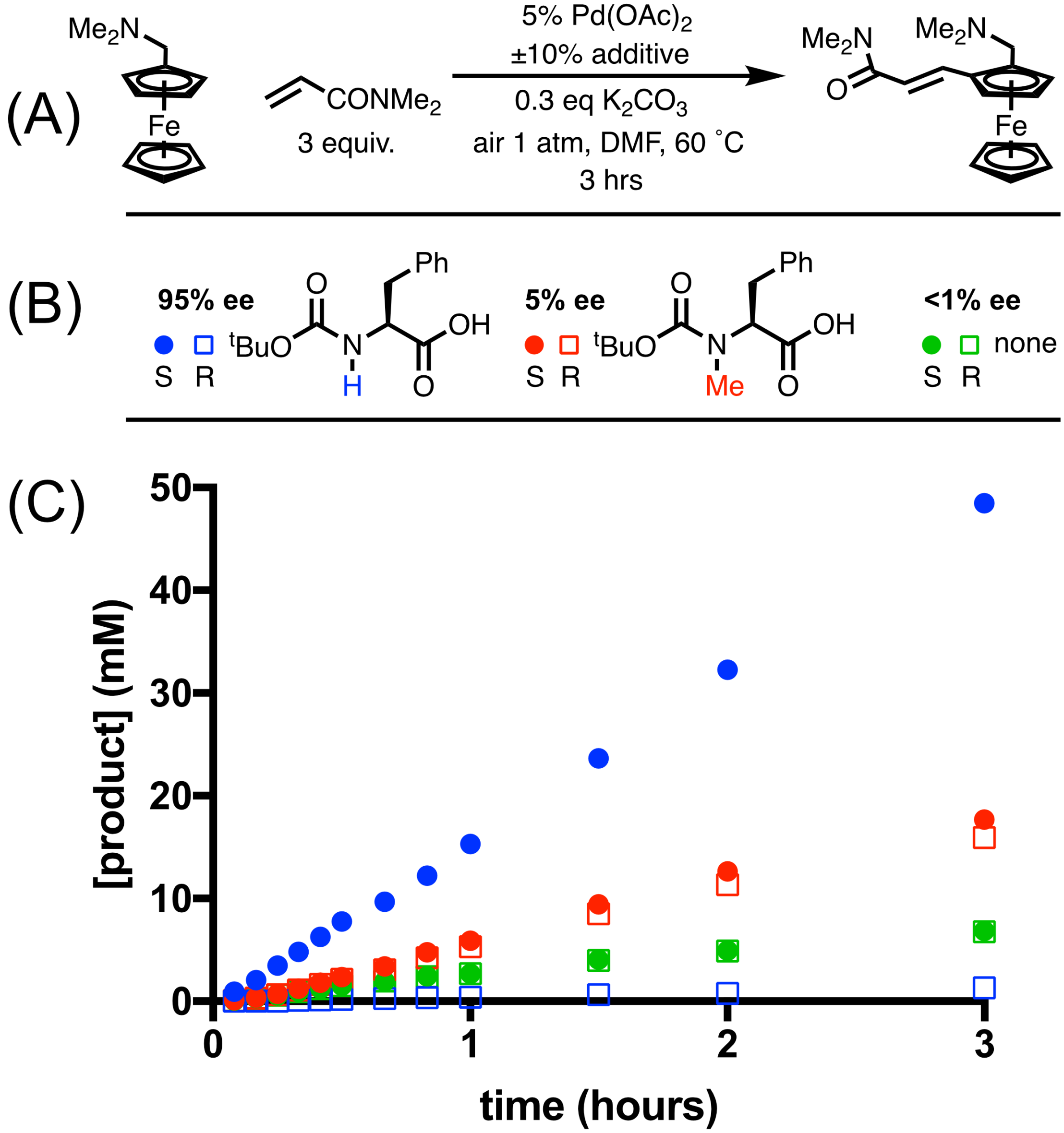

Figure 134 (A) reaction conditions; (B) legend of additives and their corresponding product symbols and enantiomeric excesses; (C) reaction profiles showing total product formation over time in the presence of Boc-NH-Phe (blue), Boc-NMe-Phe (red), and no additive (green) where solid circles indicate major enantiomer and empty squares indicate minor enantiomer.

MPAA Accelerated Cyclopalladation

Catalytic reaction kinetics and computational analysis of MPAA promoted cyclopalladation both indicate that a bimetallic catalyst ($Pd_2MPAA_1X_1$) lowers the barrier to C-H activation in dmaf olefination. Given the centrality of this step to a range of C-H functionalization reactions, we next sought to directly evaluate enantioselective MPAA accelerated C-H activation without possible complications from other steps in the catalytic cycle by explicitly measuring the effect of MPAA ligands on the rate of cyclopalladation (in the absence of catalyst turnover). [240,312] Moreover, to evaluate the relevance of $Pd_2MPAA_1X_1$ rate acceleration toward other substrates in Pd-MPAA catalysis, **3** was chosen as model substrate for stoichiometric C-H activation because bhp derivatives are the most frequently studied in computational models that directly probe MPAA-promoted cyclopalladation (separated from other steps in catalysis). [164,313-317]

Determination of C-H activation rates necessitated an experimental observable with a response proportional to cyclopalladated product. This proved challenging because the products of bhp cyclopalladation have not been characterized in detail (Figure 135A). The acetate complex crystallized as a heterochiral dimer, foreshadowing potential complexity from ensembles of stereoisomeric dimers.[199,203,232] There are two reports of experimental characterization bhp-MPAA palladacycles, both of which were assigned as MPAA chelated monomers.[164,313] In one case, however, the reported NMR spectrum does not delineate the palladacycle aggregation state.[313] In the second case, an ion consistent with a Pd_1MPAA_1 palladacycle was observed by high resolution mass-spectrometry;[164]

however subsequent analysis in our laboratory with a wider spectral window revealed the Pd_2MPAA_1 ion (Figure 135B).[243]

Monitoring cyclopalladation of **3** by ^{19}F NMR reveals a complicated ensemble of cyclopalladated products (Figure 135A). We were relieved to discover, however, that the entire ensemble is rapidly converted to two diastereomers (**8** and **9**) upon treatment with (*S*)-*N*,*N*-dimethylaminophenylalanine (Phe-NMe_2) (Figure 135). [197,254,318] The chelating resolving agent (see **10,** Figure 135C) halts the reaction by sequestering un-reacted palladium acetate as the di-chelate **11** (Figure 135D). The resolved diastereomers (**7** and **8**) are readily separated and quantified by SFC. Thus, by halting the reaction and enabling quantification of cycloplalladated products, Phe-NMe_2 provides a method to evaluate the effect of MPAA ligands on the rate of C-H activation of benzhydryl-pyridine derivative **3**.

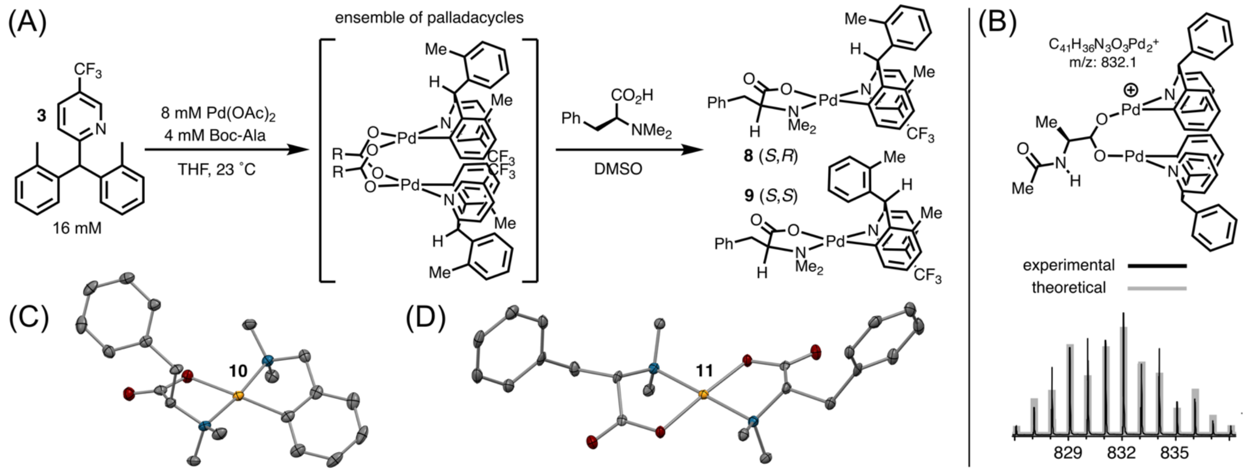

Figure 135: (A) Cyclopalladation of **3** to give an ensemble of palladacycles and subsequent resolution; (B) Pd_2MPAA_1 palladacycle observed by high resolution mass spectrometry and the corresponding theoretical and observed isotope patterns; (C) model palladacycle (**10**) illustrating Phe-NMe_2 chelation; (D) product of $Pd(OAc)_2$ scavenging by Phe-NMe_2, **11**.

Once a method to quantify the rate of C-H activation was established, kinetic MCV was used to determine the optimal stoichiometry of the transition state of MPAA-accelerated, enantioselective cyclopalladation (Figure 136A). Within the constraints of MCV, the reaction conditions are similar to those used in the catalytic system (i.e., same solvent and similar concentrations of each component). Visual inspection of Figure 136B reveals a very small y-intercept, indicative of slow cyclopalladation in the absence of MPAA. To quantify the relative stoichiometry of the Pd-MPAA species that accelerates enantioselective cyclopalladation, the data in Figure 136B were fit to Equation 9, which does not include additional adjustable parameters to account for the background reaction. This simplification is possible because of the negligible background reaction noted above. Non-linear curve fitting of the data in Figure 136B to Equation 9 provided a best fit for the relative stoichiometry of palladium with respect to MPAA of $a = 1.96 \pm 0.05$ (Figure 16B, solid curve). A poor fit is obtained when the stoichiometry is constrained to 1:1 Pd:MPAA (Figure 16B, dashed curve). These results indicate that the bimetallic species ($Pd_2MPAA_1X_1$) implicated in our structural, kinetic and computational studies of dmaf olefination are also responsible for MPAA-accelerated C-H activation of bhp. The differences between both the substrates and the conditions used for the dmaf and bhp studies suggest that Pd_2MPAA_1 complexes could be relevant to a broader range of C-H functionalization reactions involving MPAA ligands than those evaluated in this study.

Equation 9: $initial\ rate\ major\ diastereomer\ = m(\chi_{MPAA})(\chi_{Pd})^a$

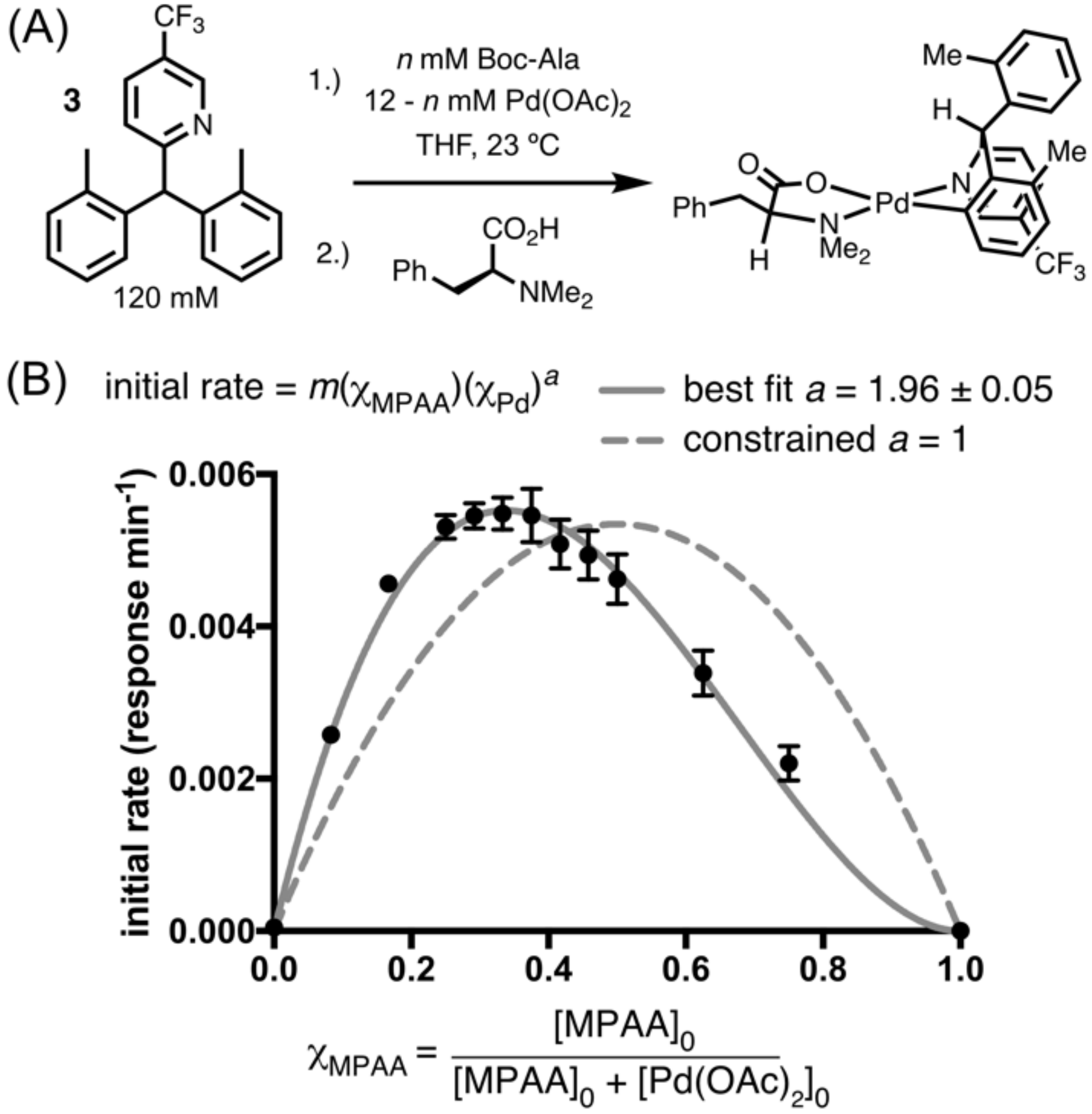

Figure 136 (A) Conditions for kinetic method of continuous variation in enantioselective cyclopalladation of **3**; (B) plot of initial rate of major diastereomer formation versus χ_{MPAA} with fits to equation 4.

Summary- Proposed Mechanism of MPAA Accelerated, Enantioselective Olefination

Structural, kinetic, and computational analyses of Pd-MPAA catalyzed olefination all implicate a bimetallic species $Pd_2MPAA_1X_1$ in MPAA-accelerated C-H functionalization. A catalytic cycle consistent with these studies is proposed in Figure 137. The experimental results provide a framework for understanding the intermediates and steps in the cycle that contribute to turnover limitation, rate acceleration, and enantioinduction. Within this framework, experimentally elusive molecular details are evaluated by comparing computational models of plausible pathways (guided and constrained by experimental observables).

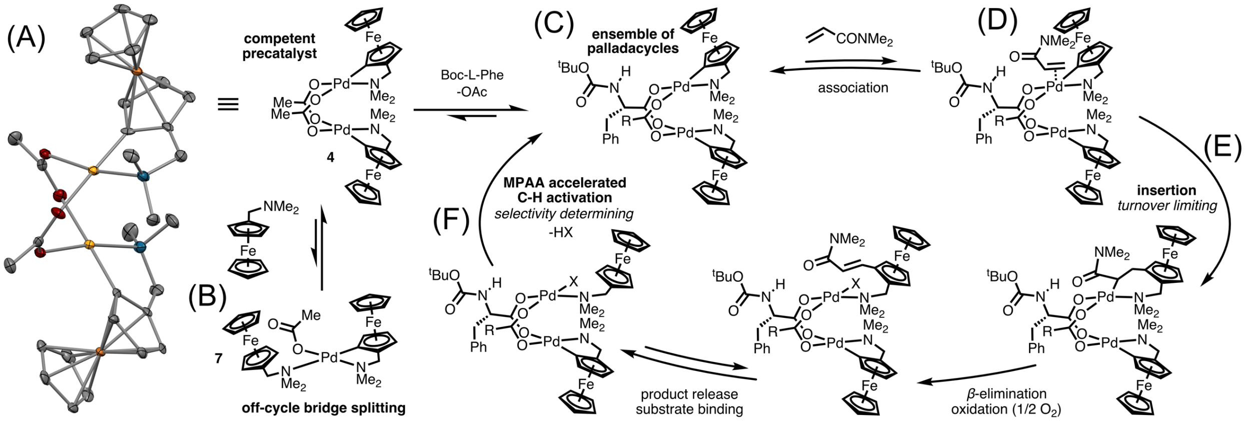

Figure 137: Proposed catalytic cycle for MPAA-accelerated olefination of dmaf.

The kinetically competent pre-catalyst **4** was characterized in DMF using NOESY and structural MCV. The solution state structure matches that of the acetate bridged dimer observed in the solid state (Figure 137A). Complex **4** is in equilibrium with a bridge-split monomer (**7**), which was characterized by ^{1}H NMR and MCV. Under catalytic conditions, inverse order in dmaf suggests that driving the equilibrium toward the monomer **7** inhibits catalytic activity (Figure 17B). MPAA ligands displace acetate on precatalyst **4** resulting in an ensemble of diastereomeric, mono- and di-MPAA complexes (Figure 137C). The formation of mono-MPAA complexes followed by conversion to di-

MPAA complexes upon titration of MPAA ligands closely resembles results from our previous work and strongly suggests that dmaf palladacycles exist as carboxylate bridged dimers in the presence of MPAA ligands.

Moving forward in the productive cycle, the observed first order rate dependence on olefin concentration (from 0.1-1.2M) demonstrates that olefin insertion contributes to turnover limitation. Saturation kinetics at higher olefin concentrations are consistent with reversible olefin coordination prior to insertion (Figure 137 D,E). These data demonstrate the relevance of olefin insertion to the rate of catalyst turnover; however, steps that take place after insertion (*β*-elimination, O_2 redox chemistry, and ligand exchange) may also contribute to turnover limitation.

KIE experiments revealed an essential of MPAA catalysis in dmaf olefination; specifically, MPAA ligands *change the turnover limiting step*. The significant decrease in KIE of dmaf olefination in the presence of MPAA ligands confirms that MPAA-dependent rate acceleration is a result of lower barriers to C-H cleavage of both enantiotopic C-H bonds (i.e. those leading to both the major and minor product enantiomer, Figure 137E). The greater decrease in KIE for the reaction leading to formation of the major enantiomer is consistent with selectivity determining C-H activation, which is achieved by partitioning between two low barrier pathways after turnover limiting olefin insertion.

Conclusion

This work builds on structural characterization of MPAA-palladacycles to understand the species responsible for MPAA-accelerated C-H activation of the two substrates that are most frequently employed in models of MPAA-catalysis, dmaf (**1**) and bhp (**3**). Structural, kinetic, and computational studies provide complementary insights and converge on the significance of the core structure $Pd_2MPAA_1X_1$. Identification of the molecular framework that achieves rate acceleration, in turn, provides a foundation for understanding the structures and interactions through which these species improve catalytic outcomes. Throughout this work, characterization of palladacycle structure (aggregation and speciation) motivated to verifiable hypotheses regarding function. Most notably, observation of $Pd_2MPAA_1OAc_1$ in equilibrium with Pd_2MPAA_2 and **4**, led to the hypothesis that the essential features of MPAA-catalysis (rate acceleration and enantioselectivity) could be achieved via a transition state containing a bimetallic core bridged by a single MPAA ligand with minimal dependence on a second bridging ligand.

Designing experiments to test this hypothesis relied heavily on understanding of the underlying organometallic speciation in solution. For example, observation of $Pd_2MPAA_1OAc_1$ prompted kinetics experiments with MPAA loadings less than Pd_1MPAA_1. Under these conditions, competing saturation behavior between multiple catalysts reveals a wealth of mechanistic complexity, which is easily missed by only examining the saturated regime, $[MPAA]_{total} \geq [Pd]_{total}$. Characterization of the underlying organometallic speciation suggested that attempts to identify the rate, order, *and absolute stoichiometry* of each catalyst in solution would lead to a poorly constrained system of equations that was unlikely to afford compelling mechanistic insights. Fortunately, the kinetic method of continuous variation provides an alternative representation of the same competing pathways that directly evaluates the optimal relative stoichiometry of ligand accelerated catalysis. In catalytic and stoichiometric reactions (with different substrates, MPAAs, and conditions) kinetic MCV clearly illustrates the relevance of $Pd_2MPAA_1X_1$ in MPAA-accelerated, enantioselective C-H activation.

Observation of structure continued to inform our investigation of function with respect to how a Pd_2MPAA_1 core might enhance rates and confer enantioselectivity. In particular, observation of hydrogen bonding interactions in solid state structures of MPAA palladacycles led to the hypothesize that MPAA ligands could achieve enantionduction and rate enhancements through secondary sphere hydrogen bond catalysis. This hypothesis was tested by comparing the rates and selectivities of N-H and N-Me amino acid ligands, which revealed that the N-H functional group exerted substantial influence of reaction rate and remarkable control over product selectivity. Notably, the lack of enantioselectivity with N-Me ligands has been observed in other systems and has been interpreted as evidence for the importance of MPAA chelation via nitrogen coordination. The significant rate enhancement with N-Me ligands, however, provides strong evidence againts MPAA chelation via nitrogen coordination and suggests that electronic differences between MPAA ligands and acetate may contribute to MPAA catalysis. Observation of enhanced rates and selectivities with N-H vs N-Me provides preliminary evidence, consistent with computational analysis, to suggest relevance of secondary sphere H-bond catalysis in MPAA accelerated C-H activation at bimetallic intermediates.

References

(1) Davies, H. M. L.; Morton, D. *J. Org. Chem.* **2016**, *81* (2), 343.
(2) Hartwig, J. F.; Larsen, M. A. *ACS Cent. Sci.* **2016**, *2* (5), 281.
(3) Bergman, R. G.; Bergman, R. G. *Nature* **2007**, *446*, 391.
(4) Lyons, T. W.; Sanford, M. S. *Chem. Rev.* **2010**, *110* (2), 1147.
(5) Cernak, T.; Dykstra, K. D.; Tyagarajan, S.; Vachal, P.; Krska, S. W. *Chemical Society Reviews* **2016**, *45* (3), 546.
(6) Liao, K.; Negretti, S.; Musaev, D. G.; Bacsa, J.; Davies, H. M. L. *Nature Publishing Group* **2016**, *533* (7602), 230.
(7) Kuhl, N.; Hopkinson, M. N.; Wencel-Delord, J.; Glorius, F. **2012**, *51* (41), 10236.
(8) Davies, H. M. L.; Manning, J. R. *Nature* **2008**, *451* (7177), 417.
(9) Lewis, J. C.; Coelho, P. S.; Arnold, F. H. *Chemical Society Reviews* **2011**, *40* (4), 2003.
(10) Arnold, F. H. *Acc. Chem. Res.* **1998**, *31* (3), 125.
(11) Tracewell, C. A.; Arnold, F. H. *Current Opinion in Chemical Biology* **2009**, *13* (1), 3.
(12) Schwizer, F.; Okamoto, Y.; Heinisch, T.; Gu, Y.; Pellizzoni, M. M.; Lebrun, V.; Reuter, R.; Kohler, V.; Lewis, J. C.; Ward, T. R. *Chem. Rev.* **2018**, *118* (1), 142.
(13) Osakada, K.; Yamamoto, T. *Coordination Chemistry Reviews* **2000**, *198* (1), 379.
(14) Suzaki, Y.; Yagyu, T.; Osakada, K. *Journal of Organometallic Chemistry* **2007**, *692* (1-3), 326.
(15) Hirner, J. J.; Shi, Y.; Blum, S. A. *Acc. Chem. Res.* **2011**, *44* (8), 603.
(16) Pérez-Temprano, M. H.; Casares, J. A.; Espinet, P. *Chem. Eur. J.* **2012**, *18* (7), 1864.
(17) Coad, J. R.; Ingold, C. K. *J. Chem. Soc. B* **1968**, *0* (0), 1455.
(18) Gregory, B. J.; Ingold, C. K. *Journal of the Chemical Society B: Physical …* **1969**, *0* (0), 276.
(19) Dong, D.; Slack, D. A.; Baird, M. C. *Inorg. Chem.* **1979**, *18* (1), 188.
(20) Dizikes, L.; Wojcicki, A. *J. Am. Chem. Soc.* **1977**, *99* (25), 8373.
(21) Fritz, H. L.; Espenson, J. H.; Williams, D. A.; Molander, G. A. *J. Am. Chem. Soc.* **1974**, *96* (8), 2378.
(22) Janowicz, A. H.; Bergman, R. G. *J. Am. Chem. Soc.* **1983**, *105*, 3929.
(23) Bryndza, H. E.; Evitt, E. R.; Bergman, R. G. *J. Am. Chem. Soc.* **1980**, *102* (15), 4948.
(24) Yoshigoe, Y.; Suzaki, Y.; Osakada, K. *Chem. Lett.* **2014**, *43* (8), 1337.
(25) Suzaki, Y.; Osakada, K. *Bull. Chem. Soc. Jpn.* **2004**, *77* (1), 139.
(26) Friis, S. D.; Pirnot, M. T.; Buchwald, S. L. *J. Am. Chem. Soc.* **2016**, *138* (27), 8372.
(27) Ackerman, L. K. G.; Lovell, M. M.; Weix, D. J. *Nature* **2015**, *524* (7566), 454.
(28) Lee, S. Y.; Hartwig, J. F. *J. Am. Chem. Soc.* **2016**, *138* (46), 15278.

(29) Wang, D.; Izawa, Y.; Stahl, S. S. *J. Am. Chem. Soc.* **2014**, *136* (28), 9914.
(30) Durak, L. J.; Lewis, J. C. *Organometallics* **2013**, *32* (11), 3153.
(31) Durak, L. J.; Lewis, J. C. *Organometallics* **2014**, *33* (3), 620.
(32) Stille, J. K. *J. Am. Chem. Soc.* **1983**, 6129.
(33) Bock, P. L.; Boschetto, D. J.; Rasmussen, J. R.; Demers, J. P.; Whitesides, G. M. *J. Am. Chem. Soc.* **1974**, *96* (9), 2814.
(34) Bock, P. L.; Whitesides, G. M. *J. Am. Chem. Soc.* **1974**, *96* (9), 2826.
(35) Peterson, T. H.; Golden, J. T.; Bergman, R. G. *Organometallics* **1999**, *18* (10), 2005.
(36) Pamplin, C. B.; Legzdins, P. *Acc. Chem. Res.* **2003**, *36* (4), 223.
(37) Schwartsburd, L.; Iron, M. A.; Konstantinovski, L.; Ben Ari, E.; Milstein, D. *Organometallics* **2011**, *30* (10), 2721.
(38) Gunanathan, C.; Milstein, D. *Acc. Chem. Res.* **2011**, *44* (8), 588.
(39) Milstein, D. *Philos Trans A Math Phys Eng Sci* **2015**, *373* (2037).
(40) Robinson, R., Jr.; Sharp, P. R. *Organometallics* **2010**, *29* (6), 1388.
(41) Sugie, A.; Furukawa, H.; Suzaki, Y.; Osakada, K.; Akita, M.; Monguchi, D.; Mori, A. *Bull. Chem. Soc. Jpn.* **2009**, *82* (5), 555.
(42) Shekhar, S.; Hartwig, J. F. *J. Am. Chem. Soc.* **2004**, *126* (40), 13016.
(43) Liberman-Martin, A. L.; Bergman, R. G.; Tilley, T. D. *J. Am. Chem. Soc.* **2013**, *135* (26), 9612.
(44) Shiba, Y.; Inagaki, A.; Akita, M. *Organometallics* **2015**, 150707141947001.
(45) Mateo, C.; Fernández-Rivas, C.; Cárdenas, D. J.; Echavarren, A. M. *Organometallics* **1998**, *17* (17), 3661.
(46) Liberman-Martin, A. L.; Levine, D. S.; Ziegler, M. S.; Bergman, R. G.; Tilley, T. D. *Chem. Commun. (Camb.)* **2016**, *52* (43), 7039.
(47) Bedford, R. B.; Hazelwood, S. L.; Albisson, D. A. *Organometallics* **2002**, *21* (13), 2599.
(48) Brune, H.-A.; Klotzbücher, R.; Berhalter, K.; Debaerdemaeker, T. *Journal of Organometallic Chemistry* **1989**, *369* (3), 321.
(49) Braterman, P. S.; Cross, R. J.; Young, G. B. *J. Chem. Soc., Dalton Trans.* **1976**, No. 14, 1306.
(50) Brune, H.-A.; Hupfer, E.; Schmidtberg, G.; Ziegler, U. *Journal of Organometallic Chemistry* **1992**, *440* (3), 303.
(51) Brune, H.-A.; Stapp, B.; Schmidtberg, G. *Journal of Organometallic Chemistry* **1986**, *307* (1), 129.
(52) Brune, H.-A.; Hupfer, E.; Schmidtberg, G.; Baur, A. *Journal of Organometallic Chemistry* **1992**, *424* (2), 225.
(53) Osakada, K. *Platinum–Carbon σ-Bonded Complexes*; Elsevier, 2007; pp 445–609.
(54) Kakeya, M.; Tanabe, M.; Nakamura, Y.; Osakada, K. *Journal of Organometallic Chemistry* **2009**, *694* (14), 2270.
(55) Phelps, J.; Butikofer, J. L.; Thapaliya, B.; Gale, E.; Vowell, C. L.; Debnath, S.; Arulsamy, N.; Roddick, D. M. *Polyhedron* **2016**, *116*, 197.
(56) Butikofer, J. L.; Hoerter, J. M.; Peters, R. G.; Roddick, D. M. *Organometallics*

2004, *23* (3), 400.
(57) Stang, P. J.; Kowalski, M. H. *J. Am. Chem. Soc.* **1989**, *111* (9), 3356.
(58) Stang, P. J.; Kowalski, M. H.; Schiavelli, M. D.; Longford, D. *J. Am. Chem. Soc.* **1989**, *111* (9), 3347.
(59) Widenhoefer, R. A.; Buchwald, S. L. *J. Am. Chem. Soc.* **1998**, *120* (26), 6504.
(60) Laurent, P.; Veyre, L.; Thieuleux, C.; Donet, S.; Copéret, C. *Dalton Trans.* **2013**, *42* (1), 238.
(61) Brusoe, A. T.; Hartwig, J. F. *J. Am. Chem. Soc.* **2015**.
(62) Khadra, A.; Mayer, S.; Mitchell, D.; Rodriguez, M. J.; Organ, M. G. *Organometallics* **2017**, *36* (18), 3573.
(63) Bhayana, B.; Fors, B. P.; Buchwald, S. L. *Org. Lett.* **2009**, *11* (17), 3954.
(64) Chung, K. H.; So, C. M.; Wong, S. M.; Luk, C. H.; Zhou, Z.; Lau, C. P.; Kwong, F. Y. *Chem. Commun.* **2012**, *48* (14), 1967.
(65) Wong, S. *Org. Synth.* **2015**, *92*, 195.
(66) Alsabeh, P. G.; Stradiotto, M. **2013**, *52* (28), 7242.
(67) Legzdins, P. *Organometallics* **1991**, 986.
(68) Dryden, N. H.; Legzdins, P.; Trotter, J.; Yee, V. C. *Organometallics* **1991**, *10* (8), 2857.
(69) Love, B. E.; Jones, E. G. *J. Org. Chem.* **1999**, *64* (10), 3755.
(70) Gair, J. J.; Qiu, Y.; Chan, N. H.; Filatov, A. S.; Lewis, J. C. *Organometallics* **2017**, *36* (24), 4699.
(71) Anaby, A.; Feller, M.; Ben-David, Y.; Leitus, G.; Diskin-Posner, Y.; Shimon, L. J. W.; Milstein, D. *J. Am. Chem. Soc.* **2016**, *138* (31), 9941.
(72) Ben Ari, E.; Cohen, R.; Gandelman, M.; Shimon, L. J. W.; Martin, J. M. L.; Milstein, D. *Organometallics* **2006**, *25* (13), 3190.
(73) Ben Ari, E.; Leitus, G.; Shimon, L. J. W.; Milstein, D. *J. Am. Chem. Soc.* **2006**, *128* (48), 15390.
(74) Zhang, X.; Kanzelberger, M.; Emge, T. J.; Goldman, A. S. *J. Am. Chem. Soc.* **2004**, *126* (41), 13192.
(75) Feller, M.; Ben Ari, E.; Diskin-Posner, Y.; Carmieli, R.; Weiner, L.; Milstein, D. *J. Am. Chem. Soc.* **2015**, 150401074058002.
(76) Gatard, S.; Çelenligil-Çetin, R.; Guo, C.; Foxman, B. M.; Ozerov, O. V. *J. Am. Chem. Soc.* **2006**, *128* (9), 2808.
(77) Puri, M.; Gatard, S.; Smith, D. A.; Ozerov, O. V. *Organometallics* **2011**, *30* (9), 2472.
(78) Fan, L.; Parkin, S.; Ozerov, O. V. *J. Am. Chem. Soc.* **2005**, *127* (48), 16772.
(79) Gatard, S.; Guo, C.; Foxman, B. M.; Ozerov, O. V. *Organometallics* **2007**, *26* (25), 6066.
(80) Sun, C.-L.; Shi, Z.-J. *Chem. Rev.* **2014**, *114* (18), 9219.
(81) Sun, C.-L.; Li, H.; Yu, D.-G.; Yu, M.; Zhou, X.; Lu, X.-Y.; Huang, K.; Zheng, S.-F.; Li, B.-J.; Shi, Z.-J. *Nature Chemistry* **2010**, *2* (12), 1044.
(82) Studer, A.; Curran, D. P. *Nature Chemistry* **2014**, *6* (9), 765.
(83) Neely, J. M.; Bezdek, M. J.; Chirik, P. J. *ACS Cent. Sci.* **2016**, *2* (12), 935.

(84) Obligacion, J. V.; Semproni, S. P.; Pappas, I.; Chirik, P. J. *J. Am. Chem. Soc.* **2016**, *138* (33), 10645.

(85) Bernskoetter, W. H.; Hanson, S. K.; Buzak, S. K.; Davis, Z.; White, P. S.; Swartz, R.; Goldberg, K. I.; Brookhart, M. *J. Am. Chem. Soc.* **2009**, *131* (24), 8603.

(86) Duplais, C.; Krasovskiy, A.; Wattenberg, A.; Lipshutz, B. H. *Chem. Commun.* **2010**, *46* (4), 562.

(87) Ilangovan, A.; Anandhan, K.; Kaushik, M. P. *Tetrahedron Letters* **2015**, *56* (9), 1080.

(88) Giordano, G.; Crabtree, R. H. *Inorganic Syntheses*; John Wiley & Sons, Inc.: Hoboken, NJ, USA, 1990; Vol. 28, pp 90–91.

(89) Leung, W.-P.; Ip, Q. W.-Y.; Wong, S.-Y.; Mak, T. C. W. *Organometallics* **2003**, *22* (22), 4604.

(90) Kawatsura, M.; Hartwig, J. F. *Organometallics* **2001**, *20* (10), 1960.

(91) Feller, M.; Diskin-Posner, Y.; Leitus, G.; Shimon, L. J. W.; Milstein, D. *J. Am. Chem. Soc.* **2013**, *135* (30), 11040.

(92) Hermann, D.; Gandelman, M.; Rozenberg, H.; Shimon, L. J. W.; Milstein, D. *Organometallics* **2002**, *21* (5), 812.

(93) Hanson, S. K.; Heinekey, D. M.; Goldberg, K. I. *Organometallics* **2008**, *27* (7), 1454.

(94) Kubota, Y.; Hanaoka, T.-A.; Takeuchi, K.; Sugi, Y. *J. Chem. Soc. Chem. Commun.* **1994**, No. 13, 1553.

(95) Feller, M.; Ben Ari, E.; Diskin-Posner, Y.; Carmieli, R.; Weiner, L.; Milstein, D. *J. Am. Chem. Soc.* **2015**, *137* (14), 4634.

(96) *Gaussian 09, Revision D.01, M. J. Frisch, G. W. Trucks, H. B. Schlegel, G. E. Scuseria, M. A. Robb, J. R. Cheeseman, G. Scalmani, V. Barone, B. Mennucci, G. A. Petersson, H. Nakatsuji, M. Caricato, X. Li, H. P. Hratchian, A. F. Izmaylov, J. Bloino, G. Zheng, J. L. Sonnenberg, M. Hada, M. Ehara, K. Toyota, R. Fukuda, J. Hasegawa, M. Ishida, T. Nakajima, Y. Honda, O. Kitao, H. Nakai, T. Vreven, J. A. Montgomery, Jr., J. E. Peralta, F. Ogliaro, M. Bearpark, J. J. Heyd, E. Brothers, K. N. Kudin, V. N. Staroverov, T. Keith, R. Kobayashi, J. Normand, K. Raghavachari, A. Rendell, J. C. Burant, S. S. Iyengar, J. Tomasi, M. Cossi, N. Rega, J. M. Millam, M. Klene, J. E. Knox, J. B. Cross, V. Bakken, C. Adamo, J. Jaramillo, R. Gomperts, R. E. Stratmann, O. Yazyev, A. J. Austin, R. Cammi, C. Pomelli, J. W. Ochterski, R. L. Martin, K. Morokuma, V. G. Zakrzewski, G. A. Voth, P. Salvador, J. J. Dannenberg, S. Dapprich, A. D. Daniels, O. Farkas, J. B. Foresman, J. V. Ortiz, J. Cioslowski, and D. J. Fox, Gaussian, Inc., Wallingford CT, 2013.*

(97) Grimme, S.; Antony, J.; Ehrlich, S.; Krieg, H. *J. Chem. Phys.* **2010**, *132* (15), 154104.

(98) Mennucci, B.; Tomasi, J. *J. Chem. Phys.* **1997**, *106* (12), 5151.

(99) Cancès, E.; Mennucci, B.; Tomasi, J. *J. Chem. Phys.* **1997**, *107* (8), 3032.

(100) Scalmani, G.; Frisch, M. J. *J. Chem. Phys.* **2010**, *132* (11), 114110.

(101) Essafi, S.; Tomasi, S.; Aggarwal, V. K.; Harvey, J. N. *J. Org. Chem.* **2014**,

79 (24), 12148.
(102) Plata, R. E.; Singleton, D. A. *J. Am. Chem. Soc.* **2015**, *137* (11), 3811.
(103) Schramm, V. L. *Annu. Rev. Biochem.* **2011**, *80* (1), 703.
(104) Wolfenden, R. *Acc. Chem. Res.* **1972**, *5* (1), 10.
(105) Wolfenden, R.; Kati, W. M. *Acc. Chem. Res.* **1991**, *24* (7), 209.
(106) Kurz, J. L. *J. Am. Chem. Soc.* **1963**, *85* (7), 987.
(107) Kurz, J. L. *Acc. Chem. Res.* **1972**, *5* (1), 1.
(108) Hoffmann, R. *Angew. Chem. Int. Ed. Engl.* **1982**, *21* (10), 711.
(109) Albright, T. A.; Burdett, J. K.; Whangbo, M.-H. *Orbital Interactions in Chemistry*; John Wiley & Sons, Inc.: Hoboken, NJ, USA, 2013.
(110) Powers, D. C.; Ritter, T. *Organometallics* **2013**, *32* (7), 2042.
(111) van der Vlugt, J. I.; Reek, J. N. H. *Angew. Chem. Int. Ed. Engl.* **2009**, *48* (47), 8832.
(112) Khusnutdinova, J. R.; Milstein, D. *Angew. Chem. Int. Ed. Engl.* **2015**, *54* (42), 12236.
(113) Gunanathan, C.; Milstein, D. In *Bifunctional Molecular Catalysis*; Ikariya, T., Shibasaki, M., Eds.; Topics in Organometallic Chemistry; Springer Berlin Heidelberg: Berlin, Heidelberg, 2011; Vol. 37, pp 55–84.
(114) Milstein, D. *Top. Catal.* **2010**, *53* (13-14), 915.
(115) Ess, D. H.; Goddard, W. A., III; Periana, R. A. *Organometallics* **2010**.
(116) Iron, M. A.; Ben Ari, E.; Cohen, R.; Milstein, D. *Dalton Trans.* **2009**, No. 43, 9433.
(117) Li, H.; Hall, M. B. *ACS Catal.* **2015**, *5* (3), 1895.
(118) Cadenbach, T.; Bollermann, T.; Gemel, C.; Tombul, M.; Fernandez, I.; Hopffgarten, M. V.; Frenking, G.; Fischer, R. A. *J. Am. Chem. Soc.* **2009**, *131* (44), 16063.
(119) Raubenheimer, H. G.; Schmidbaur, H. *Organometallics* **2012**, *31* (7), 2507.
(120) Paenurk, E.; Gershoni-Poranne, R.; Chen, P. *Organometallics* **2017**, *36* (24), 4854.
(121) Baya, M.; Belío, Ú.; Fernandez, I.; Fuertes, S.; Martín, A. *Angew. Chem.* **2016**, *128* (24), 7092.
(122) Kloek, S. M.; Heinekey, D. M.; Goldberg, K. I. **2007**, *46* (25), 4736.
(123) Schwartsburd, L.; Iron, M. A.; Konstantinovski, L.; Diskin-Posner, Y.; Leitus, G.; Shimon, L. J. W.; Milstein, D. *Organometallics* **2010**, *29* (17), 3817.
(124) Bollermann, T.; Gemel, C.; Fischer, R. A. *Coordination Chemistry Reviews* **2011**, *256* (5-8), 537.
(125) Bauer, J.; Braunschweig, H.; Dewhurst, R. D. *Chem. Rev.* **2012**, *112* (8), 4329.
(126) Oeschger, R. J.; Chen, P. *Organometallics* **2017**, *36* (8), 1465.
(127) Oeschger, R. J.; Chen, P. *J. Am. Chem. Soc.* **2017**, *139* (3), 1069.
(128) Cordero, B.; Gómez, V.; Platero-Prats, A. E.; Revés, M.; Echeverría, J.; Cremades, E.; Barragán, F.; Alvarez, S. *Dalton Trans.* **2008**, *40* (21), 2832.
(129) Bader, R. F. W. *Acc. Chem. Res.* **1974**, *8* (1), 34.
(130) Bader, R. F. W. *Chem. Rev.* **1991**, *91* (5), 893.

(131) Bader, R. F. W. *J. Phys. Chem. A* **2009**, *113* (38), 10391.
(132) Zhang, Y.; Lewis, J. C.; Bergman, R. G.; Ellman, J. A.; Oldfield, E. *Organometallics* **2006**, *25* (14), 3515.
(133) Yao, W.; Eisenstein, O.; Crabtree, R. H. *Inorganica Chimica Acta* **1997**, *254* (1), 105.
(134) Popelier, P. L. A.; Logothetis, G. *Journal of Organometallic Chemistry* **1998**, *555* (1), 101.
(135) Allen, F. H.; Bruno, I. J. *Acta Cryst Sect A Found Cryst* **2010**, *66* (3), 380.
(136) Ekkert, O.; White, A. J. P.; Toms, H.; Crimmin, M. R. *Chem. Sci.* **2015**, *6* (10), 5617.
(137) Papp, T.; Kollar, L.; Kegl, T. *Journal of Quantum Chemistry* **2014**, *2014* (6), 1.
(138) Hamdaoui, M.; Ney, M.; Sarda, V.; Karmazin, L.; Bailly, C.; Sieffert, N.; Dohm, S.; Hansen, A.; Grimme, S.; Djukic, J.-P. *Organometallics* **2016**, *35* (13), 2207.
(139) Cheng, F.; Sun, H.; Zhang, Y.; Mukkamala, D.; Oldfield, E. *J. Am. Chem. Soc.* **2005**, *127* (36), 12544.
(140) Brammer, L. *Dalton Trans.* **2003**, No. 16, 3145.
(141) Brookhart, M.; Green, M. L. H.; Parkin, G. *Proceedings of the National Academy of Sciences* **2007**, *104* (17), 6908.
(142) Weinhold, F.; Landis, C. R. *Valency and bonding: a natural bond orbital donor-acceptor perspective*; 2005.
(143) Burfield, D. R.; Lee, K.-H.; Smithers, R. H. *J. Org. Chem.* **1977**, *42* (18), 3060.
(144) BieglerKönig, F. *Journal of Computational Chemistry* **2001**, *22* (5), 545.
(145) Neufeldt, S. R.; Sanford, M. S. *Acc. Chem. Res.* **2012**, *45* (6), 936.
(146) Davies, H. M. L.; Morton, D. *Chemical Society Reviews* **2011**, *40* (4), 1857.
(147) Hartwig, J. F. *J. Am. Chem. Soc.* **2016**, *138* (1), 2.
(148) Engle, K. M.; Mei, T.-S.; Wasa, M.; Yu, J.-Q. *Acc. Chem. Res.* **2012**, *45* (6), 788.
(149) Chen, X.; Engle, K. M.; Wang, D.-H.; Yu, J.-Q. **2009**, *48* (28), 5094.
(150) Engle, K. M.; Wang, D. H.; Yu, J. Q. *J. Am. Chem. Soc.* **2010**, *132* (40), 14137.
(151) Baxter, R. D.; Sale, D.; Engle, K. M.; Yu, J. Q.; Blackmond, D. G. *J. Am. Chem. Soc.* **2012**, *134* (10), 4600.
(152) Chu, L.; Xiao, K. J.; Yu, J. Q. *Science* **2014**, *346* (6208), 451.
(153) Cheng, X.-F.; Li, Y.; Su, Y.-M.; Yin, F.; Wang, J.-Y.; Sheng, J.; Vora, H. U.; Wang, X.-S.; Yu, J.-Q. *J. Am. Chem. Soc.* **2013**, *135* (4), 1236.
(154) Chu, L.; Wang, X.-C.; Moore, C. E.; Rheingold, A. L.; Yu, J.-Q. *J. Am. Chem. Soc.* **2013**, *135* (44), 16344.
(155) Xiao, K.-J.; Chu, L.; Yu, J.-Q. *Angew. Chem.* **2016**, *128* (8), 2906.
(156) Laforteza, B. N.; Chan, K. S. L.; Yu, J.-Q. *Angew. Chem.* **2015**, *127* (38), 11295.
(157) Shi, B.-F.; Maugel, N.; Zhang, Y.-H.; Yu, J.-Q. **2008**, *47* (26), 4882.

(158) Engle, K. M. *Pure and Applied Chemistry* **2016**.
(159) Haines, B. E.; Musaev, D. G. *ACS Catal.* **2015**, *5* (2), 830.
(160) Musaev, D. G.; Figg, T. M.; Kaledin, A. L. *Chemical Society Reviews* **2014**, *43* (14), 5009.
(161) Musaev, D. G.; Kaledin, A.; Shi, B. F.; Yu, J. Q. *J. Am. Chem. Soc.* **2012**, *134* (3), 1690.
(162) Zhong, X. M.; Cheng, G. J.; Chen, P.; Zhang, X. H.; Wu, Y. D. *Org. Lett.* **2016**, *18* (20), 5240.
(163) Cong, X. F.; Tang, H. R.; Wu, C.; Zeng, H. M. *Organometallics* **2013**, *32* (21), 6565.
(164) Cheng, G. J.; Chen, P.; Sun, T. Y.; Zhang, X. H.; Yu, J. Q.; Wu, Y. D. *Chem. Eur. J.* **2015**, *21* (31), 11180.
(165) Cheng, G.-J.; Yang, Y.-F.; Liu, P.; Chen, P.; Sun, T.-Y.; Li, G.; Zhang, X.; Houk, K. N.; Yu, J.-Q.; Wu, Y.-D. *J. Am. Chem. Soc.* **2014**, *136* (3), 894.
(166) Baxter, R. D.; Sale, D.; Engle, K. M.; Yu, J.-Q.; Blackmond, D. G. *J. Am. Chem. Soc.* **2012**, *134* (10), 4600.
(167) Biswas, B.; Sugimoto, M.; Sakaki, S. *Organometallics* **2000**, *19* (19), 3895.
(168) Davies, D. L.; Donald, S. M. A.; Macgregor, S. A. *J. Am. Chem. Soc.* **2005**, *127* (40), 13754.
(169) Gorelsky, S. I.; Lapointe, D.; Fagnou, K. *J. Am. Chem. Soc.* **2008**, *130* (33), 10848.
(170) Ackermann, L. *Chem. Rev.* **2011**, *111*, 1315.
(171) Gaunt, J. C.; Shaw, B. L. *Journal of Organometallic Chemistry* **1975**, *102* (4), 511.
(172) **2003**, 1.
(173) Ryabov, A. D.; Sakodinskaya, I. K.; Yatsimirsky, A. K. *J. Chem. Soc., Dalton Trans.* **1985**, No. 12, 2629.
(174) Thompson, J. M.; Heck, R. F. *J. Org. Chem.* **1975**.
(175) Van Der Ploeg, A.; Van Koten, G.; Vrieze, K. *Journal of Organometallic Chemistry* **1981**, *222* (1), 155.
(176) *Footnote Geometry optimizations and frequency calculations were performed at the B3LYP-D3BJ/[6-31G(d,p) + Lanl2dz (Pd, I)] level of theory (B3LYP-D3BJ/BS1) with a polarizable continuum model (PCM) using dichloromethane to account for solvent effects. The reported energies are calculated at the B3LYP-D3BJ/[6-311+G(2d,p) + SDD (Pd, I)] level with Gibbs free energy corrections to a solution standard state of 1M at 298.15 K with either the PCM model for methanol or dichloromethane. (See SI for full description of computational methodology).*
(177) Deprez, N. R.; Sanford, M. S. *J. Am. Chem. Soc.* **2009**, *131* (31), 11234.
(178) Cook, A. K.; Cook, A. K.; Sanford, M. S.; Sanford, M. S. *J. Am. Chem. Soc.* **2015**, *137* (8), 3109.
(179) Powers, D. C.; Lee, E.; Ariafard, A.; Sanford, M. S.; Yates, B. F.; Canty, A. J.; Ritter, T. *J. Am. Chem. Soc.* **2012**, *134* (29), 12002.
(180) Powers, D. C.; Xiao, D. Y.; Geibel, M. A. L.; Ritter, T. *J. Am. Chem. Soc.*

2010, *132* (41), 14530.

(181) Powers, D. C.; Ritter, T. *Nature Chemistry* **2009**, *1* (4), 302.

(182) Powers, D. C.; Benitez, D.; Tkatchouk, E.; Goddard, W. A., III; Ritter, T. *J. Am. Chem. Soc.* **2010**, *132* (40), 14092.

(183) Haines, B. E.; Berry, J. F.; Yu, J.-Q.; Musaev, D. G. *ACS Catal.* **2016**, *6* (2), 829.

(184) Liou, L. R.; McNeil, A. J.; Ramirez, A.; Toombes, G. E. S.; Gruver, J. M.; Collum, D. B. *J. Am. Chem. Soc.* **2008**, *130* (14), 4859.

(185) Liou, L. R.; McNeil, A. J.; Toombes, G. E. S.; Collum, D. B. *J. Am. Chem. Soc.* **2008**, *130* (51), 17334.

(186) Stejskal, E. O.; Tanner, J. E. *J. Chem. Phys.* **1965**, *42* (1), 288.

(187) Pregosin, P. S.; Kumar, P. G. A.; Fernández, I. *Chem. Rev.* **2005**, *105* (8), 2977.

(188) Perrin, C. L.; Dwyer, T. J. *Chem. Rev.* **1990**, *90* (6), 935.

(189) Renny, J. S.; Tomasevich, L. L.; Tallmadge, E. H.; Collum, D. B. *Angew. Chem. Int. Ed. Engl.* **2013**, *52* (46), 11998.

(190) *Footnote Mixed MPAA/OAc complex* ***10*** *is also observed in the equilibrium mixture and is shown in the supporting information in section S1.8.*

(191) *Footnote We also calculated the mixed intermediate species in the exchange equilibrium with Gly. The overall equilibrium is* ***2e*** *+ 2 AcNH-Gly-OH* ***2h*** *+ AcOH + AcNH-Gly-OH* ***2a*** *+ 2 AcOH with ΔG = -2.3 and -1.7 kcal/mol for each step. These energy values are consistent with a produce distribution of* ***2a/2h/2e*** *= 89.7%/10.2%/0.1%. Thus, the DFT calculations slightly overestimate the ligand exchange equilibrium but the trend is consistent with the experimental results.*

(192) Gao, D.-W.; Shi, Y.-C.; Gu, Q.; Zhao, Z.-L.; You, S.-L. *J. Am. Chem. Soc.* **2013**, *135* (1), 86.

(193) Pi, C.; Li, Y.; Cui, X.; Zhang, H.; Han, Y.; Wu, Y. *Chem. Sci.* **2013**, *4* (6), 2675.

(194) Sokolov, V. I.; Troitskaya, L. L.; Reutov, O. A. *Journal of Organometallic Chemistry* **1979**, *182* (4), 537.

(195) Sokolov, V. I.; Troitskaya, L. L.; Khrushchova, N. S. *Journal of Organometallic Chemistry* **1983**, *250* (1), 439.

(196) Dendele, N.; Bisaro, F.; Gaumont, A.-C.; Perrio, S.; Richards, C. J. *Chem. Commun.* **2012**, *48* (14), 1991.

(197) Günay, M. E.; Richards, C. J. *Organometallics* **2009**, *28* (19), 5833.

(198) Desai, L. V.; Stowers, K. J.; Sanford, M. S. *J. Am. Chem. Soc.* **2008**, *130* (40), 13285.

(199) Canty, A. J.; Minchin, N. J.; Skelton, B. W.; White, A. H. *J. Chem. Soc., Dalton Trans.* **1986**, No. 10, 2205.

(200) Hollis, T. K.; Overman, L. E. *Tetrahedron Letters* **1997**, *38* (51), 8837.

(201) *Footnote The observed ions are represented as carboxylate bridged dimers based on our characterization of* ***1a*** *and* ***2a-e,*** *as well as reported acetate and trifluoroacetate bridged analogues of* ***3c*** *and* ***3b,*** *though further*

structural work would be required to rigorously establish the proposed connectivity.

(202) Yakushev, I. Y.; Gekhman, A. E.; Klyagina, A. P. *Russian Journal of Coordination Chemistry* **2016**, *42* (9), 604.

(203) Fuchita, Y. *Inorg. Chem.* **1982**, *20* (12), 4316.

(204) Shi, B.-F.; Zhang, Y.-H.; Lam, J. K.; Wang, D.-H.; Yu, J.-Q. *J. Am. Chem. Soc.* **2010**, *132* (2), 460.

(205) Tang, R.-Y.; Li, G.; Yu, J.-Q. *Nature* **2014**, *507* (7491), 215.

(206) Wang, X.-C.; Hu, Y.; Bonacorsi, S.; Hong, Y.; Burrell, R.; Yu, J.-Q. *J. Am. Chem. Soc.* **2013**, *135* (28), 10326.

(207) *Footnote Bromination of* ***6b*** *proceeds orders of magnitude faster than iodination, consistent with calculated barriers to palladacycle halogenation: see figure S1.2 in the supporting information.*

.

(208) Vicente, J.; Saura-Llamas, I.; Palin, M. G.; Jones, P. G.; Ramírez de Arellano, M. C. *Organometallics* **1997**, *16* (5), 826.

(209) *Footnote It should be noted that the lowest energy dimer pathway for C-H activation calculated here is different than the pathway reported by us in ref. 45. See Figure S2.1 for a comparison of these pathways.*

(210) Haines, B. E.; Xu, H.; Verma, P.; Wang, X.-C.; Yu, J.-Q.; Musaev, D. G. *J. Am. Chem. Soc.* **2015**, *137* (28), 9022.

(211) Rogachev, A. Y.; Hoffmann, R. *J. Am. Chem. Soc.* **2013**, *135* (8), 3262.

(212) Umakoshi, K.; Ichimura, A.; Kinoshita, I.; Ooi, S. *Inorg. Chem.* **1990**, *29* (20), 4005.

(213) Powers, D. C.; Ritter, T. *Acc. Chem. Res.* **2012**, *45* (6), 840.

(214) Kornecki, K. P.; Berry, J. F.; Powers, D. C.; Ritter, T. In *Metal-Metal Bond-Containing Complexes as Catalysts for C-H Functionalization*; Progress in Inorganic Chemistry; John Wiley & Sons, Inc.: Hoboken, New Jersey, 2014; Vol. 58, pp 225–302.

(215) Cammarota, R. C.; Lu, C. C. *J. Am. Chem. Soc.* **2015**, *137* (39), 12486.

(216) Siedschlag, R. B.; Bernales, V.; Vogiatzis, K. D.; Planas, N.; Clouston, L. J.; Bill, E.; Gagliardi, L.; Lu, C. C. *J. Am. Chem. Soc.* **2015**, 150323142749002.

(217) Borovik, A. S. *Acc. Chem. Res.* **2005**, *38* (1), 54.

(218) Cook, S. A.; Borovik, A. S. *Acc. Chem. Res.* **2015**, *48* (8), 2407.

(219) Powers, D. C.; Ritter, T. *Nature Chemistry* **2009**, *1* (4), 302.

(220) Jones, T. C.; Nielson, A. J.; Rickard, C. E. *Australian Journal of Chemistry* **1984**, *37*, 2179.

(221) Cope, A. C.; Friedrich, E. C. *Journal of the American Chemical …* **1968**, *90* (4), 909.

(222) Pfeffer, M. *Inorganic Syntheses* **1989**, *26*, 211.

(223) Hiraki, K.; Fuchita, Y.; Pfeffer, M. *Inorganic Syntheses* **2007**, *16*, 208.

(224) Milani, J.; Pridmore, N. E.; Whitwood, A. C.; Fairlamb, I. J. S.; Perutz, R. N. *Organometallics* **2015**, *34* (17), 4376.

(225) Tayama, E.; Kimura, H. **2007**, *46* (46), 8869.

(226) Wang, D.-H.; Engle, K. M.; Shi, B.-F.; Yu, J.-Q. *Science* **2010**, *327* (5963), 315.

(227) Leow, D.; Li, G.; Mei, T.-S.; Yu, J.-Q. *Nature* **2012**, *486* (7404), 518.

(228) Chan, K.; Wasa, M.; Chu, L.; Laforteza, B. N.; Miura, M. *Nature Chemistry* **2014**.

(229) Chu, L.; Shang, M.; Tanaka, K.; Chen, Q.; Pissarnitski, N.; Streckfuss, E.; Yu, J.-Q. *ACS Cent. Sci.* **2015**, *1* (7), 394.

(230) Zhang, Z.; Tanaka, K.; Yu, J.-Q. *Nature* **2017**, *543* (7646), 538.

(231) Zhu, Y.; Chen, X.; Yuan, C.; Li, G.; Zhang, J.; Zhao, Y. *Nature Communications* **2017**, *8*, 1.

(232) Shi, B.-F.; Maugel, N.; Zhang, Y.-H.; Yu, J.-Q. **2008**, *47* (26), 4882.

(233) Li, G.; Wan, L.; Zhang, G.; Leow, D.; Spangler, J.; Yu, J.-Q. *J. Am. Chem. Soc.* **2015**, *137* (13), 4391.

(234) Upp, D. M.; Lewis, J. C. *Current Opinion in Chemical Biology* **2017**, *37*, 48.

(235) Breslow, R.; Campbell, P. *J. Am. Chem. Soc.* **1969**, *91* (11), 3085.

(236) Yang, J.; Gabriele, B.; Belvedere, S.; Huang, Y.; Breslow, R. *J. Org. Chem.* **2002**, *67* (15), 5057.

(237) Leung, D. H.; Fiedler, D.; Bergman, R. G.; Raymond, K. N. **2004**, *43* (8), 963.

(238) Das, S.; Brudvig, G. W.; Crabtree, R. H. *J. Am. Chem. Soc.* **2008**, *130* (5), 1628.

(239) Mihai, M. T.; Davis, H. J.; Genov, G. R.; Phipps, R. J. *ACS Catal.* **2018**, 3764.

(240) Plata, R. E.; Hill, D. E.; Haines, B. E.; Musaev, D. G.; Chu, L.; Hickey, D. P.; Sigman, M. S.; Yu, J.-Q.; Blackmond, D. G. *J. Am. Chem. Soc.* **2017**, *139* (27), 9238.

(241) Hill, D. E.; Bay, K. L.; Yang, Y.-F.; Plata, R. E.; Takise, R.; Houk, K. N.; Yu, J.-Q.; Blackmond, D. G. *J. Am. Chem. Soc.* **2017**, *139* (51), 18500.

(242) Navarro, R.; García, J.; Urriolabeitia, E. P.; Cativiela, C.; Diaz-de-Villegas, M. D. *Journal of Organometallic Chemistry* **1995**, *490* (1-2), 35.

(243) Gair, J. J.; Haines, B. E.; Filatov, A. S.; Musaev, D. G.; Lewis, J. C. *Chem. Sci.* **2017**, *8* (8), 5746.

(244) Deprez, N. R.; Sanford, M. S. *J. Am. Chem. Soc.* **2009**, *131* (31), 11234.

(245) Powers, D. C.; Geibel, M. A. L.; Klein, J. E. M. N.; Ritter, T. *J. Am. Chem. Soc.* **2009**, *131* (47), 17050.

(246) Haines, B. E.; Berry, J. F.; Yu, J. Q.; Musaev, D. G. *ACS Catal.* **2016**, 829.

(247) Bercaw, J. E.; Durrell, A. C.; Gray, H. B.; Green, J. C.; Hazari, N.; Labinger, J. A.; Winkler, J. R. *Inorg. Chem.* **2010**, *49* (4), 1801.

(248) Gao, D.-W.; Gu, Q.; Zheng, C.; You, S.-L. *Acc. Chem. Res.* **2017**, *50* (2), 351.

(249) Gao, D.-W.; Gu, Q.; You, S.-L. *J. Am. Chem. Soc.* **2016**, *138* (8), 2544.

(250) Pi, C.; Cui, X.; Liu, X.; Guo, M.; Zhang, H.; Wu, Y. *Org. Lett.* **2014**, *16* (19), 5164.

(251) Shi, Y.-C.; Yang, R.-F.; Gao, D.-W.; You, S.-L. *Beilstein J. Org. Chem.* **2013**,

9 (1), 1891.
(252) Colquhoun, H. M.; Powell, C. T.; Zhu, Z.; Cardin, C. J.; Gan, Y.; Tootell, P.; Tsang, J. S. W.; Boag, N. M. *Eur. J. Inorg. Chem.* **2009**, *2009* (8), 999.
(253) Khrushchova, N. S.; Troitskaya, L. L.; Sokolov, V. I. *Journal of Organometallic …* **1983**, 439.
(254) Komatsu, T.; Nonoyama, M.; Fujita, J. *Bull. Chem. Soc. Jpn.* **1981**, *54* (1), 186.
(255) Schaarschmidt, D.; Lang, H. *Organometallics* **2013**, *32* (20), 5668.
(256) Djukic, J.-P.; Hijazi, A.; Flack, H. D.; Bernardinelli, G. *Chem. Soc. Rev.* **2008**, *37* (2), 406.
(257) Günay, M. E.; Ilyashenko, G.; Richards, C. J. *Tetrahedron Asym.* **2010**, *21* (23), 2782.
(258) Zhu, D.-Y.; Chen, P.; Xia, J.-B. *ChemCatChem* **2015**, *8* (1), 68.
(259) Davies, H. M. L.; Morton, D. *ACS Cent. Sci.* **2017**, *3* (9), 936.
(260) Andorfer, M. C.; Park, H. J.; Vergara-Coll, J.; Lewis, J. C. *Chem. Sci.* **2016**, *7* (6), 3720.
(261) Davis, H. J.; Phipps, R. J. *Chem. Sci.* **2017**, *8* (2), 864.
(262) Hartwig, J. F. *Acc. Chem. Res.* **2017**, *50* (3), 549.
(263) Váňa, J.; Lang, J.; Šoltésová, M.; Hanusek, J.; Růžička, A.; Sedlák, M.; Roithová, J. *Dalton Trans.* **2017**, *46* (46), 16269.
(264) Ryabov, A. D. *Inorg. Chem.* **1987**, *26*, 1252.
(265) Wang, D.; Weinstein, A. B.; White, P. B.; Stahl, S. S. *Chem. Rev.* **2018**, *118* (5), 2636.
(266) Stahl, S. S. *Angew. Chem. Int. Ed. Engl.* **2004**, *43* (26), 3400.
(267) Blackmond, D. G. *Angew. Chem. Int. Ed. Engl.* **2005**, *44* (28), 4302.
(268) Blackmond, D. G. *J. Am. Chem. Soc.* **2015**, *137* (34), 10852.
(269) Hill, D. E.; Pei, Q.-L.; Zhang, E.-X.; Gage, J. R.; Yu, J.-Q.; Blackmond, D. G. *ACS Catal.* **2018**, 1528.
(270) Stegelmann, C.; Andreasen, A.; Campbell, C. T. *J. Am. Chem. Soc.* **2009**, *131* (23), 8077.
(271) Kozuch, S.; Shaik, S. *Acc. Chem. Res.* **2011**, *44* (2), 101.
(272) Campbell, C. T. *ACS Catal.* **2017**, *7* (4), 2770.
(273) Campbell, C. T. *Top. Catal.* **1994**, *1* (3-4), 353.
(274) Dumesic, J. A. *Journal of Catalysis* **1999**, *185* (2), 496.
(275) Campbell, C. T. *Journal of Catalysis* **2001**, *204* (2), 520.
(276) Michaelis, L.; Menten, M. L.; Johnson, K. A.; Goody, R. S. *Biochemistry* **2011**, *50* (39), 8264.
(277) Simmons, E. M.; Hartwig, J. F. *Angew. Chem. Int. Ed.* **2012**, *51* (13), 3066.
(278) Algera, R. F.; Gupta, L.; Hoepker, A. C.; Liang, J.; Ma, Y.; Singh, K. J.; Collum, D. B. *J. Org. Chem.* **2017**, *82* (9), 4513.
(279) Liang, J.; Hoepker, A. C.; Bruneau, A. M.; Ma, Y.; Gupta, L.; Collum, D. B. *J. Org. Chem.* **2014**, *79* (24), 11885.
(280) Murdoch, J. R. *J. Chem. Educ.* **1981**, *58* (1), 32.
(281) Laidler, K. J. *J. Chem. Educ.* **1988**, *65* (3), 250.

(282) Ray, W. J., Jr. *Biochemistry* **2002**, *22* (20), 4625.
(283) Ma, Y.; Hoepker, A. C.; Gupta, L.; Faggin, M. F.; Collum, D. B. *J. Am. Chem. Soc.* **2010**, *132* (44), 15610.
(284) Gupta, L.; Hoepker, A. C.; Ma, Y.; Viciu, M. S.; Faggin, M. F.; Collum, D. B. *J. Org. Chem.* **2013**, *78* (9), 4214.
(285) Louillat, M.-L.; Patureau, F. W. *Org. Lett.* **2012**, *15* (1), 164.
(286) Shevlin, M.; Friedfeld, M. R.; Sheng, H.; Pierson, N. A.; Hoyt, J. M.; Campeau, L.-C.; Chirik, P. J. *J. Am. Chem. Soc.* **2016**, *138* (10), 3562.
(287) Nielsen, L. P. C.; Stevenson, C. P.; Blackmond, D. G.; Jacobsen, E. N. *J. Am. Chem. Soc.* **2004**, *126* (5), 1360.
(288) Huang, C. Y. *Meth. Enzymol.* **1982**, *87*, 509.
(289) Jamakhandi, A. P.; Kuzmic, P.; Sanders, D. E.; Miller, G. P. *Biochemistry* **2007**, *46* (35), 10192.
(290) Miwa, G. T.; West, S. B.; Huang, M. T.; Lu, A. Y. *Journal of Biological Chemistry* **1979**, *254* (13), 5695.
(291) Miwa, G. T.; Lu, A. Y. H. *Arch. Biochem. Biophys.* **1981**, *211* (1), 454.
(292) Miwa, G. T.; Lu, A. Y. *Arch. Biochem. Biophys.* **1984**, *234* (1), 161.
(293) Doiuchi, T.; Yamaguchi, H.; Minoura, Y. *European Polymer Journal* **1981**, *17* (9), 961.
(294) Cowie, J. M. G.; Cree, S. H.; Ferguson, R. *European Polymer Journal* **1989**, *25* (7-8), 737.
(295) Prince, R. H.; Woolley, P. R. *J. Chem. Soc., Dalton Trans.* **1972**, No. 14, 1548.
(296) Fubin, J.; Bingying, J.; Yong, C.; Xiaoqi, Y.; Xiancheng, Z. *Journal of Molecular Catalysis A: Chemical* **2004**, *210* (1-2), 9.
(297) Wang, L.; Ye, Y.; Lykourinou, V.; Yang, J.; Angerhofer, A.; Zhao, Y.; Ming, L.-J. *Eur. J. Inorg. Chem.* **2017**, *2017* (42), 4899.
(298) Qiu, L.-G.; Xie, A.-J.; Shen, Y.-H. *Journal of Molecular Catalysis A: Chemical* **2006**, *244* (1-2), 58.
(299) Fujita, T.; Inaba, Y.; Ogino, K.; Tagaki, W. *Bull. Chem. Soc. Jpn.* **1988**, *61* (5), 1661.
(300) Benjelloun, A.; Lochon, P.; Brembilla, A. *Journal of Molecular Catalysis A: Chemical* **1999**, *140* (3), 215.
(301) Song, Y.; Han, X.; Guo, X.; Zeng, Q.; Jiang, F. *Colloids and Surfaces A: Physicochemical and Engineering Aspects* **2011**, *392* (1-1), 110.
(302) Jiang, H.-Y.; Zhou, C.-H.; Luo, K.; Chen, H.; Lan, J.-B.; Xie, R.-G. *Journal of Molecular Catalysis A: Chemical* **2006**, *260* (1-2), 288.
(303) Bhattacharya, S.; Snehalatha, K.; Kumar, V. P. *J. Org. Chem.* **2003**, *68* (7), 2741.
(304) Lykourinou, V.; Hanafy, A. I.; Bisht, K. S.; Angerhofer, A.; Ming, L.-J. *Eur. J. Inorg. Chem.* **2009**, *2009* (9), 1199.
(305) Lönnberg, T. A.; Helkearo, M.; Jancsó, A.; Gajda, T. *Dalton Trans.* **2012**, *41* (11), 3328.
(306) You, J.-S.; Yu, X.-Q.; Su, X.-Y.; Wang, T.; Xiang, Q.-X.; Yang, M.; Xie, R.-G.

Journal of Molecular Catalysis A: Chemical **2003**, *202* (1-2), 17.
(307) Faivre, V.; Brembilla, A.; Lochon, P. *Journal of Molecular Catalysis* **1993**, *85* (1), 45.
(308) Wang, L.; Ye, Y.; Lykourinou, V.; Angerhofer, A.; Ming, L.-J.; Zhao, Y. *Eur. J. Inorg. Chem.* **2011**, *2011* (5), 674.
(309) Xiang, Q. X.; Yu, X. Q.; Su, X. Y.; Yan, Q. S.; Wang, T. *Journal of Molecular Catalysis A: Chemical* **2002**.
(310) Mancin, F.; Tecilla, P.; Tonellato, U. *Langmuir* **2000**, *16* (1), 227.
(311) Budka, J.; Hampl, F.; Liska, F.; Scrimin, P.; Tecilla, P.; Tonellato, U. *Journal of Molecular Catalysis A: Chemical* **1996**, *104* (3), L201.
(312) Engle, K. M.; Wang, D.-H.; Yu, J.-Q. *J. Am. Chem. Soc.* **2010**, *132* (40), 14137.
(313) Musaev, D. G.; Kaledin, A.; Shi, B.-F.; Yu, J.-Q. *J. Am. Chem. Soc.* **2012**, *134* (3), 1690.
(314) Haines, B. E.; Musaev, D. G. *ACS Catal.* **2015**, *5* (2), 830.
(315) Park, Y.; Niemeyer, Z. L.; Yu, J.-Q.; Sigman, M. S. *Organometallics* **2018**, *37* (2), 203.
(316) Haines, B. E.; Yu, J.-Q.; Musaev, D. G. *ACS Catal.* **2017**, *7* (7), 4344.
(317) Davies, D. L.; Macgregor, S. A.; McMullin, C. L. *Chem. Rev.* **2017**, *117* (13), 8649.
(318) Dunina, V. V.; Razmyslova, E. D.; Kuz'mina, L. G.; Churakov, A. V.; Rubina, M. Y.; Grishin, Y. K. *Tetrahedron Asym.* **1999**, *10* (16), 3147.